Investigation into wind flow over complex topography and escarpments for wind turbine siting

Jerome Rowcroft

Bachelor of Engineering (Mechanical) (Hons)

Doctor of Philosophy

October 2015

Table of Contents

Abstract

Flow over cliffs is examined in a wind tunnel to determine how to improve wind turbine micro-siting. The research builds on existing research into flow over forward facing steps. It highlights the role of turbulence intensity in controlling the size of the mean recirculation bubble. Complexity is added to the forward facing step geometry by considering the effect of wind direction. The natural ruggedness associated with cliffs is then investigated, first by applying a sawtooth lateral variation to the crest of the forward facing step, and then by applying a sinusoidal lateral variation.

In considering wind direction, flow visualisation and pressure probe measurements demonstrate the presence of the separation region at the crest of the step, as well as the ejection of vortices from the separation region. Such features could adversely affect wind turbine performance. Based on the flow structure that was observed, it was recommended that the optimal site for a wind turbine should be half a step height downstream of the step, with the blades passing no lower than half a step height above the surface. Such a location would subject the wind turbines to maximum wind speeds, whilst minimising fluctuating loads and unbalanced loads across the wind turbine rotor.

Considering ruggedness, the amplitude to wavelength ratio of the sawtooth and sinusoidal lateral variations is varied. The development of the flow topology is observed using surface shear stress visualisation, pressure probe measurements and surface pressure tap measurements. The sawtooth cases are in good agreement with computational work performed. Delta wing style vortices were observed in all the cases where ruggedness was modelled. Sawtooth cases exhibit topological development as the amplitude to wavelength ratio is increased. With corresponding increases in amplitude to wavelength ratio, the flow topology in the sinusoidal cases remains constant. It was concluded that the curvature of the crest in the sinusoidal cases controls the development of secondary vortex structures that are induced by the delta wing vortices, keeping the secondary structures from increasing in size, thus causing the flow topology to remain equivalent as a function of the amplitude to wavelength ratio of the sinusoid.

Pressure probe measurements indicate that the vortex structures remains close to the surface over the rugged protrusions, but increase significantly in height with distance downstream, indicating that if wind turbines are to be sited in the vicinity of rugged cliffs, they ought to be sited on the centre of the protrusions, with the wind turbine rotors passing above a minimum height of half a step height.

Acknowledgements

Thanks for putting up with me! Particularly Karina.

Declaration of Originality

I declare that this is my own work, except where otherwise acknowledged.

This work has not been used to fulfil the requirements of any other degree or diploma.

Signed: *Rowcroft*

Date: 27th October 2015

List of Symbols and Abbreviations

A	Peak-to-peak amplitude of the lateral variations applied to the forward facing step
AS/NZS1170.2	Australian Standard/New Zealand Standard – Wind Loading Standard.
BL	Boundary Layer
C	Celsius
CFD	Computational Fluid Dynamics
C_P	Pressure Coefficient
DAQ	Data Acquisition
DIU	Data-acquisition Interface Unit
DNS	Direct Numerical Simulation
DPMS	Dynamic Pressure Measurement System
E_K	Kinetic Energy
f	Frequency
f_p	Peak frequency
FFS	Forward Facing Step
FFT	Fast Fourier Transform
g	Gravitational acceleration
h	Height of the forward facing step
Hz	Hertz
IEC	International Electro-technical Commission
$I_{uu}, I_{vv}, I_{ww}, I_{uvw}, I_{uv}$	Turbulence intensity. Subscript indicates velocity components considered
I_h	Stream-wise component of turbulence intensity at the step height
k	kilo-
l	Size of Cobra Probe head
L	Litre
L	Length of the forward facing step
LES	Large Eddy Simulation
$^xL_u, ^xL_v, ^xL_w$	Integral length scale. Subscript indicates dimension considered
m	milli-

m	Mass
M	Mega-
N	Number of node points in a topological analysis
P	Power; Pressure
PIV	Particle Image Velocimetry
PSD	Power Spectral Density
R	Wind Turbine Rotor Radius
$R_{uu}, R_{vv}, R_{ww}, R_{uv}, R_{uw}, R_{vw}$	Reynolds Stresses. Subscript indicates dimension considered
R_{xx}	Auto-correlation function
RANS	Reynolds Averaged Navier-Stokes
Re	Reynolds Number – specific form denoted by subscript. Where no subscript present, Reynolds number is based on step height, h.
Ri	Richardson Number – specific form denoted by subscript.
S	Speed-up; Number of Saddle points; Spectral Power
S_{Pr}	Predicted speed-up, based on Baker's hypothesis
St	Strouhal Number, based on height, h, unless otherwise stated
S_{xx}	Single-sided PSD
t	Time
T	Period
TFI	Turbulent Flow Instrumentation
TI	Turbulence Intensity
u, u'	Stream-wise velocity fluctuation
U	Mean stream-wise velocity
U_c	Convection velocity
U_P	Reference velocity measured at the up-stream Pitot-Static tube.
$\overline{uw}, u'w', <u'w'>$	Stream-wise – lateral Reynolds Stress
u_*	Friction velocity
v, v'	Lateral velocity fluctuation
V	Lateral velocity component; Volume
w, w'	Vertical velocity fluctuation

W	Vertical velocity component
x'	Distance perpendicular from the crest of the forward facing step.
x	Distance from datum in the direction of the free-stream flow; Time-series
X_L	Mean reattachment length
y'	Distance from datum along the crest of the forward facing step.
y	Distance from the datum in the direction perpendicular to the free-stream flow and parallel to the ground plane
z	Vertical distance from the datum
z_0	Roughness length
α	Power law shear exponent
δ, δ_{99}	Boundary layer thickness
∂	Denoting partial derivative
Δ	Finite difference
ϵ	Angle through which shear stress vector passes over the plane
κ	von Kármán constant
λ	Wavelength of sawtooth and sinusoidal variations to the forward facing step
θ	Yaw angle
$\bar{\theta}_m$	Mean virtual potential temperature
$\overline{\theta_v(z)}$	Mean virtual potential temperature at height z
ρ	Density
σ	Standard deviation of the measured parameter identified in the subscript
$\tau_{xx,0}$	Temporal integral length scale
τ_s	Near-surface Reynolds stress
Ω	The angle between the direction of the free-stream flow and the surface shear stress lines

1. Introduction

The Australian Government's Renewable Energy (Electricity) Amendment Bill (2009) mandated to increase renewable energy generation from 7% in 2008/09 to 20% by 2020, guaranteeing the generation of 45 000 GWh of energy from renewable sources (Cuevas-Cubria et al. 2011). With 475 MW of wind energy capacity installed in the first half of 2013 in Australia, wind energy is set to follow global trends of extraordinary growth in coming years (Cuevas-Cubria et al. 2011, Kaldellis and Zafirakis 2011, Gsänger 2013).
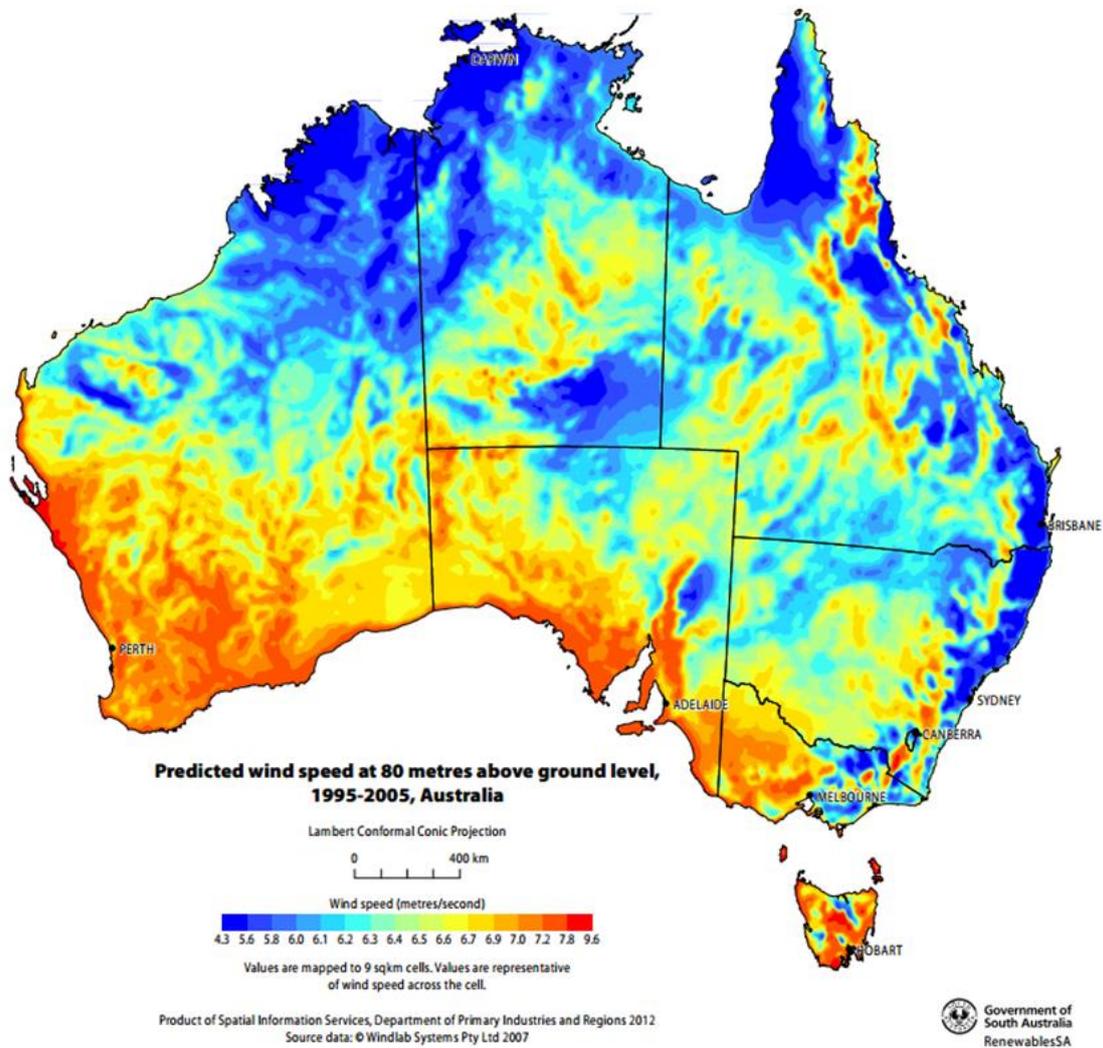
Figure 1: Map of mean wind speeds across Australia. Map produced by Windlab Systems (2012) for the South Australian government.

Australian investment in wind energy is well justified. A wind farm sited in Australia is likely to generate 50% more energy than a wind farm of the same installed capacity installed in Europe due to the higher wind speeds at Australian sites (Kaldellis and Zafirakis 2011, Miskelly 2011). Mean wind speeds in excess of 7 ms^{-1} at 80 m above ground level are quite common across Australia, as demonstrated in Figure 1.

Despite opinions to the contrary from the Energy Users Association of Australia (2012), Australia's access to fossil fuels has meant that Australian electricity prices are some of the lowest in the world, putting enormous pressure on prospective wind farms to ensure that their capacity factors are as high as possible, and that the wind farms are able to reach their design life with minimal down-time (Cuevas-Cubria et al. 2011, ESAA 2012).

Despite this immense development, there remain many technical challenges in the wind energy industry relating to maximising energy production, reducing fatigue loading and wind turbine survival in extreme wind events. Within the context of this thesis, problems in each of these areas are addressed.

The body of this dissertation relates to neutral boundary layer flow over forward facing steps (FFS), that is, complex terrain. Additionally, an appendix presents work conducted with data from Hydro Tasmania examining thunderstorm downburst events.

The term "complex terrain" is frequently used in the wind energy and wind engineering fields. It means that there exist regions of flow separation that render a terrain "complex" as opposed to "simple". This flow separation is seen to occur where the gradient of the terrain exceeds 0.3, or has a slope greater than 16.7° (Mortensen et al. 2009). Simpler computational and numerical approaches that are commonly implemented in the wind energy industry do not provide an accurate analysis of the development of the flow where these regions of flow separation occur (Bitsuamlak et al. 2004, Ayotte 2008). This can result in increased uncertainty in energy yield calculations.

Furthermore, the separation regions are, by definition, regions of increased turbulence and high

shear that will increase fatigue loading on wind turbines and generate a load imbalance across the

rotor diameter.

In the Australian wind energy context, this problem of "complex terrain" is relevant in at least 13 of

the approximately 40 operational wind farms (survey performed in January 2012) as developers seek

to take advantage of the speed up associated with hills and escarpments (Jackson and Hunt 1975,

Bowen and Lindley 1977). Seven of the 13 wind farms identified are located in the vicinity of steep

escarpments that could be approximated by an FFS. The list of these wind farms is presented in

Table 1.

Table 1: List of operational Australian wind farms potentially affected by flow separation off steep terrain. Separation assumed to occur where gradient of terrain greater than 0.3 (16.7°) (Mortensen et al. 2009). Gradients and cliff heights calculated from Google Earth. Cases that can be approximated by a FFS are shown in boldface.

Wind Farm	Location	Terrain Feature Height
Blayney Wind Farm	NSW, Australia	140 m
Capital Wind Farm	NSW, Australia	160 m
Cullerin Range Wind Farm	NSW, Australia	90 m
Woodlawn Wind Farm	**NSW, Australia**	**110 m**
Challicum Hills Wind Farm	VIC, Australia	60 m
Portland Wind Farm	**VIC, Australia**	**90 m**
Waubra Wind Farm	VIC, Australia	50 m
Woolnorth Wind Farm	**TAS, Australia**	**110 m**
Cathedral Rocks Wind Farm	**SA, Australia**	**140 m**
Mt Millar Wind Farm	SA, Australia	70 m
Starfish Hill Wind Farm	**SA, Australia**	**150 m**
Albany Wind Farm	**WA, Australia**	**70 m**
Nine Mile Beach Wind Farm	**WA, Australia**	**70 m**

Siting wind turbines on top of ridges, hills, and escarpments to take advantage of speed up effects is

considered necessary to ensure the economic viability of wind farms. However, the wind direction is

often not aligned perpendicular to the crest of cliffs and escarpments, that is, the yaw angle is often

not equal to zero. Furthermore, most cliffs and escarpments are not two-dimensional in shape but

are rugged along their span. Little research has been done on the effect of yaw angle, or the effect of

lateral variations, such as sawtooth or sinusoidal leading edges, on the wind flow. The flow

structures induced by these effects will have a significant impact on both the instantaneous energy production of a wind turbine and the fatigue loading. The aim of this research is to fill this gap in knowledge through experimental investigation in the Monash University 450 kW wind tunnel. It will provide some of the necessary information for developers to identify topographies that will induce the best performance from wind turbines and avoid adverse conditions.

Prior to presenting the findings of this research, a literature review is presented in Chapter 2. Within that chapter is a background on the atmospheric boundary layer, which is the environment in which wind turbines operate; this is followed by a review of the parameters affecting the performance of wind turbines. The current understanding of flow over forward facing steps (FFSs) is then identified, as presented in the academic literature. The literature review specifically considers research related to the effect of wind direction of flow over cliffs, as well as research into the effect of ruggedness on the flow over cliffs. Because there is little published work in these areas, the literature review also considers analogous work in areas such as aerodynamics, particularly related to the effect of wind direction on the flow over cliffs, as well as the modelling of roughness. Based on this literature review, decisions can be made regarding the appropriate methodology to be applied to modelling flow over complex topography. The various aspects of the literature are tied together and placed within the context of real-world parameters, before being summarised.

In Chapter 3, three experimental regimes are outlined: FFS validation studies, investigation into the effect of wind direction on flow over a FFS, and modelling a rugged FFS. The Monash University 450 kW wind tunnel is described followed by the inflow conditions generated in the wind tunnel. Detailed descriptions of the three experimental techniques are then provided: discrete, point based velocity measurements; paint droplet surface shear stress visualisation; and surface pressure measurements. General wind tunnel flow monitoring and the logging regimes are finally described.

Chapter 4 through to Chapter 7 provide results and discussion of those results. The chapters address the following areas:

- Validation

- Modelling yaw angle

- Modelling ruggedness: sawtooth approximation

- Modelling ruggedness: sinusoidal approximation

The validation work, in Chapter 4, begins by comparing quantitative wind tunnel and field results obtained in the literature against measurements from FFSs tested in the Monash University 450 kW wind tunnel, beginning with point measurements quantifying speed-up, turbulence statistics and shedding frequencies, before comparing mean reattachment lengths associated with flow separation from the crest of the FFS. This chapter provides a context for the topographical developments that are tested.

Research pertaining to the flow over a FFS through different wind directions is then presented in Chapter 5, building on the results presented in Chapter 4. Conclusions regarding the siting of wind turbines on straight-edged cliffs are then drawn. The yawed FFS cases also provide insight into the effect of wind direction on the ruggedness modelling presented in the ensuing sections.

The ruggedness associated with real-world FFSs is modelled. A first pass approximation is a sawtooth lateral variation of the crest, which is presented in Chapter 6. A second pass approximation is a sinusoidal lateral variation of the crest, which is presented in Chapter 7, along with a comparison with the other cases. In each of these approximations the amplitude of the lateral variation is varied. The development of the flow structure induced by the lateral variations precipitates further conclusions regarding the optimal siting of wind turbines.

In Chapter 8, major conclusions related to the fluid mechanics are highlighted alongside applications relating to the siting of wind turbines on FFSs. The limitations of the research program are emphasised.

2. Literature Review

Fluid flow over complex topography has been explored in various contexts within the academic literature. While the context of this research is wind energy, analogous systems can be observed within the broader field of wind engineering where topographic speed-up is considered for wind loading (Holmes et al. 1997, Holmes 2007), and pressure fields are measured over buildings to determine wind actions (Davenport et al. 1992, Ginger and Letchford 1992); and again more broadly in the field of aerodynamics, for example the fundamental study of flow over rectangular bodies (Castro and Dianat 1983), or vortex breakdown over a delta wing aerofoil (Werle 1954, Hoerner and Borst 1985).

As alluded to in the introduction, the scope of this research will not encompass the full set of complex terrain, but instead will be limited to cliffs that can be approximated as FFSs.

Prior to assessing the literature on flow over the topography of interest, two background sections are provided. First, an introduction to the atmospheric boundary layer is included, before the key variables associated with wind turbine performance are presented.

Having provided background on the atmospheric boundary layer and wind turbine performance, the first aim of the literature review is to critically evaluate the fluid mechanics associated with flow over a FFS. Secondly, the literature review will examine topographical developments associated with the FFS, namely, the effect of wind direction on the flow over a FFS, and the effect of ruggedness on the flow over a FFS. This will highlight the fact that very little work has been published on such topographic developments to date. Finally, the important variables are summarised, and put into the context of the broader problem: siting wind turbines.

2.1 The Atmospheric Boundary Layer

Wind turbines operate within the atmospheric boundary layer (Stull 1997, Burton et al. 2001). The wind itself is driven by the differential heating and cooling of the Earth's surface, which drives pressure variations over the surface of the Earth (Stull 1997). The rotation of the Earth induces the

Coriolis Effect, which causes the wind to spiral out from high pressure regions and spiral towards low pressure regions (Stull 1997). The atmospheric boundary layer is characterised by vertical profiles of velocity and turbulence intensity, whereby the stratification of these parameters is controlled by the interaction between the wind and the Earth's surface (Stull 1997).

The atmospheric boundary layer is characterised by describing the wind velocity distribution, the turbulence intensity, the turbulence spectrum, and the atmospheric stability. Each of these elements is addressed below.

2.1.1 Velocity Profiles in the Atmospheric Boundary Layer

The vertical velocity profile of the atmospheric boundary layer is described through various means including a power law approximation and a logarithmic profile.

In the wind energy industry, a power law description is often employed. The power law is an empirical fit, where the shape of the boundary layer's velocity profile is described with a single shear exponent, α as described by the equation below (Burton et al. 2001, IEC 2005):

$$\frac{U(z)}{U(h)} = \left(\frac{z}{h}\right)^{\alpha} \tag{2-1}$$

Here, *h* is the reference height, which is typically the hub height of the wind turbine, *z* is the vertical height variable, and *U* is the velocity.

The shear exponent is prescribed in the International Electro-technical Commission's (IEC) wind turbine design requirement standard IEC 61400-1: for extreme winds it is set as 0.11, whereas their Normal Wind Profile prescribes an exponent of 0.2 (Burton et al. 2001, IEC 2005), which, according to Davenport (1960) corresponds to "rough coast" (α = 0.2), and is a similar terrain to "open fields divided by low stone walls and hedges" (α = 0.17) and "gently rolling country with many bushes and small trees" (α = 0.22). However, the validity of the power law has been questioned for extreme wind speed conditions. In his work examining wind records at various sites across Australia and New Zealand, Rowcroft (2011) highlighted the fact that vertical velocity profiles in extreme wind

conditions were not well described by power law profiles because the extreme wind speeds were often driven by thunderstorm downburst events (Holmes 2007). Downburst events can be modelled as impinging jets (Holmes and Oliver 2000, Letchford et al. 2002, Choi 2004, Chay et al. 2006, Kim and Hangan 2007, Sengupta and Sarkar 2008, Mason et al. 2009, McConville 2009); their vertical velocity profile does not follow a typical boundary layer velocity profile, but rather features a "nose" profile, as illustrated in Figure 2.
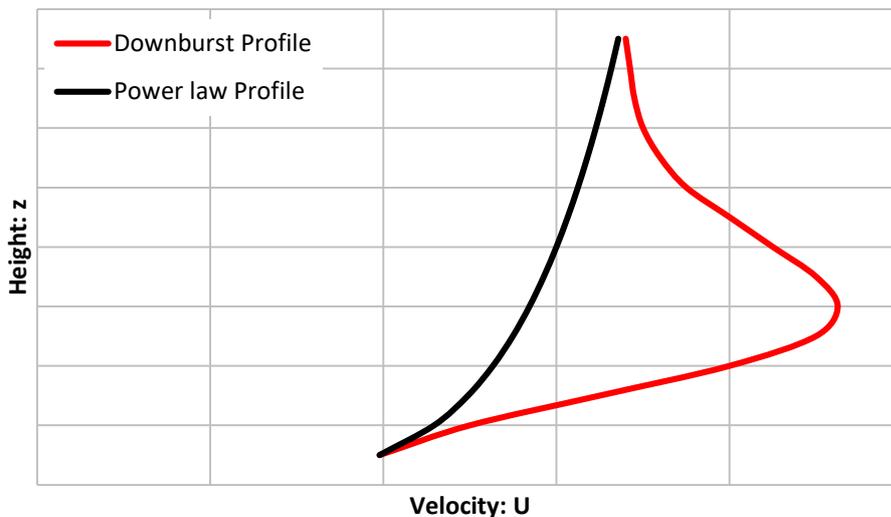
Figure 2: Comparison of downburst vertical velocity profile with power law vertical velocity profile with α = 0.11. Note the "nose" on the down burst profile.

While the wind engineering community has been vocal in highlighting the fact that downbursts are responsible for significant damage of structures (Oliver et al. 2000), the vertical velocity profiles used in the standards do not reflect this (IEC 2005, AS/NZS 2011). The Australian and New Zealand wind loading code (AS1170.2 2011) uses a logarithmic profile to model extreme winds that are outside of regions affected by tropical cyclones (AS/NZS 2011).

The logarithmic wind profile is commonly used in meteorology and wind engineering, being favoured over the power law model because it relates physical quantities, rather than being simply empirical (Stull 1997). Many variations and corrections have been made to this model to allow for things such as atmospheric stability and the displacement distance (the height above the ground at which the velocity is assumed to be zero) (Davenport et al. 1992, Stull 1997). The logarithmic velocity profile

presented below, was derived by Sverdrup (1934) based on the previous work of Prandtl and von

Kármán (Counihan 1975). It can be derived asymptotically from mixing length theory (Stull 1997).

$$\frac{U(z)}{u_*} = \frac{1}{\kappa}\ln\frac{z}{z_0}$$ (2-2)

In this equation u_* is the friction velocity, κ is the von Kármán constant, which is normally assumed

to be 0.4, and z_0 is the roughness length. As a rule of thumb, the roughness length can be taken as

one-tenth the size of the obstacles over which the flow passes (Oke 1978). A number of other values

for roughness length are presented by Stull (1997), relating the roughness length to the height of the

elements, the breadth and depth of the elements, and the population density of roughness elements

within the region of interest.

The friction velocity is defined by the following equation (Stull 1997):

$$u_* = \sqrt{\frac{\tau_s}{\rho}}$$ (2-3)

Reynolds stress near the surface is denoted by τ_s, and ρ represents the fluid density.

The shape of the velocity profile through the boundary layer is important for the calculation of

design loads on wind turbines. When applying these velocity profiles to flow over cliffs and hills, the

velocity profiles vary significantly from inflow conditions (Bowen and Lindley 1977). This renders

design standards based on shear exponents or logarithmic profiles inappropriate, whether they be

for buildings or wind turbines (IEC 2005, AS/NZS 2011) that are sited in any kind of complex terrain.

The thickness of the boundary layer is also a significant parameter in the investigation on the effects

of topography on the wind flow. The definition of boundary layer thickness, δ, most commonly used

in laboratory and computational analyses of flow over topography, is the height at which the velocity

profile reaches 99% of the free-stream velocity. While in the laboratory, the boundary layer

thickness can be readily measured by traversing through the experimental domain; determining the

boundary layer thickness is not straight-forward in the field. Stull (1997) highlights this difficulty,

identifying that the atmospheric boundary layer ranges hundreds of metres to several kilometres, which is consistent with the dimensional analysis of Deaves and Harris (1978) who proposed a model that Cook (1997) describes as "logarithmic with parabolic defect". From this model, the gradient height can be calculated as a function of the friction velocity and the Coriolis parameter (typically denoted as f, and equalling twice the Earth's rate of rotation, multiplied by the sine of the latitude). The resulting equation for boundary layer thickness, $\delta = kU_*/f$ (from the work of Deaves and Harris, k is 1/6), applies to an equilibrium boundary layer, and predicts values for δ in the order of kilometres rather than in the order of hundreds of metres. In contrast, The Handbook for Structural Engineering (Chen and Lui 2005) simplistically asserts that boundary layer thickness varies with surface conditions: boundary layers over water being in the order of 200 m, while over large cities they recommend designing based on a boundary layer thickness in the order of 450 m. These values appear to be in reasonable agreement with the gradient heights measured by Nieuwstadt (1984) in stable conditions. More recently, Steeneveld et al. (2007) disseminated a number of stable boundary layer height datasets, and applying the data to the dimensional analysis, found values of k between 7 and 13 to provide good results, based on the work of Vogelezang and Holtslag (1996). Thus, the atmospheric stability plays a significant role in determining the thickness of the boundary layer.

In contrast, Table 1 highlights cliff heights in the field between 50 m and 150 m, implying boundary layer thickness to step height ratios greater than unity. The relationship between the height of a flow feature and the boundary layer thickness plays a causal role in determining the size of flow separation regions (Sherry et al. 2010). This relationship is explored in more detail in Section 2.3 *Mechanics of the Flow over a FFS*.

2.1.2 Turbulence Intensity through the Atmospheric Boundary Layer

Turbulence intensity is the ratio of the standard deviation of the wind speed to the local mean wind speed[1]. It is a measure of how gusty the wind is, and is one of the parameters prescribed in IEC 61400-1 for the design of wind turbines, whereby wind turbines are categorised based on their ability to withstand levels of turbulence intensity to certain thresholds (IEC 2005).

The development of turbulence intensity within the atmospheric boundary layer is highly dependent on the proximity to the ground, to the ground surface and any obstacles – typically parameterised by the roughness length, as well as the atmospheric stability (ESDU 1985, Stull 1997, Burton et al. 2001).

The turbulence intensity at the surface approaches infinity as the mean velocity approaches zero, and decreases with height above the surface. However, the work of Shir shows that the turbulent length scale approaches zero as height above the surface, z, approaches zero, while the velocity fluctuations, measured through the proxy of the standard deviation of the stream-wise velocity component, σ_u, reduces with increasing height above the ground (Shir 1973). Lenschow et al. (1980) measured vertical profiles through the atmospheric boundary layer above the East China Sea. Their field data revealed an almost constant value for the normalised stream-wise velocity variance, increasing slightly with proximity to the surface. In both of these cases, the increase in wind speed with height through the boundary layer results in a reduction in turbulence intensity with increasing height.

Various researchers have developed vertical profiles of turbulence intensity (Burton et al. 2001). Wind loading codes often prescribe such vertical profiles based on the land type with rougher

---

[1] On some occasions, the free-stream wind speed has been used. See Bowen, A. J. and D. Lindley (1977). "A wind tunnel investigation of the wind speed and turbulence characteristics close to the ground over various shaped escarpments." <u>Boundary Layer Meterology</u> **12**: 259-271.

surfaces resulting in higher levels of turbulence intensity (ESDU 1985, AS/NZS 2011). Burton et al. (2001) in their *Wind Energy Handbook*, have published a number of these profiles.

IEC 614000-1 (2005) takes a simplified approach. It relies solely on the turbulence intensity at hub height, enabling wind energy engineers to rely on turbulence intensity measurements from a single location (though additional anemometers are required to determine the shear profile).

The type of anemometer is another important factor when comparing turbulence intensity values. A single Pitot-static tube, for example, will only give a stream-wise velocity. Four-hole pressure probes measure the three velocity components. Cup anemometers, which are often used to collect field measurements, measure only the speed of the flow in the *x-y* plane, not capturing the vertical component of velocity. These variations in measurement techniques make direct comparisons between field measurements and wind tunnel measurements difficult.

In addition to the differences in what is sampled, the sampling frequency also affects the value of turbulence intensity, as higher sample rates will capture finer turbulent fluctuations. Four-hole pressure probes designed for the wind tunnel have excellent frequency response up to frequencies in the order of 1500 Hz, while cup anemometers used in field measurements are designed to achieve frequency response in the order of 1 Hz (Hooper and Musgrove 1997, Yahaya and Frangi 2003). If the dominant flow structures are smaller than what can be captured by the instrument, the turbulence intensity will tend to be under-estimated.

2.1.3 Turbulence Spectra of the Atmospheric Boundary Layer

In his text book on boundary layer meteorology, Stull (1997) introduces the concept of the spectrum of turbulence in the atmospheric boundary layer by observing that over given periods of time a statistically stable mean can be observed; and that the variance of the wind speed is also statistically stable over certain periods, say, overnight, or in the early afternoon. Figure 3 is an idealised representation of this. Through the years, a repetition of seasonal winds is observed, which is denoted by the largest peak in Figure 3. Further periodicity is observed diurnally, explaining the

second and smallest peak in Figure 3. These peaks are driven by synoptic events caused by large-scale meteorological events. These large-scale events take longer than one hour to pass through a region; hence, there is a minimum in the spectrum around a period of one hour. Various researchers have considered the spectral gap, including Vincent et al. (2010) whose research demonstrated that the presence of the spectral gap was a function of atmospheric stability. In their review of the literature, Vincent et al. (2010) highlight that cumulus clouds (Stull 1997), convective cells (Gjerstad et al. 1995, Heggem et al. 1998), and horizontal roll vortices (Heggem et al. 1998) all contribute to the variation in spectral gap, rendering the spectral gap poorly defined.

The right-most peak in Figure 3 corresponds to the turbulent motion of the wind. This is the variation that is summarised by the turbulence intensity statistic that was described in Section 2.1.2 *Turbulence Intensity through the Atmospheric Boundary Layer*.
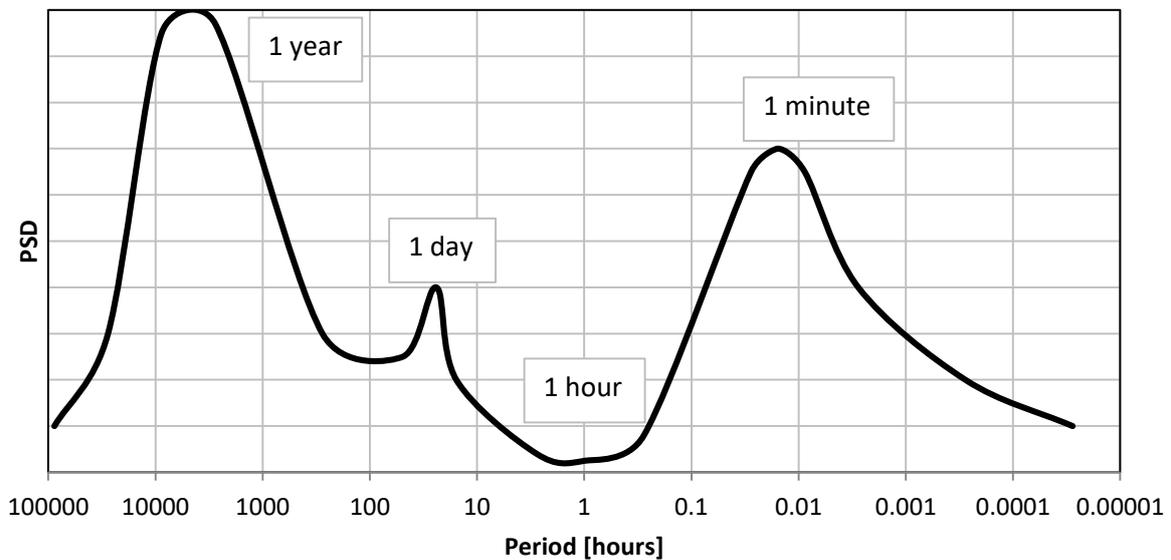
Figure 3: Illustration of PSD from annual, synoptic scale, to turbulent scales on the scale of minutes. Figure based on those presented by Stull (1997), Davenport et al. (1992) and Van der Hoven (1957).

When considering the part of the spectrum associated with the turbulent motion of the wind, as shown in Figure 3, the energy content of the turbulence as a function of the size of the turbulent structures can be determined (Davenport et al. 1992, Stull 1997). The size of the turbulent structures is typically represented by the reduced frequency or Strouhal number rather than by the period, as

13

used in Figure 3. Spectra are calculated by converting time-series data from the time domain to the frequency domain using a Fast Fourier Transform method. The spectra are often presented as Power Spectral Densities (PSDs).

The PSD is formally defined as the Fourier transform of the auto-correlation function of a stationary, random time-series (Bendat and Piersol 1993). In this thesis, only the single-sided function is implemented, so as to use only positive frequencies.

After Bendat and Piersol (1993), the auto-correlation function and subsequent single-sided PSD are presented below.

The auto-correlation function R_{xx} of the time-series $x(t)$ of length T, is given by Equation 2-4:

$$R_{xx} = \lim_{T \to \infty} \frac{1}{T} \int_0^T x(t)x(t+\tau)\mathrm{d}t \qquad (2\text{-}4)$$

The single-sided PSD is defined in Equation 2-5 for positive frequencies, f:

$$S_{xx} = 2 \int_{-\infty}^{\infty} R_{xx}(\tau)e^{-i2\pi f\tau}\mathrm{d}\tau \qquad (2\text{-}5)$$

The units of S_{xx} are the units of the variance of the original signal, $x(t)$, squared (Stull 1997).

From the PSD, integral length scales can be determined, which represent the size of the most energetic eddies.

From Tropea et al. (2007) the temporal integral length scale $\tau_{xx,0}$, which is related to the spatial integral length scale by the convection velocity, U_C, of the eddies is given by Equation 2-6:

$$\tau_{xx,0} = \int_0^{\infty} R_{xx}(x,t,\tau)\mathrm{d}\tau \qquad (2\text{-}6)$$

This implies the spatial integral length scale is given by Equation 2-7:

$$^{x}L_u = \tau_{xx,0}U_C \qquad (2\text{-}7)$$

Thus, the energy content of a turbulent flow can be summarised by a single length-scale parameter. In practice, it is impossible to evaluate the integral to infinity, resulting in various conventions as to the upper limit for the summation of the integral. The integral length scale is commonly approximated by matching an empirical function to the PSD. This is the approach taken in this thesis. There are many different matching functions that have been derived, however, Davenport et al. (1992) highlighted that the differences between these functions are minor. Nonetheless, two functions are typically used to match the PSD: the von Kármán spectrum and the Kaimal spectrum (Burton et al. 2001).

For the stream-wise component, the von Kármán spectrum is given in Equation 2-8 (von Kármán 1948, Burton et al. 2001, Hui et al. 2009):

$$\frac{fS_u(f)}{\sigma_u^2} = \frac{4f\,{}^xL_u/U}{\left[1+70.8\left(\frac{f\,{}^xL_u}{U}\right)^2\right]^{5/6}} \tag{2-8}$$

The stream-wise component of the Kaimal spectrum is presented in Equation 2-9 (Kaimal et al. 1972, Burton et al. 2001):

$$\frac{fS_u(f)}{\sigma_u^2} = \frac{4f\,{}^xL_u/U}{\left[1+6f\left(\frac{{}^xL_u}{U}\right)\right]^{5/3}} \tag{2-9}$$

The former is said to match the turbulence spectra found in wind tunnels well (Petersen et al. 1998, Burton et al. 2001). The latter provides a better match for turbulence spectra in the field (Petersen et al. 1998, Burton et al. 2001). Further details of these functions and how they are calculated are provided in the references listed as well as in the methodology section presented in Chapter 3.

2.1.4 Atmospheric Stability within the Atmospheric Boundary Layer

Several relevant concepts are associated with atmospheric stability. On one hand, the stability criterion can provide an indication as to whether a flow is laminar or turbulent, or becoming laminar, or becoming turbulent (Stull 1997). On the other hand, the stability criterion is a measure of an air

parcel's buoyancy due to thermal effects (Rohli and Vega 2011). These two notions are interrelated, as it is the turbulence suppressing effect of buoyancy in stably stratified flow that acts to negate the turbulence generation associated with wind shear (Stull 1997). The atmospheric stability conditions impact wind flow over various geometries and affect loads on wind turbines (Hand et al. 2003). It can, for example, affect the size of separation regions (Emeis et al. 1995).

In the context of this research, an understanding of atmospheric stability is important for two reasons. The first is to determine the most appropriate atmospheric stability class to model. The second is to determine how that stability class can be modelled with the available experimental facilities.

There are three classes of atmospheric stability: stable, unstable, and neutral stability. Stability classes can be understood by considering a hypothetical parcel of air that is adiabatically raised through the atmospheric boundary layer (Bowen 1979).

Unstable conditions are associated with the heating of the earth's surface during the day, resulting in the hypothetical air parcel being warmer than its new surrounds. The increased temperature results in the air parcel having a lower density than its surrounds, causing the parcel of air to rise, mix and generate turbulence (Bowen 1979, Stull 1997).

Stable conditions are associated with the cooling of the earth's surface, often at night. The hypothetical air parcel is thus cooler than its surrounds, and denser. Thus, the air parcel will tend to return to its original altitude (Bowen 1979). Stable conditions are also associated with low turbulence conditions (Stull 1997).

Neutral stability conditions are associated with high winds and turbulent atmospheric conditions, which cause vertical mixing (Stull 1997). The turbulence is generated by a range of means, including the interaction between the wind and the surface (Jacobson 2005). The interaction between the wind and the surface implies that a vertical shear is generated, and the increased mixing implies that

there will be a small change in potential temperature across the heights of interest. By definition, the density of the hypothetical air parcel, in neutral conditions, changes at the same rate as the atmosphere in which it is in (Bowen 1979). Thus, when raised adiabatically, the hypothetical parcel of air will tend to neither return to the ground, nor to rise due to buoyancy.

To quantify the stability, a class of non-dimensional numbers is used, generally referred to as the Richardson number. The Richardson number in any of its various forms is a common atmospheric stability criterion, based on the ratio of the buoyant production term and the mechanical production term from the Turbulent Kinetic Energy budget equation (Stull 1997); in other words, it is the ratio of natural convection to forced convection. In this form, it is known as the flux Richardson Number, as shown in Equation 2-10 (Stull 1997).

$$\text{Ri}_{\text{flux}} = \frac{\left(g/\overline{\theta_v}\right)\overline{(w'\theta_v')}}{\overline{(u'w')}\frac{\partial \overline{U}}{\partial z} + \overline{(v'w')}\frac{\partial \overline{V}}{\partial z}} \tag{2-10}$$

Stull (1997) points out that the flux Richardson Number can only be calculated for turbulent flow, as it relies on the measurement of Reynolds Stress terms *u'w'* and *v'w'* which, by definition, are zero in laminar flow. This issue can be circumvented by assuming that the vertical turbulent correlations are proportional to the vertical shear, which results in the gradient Richardson number, given in Equation 2-11.

$$\text{Ri}_{\text{gradient}} = \frac{\left(g/\overline{\theta_v}\right)\frac{\partial \overline{\theta_v}}{\partial z}}{\left(\frac{\partial \overline{U}}{\partial z}\right)^2 + \left(\frac{\partial \overline{V}}{\partial z}\right)^2} \tag{2-11}$$

The bulk Richardson number is a further approximation where the vertical shear is approximated by finite differences. The bulk Richardson number is typically used in field work as it provides an approximation of the stability, using discrete spatial points (Stull 1997). The bulk Richardson number is given in Equation 2-12.

$$\text{Ri}_{\text{bulk}} = \frac{\left(g/_{\bar{\theta}_m}\right)\left(\overline{\Delta\theta_v(z)}/_{\Delta z}\right)}{\left(\overline{\Delta U(z)}/_{\Delta z}\right)^2 + \left(\overline{\Delta V(z)}/_{\Delta z}\right)^2} \qquad\qquad (2\text{-}12)$$

The terms in the various forms of the Richardson number are defined below.

g = gravitational acceleration, [ms^{-2}]

$\bar{\theta}_m$ = mean virtual potential temperature, [K]

$\overline{\theta_v(z)}$= mean virtual potential temperature at height z, [K]

z = height above ground, [m]

$\overline{U(z)}$= mean flow in the x direction at height z, [ms^{-1}]

$\overline{V(z)}$= mean flow in the y direction at height z, [ms^{-1}]

In terms of the various forms of the Richardson number, unstable conditions are described by a negative value; stable conditions are described by a positive value; and neutral conditions by a zero value (Stull 1997).

The question of which is the most appropriate atmospheric stability class to model can be addressed by identifying which atmospheric stability class will most commonly generate the highest loads on wind turbines.

Measurements from an instrumented, pitch controlled wind turbine conducted by Hand et al. (2003) demonstrated that the largest fatigue loads occurred at bulk Richardson numbers in the vicinity of zero. This is illustrated in Figure 4, taken from the paper of Hand et al. (2003). The blade flap equivalent fatigue load, measured in [kNm], is plotted on the vertical axis, while the bulk Richardson number is plotted on the horizontal axis. The data points are colour coded by wind speed. It can be seen that lower wind speed colour bins (5 – 7 ms^{-1}, 7 – 9 ms^{-1}), had the broadest range of bulk Richardson number, and correspondingly resulted in the lowest blade flap equivalent fatigue load.

The points in the lower wind speed colour bins that did generate higher loads were at bulk

Richardson numbers close to zero, implying near-neutral stability. Similarly, coloured bins

associated with wind speeds greater than 9 ms^{-1} tended to fall in the same region associated with

higher loads on the wind turbine at bulk Richardson numbers near zero. Thus, the field data from

Hand et al. (2003) demonstrates that neutral or near neutral stability classes generated the highest

blade flap equivalent fatigue loads.

While Hand et al. (2003) obtained load data from an instrumented wind turbine, Sathe et al. (2013)

collected data from four off-shore wind energy sites and applied the observed vertical wind speed

profiles and stability classes to the HAWC2 aero-elastic code, developed at Risø-DTU for wind

turbine loading, with the aim of determining which stability class should be modelled to best

estimate the design loads for wind turbines. They presented load data for the tower, the blades and

the rotor. The rotor loads were the loads experienced at the hub from all three blades, in contrast to

the blade loads measured at the blade root. The tower loads were largest under neutral conditions

and most reduced under stable conditions; the blade loads were relatively consistent across the

stability classes, with the self-weight of the blades being the dominant factor; the rotor loads were

largest under stable conditions and reduced under unstable conditions, driven by the increased

shear associated with a stable boundary layer.

It is variously reported in the academic literature that wind speeds greater than 10 ms^{-1} are

associated with near neutral conditions as mechanical turbulence dominates over thermal effects

(Cook 1978, Emeis et al. 1995, Fritz 2003). More recently, Hansen et al. (2012) highlighted that non-

neutral atmospheric stability conditions can be observed in wind speeds up to 15 ms^{-1} and Sathe et

al. (2013) observed non-neutral conditions off-shore at wind speeds of 16 ms^{-1} and beyond, though

the bulk of observed measurements at wind speeds greater than 10 ms^{-1} occurred in neutral and

near-neutral stability conditions.

Generating a temperature gradient in a wind tunnel is a difficult and expensive exercise; ordinarily wind tunnel flow is neutrally stratified (Stull 1997). While some environmental test facilities do feature heat benches to model thermal stratification by generating a vertical temperature gradient, this is not generally the case.

In recent years, various authors (Porté-Agel et al. 2010, Sathe et al. 2013, Porté-Agel et al. 2014) have investigated the effect of atmospheric stability, finding that the effect of atmospheric stability is an important consideration in the design of wind turbines and wind farms. However, the field work of Hand et al. (2003) and the load modelling from Sathe et al. (2013) imply that the neutral case ought to be modelled as a first priority, so as to capture both the largest loads and the most common loads on wind turbines.
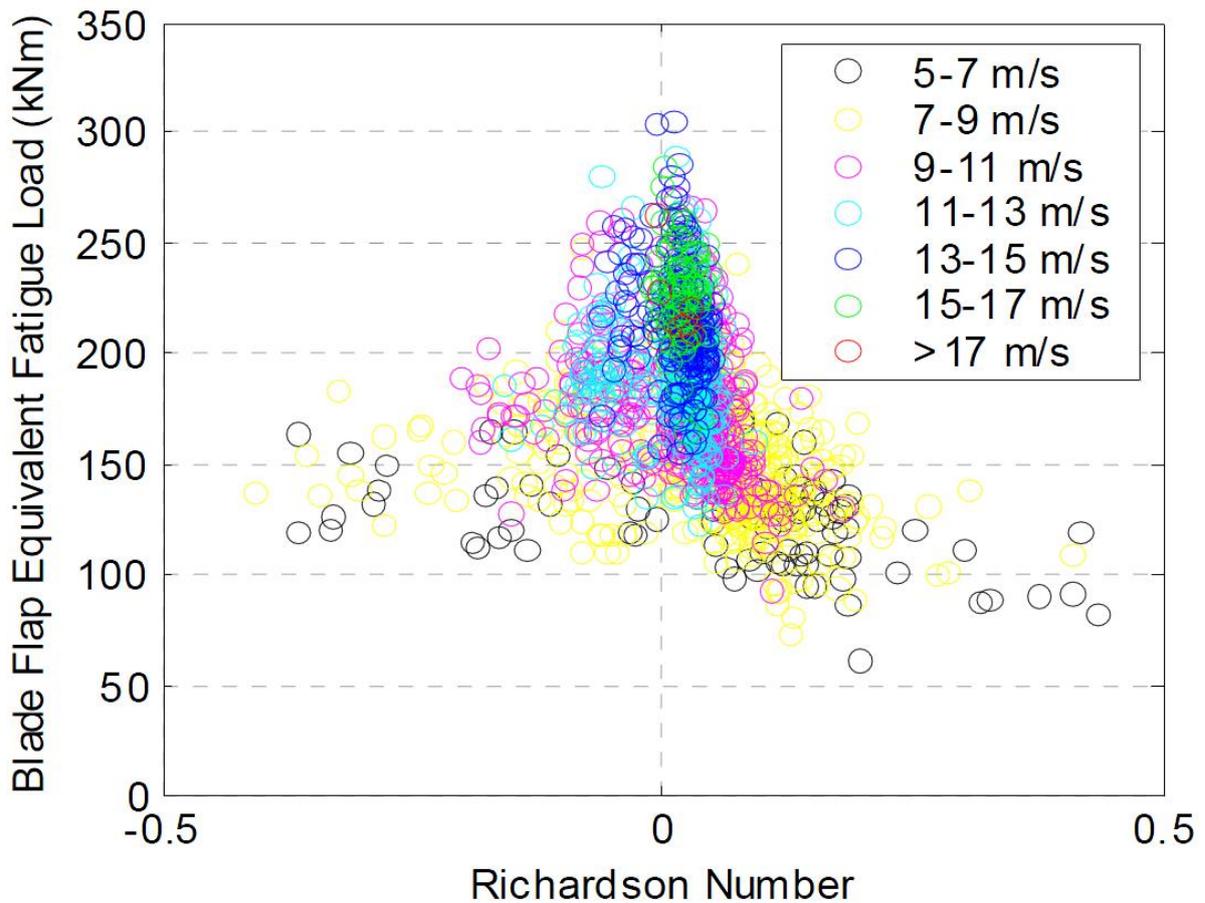
Figure 4: Bulk Richardson Number v Equivalent fatigue load. From Hand et al. (2003)[2].

2.2 Background on Wind Turbine Performance

One of the aims of this research is to maximise energy output from wind turbines over their lifetime.

There are two aspects to this: first, the instantaneous energy generation; and secondly, the

structural loading on the wind turbine.

The instantaneous power output from a wind turbine is related to the amount of power in the wind.

The power of the wind can be easily quantified by considering the kinetic energy of the wind, with

the kinetic energy, E_K, given in Equation 2-13.

---

[2] This figure, captioned "Blade root flap bending moment equivalent fatigue load as a function of atmospheric stability, Ri" in the original report is reprinted from National Renewable Energy Laboratory technical report titled **"Mitigation of wind turbine/vortex interaction using disturbance accommodating control"** (2003), by M. M. Hand, http://www.nrel.gov/docs/fy04osti/35172.pdf, Accessed April 11, 2014.

$$E_K = \frac{1}{2}mU^2 \tag{2-13}$$

Here m is the mass of the fluid parcel of interest, and U is the velocity of the fluid parcel of interest. The mass of the fluid can be more readily considered as the fluid density, ρ, multiplied by the fluid volume, V.

$$E_K = \frac{1}{2}\rho V U^2 \tag{2-14}$$

The fluid volume of interest is the volume of fluid passing through the wind turbine rotor, which has a radius R, at velocity U. The fluid volume per unit time is then given by:

$$V/_t = \pi R^2 U \tag{2-15}$$

Substituting velocity into the equation causes the left hand side of the equation to become a rate of production: kinetic energy per unit time.

$$E_K/_t = \frac{1}{2}\rho \pi R^2 U^3 \tag{2-16}$$

Because power, P, is defined as energy per unit time, the available power in the wind can be calculated according to Equation 2-17:

$$P = \frac{1}{2}\rho \pi R^2 U^3 \tag{2-17}$$

Similar derivations are available in numerous references and lectures on the subject, including Kalmikov et al. (2011) and Burton et al. (2001).

The amount of energy that can be extracted from the wind by a traditional wind turbine is limited by the Betz limit, which is a maximum efficiency based on the momentum change across the wind turbine rotor. This can be determined analytically as $\frac{16}{27}$. Again, the full derivation can be found in various texts, including Burton et al.'s Wind Energy Handbook (2001), as well as in Betz's original paper on the subject (Betz 1919).

The key points relating to theoretical maximum power output of a wind turbine are that the available power is proportional to the square of the rotor blade length, and proportional to the cube of the wind speed. The aim of this research is thus to identify regions where wind speeds will be increased due to topographic effects. Similarly, comments regarding the size of the wind turbines are pertinent in the context of the power output equation.

This understanding of wind turbine performance is a useful starting point to highlight the importance of energy output as a function of wind speed and rotor size. However, the assumption of a constant flow field is unlikely to be a valid one. Clearly, the wind turbine's environment is turbulent and the wind turbine rotor operates in the atmospheric boundary layer, where, by definition, a vertical shear profile exists. Thus, momentum theory in a one-dimensional form is not sufficient to determine a wind turbine's energy output.

2.2.1 Effects of Turbulence Structure
The energy output of a wind turbine is affected by the fluctuations in wind speed across the rotor's swept area. Furthermore, the turbulence adds to the fatigue loading. Mouzakis et al. (1998) presented a method for determining the significant parameters and their impact on energy output and fatigue loading on the turbine. Using a multivariate regression analysis Mouzakis et al. (1998) determined that the turbulence structure of the wind was the primary parameter causing fatigue. The wind speed and wind speed distribution also had a significant impact on the fatigue of the structure. Field experiments near Golden, Colorado by Hand et al. (2003) on a two-bladed, variable pitch, 43 m diameter wind turbine examined the statistical similarities in the largest two percent of fatigue loads, based on 10-minute averaged data. This work was comparable to the work completed by Mouzakis et al. (1998) despite a slightly different approach. The investigation by Hand et al. (2003) identified some parameters that did not feature in the Mouzakis investigation, such as the atmospheric stability, but tended to agree that the turbulent structure of the wind was of primary importance to the fatigue loading of the wind turbine. Their views diverged slightly in their interpretation of the significance of the wind speed, with Mouzakis et al. (1998) taking the view that

there was a causal link between wind speed and high fatigue loads. Hand et al. (2003) tended to identify frameworks within which these high fatigue loads might be found, for example, they demonstrated that the higher loads generally occurred at wind speeds greater than 10 ms^{-1}, which were associated with near neutral atmospheric stability conditions.

Figure 5, from Hand et al. (2003) shows that higher magnitude Reynolds stresses, in particular $\overline{uw}$ coincides with high fatigue loads. However, Hand et al. (2003) concluded that the averaging period of 10 minutes was too long as the significant Reynolds stress events tended to occur over a period of 10 s to 100 s, and so the values reported in a 10-minute (600 s) average were not representative of the large loads experienced. Hand et al. (2003) concluded that a turbulent event within a 10-minute period would cause significant fatigue damage, even though the surrounding periods are free from such events.

Travner et al. (2006) described failure rate of wind turbine components as a function of time using a "bathtub model". As the components "wear in" the failure rates reduce and then remain at a constant low rate. Towards the end of the lifespan the failure rate tends to increase again due to the fatigue. The effect of the high turbulence events described by Hand et al. (2003) is to increase the failure rate and to curtail the constant low failure rate period after the turbine is worn in (Travner et al. 2006). The significance of this in terms of the current body of work, particularly from the conclusions of Hand et al. (2003), is that high magnitude Reynolds stress occurrences induce the largest fatigue loads on the wind turbines.

The relationship between fatigue loading and turbulence intensity is unclear. Figure 5 (bottom right) from Hand et al. (2003) illustrates a lack of correlation between fatigue loading and turbulence intensity. Further confusing the issue is that the plot refers to turbulence intensities within the range of 0 – 0.4%. This level of turbulence intensity is extremely low for hub height measurements in the atmospheric boundary layer, with values in the range 0 – 40% being typical of the atmospheric boundary layer. 0 – 40% is assumed to be the correct range.
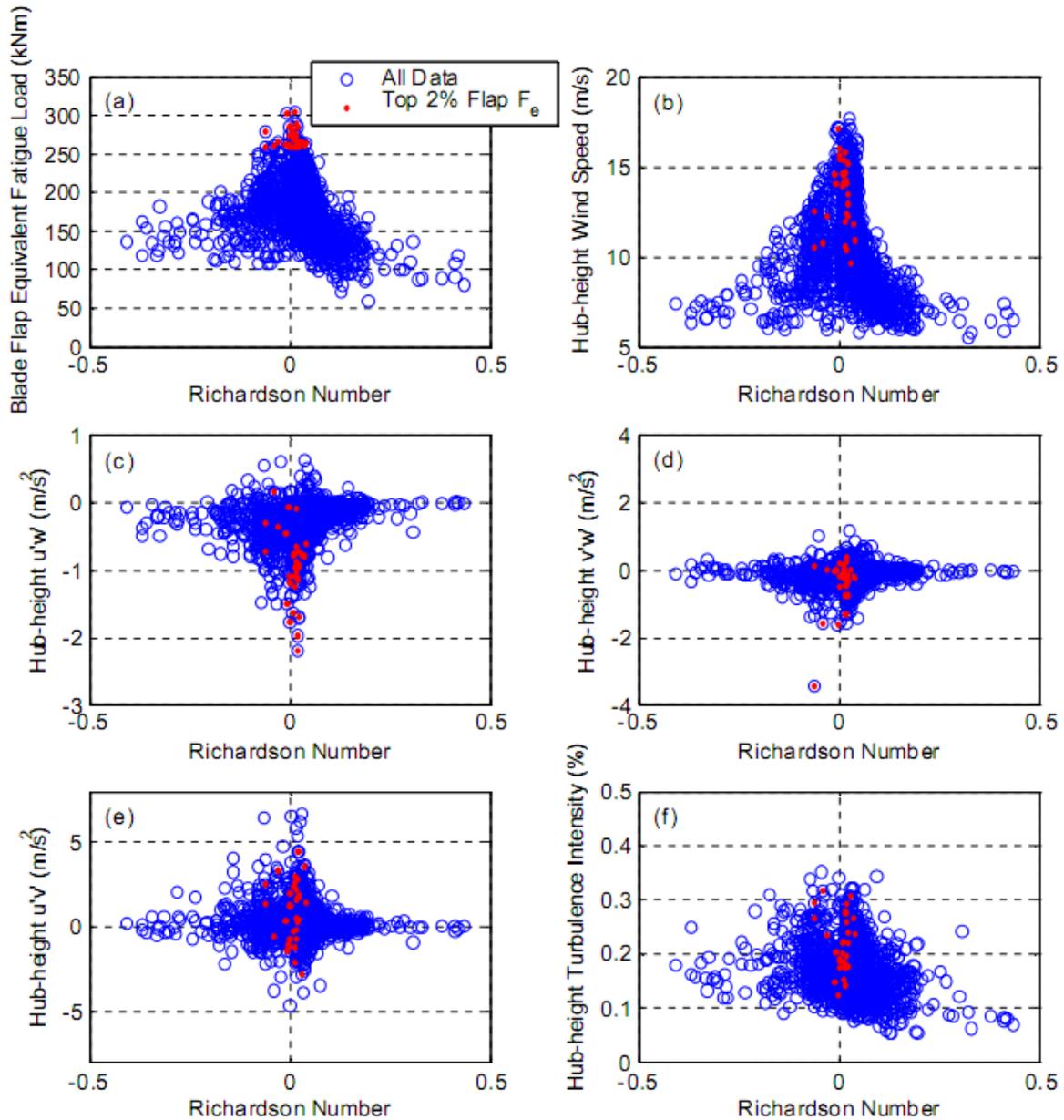
Figure 5: Richardson Number initially plotted against fatigue load (top left) and then plotted against wind speed and turbulence parameters. Highest 2% of loads are marked in red. Plots are taken from Hand et al. (2003)[3].

Swalwell et al. (2001) completed wind tunnel testing of the NACA0021 aerofoil, investigating the

effect of varying the turbulence intensity for different angles of attack. They observed that increased

turbulence intensity increased lift and delayed stall, varying the turbulence intensity between 0.6%

---

[3] This figure, captioned "Top 2% blade flap equivalent fatigue load in relation to balance of database. Inflow parameters represent 10-minute mean values from hub-height anemometer." in the original report is reprinted from National Renewable Energy Laboratory technical report titled **"Identification of Wind Turbine Response to Turbulent Inflow Structures"** (2003), by M. M. Hand, Kelley, N.D., Balas, M.J., http://www.nrel.gov/docs/fy03osti/33465.pdf, Accessed May 8, 2014.

and 7%, resulting in an initial increase in the lift coefficient of over 10%. While the results from Delnero et al. (2005) validated the conclusion that the stall is delayed, Delnero et al. (2005) found that the lift was reduced with increased turbulence intensity (except in the laminar case, which exhibited much lower lift coefficients in all tests). However, Delnero et al.'s work featured some ambiguity, as it was unclear to what extent the changes were caused by increased turbulence intensity, and which changes were caused by an increase in the integral length scale of the turbulence.

Delnero et al. (2005) and Swalwell et al. (2001, 2005) took similar approaches by conducting wind tunnel investigations, measuring lift and drag profiles for various angles of attack, whilst varying the integral length scale of the turbulence and the turbulence intensity. Their results both demonstrated that increased turbulence intensity resulted in delayed stall. The primary mechanism for this delayed stall is that the boundary layer of an aerofoil is able to withstand adverse pressure gradients to a greater extent if it is in a turbulent state. This slows the progression of the flow separation line back toward the leading edge of the aerofoil, which ultimately provides the stall condition (Swalwell 2005).

In addition to the delayed stalled caused by increases in turbulence intensity, Burton et al. (2001) reported that the rotation associated with wind turbine rotors resulted in further stall delay. Manwell et al. (2009) cite the work of Sorensen (1986) and the ensuing work of Snel and Schepers (1991) that attributes the delayed stall associated with wind turbine aerofoils to the rotation of the rotor causing a span-wise pressure gradient and associated span-wise velocity.

Nevertheless, there is general agreement that stall is delayed by increasing the turbulence intensity of the inflow. However, stall is a function of the angle of attack, which, by extension, is a function of wind speed, as angle of attack is a function of wind speed for a rotating aerofoil (Burton et al. 2001). The significance of this delayed stall being caused by turbulence is that wind turbine rotors will experience larger fatigue loads as the rotor is extracting energy from the wind at higher than

predicted flow speeds, though this effect is reduced by controlling the blade pitch in modern wind turbines (Manwell et al. 2009).

2.2.2 Integral Length Scale

The integral length scale was defined in Section *2.1.3 Turbulence Spectra of the Atmospheric Boundary Layer*, in Equation 2-7. In physical terms, it represents the size of the most energetic eddies. The impact of the integral length scale of the turbulence on wind turbine performance is significant, impacting the structural loading of wind turbines.

The current international standard for wind turbines (IEC 2005) provides design criteria for turbulence intensity and length scale, specifying classes based on a reference turbulence intensity at 15 ms^{-1} and the length scale is given by the following expression:

$$^{x}L_U = \begin{cases} 0.7z & z < 60 \text{ m} \\ 42 \text{ m} & z \geq 60 \text{ m} \end{cases}$$

(2-18)

$^{x}L_u$ is the longitudinal integral length scale parameter and *z* is the height above ground. Lengths are in metres [m].

These length scales are very conservative, with the Australian Standard for wind loading: AS1170.2 designating the following expression (using the terms defined above):

$$^{x}L_U = 85(\frac{z}{10})^{0.25}$$

(2-19)

This corresponds to a value of 133 m at 60 m above ground level (AGL).

Isyumov (1999) compared integral length scales from field measurements with wind tunnel measurements, as shown in Figure 6. This shows integral length scales much larger than each of the aforementioned standards.

Alongside the effect of turbulence intensity, Swalwell (2005) also experimentally investigated the effect of the integral length scale on aerofoil stall. While she concluded that stall was delayed as integral length scale increased, she noted that the relationship was weak; she also noted that the

turbulence intensity was not independent of integral length scale: integral length scale increased as turbulence intensity increased.
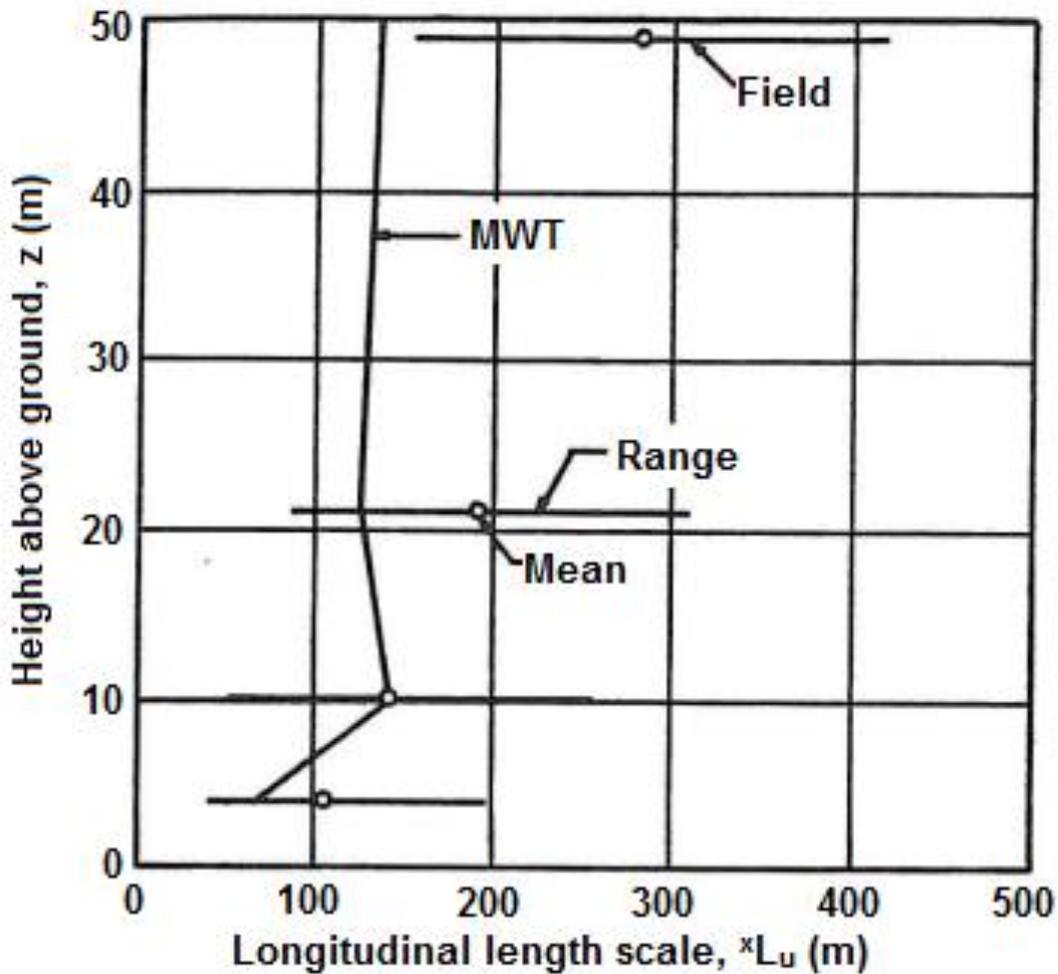
Figure 6: Longitudinal length scales from Isyumov (1999). MWT is "Meteorological wind tunnel". Reproduced with permission from ASCE. This material may be downloaded for personal use only. Any other use requires prior permission of the American Society of Civil Engineers.

Larsen (1998) examined the effect of integral length scale on turbine fatigue loading. Using an aero-elastic code, he calculated response characteristics of a group of small wind turbines and determined the change in loading resulting from varying the longitudinal integral length scale of turbulence. He measured fatigue loading on the tower, the blades and the shaft and found that by reducing the integral length scale from 60 m to 30 m, in each instance, the loading was increased by approximately 10%. While his results demonstrated that the integral length scale had a definite effect on the structural loading of the wind turbines, he did not suggest a causal mechanism.

However, a reduction in integral length scale that is independent of turbulence intensity implies more frequent buffeting of the wind turbines, which may be the cause.

2.2.3 Horizontal shear

Horizontal shear is defined as the change in wind speed as a function of lateral direction, that is, *U(y)*. Changes in roughness with lateral spatial location or the ruggedness along the lateral extent of a cliff face are two cases where horizontal shear will occur. Hansen (1992) examined the effect of horizontal shear on wind turbines, concluding that it would result in yaw misalignment because the horizontal shear causes a maximum difference in blade flap loads when the blades are horizontal. Hansen and Butterfield (1993) cite Lynette (1988) stating that yaw misalignment was the second most common cause of wind turbine downtime. Faulstich et al. (2010) used data gathered between 1989 and 2006 from a survey of 1500 wind turbines to determine the instances of mechanical breakdown, their results agree with Lynette's assertion that the yaw system is the second most prone part of the turbine to fail, behind the hydraulic systems. Faulstich et al. (2010) identified electrical systems, electronic control and sensors as each having a greater likelihood to cause downtime. Kragh and Hansen (2014) identified that an intentional yaw misalignment could be used to reduce the fatigue loading on wind turbines by reducing the once per revolution load induced by the vertical wind shear. However, the crux of the problem remains the same: the inflow conditions need to be known to either avoid yaw misalignment or to take advantage of the load reduction from yaw misalignment. Thus, terrain effects that cause horizontal wind shear are also important for wind turbine performance.

2.2.4 Summary

Many parameters affect the performance of wind turbine rotors. In terms of the energy output, the wind speed is the most significant parameter, and the siting of wind turbines is likely to be dominated by the search for sites with the greatest mean wind speed. The delayed onset of stall induced by increased turbulence intensity and reduced integral length scales have the potential to increase energy extraction. However, the delayed onset of stall tends to relate to fixed pitch

machines rather than wind turbines with variable pitch control, which is standard in most modern utility-scale wind turbines. These turbines will generate their constant maximum power at wind speeds between the rated power and the cut-out wind speed because of the ability to pitch the blades.

However, the effect of increased turbulence intensity and reduced integral length scale on delayed stall also has implications in terms of fatigue loading with these conditions being associated with higher loads on the wind turbines. Other parameters that will affect the fatigue loading of the turbine are the atmospheric stability, with high fatigue load cases tending to occur in neutral or near neutral atmospheric conditions; the Reynolds stresses, in particular the peak values of $\overline{uw}$ corresponding to the highest loads; and the wind speed, with wind speeds below approximately 10 ms^{-1} not causing significant fatigue loads. Horizontal shear is also responsible for extended periods of yaw misalignment, and the yaw mechanism has been shown to be one of the largest sources of machine downtime.

2.3 Mechanics of the Flow over a FFS

In examining the flow over a FFS, four elements are highlighted. First, the structure of the flow as it passes over a FFS is described. Secondly, the aspect ratio is considered, which leads to a discussion surrounding the three-dimensionality generated by the geometry. Thirdly, a discussion of the periodicity identifies peak Strouhal numbers associated with the downstream region. Finally, the parameters controlling the size of the recirculation region are examined. A simplified schematic of flow over a FFS is presented in Figure 7.
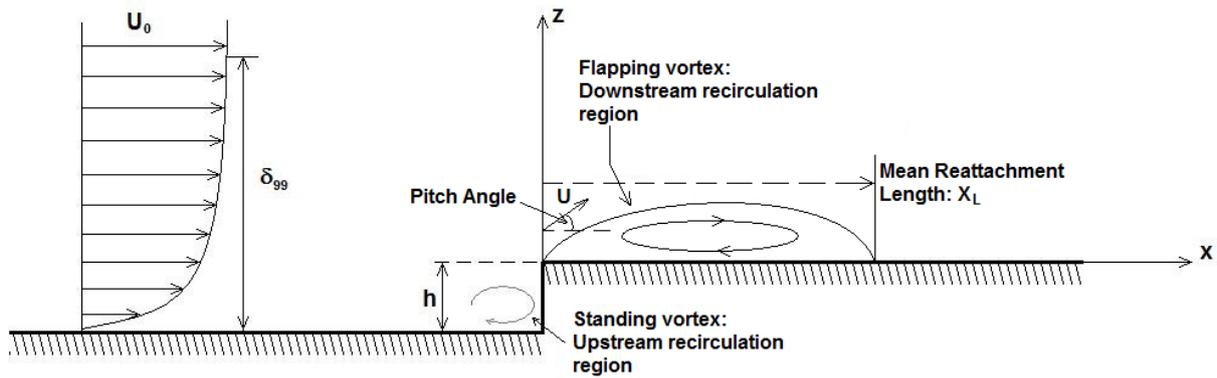
Figure 7: Schematic of a FFS.
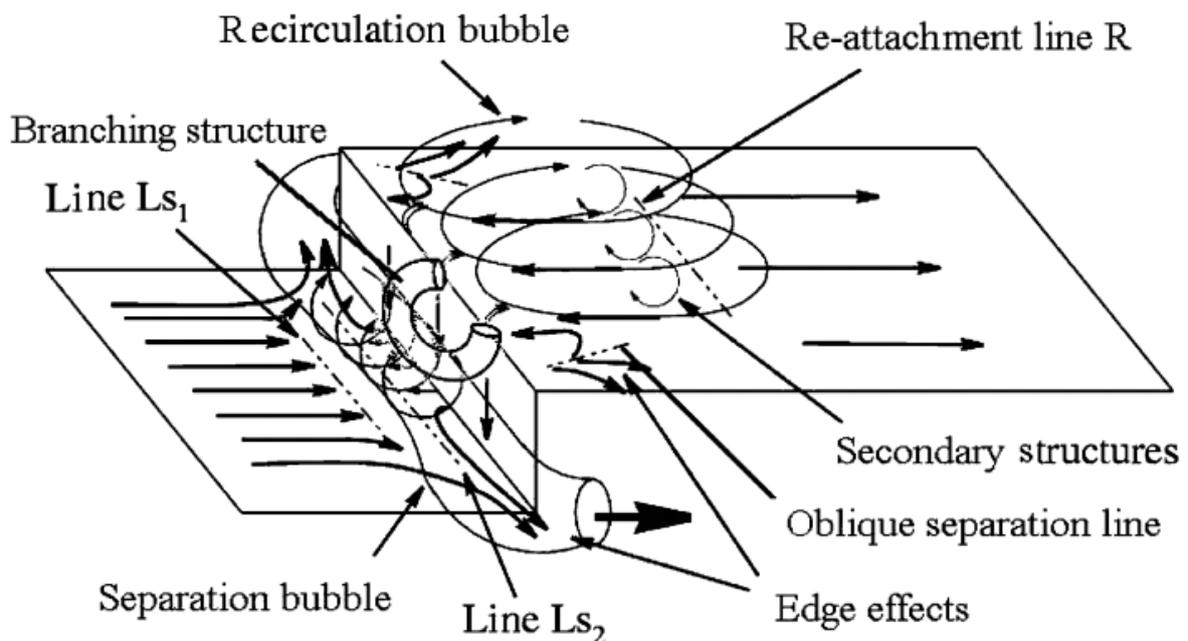
Figure 8: Flow structure over a FFS in an open jet wind tunnel. Diagram from Largeau and Moriniere (2007). Used with permission.

2.3.1 FFS Flow Structure, Three-Dimensionality, and Periodicity

Flow over this geometry is characterised by an upstream, standing vortex, and a downstream

recirculation region, characterised by weakly periodic shedding. Bowen and Lindley (1977), citing

Sacré (1973), described the upstream, standing vortex as an extension of the escarpment, that is,

providing cliffs with an effective slope, determined by the size of the vortex. They concluded that the

flow, particularly flow speed-up, was largely insensitive to escarpment slope angle above the

31

threshold at which upstream separation occurs. However, Bowen and Lindley (1977) concluded that the wake region downstream of the crest of the escarpment increased with escarpment slope angle. Because of this, analysis at a single escarpment slope angle of 90° provides a reasonable but conservative estimate of the flow over escarpments with separation, through to the 90° case.

The extent of lateral variations in the FFS case is impacted by the aspect ratio of the model, that is, the height of the model compared to the width of the model, and whether modelling is performed in an open or closed jet wind tunnel. Moss and Baker (1980) stated that the aspect ratio should be larger than 10 to maintain two-dimensionality in the central region of the flow, as the total entrainment of fluid in the recirculation region is a function of the width of the model. The purpose of having a large aspect ratio is not to eliminate any three-dimensional flow structures, but rather to ensure that the three-dimensional flow structures are driven by the FFS geometry and not by the end effects. Camussi et al. (2008) suggest, however, that the central region could be considered to be two-dimensional in a statistical sense.

Largeau and Moriniere (2007) implemented an open jet wind tunnel setup, and were able to identify the flow structure over the FFS, which is reproduced in Figure 8. Their study demonstrated that three-dimensionality within the recirculation region was not merely associated with the end effects, and three-dimensional structures, in the time-varying sense, existed through the central region of the flow, driven largely by branching structures that develop in the upstream recirculation region, and propagate over the crest. Visualisations completed by Largeau and Moriniere (2007) suggest that aspect ratios above 10 are necessary for the central flow region to not be dominated by end effects.

The work of Largeau and Moriniere (2007) also added insight to the work of Kiya and Sasaki (1983b) who described the structure of the recirculation bubble as a flapping vortex controlled by the growth of the recirculation region, which reaches a maximum containable size before a vortex is ejected. Largeau and Moriniere (2007) observed that the accumulation of fluid in the upstream recirculation

region occurred at a faster rate than could be drained laterally, thus forcing the flow over the crest of the step even at larger aspect ratios. By removing the lateral drainage, the infinitely wide FFS case is more accurately modelled. Thus, in the current investigation, experiments were performed in a closed jet wind tunnel, where there is no avenue for drainage flow to pass around the model. Consequently, the mass balance associated with the lateral drainage becomes much simpler to compute as all flow must pass over the crest of the FFS. However, the conservation of mass problem becomes significant again in the yawed flow cases due to the lateral drainage induced by the geometry.

Accumulation and ejection of fluid, or more specifically, the shedding of vortices drives a periodicity observed downstream of the recirculation region. Largeau and Moriniere (2007) estimated the shedding frequency beyond the downstream recirculation structure, identifying peak Strouhal numbers of 0.5 – 0.6, based on the height of the FFS, and calculating the frequency based on vortex convection speed to free-stream velocity ratio. In water channel investigations of flow over a FFS, Camussi et al. (2008) reported a peak Strouhal number of 0.2 beyond the downstream recirculation region. The PSDs of the surface pressure measurements presented by Camussi et al. (2008) exhibited a broad peak, which implies that the shedding is characterised by intermittency. Thus, a Strouhal number calculated based on a ratio of vortex convection speed to free-stream velocity is highly susceptible to uncertainty induced by the intermittency. Thus, the Strouhal number of 0.2 reported by Camussi et al. (2008) provides a useful point of comparison between the literature and the current investigation.

2.3.2 Controlling the Separation Region: δ/h, Turbulence Intensity, Reynolds Number
The size of the downstream recirculation bubble has been investigated by many researchers. Typically, the mean reattachment length is reported as a proxy for the size of the recirculation bubble. Throughout the academic literature, a number of parameters have been linked to the mean reattachment length, including boundary layer thickness to step height ratio, turbulence intensity,

and Reynolds number. Sherry et al. (2010) have catalogued this previous work, which is presented in

Table 2.

Table 2: Mean downstream reattachment lengths normalised by step height (X_L/h) as a function of boundary layer thickness to step height δ/h, step length aspect ratio (L/h) and step-height based Reynolds number (Re$_h$). From Sherry et al. (2010).

Study	δ/h	L/h	Re$_h$	X_L/h
Largeau and Moriniere (2007)	≤ 0.3	≥ 9	2.88–12.82 × 10^4	3.5–5
Hattori and Nagano (2010)	0.33–0.66	23.3	0.9–3 × 10^3	1.82–2.04
Bergeles and Athanassiadis (1983)	0.48	4	2.7 × 10^4	3.75
Moss and Baker (1980)	0.7	12.7	5 × 10^4	4.7
Gasset et al. (2005)	~0.7	> 6	5 × 10^4	5
Zhang (1994)	0.7	32	-	4.02
Leclercq et al. (2001)	0.7	10	1.7 × 10^5	3.2
Sherry et al. (2010)	0.83–2.5	≥ 11.1	1.4–19 × 10^3	1.9–4
Arie et al. (1975)	1.96	4	-	2.5
Farabee and Casarella (1986)	2.4	> 10	2.1 × 10^4	~3
Camussi et al. (2008)	5	> 8	8.8–26.3 × 10^3	1.5–2.1
Castro and Dianat (1983)	5.2	2	5 × 10^4	1.4
Agelinchaab and Tachie (2008)	9.3	6	1.92 × 10^3	4.1

The boundary layer thickness to model height ratio, δ/h, affects the length and height of the downstream separation bubble. This effect has been nominally quantified. Largeau and Moriniere (2007), comparing the work of Moss and Baker (1980), Mohsen (1967), Tashie et al. (2001) and Farabee and Casarella (1991) state that the size of the separation bubble increases as δ/h is reduced, and that the effect is more significant where δ/h is greater than 1. They suggest that this is due to the interaction between the separation bubble and the up-stream turbulence intensity, which is higher closer to the surface. The other factor that they consider is whether the separation bubble is fully contained by the boundary layer. Higher turbulence intensity associated with the bottom of the boundary layer may reduce the mean size of the downstream recirculation region by breaking down the vortex structure.

Hillier and Cherry (1981), Kiya and Sasaki (1983a) and Saathoff and Melbourne (1996) provided initial investigations into the effect of inflow turbulence intensity on the separation bubble on a blunt flat plate aligned with the oncoming flow. Kiya and Sasaki (1983a) generated turbulence intensity by

placing a thin rod in front of the leading edge of a blunt flat plate, with the turbulence intensity controlled by varying the diameter of the rod and the distance of the rod from the plate. Their results quantified the reattachment length, which they normalised against the half-thickness of the blunt, flat plate. As the turbulence intensity was increased from 1% through to 7%, the normalised reattachment length decreased from 10 to 3.

The size of the recirculation region is also affected by Reynolds number. It is the momentum of the fluid as it passes over the crest of the FFS that drives the low pressure region that induces the vorticity associated with the recirculation region. In their water channel experiments examining flow over FFSs at Reynolds numbers based on step height ranging from 1400 to 19 000, Sherry et al. (2010) identified two flow regimes. In the low Reynolds number region, up to a threshold value of 8500, the reattachment length was observed to increase linearly with increases in Reynolds number. In the second regime, the sensitivity to Reynolds number was greatly reduced. A gradual increase in the reattachment length with increasing Reynolds Number was still observed.

2.4 Review of Topographic Developments to the FFS

The aim of this research is to build on the knowledge associated with flow over FFSs, to make the derived knowledge more applicable to wind turbine siting. Two areas of further investigation with direct applicability to Australian wind farms were identified within the introduction: the effect of wind direction on flow over a FFS; and the effect that the natural ruggedness, typically associated with a coastline, will have on flow over a FFS.

To date, there is very little research presented within the academic literature that is directly related to either of the two areas earmarked for further investigation.

With respect to the effect of wind direction, a journal article by Johnston (1970) considered the region upstream of a FFS oriented at 45° to the oncoming flow in a wind tunnel investigation. While Largeau and Moriniere (2007) subsequently identified that the two-dimensional geometry associated with a FFS inevitably induced time-varying three-dimensionality within its associated flow

fields, no research has been published to date examining how this three-dimensionality is affected by wind direction.

A number of cases with similarities to the FFS geometry have been considered in the academic literature. Experimental investigations of flow over ridge lines have considered the effect of wind direction, namely the wind tunnel and field testing of Baker (1985), and the wind tunnel testing of Lubitz and White (2007). Kaltenbach (2003) completed Direct Numerical Simulation (DNS) modelling of a backward facing step at yaw angles of 0° to 60° in 10° increments, at a step height based Reynolds number of 3000, while di Mare and Jones (2003) conducted Large Eddy Simulation (LES) modelling of flow over a fence at a sweep angle of 10°, at a fence height based Reynolds number of 3900. The swept wing is another case from which comparison can be drawn. While some insight into the flow over FFSs at non-zero yaw will be inferred from these cases in the following subsection, there remains a gap in the literature.

Similar observations can be made regarding the problem of ruggedness. Even in the seminal work by Jackson and Hunt (1975), which provided an analytical description of turbulent flow over low hills, and again in Bowen and Lindley's (1977) wind tunnel testing of escarpments with varying up-slopes, it was commented that the speed-up would make analogous topographies in the real world desirable for the siting of wind turbines. Yet, the first study to investigate the natural ruggedness associated with cliffs was published some thirty-four years later by Cochard et al. (2011), considering triangular shaped cliffs.

Despite the lack of direct research into these areas, some understanding of these problems can be derived by piecing together associated research. Such an analysis is presented in the following two sections.

2.4.1 A Theoretical Understanding of Flow over a FFS as a Function of Wind Direction
There is limited data on the flow over a FFS as a function of wind direction. Baker (1985), whilst researching flow over railway embankments, proposed that only the flow component perpendicular

to an escarpment is accelerated. Both his wind tunnel testing and his field data showed that this is a reasonable assumption. Lubitz and White (2007) varied the wind direction over a two-dimensional hill and an axi-symmetric hill, each time comparing their results with a number of different theoretical equations for speed-up that were modified so as to consider the wind direction. Their results were inconclusive, reporting that the uncertainty in their modelling was of a comparable scale to the differences between the various empirical models that they were testing. Nonetheless, their approach of comparing measured results with those derived analytically or empirically can be applied to the analysis of yawed flow over an FFS to determine the reasonableness of these alternative methods.

While Baker (1985) and Lubitz and White (2007) have concerned themselves only with the resultant effects of wind direction, they have not provided a description of the fluid mechanics associated with the varying wind direction. Thus, one must rely on the mechanics associated with the base FFS case to provide the foundation for understanding the effect of wind direction or yaw angle (θ) on the system.

As previously established, Sherry et al. (2010) performed water channel experiments on flow over a FFS for a range of Reynolds numbers from 1400 to 19000. They observed that, in this Reynolds number range, the size of the downstream recirculation region became largely insensitive to Reynolds number above a critical Reynolds number of 8500. It follows that if the size of the separation region remains independent of the flow speed while the component of the flow perpendicular to the escarpment results in a Reynolds number greater than the critical Reynolds number, Baker's assumption can be applied. Thus, if Baker's (1985) assumption is correct, the downstream recirculation region would extend a constant distance perpendicular to the crest of the escarpment, independent of the flow speed and hence yaw angle, since the effect of the yaw angle is to change the component of the flow perpendicular to the escarpment.

The conclusions drawn from the work of Largeau and Moriniere (2007) becomes more significant under yawed flow conditions. They studied flow over an FFS in an open jet wind tunnel, operating over the Reynolds number range of 2880 to 1.3×10^5. They concluded that the accumulation of fluid in the upstream recirculation region occurred at a faster rate than could be drained laterally, thus forcing the flow over the crest of the step. This observation was consistent with the work of Kiya and Sasaki (1983b). Kiya and Sasaki (1983b) observed flow over a flat plate at Reynolds number of 2.6×10^4 in low turbulence intensity conditions. They described a similar forcing in terms of the growth of the downstream recirculation region, where it reaches a maximum containable size before fluid is ejected, giving the recirculation region a flapping appearance. When applied to a FFS at non-zero yaw angle, similar flow physics are expected: upstream and downstream vortices will both entrain and eject flow; however, there is a large lateral flow component. Johnston (1970), in a wind tunnel investigation of flow immediately upstream of a FFS at 45° yaw angle, established that the wind direction is affected even up to $3h$ upstream of the step. Given that there must be a conservation of mass, a high pressure accumulation of fluid downstream of the crest of the model is expected, resulting in a low pressure region upstream of the crest, which would drive a higher velocity along the far edge. This is illustrated in Figure 9. This complex interaction across the span of the wind tunnel implies that end effects will be more significant in the yawed flow cases than in the non-yaw cases.

Jackson et al. (2013) in their CFD analysis of dune formation in off-shore, oblique winds observed corkscrew vortex structures stretching along the length of dunes. This flow structure is expected, as the lateral flow induced upstream, described by Johnston (1970) generates significant lateral momentum. The corkscrew structure is a departure from the weak cellular structure observed by Largeau and Moriniere (2007), where the lateral flow of the corkscrew vortex is expected to break down any steady internal three-dimensional vortex structure. That is, by introducing three-dimensionality (the effect of non-orthogonal wind direction over the FFS), the three dimensionalities

observed over the strictly two-dimensional geometry are expected to be broken down, making the flow structure of this three-dimensional case more two-dimensional.
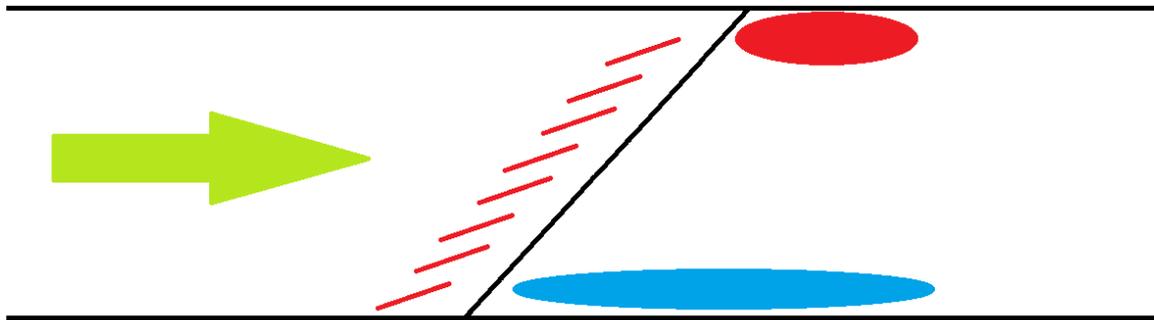
Figure 9: Plan view of flow over a yawed FFS. Crest and wind tunnel walls are denoted by the black line. Free-stream flow is indicated by the green arrow. Red lines denote wind direction upstream of crest. Red oval region indicates high pressure pooling and blue oval region indicates low pressure, high speed region.

Kaltenbach's (2003) time-averaged analysis revealed a similar corkscrew vortex structure in the separation region associated with the backward facing step geometry. However, instantaneous snapshots of iso-surfaces from the velocity gradient tensor show segmented vortices breaking away from the crest at a distinct angle, indicating a spatial periodicity. Further phase averaging of their results to visualise the generation and shedding of dominant vortex structures would have proven incisive.

2.4.2 Modelling Ruggedness

Cochard et al. (2012) observed that a number of wind farms had been recently built on escarpments in West Texas and that "On the south coast of Australia, many exposed headlands were seen as potentially the best sites for wind farms". This led them to examine the problem of FFSs with sawtooth lateral variations. Cochard et al. (2012) and Montlaur et al. (2012) completed complementary experimental and computational analyses of flow over such FFSs. Their work revealed the presence of delta wing style vortices generated from the peaks of the sawtooth elements that propagated downstream beyond the trough. While Cochard et al.'s (2012) experimental work did not reveal what was happening in the downstream region, the computational work by Montlaur et al. (2012) revealed the persistence of the vortices into the far wake. The work

of Cochard et al. (2012) and Montlaur et al. (2012) will be explored in more detail in the following subsection.

Beyond the work of Cochard et al. (2012) and Montlaur et al. (2012) there has been little research modelling the effect of the natural ruggedness associated with cliffs. However, there exist a number of investigations considering the implications of span-wise variations in other bluff-body geometries. These include investigations into flow around square cylinders and plates with wavy edges (Bearman and Tombazis 1993, Bearman and Owen 1998, Darekar and Sherwin 2001), segmented trailing edges of aerofoils (Petrusma and Gai 1994), and wavy circular cylinders (Zou and Lin 2009). Frequently, these researchers were seeking drag reduction for structural and aeronautical applications. Petrusma and Gai (1994) found that castellation of the trailing edge of their aerofoils manipulated the orientation of the vorticity in the wake. This resulted in an increased base pressure and hence a reduction in drag for flow over castellated aerofoils. Darekar and Sherwin (2001) completed numerical work, allowing them to visualise flow past a wavy square cylinder. Their visualisations depicted the change of orientation of the vortex axis, from being dominated by the cross-stream component for a straight, square cylinder, to being dominated by the stream-wise component for the wavy cylinder. The persistence of such structures into the wake and their interaction with wind turbines would result in imbalanced loads across wind turbine rotors. Zou and Lin (2009), investigating flow past a wavy circular cylinder, observed that wake maturation was delayed as the ability of the vortices to roll up was suppressed until farther downstream. It would follow that a rugged cliff might be more amenable to wind turbine siting than a uniformly two-dimensional FFS, as the ruggedness breaks down the span-wise vortex structure, reducing fatigue loading on wind turbines in the vicinity of the crest of such cliffs. However, siting wind turbines within the highly turbulent vortex break-down region would inevitably increase fatigue loading and reduce the energy output of the wind turbines.

2.4.2.1 Observations from Cochard et al. and Montlaur et al.

The sawtooth investigations by Cochard et al. (2012) and Montlaur et al. (2012) are in good

agreement with the work of Petrusma and Gai (1994), whose aerofoils with castellated trailing edges

caused, first, the lateral dislocation of the wake vortices, and secondly, the alignment of the vortex

axes with the free-stream flow. This agreement is observed in spite of the geometric contrast of a

leading edge variation in the FFS case and a trailing edge in the aerofoil case. Conceptually, it also

provided good agreement with Zou and Lin (2009), identifying the growth of the delta wing style

vortices from the peak of the sawtooth, over the sawtooth elements, and downstream, resulting in

the delayed onset of a mature wake.

Cochard et al. (2012) also made preliminary comments about the speed-up over the topography,

and the confinement of the strong vortex structures to the outer thirds of the sawtooth elements.

However, their assessment of the pitch angle indicated adverse conditions would nonetheless be

experienced by wind turbines in the vicinity of such topography. Additionally, they varied the wind

direction of the inflow, and concluded that the size of the delta wing style vortex varies significantly

as a function of wind direction. Where the flow is perpendicular to the mean crest of the step, the

delta wing style vortices develop symmetrically on each side of the peak of the sawtooth. As the

wind direction is changed, there exists a segment of the crest that is windward, and a segment that

can be described as trailing. Cochard et al. (2012) observed that as the yaw angle increased, the

vortex developing from the windward crest would increase in size and strength, while the vortex

developed off the trailing edge experienced a corresponding decrease in size and strength. Montlaur

et al. (2012) then showed that downstream of the sawtooth elements, the vortex axes became

aligned with the free-stream flow.

2.4.2.2 A Brief Review of Flow over Delta Wings

A review of some of the literature pertaining to delta wing vortices may provide a useful comparison

with the flow structure identified by Cochard et al. (2012) and Montlaur et al. (2012). However, the

parameters considered for flow over delta wings make it difficult to quantitatively reconcile delta

wing analyses with flow over a FFS with sawtooth lateral variation. For example, typical delta wing analyses consider the aerofoil independently of the ground plane, at a non-zero pitch angle, while the FFS with lateral variations is flat, and extends downstream indefinitely. Additionally, there is lateral interaction between vortices from adjacent sawtooth elements in the FFS case, in contrast to a vertical interaction between the vortices shed from the delta wing and the detaching flow on the underside of the delta wing. Qualitative and quantitative similarities might still be observable in some flow features.

Early use of the delta wing was recorded by the Polish engineer Siemienowicz in 1650, in the form of delta-type stabilisers for artillery applications (Orłowski 1973). The use of delta wings for their aerodynamic properties experienced pioneering advancement around the time of World War 2 by Lippisch, who designed the first powered delta wing aircraft to fly, as well as over fifty other aircrafts, with most based on the delta wing concept (Weyl 1945, Lippisch 1981, Naughton and Gervais 2002).

The flow structure over the delta wing aircraft is dominated by two counter-rotating vortices when flow is applied at an angle of attack (Hoerner and Borst 1985). These primary vortices induce secondary vortex structures of opposite sign to the primary vortex along the leading edge of the delta wing (Hoerner and Borst 1985). Gad-el-Hak and Blackwelder (1985) and Lowson et al. (1995) identified that the primary vortex structure is itself a merging of smaller vortex pairs. Within this primary vortex structure various authors observed a Kelvin-Helmholtz instability, before the breakdown of the vortex structure (Gad-el-Hak and Blackwelder 1985, Gordnier and Visbal 1994, Gursul 2005). According to Gursul's (2005) review of flow over slender delta wings, the shedding frequency associated with this instability was difficult to identify in each case, varying as a function of Reynolds number, as well as being susceptible to external forcing.
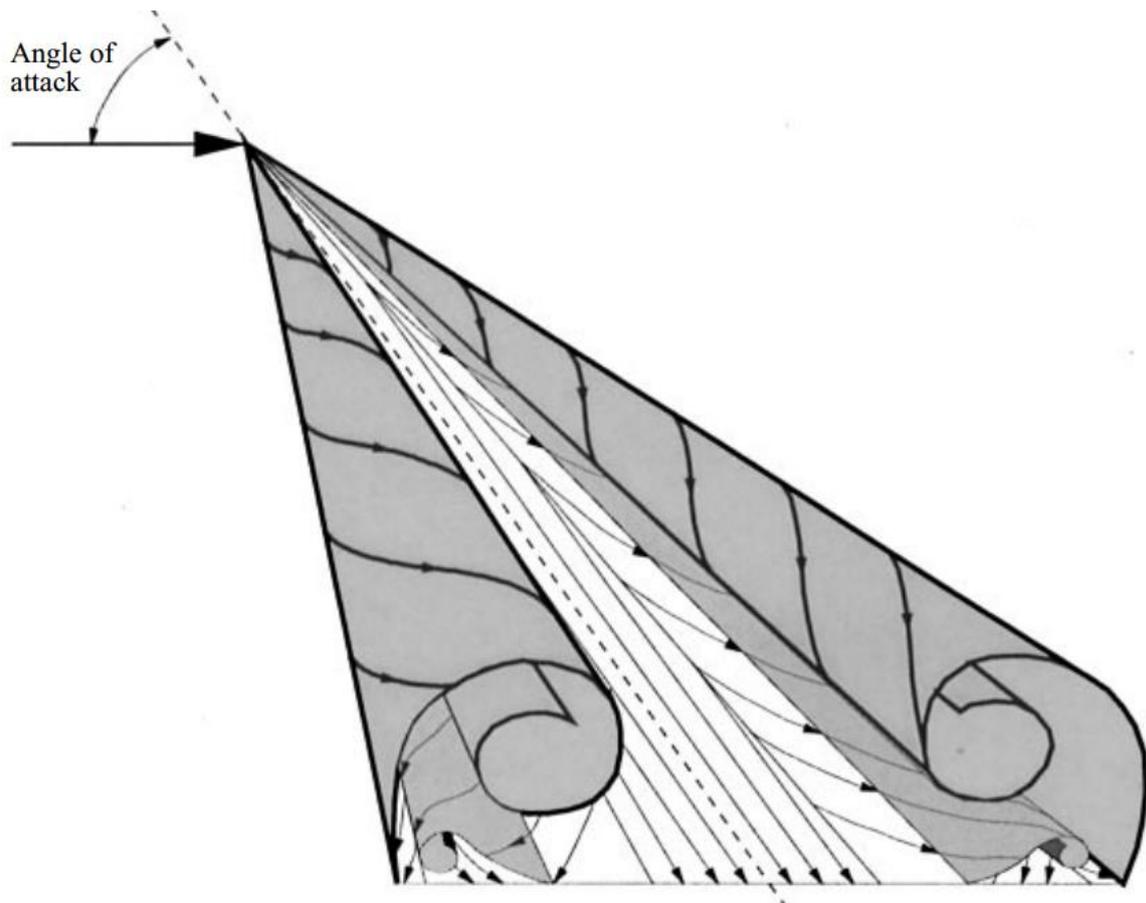
Figure 10: Vortex structure of flow over a delta wing. The primary vortex structure rolling over the secondary structure is evident. Image courtesy of Riley and Lowson (1998) and Cambridge University Press, used with permission. Publication available via the online catalogue at:
http://journals.cambridge.org/action/displayAbstract?fromPage=online&aid=14353&fulltextType=RA&fileId=S0022112098001712

The angle of attack plays a role in the topological development of the flow over the delta wing and the breakdown of the delta wing vortex (Wentz and Kohlman 1971). The angle of attack, which induces an inflow angle over the leading edge of the delta wing, might be compared to the height parameter of the FFS. This suggests that a simple geometric relationship might exist relating the angle of attack of a delta wing and the height of a rugged FFS. However, the insight provided by Pearson et al. (2013) suggests that any such relationship is likely to be complex.

Pearson et al. (2013) investigated the flow structure of the upstream recirculation region of a FFS in a fully developed turbulent boundary layer. Their wind tunnel experiments, conducted at a step height-based Reynolds number of 20 000, demonstrated that the upstream separation region and the stagnation point on the front face of the FFS both occurred at approximately 0.5h. However,

they performed conditional averaging, capturing the growth and ejection of the upstream vortex over the crest of the FFS, where the upstream separation line occurred farther upstream of the crest than in the time-averaged condition. Thus, the mean inflow pitch angle must approach 90° given that the flow stagnates on the front face of the FFS. Further investigation of the upstream separation region at non-zero yaw angles may provide some additional insight into the relationship.

The origin of the delta wing vortices is also of some significance. Most analyses of delta wings ignore the peak or apex of the delta wing, assuming that the two primary vortices are shed independently of each other. However Verhaagen and Van Bossuyt (2006) observed that there are complex interactions between the two vortex structures. The premise of their investigation was that a sharp apex of a delta wing could be magnified, and, with sufficient magnification, would appear blunt. Hence, they investigated flow over a blunt delta wing at various angles of attack and mapped the flow topology in each case. They observed significant topological development as a function of the angle of attack. The implication of the large-scale modelling of the vortex interaction is that the same interaction also occurs on a much smaller scale.

Downstream of the apex, Katz (1999) identified three modes of vortex development over delta wings, determined by the angle of attack of the delta wing and the sweep angle (Λ/λ). The first mode is a symmetric shedding of the crest vortices. At low sweep angles, an increase in the angle of attack results in the delta wing vortices breaking down or bursting. At higher sweep angles, an increase in angle of attack results in the asymmetric shedding of the crest vortices (Rediniotis et al. 1989, Rediniotis et al. 1993).

The bursting of the delta wing vortices has been the subject of much research. The review by Hall (1972) on the breakdown of vortex structures provides a useful description of the vortex breakdown, as well as bringing together various theories on why, when and how this mechanism occurs.

Hall (1972) describes vortex breakdown as the point where a vortex transitions from having the form of a regular spiral, to having a "very pronounced retardation of the flow along the [vortex] axis and a corresponding divergence of the stream surfaces near the axis (Hall 1972)". The implication of such a breakdown is that the vortex transitions from being a concentrated, organised, fast-moving stream of fluid to a less concentrated, chaotic region of slow-moving fluid. This breakdown is often referred to as "bursting".

Hall (1972) identifies three conditions necessary for vortex breakdown:

- Swirl: Angle of swirl, given by $tan^{-1}(v/w)$, is greater than 40°. Lateral and vertical components of flow velocity are given by v and w, respectively.

- Positive pressure gradient along the vortex axis.

- Divergence of stream tubes in the vortex tubes, occurring upstream of the breakdown.

Hall (1972) highlights the fact that these conditions are interrelated, and that conditions external to the vortex may induce or retard vortex breakdown. Gursul et al. (2005) highlighted the fact that the transition to vortex breakdown is less abrupt as the sweep angle of the delta wing decreases, or, relating back to the context of the sawtooth FFS, as the A/λ ratio is decreased.

The location of the bursting over the delta wing also varies as a function of sweep angle and angle of attack (Lowson et al. 1995). The location of the vortex bursting has also been shown to vary dynamically, oscillating along the vortex axis, with a characteristic chord-based Strouhal number of the order of 0.03 (Gursul 2005).

Beyond the breakdown, a broad spectral peak in pressure can be observed with the dominant Strouhal number reducing with increasing sweep angle (Gursul et al. 2005). Stating the Strouhal number range does little for comparison purposes as the dominant Strouhal number is unique to each sweep angle and angle of attack.

Rediniotis et al. (1989, 1993) surveyed the wake of a delta wing with sweep angle of 76°, varying the Reynolds number and angle of attack and measuring the Strouhal number associated with the spectral peak. They observed periodicity in the wake: a simultaneous vortex shedding from each leading edge vortex, independent of Reynolds number. Furthermore, they observed that as the angle of attack increased from 30° through to 70°, the spectral peak occurred at lower Strouhal numbers, reaching a plateau at an angle of attack of around 70° and a wing span-based Strouhal number of 0.1. However, this angle of attack also coincided with the return of a higher frequency shedding. They showed that the two leading edge vortices shedding from the leading edges were related by a 180° phase difference. This asymmetric shedding is analogous to the von Kármán vortex street observed in the wake of a flow impinging on a flat plate.

The work of Gursul (1994), who also cite Roos and Kegelman (1990), provides some perspective on the characterisation of shedding frequency. They identified that the shedding frequency reduces approximately linearly with the distance downstream of the apex of the delta wing, beyond the vortex bursting. Thus, each delta wing has a characteristic downstream distance-based Strouhal number dependent on sweep angle and angle of attack.

Thus, in comparing flow over delta wings to flow over rugged FFS models, the following features might be observed in each case:

- Pairs of counter-rotating vortices, shed from the peak and along the leading edge of the sawtooth/delta wing, inducing the formation of secondary structures.

- The height of the FFS might be considered a parallel variable to the angle of attack of the delta wing.

- Depending on the sweep angle, or the A/λ ratio in the FFS case, and the shape of the peak, the vortex interaction at the peak may play a role downstream.

- Kelvin-Helmholtz instability within the primary vortex structures, whose frequency may be difficult to identify, being highly dependent on Reynolds number.

- Sudden breakdown of the vortices, resulting in flow stagnation and an increase in the diameter of the vortex region.

- Distinct Strouhal numbers, based on the amplitude of the variation of the FFS and the step height.

- Alternating shedding of vortices off the leading edge.

2.4.2.3 Shape Development

Cochard et al. (2012) and Montlaur et al. (2012) provide the most relevant background to the modelling of ruggedness of the lateral profile of steps/escarpments applicable to wind turbine siting. The sawtooth profile considered by Cochard et al. (2012) and Montlaur et al. (2012) can be considered as a series of yawed FFS geometries. Thus, an investigation into flow over a straight-edged FFS at different yaw angles can provide insight into the particulars of the flow structures associated with sawtooth geometries to the extent that the yawed FFS cases provide limiting cases for the sawtooth geometries. This insight is not limited just to the 0° yaw case, where the wind is perpendicular to cliff, but to a broad range of wind directions.

Modelling a full sawtooth profile, however, provides insight into the flow at the interface between the yawed FFS segments – along the peak lines and trough lines, which cannot simply be inferred from the yawed FFS cases.

The advantage of simulating ruggedness using the sawtooth geometry is that the sharp vertices provide distinct separation points, implying that a robust flow topology might be expected. The flow around wavy square cylinders, investigated by Bearman and Tombazis (1993), Bearman and Owen (1998), and Dareker and Sherwin (2001) suggests a useful next step in the topographical development of the idealised rugged FFS. The use of wavy, rather than sharp edged lateral variations to the FFS provides a representation of the natural scalloping associated with the wind-sculpted cliffs often encountered in nature (Carter and Woodroffe 1994). From a topological perspective, the wavy or sinusoidal lateral variation to the FFS might be compared to flow past a cylinder, where flow

separation is less clearly defined; implying that variation in the topology might be encountered with small variations to the topography. Such variations might include the amplitude and wavelength of the sinusoidal lateral variations.

2.5 Contextualising Research within Real-World Parameters

Table 1, presented in Chapter 1: *Introduction* highlighted the size of cliffs often encountered in the siting of wind turbine in complex terrain, with the height of the topographic features generally being in the order of 100 m. At a typical rated wind speed of a wind turbine of 15 ms^{-1}, this corresponds to a Reynolds number of 10^8, three orders of magnitude higher than the Reynolds numbers achieved in the experimental work reported in the academic literature (Sherry et al. 2010). The nature of the real wind environment is that the wind speed varies from calm to extreme winds, in excess of 40 ms^{-1} (Rowcroft 2011). This implies that the flow topology, the size of flow features, the speed-up, and changes in turbulence intensity that might be measured in laboratory experiments need to be interpreted with caution.

Another aspect of the real-world is the variability in the conditions caused by the atmospheric boundary layer. There are several aspects of the atmospheric boundary layer that affect the wind environment, and hence the flow over topography. In the context of wind turbine siting near cliffs, the work of Sherry et al. (2010) has highlighted the thickness of the atmospheric boundary layer as being a significant variable in affecting the local flow. According to Stull (1997), the thickness of the atmospheric boundary layer ranges "from hundreds of metres to a few kilometres". Thus, for wind turbine siting on cliffs, the δ/h parameter can be assumed to exceed unity.

Already highlighted within this review is the fact that the turbulence intensity will be a significant parameter in understanding flow over the various FFS configurations for examination. Thus, consideration of the inflow turbulence intensity is appropriate.

The velocity and turbulence intensity profiles within an adiabatic boundary layer are determined by the surface roughness (Counihan 1973). Thus, the region upstream of an FFS will determine the

inflow turbulence intensity levels. Over a flat fetch without obstructions, the turbulence intensity will be lower than the case where there is a rough fetch. Over ocean fetches, the turbulence intensity increases as wind speed increases due to the increase in the size of the waves induced by the higher wind speeds (Türk and Emeis 2010). The turbulence intensity in each of these cases will still be higher than clean free-stream wind tunnel conditions, which are under 0.9% in the Monash University 450 kW wind tunnel (see Section 3.3.1 *Three Wind Tunnel Configurations*). While conditions with higher turbulence intensity provide a better match to real-world wind conditions, it is easier to identify the underlying flow features with lower background turbulence intensity levels.

The atmospheric stability is a parameter associated with the atmospheric boundary layer that is difficult to model in wind tunnel experiments. It has attracted significant interest in recent literature including the effects of power output, noise output and fatigue loading on the wind turbines (Emeis et al. 1995, Rohatgi and Barbezier 1999, Hand et al. 2003, Sumner and Masson 2006, Sathe and Bierbooms 2007, van den Berg 2007, Hansen et al. 2012). Whilst, as established in Section 2.1.4 *Atmospheric Stability within the Atmospheric Boundary Layer*, it is reasonable to limit modelling of the atmospheric stability conditions to near neutral cases, there are cases with wind speeds up to 15 ms^{-1} that can be associated with both stable and unstable stability conditions (Hansen et al. 2012).

There is also significant and inherent variation in the height of cliffs around the world. Similarly, there is a large range associated with the thickness of the atmospheric boundary layer. The range of applicable Reynolds numbers is typically very large. Thus, it is necessary to avoid placing too much emphasis on quantitative descriptions of, for example speed-up, with the ambition of applying them directly into an estimate of long term energy production for a given wind turbine. Rather, it is best to focus on the underlying flow structures that can be clearly attributed to physical phenomena.

2.6 Summary

The previous sections have highlighted areas worthy of further consideration. In the first instance, there is considerable data that is already published in the academic literature quantifying the downstream recirculation region associated with the basic FFS geometry. This applies, in particular, to the mean reattachment length (Bowen and Lindley 1977, Moss and Baker 1980, Leclercq et al. 2001, Largeau and Moriniere 2007, Sherry et al. 2010, Ren and Wu 2011). It has also been shown that a cellular structure, that is, three-dimensionalities exist in the recirculation region over the two-dimensional FFS geometry (Largeau and Moriniere 2007). A review of literature has highlighted that the mean reattachment length varies as a function of Reynolds number based on step height, and boundary layer thickness, normalised against the step height (Sherry et al. 2010). Additionally, related literature has also suggested that the inflow turbulence intensity would also be an important variable in determining the size of the recirculation region (Hillier and Cherry 1981, Kiya and Sasaki 1983a). Furthermore, development of velocity, turbulence intensity, and Reynolds Stress profiles have been documented for various FFS cases (Bowen and Lindley 1977, Ren and Wu 2011), and dynamic measurements have identified periodic shedding of the separation bubble (Largeau and Moriniere 2007, Camussi et al. 2008). Surface visualisations have been used to directly identify three-dimensional flow structures and to measure the mean reattachment length (Largeau and Moriniere 2007). These variables provide a starting point for comparison, with results being contextualised based on Reynolds number, inflow turbulence intensity, and boundary layer to step height ratio. The choice of inflow conditions will be addressed in Chapter 3: *Methodology*.

A gap in the literature has been identified around the effects of wind direction on the flow over a FFS. That only the component of flow perpendicular to an escarpment might be accelerated was a notion applied to marginally different applications (ridges) (Baker 1985, Lubitz and White 2007), but not to the specific case of flow over a FFS. With three-dimensionalities already observed over the two-dimensional topography (Largeau and Moriniere 2007), one might expect that further three-dimensionalities may develop, or that the lateral flow induced by the yaw angle might break down

some of the three-dimensional structures. Thus, the hypothesis related to speed-up as a function of the orthogonal wind component is a hypothesis that needs to be tested further. Additionally, a detailed examination of the effect of yaw angle on the flow structures found in such flows, including measurement of the size of the recirculation region, should also result in new insights. The effect of inflow turbulence intensity clearly will add further complexity to the problem.

Another related area identified for further research was ruggedness associated with cliffs. Sawtooth lateral variations have been considered in the literature, providing a helpful reference point (Cochard et al. 2012, Montlaur et al. 2012). The general flow structure describing the formation of delta wing style vortices over the geometry is documented; however, there remains a clear need for a more detailed examination of the flow topology. The lack of geometric variation to the FFS addressed in the academic literature also opens up avenues for further research. The shape of the lateral variation can better mimic the natural erosion by using a sinusoidal variation (Carter and Woodroffe 1994); while the sawtooth geometry provides a valuable case for validation. In the first instance, research into flow over delta wings provides important background to flow over rugged cliffs, particularly in the light of the research presented by Cochard et al. (2012) and Montlaur et al. (2012). The basic structure of the counter-rotating vortices and their breakdown is applicable to the rugged FFS case (Hoerner and Borst 1985). Further research associated with structural and aerofoil wing applications investigating castellation and wavy variations of aerofoil and cylinder sections provide additional parallels with the investigation into the ruggedness associated with eroded cliffs (Bearman and Tombazis 1993, Petrusma and Gai 1994, Bearman and Owen 1998, Darekar and Sherwin 2001). By parameterising the topographic variations based on shape, amplitude and wavelength, an experimental regime identifying resultant development of velocity and turbulence intensity fields can be established, in addition to identifying a more detailed flow structure or topology.

While the scope described above does not address all of the possible and important aspects of wind

flow over FFSs, and by extension all siting options, the thesis scope provides insight into the base FFS

case, before complexity is added to the topography, resulting in new and important insights into the

flow structure over different shaped cliffs, and by extension, the siting of wind turbines on such

cliffs.

3. Methodology

In this chapter an experimental methodology is presented, outlining the use of wind tunnel testing to, first, validate the study against the published literature, second, to assess the effect of wind direction on the FFS geometry, and finally to investigate the effect of ruggedness on the FFS, which is modelled as lateral variations of the crest of the FFS. The Monash University 450 kW wind tunnel is then described. The various inflow conditions are then specified, followed by the three testing techniques. The first technique is to complete discrete point based velocity and pressure measurements by traversing through regions of interest with four-hole pressure probes. The second technique is a surface shear stress visualisation. The final technique is the measurement of surface pressure with surface pressure taps. Harbig (2013) performed a number of CFD simulations for direct comparison with the experimental work. The specifications of the CFD modelling are presented in Appendix: *CFD Methodology*.

3.1 Experimental Regime

The literature review, presented in Chapter 2, highlighted three areas of investigation: validation of published literature, investigation of yaw angle, and investigation of ruggedness.

Throughout the academic literature, various approaches have been taken to investigate flow over topography. In the broad sense, three approaches are available: field testing, wind tunnel testing, and computational approaches. Each approach has advantages and limitations.

Field testing provides real-world data, and the uncertainty associated with scale modelling is largely eliminated. However, it is expensive, and results are typically applicable to only the site that has been tested. Furthermore, field testing requires long measurement campaigns so as to capture sufficient data representative of the desired inflow conditions.

Wind tunnel testing is less expensive than field testing, but the costs associated with wind tunnel testing are, nonetheless significant. Wind tunnel tests allow good control of inflow conditions, but, as alluded to in Section 2.5 *Contextualising Research within Real-World Parameters*, there is

inevitably a discrepancy between the flow conditions modelled in the wind tunnel, and those experienced at a potential wind turbine site.

Computational investigations solve the Navier-Stokes equations, with accuracy contingent on the resolution of the grid and the use of turbulence models that define the behaviour of the turbulent eddies as they decrease in size, and approach the magnitude of the grid. Assessment of computational approaches revolves around the trade-offs between computational resources and desired accuracy. One of the key advantages of numerical approaches is their ability to visualise results.

For the purposes of this research, wind tunnel facilities have been made available. An experimental regime to investigate the various aspects identified in Chapter 2 using the wind tunnel facilities at Monash University is thus presented.

3.1.1 FFS Models
Various wind tunnel model types have been implemented in this investigation to address the research areas identified in the literature review. The straight-edged forward facing step is the first case, and provides a point of comparison with the literature, in particular with the work of Bowen and Lindley. Varying the step height between 0.05 m and 0.15 m and using several inflow conditions allows further investigation of the relationship between the size of the recirculation region, δ/h and the inflow turbulence. The consideration of yaw angle is original research, building on the base, 0° case, again, enabling investigation of the mean reattachment length as a function of δ/h and the inflow turbulence, as well as enabling comparison with Baker's hypothesis (Baker 1985) that only the flow perpendicular to crest is accelerated. The lowest turbulence inflow has been used for collecting velocity statistics so that the flow structures can be more easily identified. Step heights of 0.05 m give a δ/h value of 2, which is broadly consistent with boundary layers over ocean fetches (Chen and Lui 2005) and the coastal cliffs identified in Table 1. The yawed forward facing step cases provide the building blocks for the rugged cases. Again, the 0.05 m step height is used with the lowest

turbulence inflow to simplify the analysis. The sawtooth case is considered first as it builds directly onto the yawed cases. A brief survey of topographic features in Google Earth identified that the amplitude to wavelength ratio was typically between 0.325 and 1, hence the use of four models with amplitude to wavelength ratios of 0.325, 0.5, 0.65 and 1. This has been paralleled in the selection of sinusoidal geometries. The sinusoidal geometry was selected as it more closely mimics wind eroded cliffs, for example the rounded cliffs at Cathedral Rocks in South Australia.

A full list of geometries considered in this research is presented below. Schematics are presented in Figure 11.

Straight-edged FFS models at h = 50 mm were modelled at six yaw angles: θ = 0°, 10°, 20°, 30°, 40°, and 50°.

Straight-edged FFS models at h = 100 mm and h = 150 mm were modelled at three yaw angles: θ = 0°, 20°, and 40°.

The sawtooth and sinusoidal models were of height h = 50 mm, and were modelled at four values of amplitude to wave-length ratio: A/λ = 0.325, 0.5, 0.65, and 1.
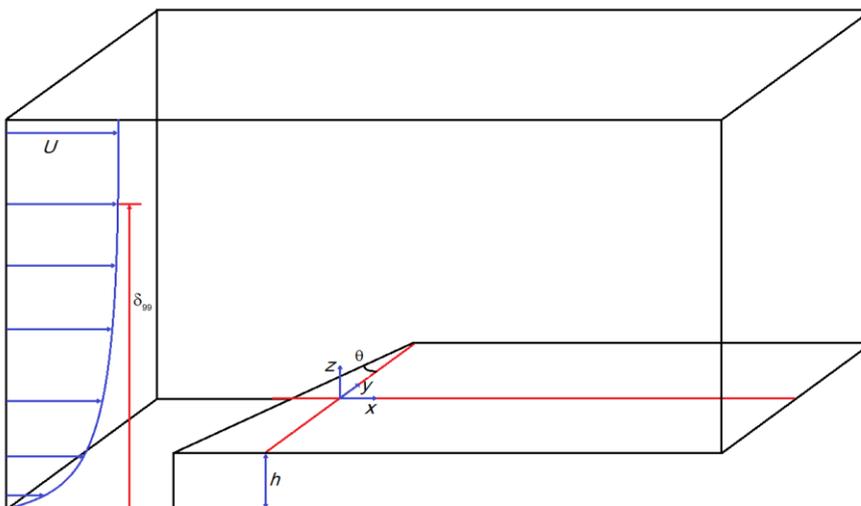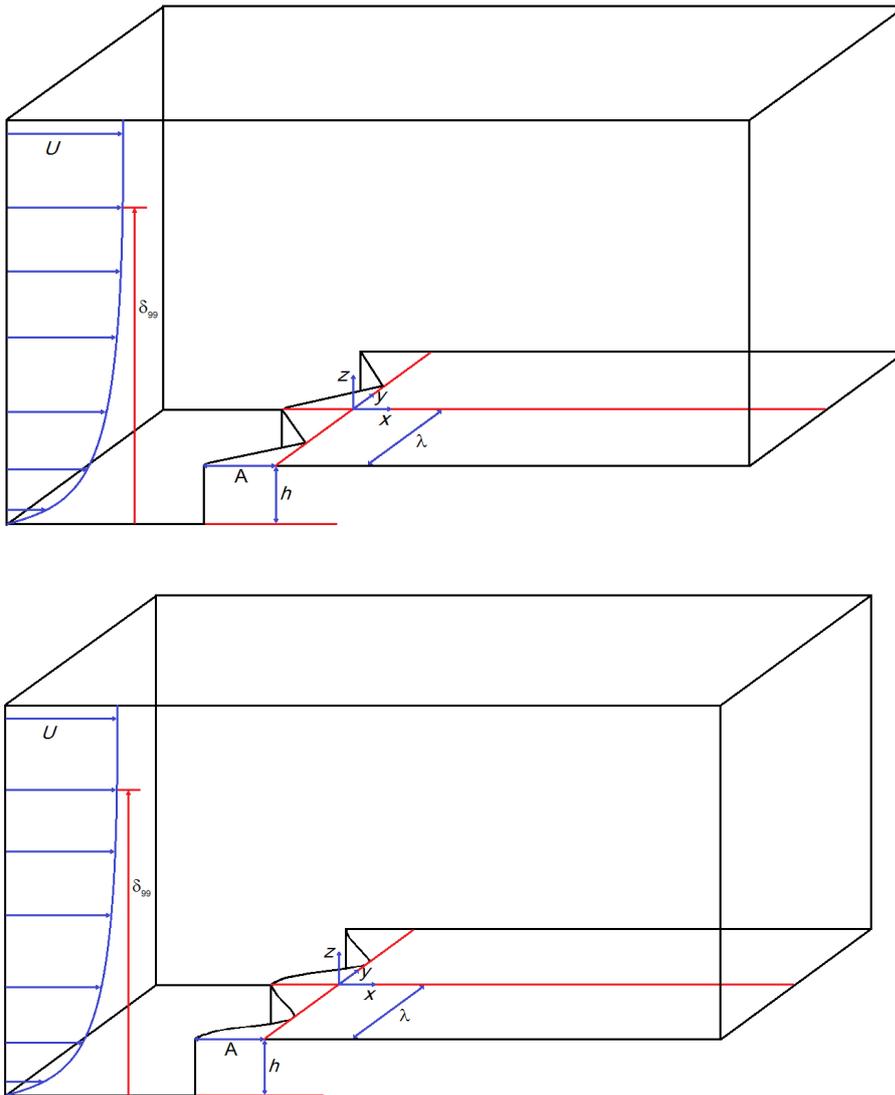
Figure 11: Schematics of FFS models implemented through this investigation.

3.1.2 FFS Validation Studies

A validation study of the base FFS case was proposed, where the effect of variations to the inflow conditions and the height of the FFS were measured. Mean and time-varying components of velocity were measured at various points above the surface of the FFS configurations using four-hole pressure probes, also known as Cobra Probes. The specifications of the probes are presented in Section 3.4 *TFI Cobra Probes*. Mean reattachment lengths can be measured using surface shear stress visualisation techniques. A description of those techniques is presented in Section 3.5 *Paint Drop Surface Shear Stress Visualisation*.

The purpose of the FFS validation studies is three-fold.

- To compare velocity statistics to previously published work, in particular the work of Bowen and Lindley (1977), and Ren and Wu (2011).

- To compare the size of recirculation bubbles for flow over FFSs using the mean reattachment length as a proxy measure.

- To provide a foundation case against which to compare the results gathered in the remainder of the research program.

Bowen and Lindley (1977) and Ren and Wu (2011) both provided vertical profiles of velocity statistics at different locations downstream of FFSs. They used hot-wire anemometry and particle image velocimetry, respectively. Bowen and Lindley (1977) documented the speed-up and the development of turbulence intensity, as a function of distance downstream of the crest. Ren and Wu (2011) provided vertical profiles of Reynolds Stresses, also as a function of distance downstream of the crest. Thus, direct comparisons can be made with this research and the results presented in the literature, ensuring that the facilities and techniques being implemented are functioning correctly.

Peak Strouhal numbers downstream of the recirculation region of a FFS were also reported by Camussi et al. (2008) and Largeau and Moriniere (2007), again, facilitating direct comparison of the current work with the literature.

The mean size of the downstream recirculation region is often measured with the proxy of the mean reattachment length. The mean reattachment length is shown in the FFS schematic, presented in Figure 7. Sherry et al. (2010) compiled a list of mean reattachment lengths for flow over FFSs from a range of researchers. This list, reproduced in Table 2, provides a good source of data for comparison.

3.1.3 Yawed Flow over a FFS
The literature review highlighted an absence of data relating to the effect of wind direction on flow over the FFS. There are two aspects to this problem: the first is to quantify speed-up and turbulence intensity, and how they develop downstream. The second aspect is to identify the underlying flow structures, and to characterise them.

The approach presented for the 0° yaw case is not unreasonable. That is, to traverse the downstream region with Cobra Probes to measure velocity and turbulence statistics; and secondly, to conduct surface shear stress visualisations, enabling the measurement of the mean reattachment length, and identifying any three-dimensionality associated with the flow. While the former approach focuses on the central region of the flow, where end effects are negligible, the latter approach highlights the flow topology and the interaction between the end effects and the central region, as discussed in the literature review.

The literature review posed a number of research questions relating to the non-zero yaw angle.

- While Baker's assumption that only the flow component perpendicular to the crest is accelerated comes from linear theory, it is often used in commercial wind modelling packages, such as Risø's Wind Atlas Analysis and Application Program. Thus, is Baker's assumption reasonable in the context of FFSs?
- How does the velocity, speed-up and turbulence intensity downstream of the step vary as a function of wind direction?
- Is the size of the recirculation region affected by the wind direction?
- Does a non-zero yaw angle break down the structures that were observed within the recirculation region of the zero yaw angle case?
- If so, what are the subsequent changes in flow topology?
- Can the predicted end effects associated with the non-zero yaw angle be identified?

These questions build on the knowledge of the zero yaw angle case that is presented in the literature. The following parameters were identified in the zero yaw angle case and require consideration in the non-zero yaw angle case.

- Reynolds number was identified as affecting the size of the recirculation region.
- Turbulence intensity was identified as affecting the size of the recirculation region.

- Boundary layer to step height ratio was identified as affecting the size of the recirculation region.

- Periodic shedding was observed from the recirculation region.

Reynolds number ought to be maintained at a value above 8500, as established by the work of Sherry et al. (2010). In the case of non-zero yaw angle, the Reynolds number ought to be kept above $8500/\cos(\theta)$.

The relationship between turbulence intensity and the size of the reattachment length in the zero yaw angle case, identified by Hillier and Cherry (1981) and Kiya and Sasaki (1983a), suggests a similar relationship would exist at non-zero yaw angles. A low turbulence environment does, however, make flow structures easier to identify.

Table 3: Independent variables, dependent variables and measurement techniques associated with examining yawed flow over a FFS.

	Step Height (Reynolds number)	Inflow conditions (Turbulence intensity, δ/h)	Yaw angle
Velocity	Probe Measurements		
Speed-up	Probe Measurements		
Turbulence intensity	Probe Measurements		
Shedding frequency	Probe Measurements		
Flow topology	Visualisation		
Size of Recirculation Region (Mean Reattachment length)	Visualisation		
Flow topology	Visualisation		
End effects	Visualisation		

The boundary layer to step high ratio, which controls the momentum deficit through the recirculation region, is another parameter that remains as pertinent in the zero yaw case as in the

non-zero yaw case. As highlighted in the literature review, modelling δ/h values greater than one is appropriate for the siting of wind turbines on cliffs.

Given that a weak periodicity in the shedding from the recirculation region was observed by Largeau and Moriniere (2007) and Camussi et al. (2008) in the zero yaw angle case, similar shedding might be expected in the non-zero yaw angle cases.

The independent and dependent variables and the measurement techniques required to answer the research questions highlighted related to yawed flow over a FFS are presented in Table 3.

3.1.4 Modelling Flow over a Rugged FFS

Like the variation of wind direction discussed in the previous section, the introduction of ruggedness needs to be approached both from the perspective of quantifying the wind flow and turbulence characteristics, as well identifying the flow structures that develop over the step.

The literature review revealed that initial investigations had been completed by Cochard et al. (2012) and Montlaur et al. (2012) on sawtooth lateral variations to the FFS. While their work did much to answer the general questions related to flow over sawtooth FFSs, in particular identifying the similarity of the flow structure to that over delta wings, their work had a finite parameter set, investigating two types of geometry. Thus, increasing the parameter space used by Cochard et al. (2012) and Montlaur et al. (2012) by varying the geometry will extend the generality of the results and identify new flow structures not previously observed. The parameter space can be expanded by varying the amplitude and the shape of the variations lateral variations. In particular, changing from a sawtooth to a sinusoidal geometry is expected to make the flow structure less stable, as the distinct shedding locations are removed.

Specifically, the areas highlighted by the literature review for further investigation are listed below.

- How do variations in the amplitude to wavelength ratio of the lateral variations affect velocity and turbulence over the topography?

- How do variations in the amplitude to wavelength ratio affect the flow topology over the topography?

- How do variations in the shape of the lateral variation affect velocity and turbulence over the topography?

- How do variations in the shape of the lateral variation affect the flow topology over the topography?

- What observations can be made regarding the flow dynamics?

While the development of velocity and turbulence statistics is important, of more significance is the underlying flow structure. Determining whether, in the first instance, changes to the amplitude to wavelength ratio affect the flow topology, and secondly understanding why this happens provides information that can be more generally applied to real world cases. Similarly, does a shift from the sharp edges of the sawtooth case to the smooth, sinusoidal curve precipitate a change in topology or does it induce instability due to not having precise shedding locations?

The notion that the flow structures that develop above the surface leave a "footprint" on the surface is the basis for surface shear stress visualisations. Additional Cobra probe measurements above the surface provide the body of the flow structure, highlighting turbulent regions and coherent vortex structures and their region of influence. In particular, the Cobra probe measurements characterise the height above the surface, identifying the vertical reach of the various vortex structures.

While the mean flow topology is a useful starting point in characterising the flow over the idealised ruggedness, and the presentation of the mean flow topology is indeed a significant result in and of itself, it would be naive to assume that there were not dynamic interactions between the various flow structures. These dynamic interactions can be measure using the dynamic measurement capabilities of the Cobra probes, but such an approach struggles to provide a broad picture of how the flow structures interact because the number of point measurements that can be made concurrently is low. Another option is to conduct surface pressure measurements. Using the

pressure measurement system available at Monash University, up to 128 discrete points can be measured concurrently. Thus, the scope of this work will provide a basis for finding the dynamic interactions present.

The dependent and independent variables are thus presented in Table 4, along with the proposed measurement techniques.

Table 4: Independent variables, dependent variables and measurement techniques associated with examining flow over a FFS with lateral variations.

	Step Height (Reynolds number)	Inflow conditions (Turbulence intensity, δ/h)	Amplitude to wavelength ratio (A/λ)	Shape (Sawtooth or sinusoidal)
Velocity	Probe Measurements			
Speed-up	Probe Measurements			
Turbulence intensity	Probe Measurements			
Shedding frequency	Probe Measurements			
Flow topology	Visualisation			
Size of Recirculation Region (Mean Reattachment length)	Visualisation			
Flow topology	Visualisation; Probe Measurements; Surface Pressure Measurements			
Dynamic interactions	Surface Pressure Measurements			

3.2 Monash University 450 kW Wind Tunnel

The Monash University 450 kW wind tunnel is a closed-loop wind tunnel with pitch control. There is

an upstream 4 m by 3 m section that is 3 m in length before a 3:1 contraction over 2.5 m leading into

the main working section, which has a 2 m × 2 m cross-section and extends 12 m downstream.
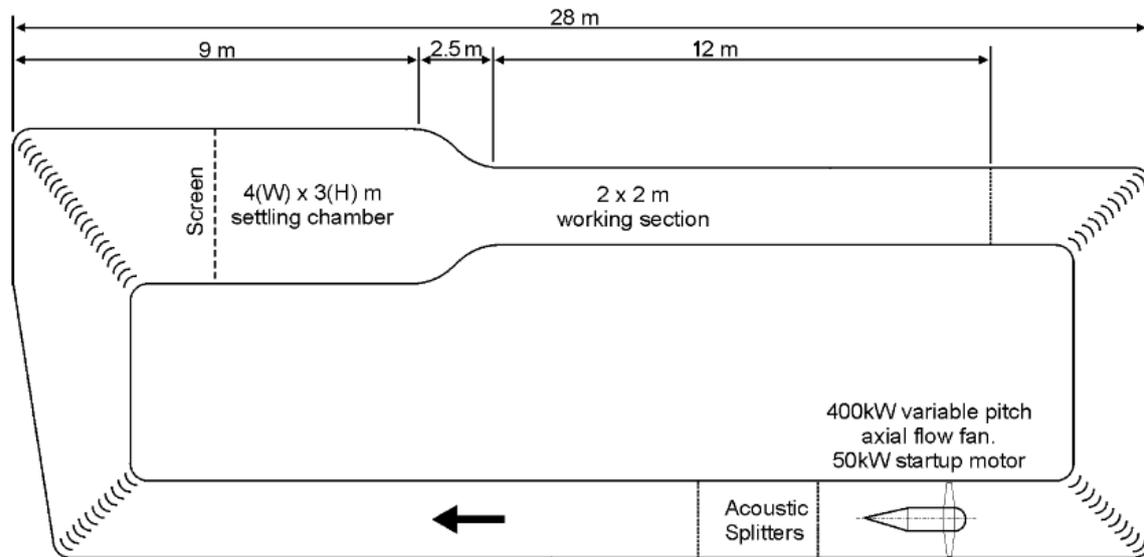
Figure 12: Schematic of Monash University 450 kW wind tunnel facility. Adapted from Eaddy (2005) and used with permission.

3.3 Inflow Conditions

The term "inflow conditions" refers to the wind conditions just upstream of the model. These inflow

conditions can have an important effect on the flow over the geometry being tested. Three different

wind tunnel configurations have been used in this testing, resulting in three different inflow

conditions. These conditions were quantified by traversing with four-hole pressure probes over the

positions where the models were placed. Flow statistics have been collected for each case. These

conditions are described in the following section. A discussion on atmospheric stability follows,

concluding that near neutral stability is the most relevant stability class to wind turbine siting. This is

also the stability class most readily modelled in the wind tunnel.

3.3.1 Three Wind Tunnel Configurations

Three wind tunnel configurations were implemented so as to vary the boundary layer thickness and turbulence conditions. The first two wind tunnel configurations used the original wind tunnel floor in the middle of the working section. The third configuration used a false floor that extended 3.2 m in front of the step location. A summary of each configuration is presented in Table 5.

Table 5: Summary of inflow conditions.

	Configuration 1	Configuration 2	Configuration 3
Wind Tunnel conditions	Clean tunnel	Upstream vortex generator	False floor
Boundary layer thickness: δ	135 mm	715 mm	100 mm
Shear exponent: α	0.11	0.07	0.08

Configuration 1 resulted in a boundary layer thickness, δ, of 135 mm, and used a clean wind tunnel configuration with no additional flow conditioners other than the acoustic splitter, turning vanes, the fine mesh screen, and the contraction, all shown in Figure 12. The wind speed, turbulence intensity and stream-wise component of integral length scale are presented in Figure 13 , with measurements completed along the centre-line, 6.4 m downstream of the contraction. The stream-wise component of the integral length scale was calculated by fitting a von Kármán curve (von Kármán 1948, Hui et al. 2009) to the power spectral density of the *U*-component velocity signal, as described in Section 3.4.1 *Calculating Power Spectral Density and Integral Length Scale*. Note that the integral length scale data was collected subsequent to the initial boundary layer traverse and the vertical resolution was increased through the boundary layer.
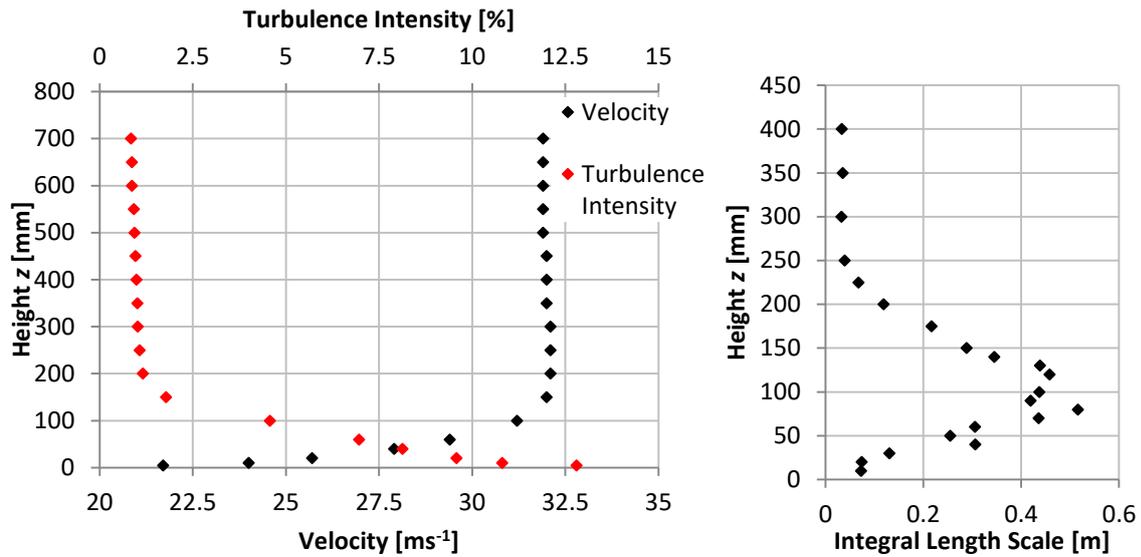
**Figure 13: Inflow conditions for Configuration 1: Velocity, Stream-wise Turbulence Intensity, and Stream-wise Integral Length Scale (*L_u). Note the difference in vertical scales between the two graphs.**

Configuration 2 used a vortex generator to increase the mixing, resulting in an increase to the turbulence intensity through the boundary layer and an increase in the boundary layer thickness. The vortex generator is pictured in Figure 14. Velocity, turbulence intensity, and stream-wise integral length scales are presented in Figure 15. Note that the integral length scale data was collected subsequent to the initial boundary layer traverse and the vertical resolution was increased through the boundary layer. The same measurement location was used for the Configuration 2 as for Configuration 1; this location is over ten times the maximum width of the vortex generator downstream of the vortex generator. The vortex generator is 800 mm high, 630 mm at the base and 100 mm at the top. Lateral traverses showed that the wind speed variation 400 mm either side of the centre-line were less than 2% at a height of z = 50 mm and less than 4% at a height of 330 mm, as seen in Figure 16.
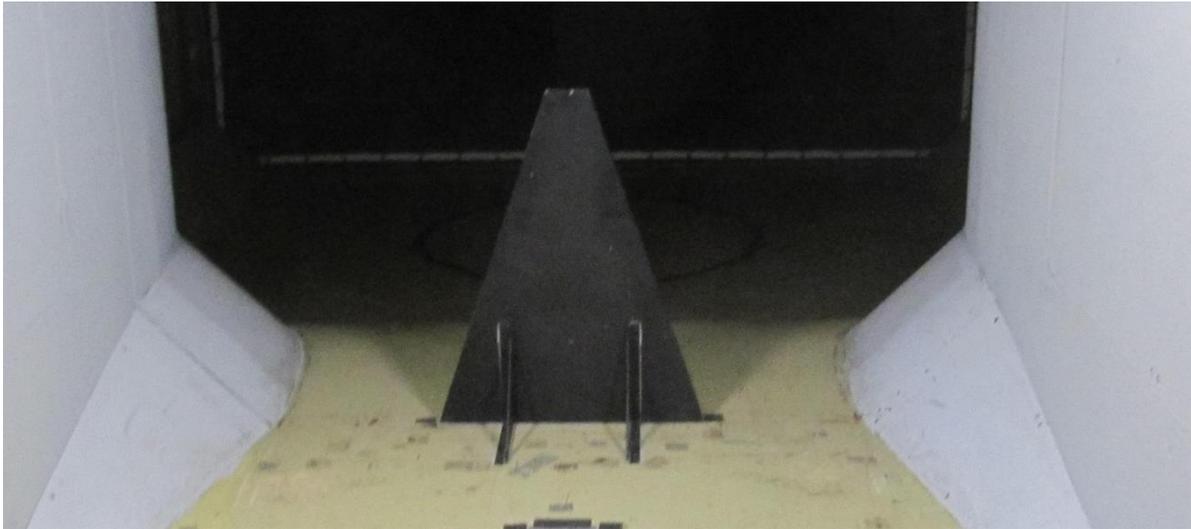
Figure 14: Vortex generator used in Configuration 2.
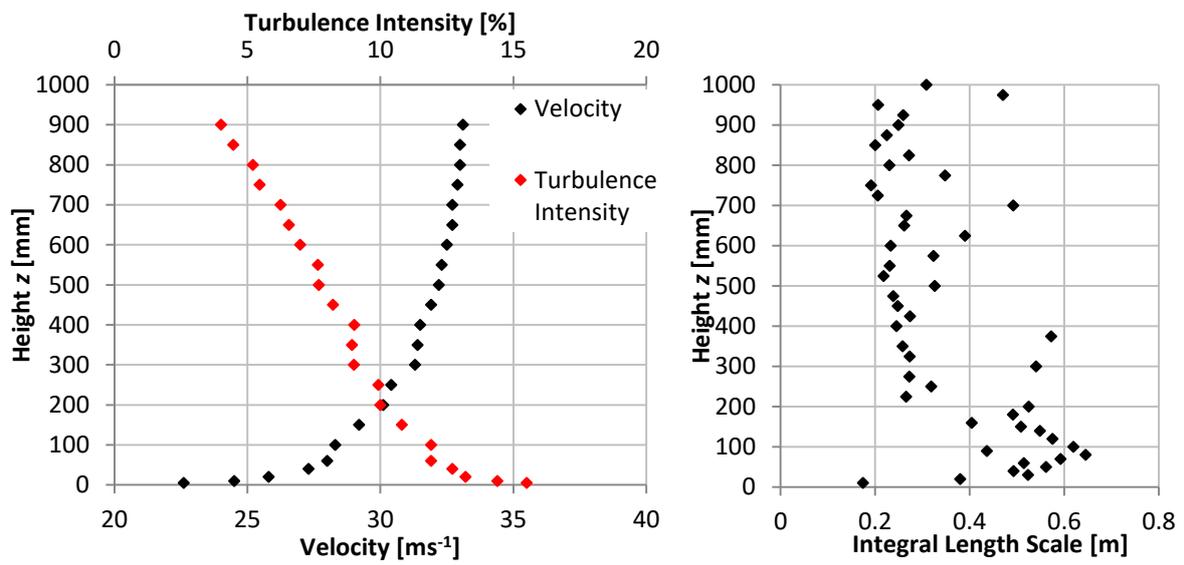
Figure 15: Inflow conditions for Configuration 2: Velocity, Stream-wise Turbulence Intensity, and Stream-wise Integral Length Scale (^xL_u).
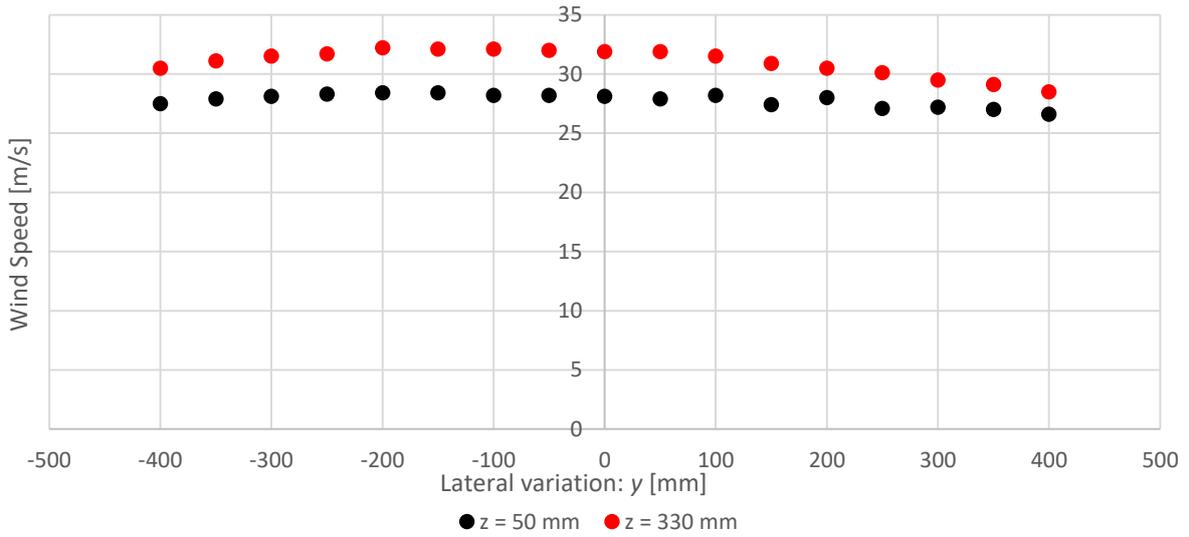
Figure 16: Lateral variation of wind speed for Inflow Configuration 2.
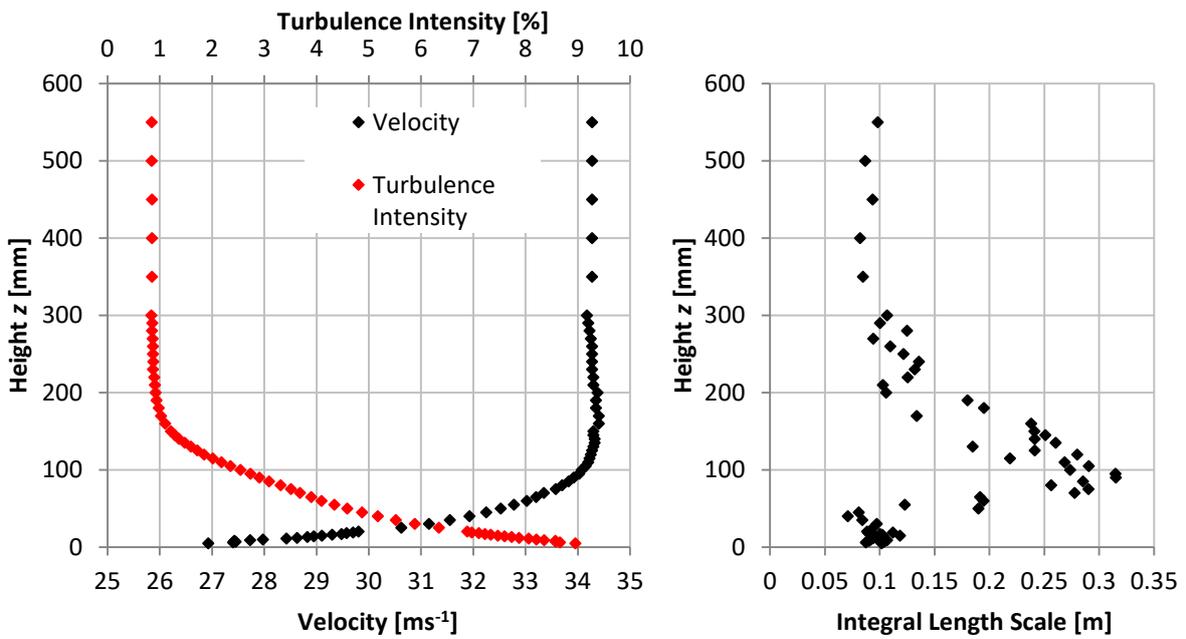
Figure 17: Inflow conditions for Configuration 3: Velocity, Stream-wise Turbulence Intensity, and Stream-wise Integral Length Scale (^xL_u).
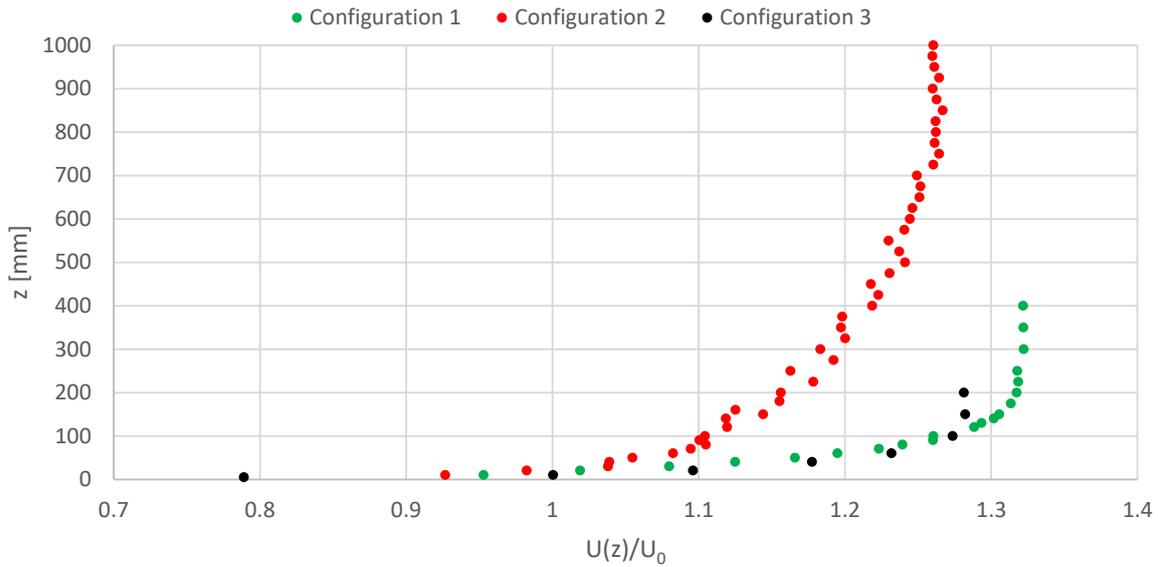
Figure 18: Normalised velocity profiles from the three configurations. Velocity normalised by upstream Pitot Tube reference.

Configuration 3 used a false floor of height 435 mm with a tapered leading edge. This configuration was used to minimise inflow turbulence, so that the flow structures would be most easily visible, not obscured by background noise. As with Configuration 1, only the upstream mesh screen was used to condition the flow. Velocity, turbulence intensity, and integral length scale profiles are presented in Figure 17. Turbulence intensity at the top of the boundary layer was 2.5%, while in the free-stream it was stable below 1%. The integral length scale increased from 0.1 m near the surface to 0.3 m at the top of the boundary layer, before decreasing beyond the top of the boundary layer back to 0.1 m.

A comparison of normalised wind speed profiles using each of the three configurations are presented in Figure 18. The wind speed was normalised by the upstream Pitot-Static tube.

3.3.2 Atmospheric Stability Conditions Impacting Wind Flow

In Section *2.1.4 Atmospheric Stability within the Atmospheric Boundary Layer*, it was established that neutral atmospheric conditions resulted in the largest fatigue loads on wind turbines, and thus neutral stability conditions were most pertinent to investigations relating to fatigue loading on wind turbines (Hand et al. 2003). Without intentional thermal stratification, wind tunnel flow can be assumed to be neutrally stratified due to mechanical mixing.

3.4 TFI Cobra Probes

This section describes the Cobra Probe and outlines the fundamental principles by which the Cobra Probe measurements are converted into velocity and pressure data. The basic specifications of the Cobra Probe, its accuracy, and a summary of the output statistics will be presented. The physical mounting and traversing system is explained, before presenting the post-processing methodology. The means by which the power spectral density and hence integral length scales were calculated is then presented. Finally some comments on the performance of the Cobra Probe in reversed flow are made.

Figure 19: TFI Cobra Probe over a ruler. Units in centimetres.

Turbulent Flow Instrumentation (TFI) four-holed Cobra Probes (Cobra Probes) have been used extensively to collect high frequency velocity data, as well as mean flow statistics. The Cobra Probe acts as four Pitot-static tubes arranged to capture flow from within a 45° cone of acceptance.

Previous multi-hole pressure probes had implemented five or more holes resulting in ambiguity in the determination of velocity components. Shepherd (1981) developed the idea of a multi-hole pressure probe, proposing the first four-holed pressure probe. The design of the current Cobra Probe is presented in the work of Musgrove and Hooper (Hooper and Musgrove 1991, Hooper and Musgrove 1997). They consider the pressure signals from the four holes of the Cobra Probe, generating ratios between the differences of each of the pressure signals. These ratios are then related back to calibration surfaces to determine the three velocity components and the static pressure. This approach is very similar to the original approach taken by Shepherd (1981). A back

pressure reference port is also used, which is plumbed back to the control room, which is at atmospheric pressure.

The size of the probe is illustrated in Figure 19. The body diameter is 12 mm. The head size is 2.6 mm, which is shown in Figure 20. The 45° cone of acceptance is illustrated in Figure 22, while the Cobra Probes' Cartesian co-ordinate system is presented in Figure 21.

Various investigations have been conducted to establish the accuracy of the Cobra Probes, considering both their static response and their dynamic response. Hooper and Musgrove (1991) showed that they are insensitive to Reynolds number for the velocity range 16 ms^{-1} – 110 ms^{-1}, giving confidence in the mean data over a broad velocity range, below speeds where measurements would be sensitive to compressibility. Hooper and Musgrove provided further dynamic validation of the Cobra Probe performance in a swirling jet (Musgrove and Hooper 1993), and validated their results against hot wire anemometers and laser Doppler anemometers in fully developed pipe flow (Hooper and Musgrove 1997). These results demonstrated excellent frequency response up to 1500 Hz. Additionally, Chen et al. (2000), in developing the calibration methodology of the Cobra Probes, suggested that the errors in the calibration surfaces affecting the pitch and yaw angles measured by the probes would be 2°, in addition to a 0.5° uncertainty associated with the alignment of the Cobra Probe relative to the stream-wise axis. They also reported an uncertainty in velocity of 2% associated with the calibration surface and an additional 0.5% uncertainty in velocity due to the calibration procedure caused by an increase in static pressure near the potential core of nozzle jets, typically used to calibrate Cobra Probes (Chen et al. 2000).

This uncertainty propagates through derived quantities, for example, the speed-up ratio, S, which is the ratio of the normalised Cobra Probe measurement over the geometry to the corresponding normalised Cobra Probe measurement through the undisturbed boundary layer, with the Cobra Probe measurements normalised against the upstream Pitot-Static tube. The 2% uncertainty associated with the calibration surface is considered as a bias error, while the additional 0.5% is

treated as a random error. Similarly, the uncertainty associated with the Pitot-Static tube is assumed to be a random error of 1.5%. In this context, the Cobra Probe uncertainties can be combined using a "Root-Sum-Square" (RSS) approach. Combining the errors in this way, for typical velocity and speed-up values ($U = 30\ ms^{-1}$, $S = 1.07$) gives an uncertainty of 4%.

In contrast, the turbulence intensity ratio (*TI Ratio*), which is the ratio of the turbulence intensity over the geometry to the corresponding turbulence intensity in the undisturbed boundary layer is affected by only the random uncertainty, as the calculation of the standard deviation relies on the difference between the mean and the instantaneous velocity, which cancels the bias error, while the random uncertainty propagates through the difference, sum, square and square root elements of the standard deviation calculation, as well as through the quotient of the standard deviation and the velocity, and between the two turbulence intensity values. For a representative *TI Ratio* of 3, this error propagation yields an uncertainty of approximately 7% giving a *TI Ratio* of 3.0±0.2.

While the literature indicates good frequency response to 1500 Hz, the manufacturer states that probes have good frequency response to 2000 Hz, but sampling frequency should be a minimum of 5000 Hz to avoid aliasing (Mousley 2011). Except where otherwise stated, sampling was conducted at 5000 Hz and down-sampled to 2500 Hz, giving a Nyquist frequency of 1250 Hz.

The TFI *Device Control* software logs instantaneous data and summary flow statistics. The instantaneous Cobra Probe data contains four parameters: Stream-wise (*U*) velocity component, lateral (*V*) velocity component, vertical (*W*) velocity component, and static pressure. Based on the traversing co-ordinates and the four instantaneous parameters the following summary flow statistics are reported by the *Device Control* software:

- *Y*-co-ordinate location
- *Z*-co-ordinate location
- Percentage good data

- Mean velocity
- Pitch
- Yaw

- Static Pressure

- Stream-wise (U) velocity component

- Lateral velocity (V) component

- Vertical velocity (W) component

- Turbulent intensity – total, stream-wise, lateral, vertical components (I_{uvw}, I_{uu}, I_{vv}, I_{ww})

- Reynolds Stresses (R_{uu}, R_{vv}, R_{ww}, R_{uv}, R_{uw}, R_{vw})

- Minimum velocity

- Maximum velocity

Calculations for these statistics are described in *Getting Started: Series 100 Cobra Probe* (Mousley 2011).
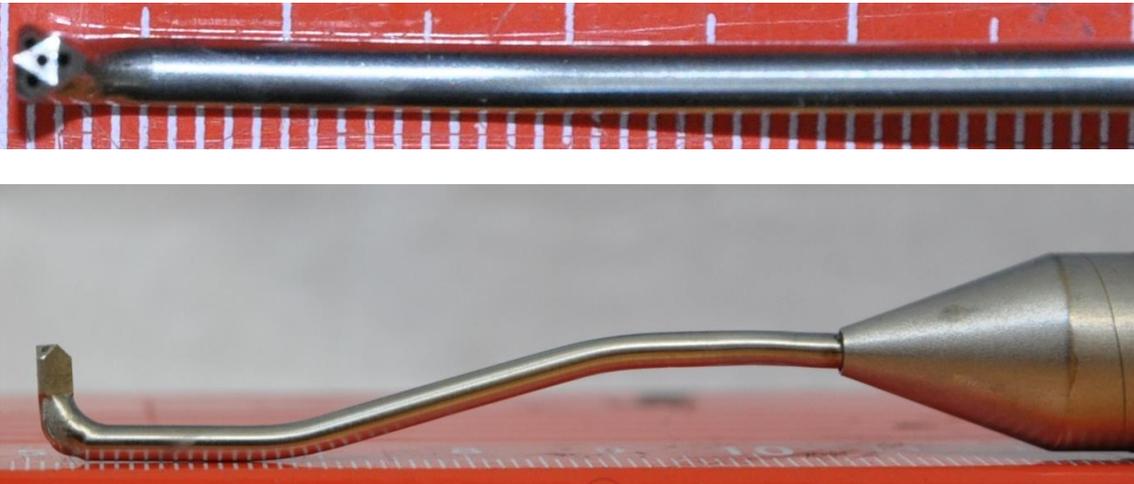
Figure 20: Close up of TFI Cobra Probe head. Top figure shows the four holes, one on each facet. The white lines indicate millimetre increments. Bottom photo shows the shape of the neck of the probe.

u: component of velocity
in X-direction

v: component of velocity
in Y-direction

w: component of velocity
in Z-direction

u

v

w
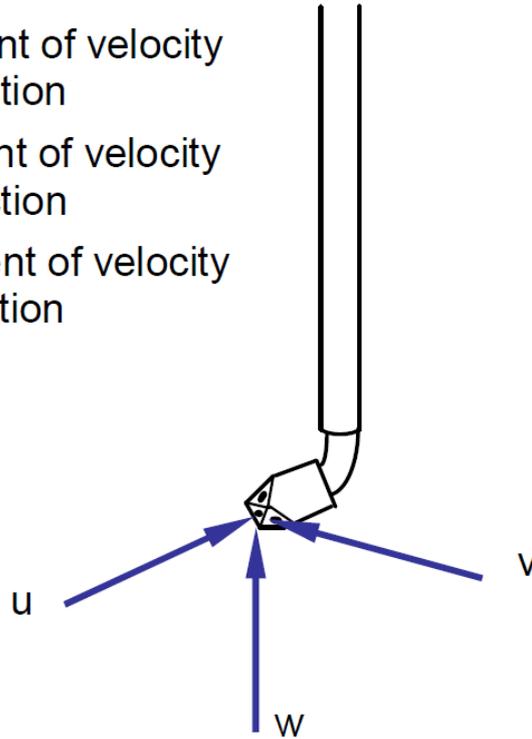
Figure 21: Cartesian co-ordinate system relative to the head of the Cobra Probe. Figure reproduced from TFI Cobra Probe "Getting Started" documentation (Mousley 2011) and used with permission.

Measures any
oncoming flow within
±45° of the Probe x-axis

45
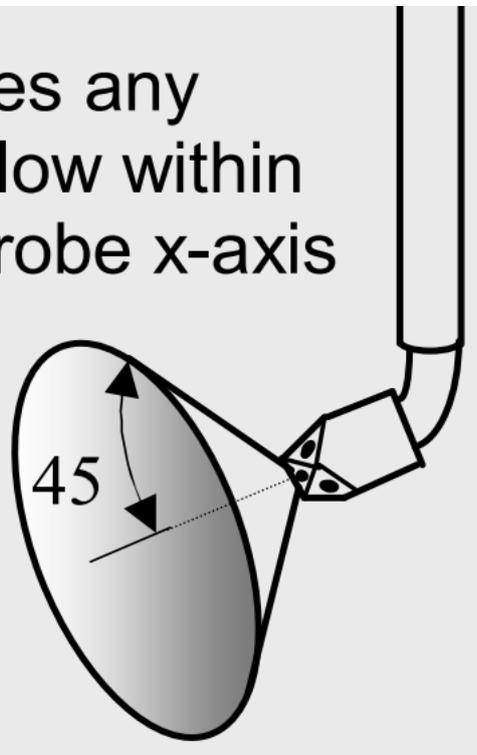
Figure 22: Cone of acceptance of TFI Cobra Probes. Figure reproduced from TFI Cobra Probe pamphlet and used with permission.

3.4.1 Calculating Power Spectral Density and Integral Length Scale

The power spectral density (PSD) is used to identify frequencies where most of the flow's energy is contained. This requires a transformation from the time to the frequency domain. From the PSDs, peak frequencies can be identified; whether periodic shedding frequencies of vortices, or integral length scales that represent the size of the turbulent eddies containing the most energy in a turbulent boundary layer.

The PSD is non-dimensionalised in the following manner:

$$\text{PSD} = \frac{f S_i(f)}{\sigma_i^2} \tag{3-1}$$

Where f is frequency, σ_i is the standard deviation of the parameter of interest, for example velocity, and $S_i(f)$ is the power of the signal, calculated using a Fast Fourier Transform (FFT). In this research, the Welch method is used to estimate the power component. Details of this method were published by Welch (1967) and involves sectioning the time history, and averaging the resultant FFTs of the sections. The length of the sections and the amount of overlap of the sections can be varied.

The approach presented by Hui et al. (2009) was used to determine the integral length scales, ^xL_u, ^xL_v and ^xL_w. They determined the length scales by fitting the von Kármán equation to the PSD according to the following equations (von Kármán 1948, Hui et al. 2009):

$$\frac{f S_u(f)}{\sigma_u^2} = \frac{4f\ ^xL_u/U}{\left[1+70.8\left(\frac{f\ ^xL_u}{U}\right)^2\right]^{5/6}} \tag{3-2}$$

$$\frac{f S_v(f)}{\sigma_v^2} = \frac{4f\ ^xL_v/U\left[1+755.2\left(\frac{f\ ^xL_v}{U}\right)^2\right]}{\left[1+283.2\left(\frac{f\ ^xL_v}{U}\right)^2\right]^{11/6}} \tag{3-3}$$

$$\frac{f S_w(f)}{\sigma_w^2} = \frac{4f\ ^xL_w/U\left[1+755.2\left(\frac{f\ ^xL_w}{U}\right)^2\right]}{\left[1+283.2\left(\frac{f\ ^xL_w}{U}\right)^2\right]^{11/6}} \tag{3-4}$$

U is the mean stream-wise velocity, ${}^{x}L_i$ is the integral length scale in a given dimension, f is the frequency and σ_i is the standard deviation of the i-component of the velocity signal.

Following Hui et al. (2009), the von Kármán equations were differentiated with the derivative set equal to zero. Thus, the length scale is defined by the frequency at which the PSD is at a peak. A Matlab script was written to perform this task, filtering out the high frequency beyond 750 Hz (Huang and Lin 1995), where the flow is dominated by small-scale vortices. Thus, taking logs of the power spectrum and the frequency, the spectrum is made up of two nominally linear sides, to which straight lines can be fitted. The intersection of this line was taken as the peak frequency. This technique is illustrated in Figure 23, where the intersection is at a frequency, log(f) = 0.786.
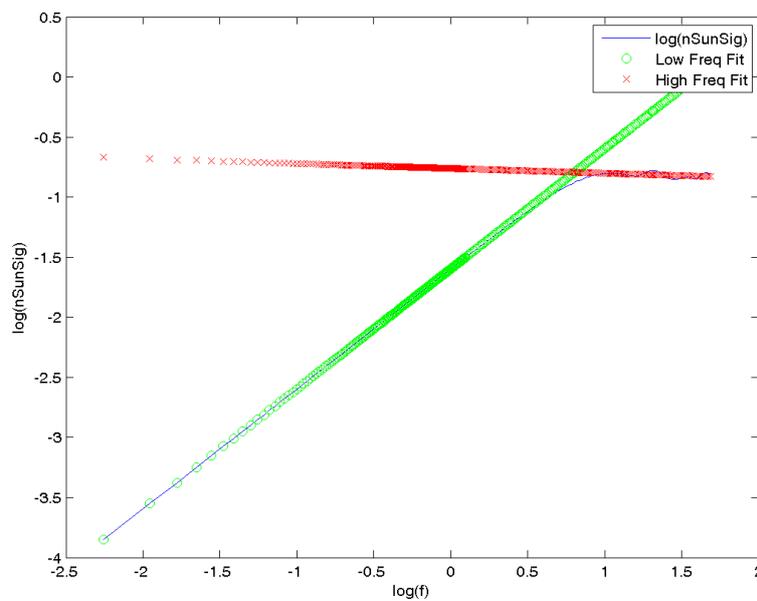
Figure 23: Logs of the PSD fitted with two linear components. Data from *x = 0.5h, z = 0.4h*.

The length scales are thus given by the following equations (Hui et al. 2009):

$${}^{x}L_u = 0.146 \frac{U}{f_p} \tag{3-5}$$

$${}^{x}L_{v,w} = 0.106 \frac{U}{f_p} \tag{3-6}$$

Here, f_p is the frequency associated with the peak of the spectrum, at the crossing of the linear sections.

Calculating integral length scales has several inherent difficulties. The most challenging aspect is associated with the poorly conditioned equations: a precise peak in the input PSD is often not obvious, and the length scales are highly sensitivity to the location of the peak. The lack of conditioning of the equations represents the intermittent and chaotic nature of the flow. The development of the length scales associated with each of the configurations, presented in Figure 13, Figure 15, and Figure 17 illustrates a consistent development of the length scales through the boundary layers, implying that the lack of conditioning of the equations did not unduly affect the final analysis.

The occurrence of acoustic spikes and high frequency peaks can also affect the results generated by these automated processes. Thus, acoustic and high frequency peaks were filtered out so as not to affect the fitting algorithm. An example of the peaks is shown in Figure 24.
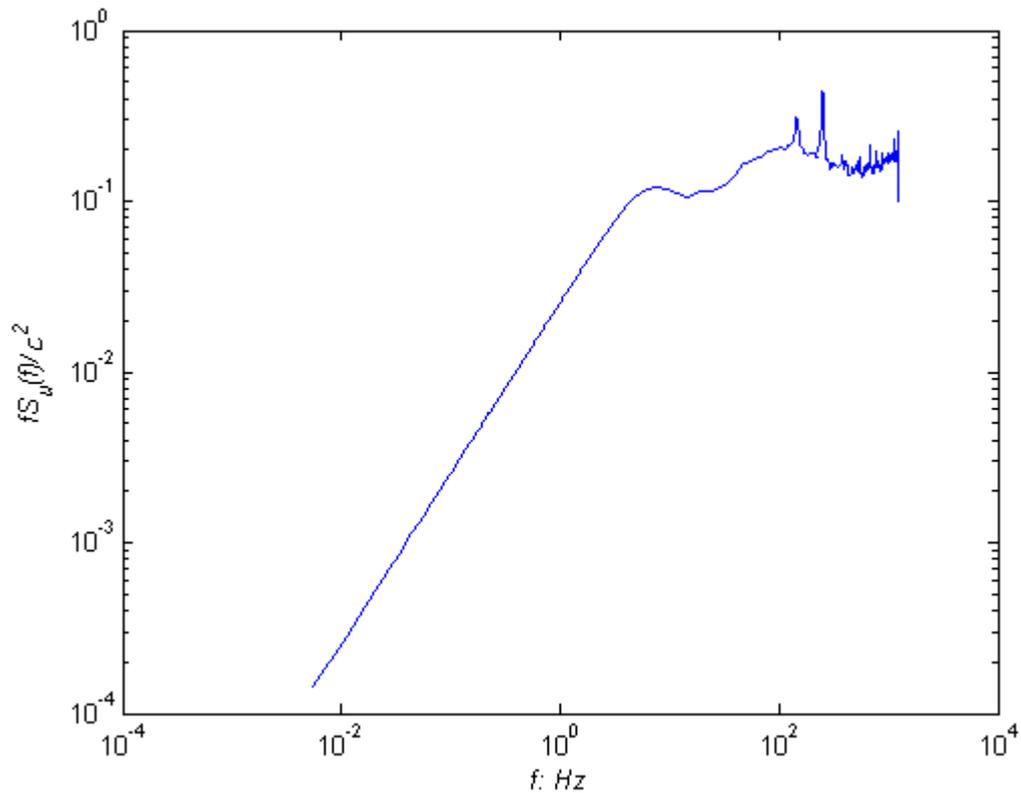
Figure 24: Example of spikes in the PSD from the top of the boundary layer (*z* = 125 mm, Configuration 3).

3.4.2 Performance of the Cobra Probe in Reversed Flow

Cobra Probes are limited to only being able to capture velocity data while the flow is aligned within

the 45° cone of acceptance (Hooper and Musgrove 1997). However, when the flow is outside of the

cone of acceptance the Cobra Probes, ideally, would not record data. This is presented as the

"Percent Good Data" parameter. This parameter divides the number of "good" points (points aligned

within the cone of acceptance), by the total number of points in a sample.

There is potentially an issue when the alignment of the probe and the flow are not within the 45°

cone of acceptance, and flow separation from the probe results in pressure being applied to the face

of the probe that could be interpreted as flow from within the cone of acceptance. Thus, a brief

validation of this assertion was conducted, and is presented in Appendix: *Performance of Cobra*

Probes in Recirculating Flow.

The result of the validation study showed that probes orientated such that they would encounter

only reversed flow, still recorded over 40% good data. This is consistent with the assertion that flow

77

separation off the probe will result in false recordings of good data. Thus, care must be taken when interpreting Cobra Probe data in recirculation regions.

3.4.3 Cobra Probe Traversing

Two single axis *Isel* traverses were used both individually and in combined configurations to allow both one-dimensional and two-dimensional traversing with Cobra Probes. The larger traverse has a range of 1600 mm, while the smaller traverse has a range 1190 mm. Both traverses were controlled through the TFI Device Control software. The traverse software recorded a precision of 0.001 mm, but operated within tolerances of 0.003 mm. They were powered by a 24 V power source. An example of a traversing configuration to traverse laterally and vertically is presented in Figure 25. This technique was used in the sawtooth and sinusoidal cases. An example of a traversing configuration to traverse vertically and in a stream-wise direction is presented in Figure 28. This approach was used for traversing over the yawed FFS cases. The crest of the FFS was used as the datum, while the Cobra Probes were aligned such that they faced directly into the free-stream flow, as described in Figure 30. Misalignment of the Cobra Probes was corrected in the post processing, described in Section 3.4.4 Cobra Probe Post Processing Calibration.

The vertical resolutions of measurement points in Cobra Probe traverses are presented in Table 6 and Table 7. In validation studies, the vertical resolution was chosen to match the data points implemented by Bowen and Lindley (1977), facilitating direct comparison with their work. This was the minimum vertical resolution implemented. Increased resolution through the recirculation regions was not implemented as the data points within these regions are associated with large uncertainties due to the limitations of the Cobra Probes in gathering data in reversed flow conditions, as described in Appendix: *Performance of Cobra Probes in Recirculating Flow*. However, in comparisons with the work of Ren and Wu (2011), in particular, in comparisons with their Reynolds stress measurements, finer increments were used. The finer increments, which were of the same order of magnitude as the size of the Cobra Probe head, were focussed around regions of high shear in the traverses nearer the crest, as documented in Table 7.

78

In the comparison with Bowen and Lindley (1977), four Cobra Probes traversed; they had lateral spacing of 25 mm, 50 mm and 25 mm, covering a 100 mm wide region, corresponding to the step height. Lateral resolution of the traverses in the remainder of the nominally two-dimensional (straight-edged FFS) cases, was at 50 mm. This corresponded to the smallest step height used. It resulted in a spacing of 19.2 times the head thickness of the probes.

Figure 25: Sawtooth model, A/λ = 0.325, shown with two-dimensional traversing equipment and four-Cobra Probe configuration.

In the FFS cases modelling ruggedness it was decided to limit Cobra Probe traversing to the lowest amplitude to wavelength ratio cases (A/λ = 0. 325). Four probes, spaced 50 mm ($1h$) apart, traversed laterally, in 10 mm increments from one peak of the sawtooth or sinusoid to the next peak of the sinusoid, sampling a full cycle of the geometry (400 mm). This provided redundancy in the measurements, allowing comparison and calibration on either side of the line of symmetry. This implies a lateral resolution, $\Delta y/\lambda$, of 0.025. Cobra Probe measurements were confined to the lowest A/λ cases for the sawtooth and sinusoidal geometries. CFD analysis in the A/λ = 0.5 case for the sawtooth geometry suggested further experimental analysis would be beneficial, precipitating

further Cobra Probe traverses over this case. These traverses focussed on the region downstream of the sawtooth trough point, a quarter of a wavelength ($\lambda/4$) either side of the trough point, with the same lateral resolution.

The downstream spacing of each of the traversing planes is presented in Table 8. The spacing is sufficient to capture the flow development, and is consistent with that observed in various FFS studies (Bowen and Lindley 1977, Ren and Wu 2011).

Table 6: Vertical resolution of Cobra Probe traverses.

Bowen & Lindley FFS Comparison (y/h = 0, 0.25, 0.75, 1)		Ren & Wu FFS Comparison (Downstream) (y = 0)		Yawed FFS Cases (y = 5h, 6h)		Sawtooth FFS: A/λ = 0.325 (y = -λ/2:0.025 λ:λ/2)		Sawtooth FFS: A/λ = 0.5 (y = -λ/4:0.025 λ:λ/4)		Sinusoid FFS: A/λ = 0.325 (y = -λ/2:0.025 λ:λ/2)	
z [mm]	z/h	z [mm]	z/h	z [mm]	z/h	z [mm]	z/h	z [mm]	z/h	z [mm]	z/h
10	0.1	5	0.05	10	0.2	5	0.1	10	0.2	10	0.2
25	0.25	10	0.1	20	0.4	25	0.5	20	0.4	25	0.5
40	0.4	20	0.2	25	0.5	50	1	30	0.6	50	1
60	0.6	40	0.4	30	0.6	75	1.5	40	0.8	75	1.5
80	0.8	80	0.8	40	0.8	100	2	50	1	100	2
100	1	120	1.2	50	1	150	3	60	1.2	150	3
150	1.5	160	1.6	75	1.5	200	4	70	1.4	200	4
200	2	200	2	100	2			80	1.6		
300	3	250	2.5	125	2.5			90	1.8		
400	4	300	3	150	3			100	2		
500	5	350	3.5					110	2.2		
600	6	400	4					120	2.4		
		450	4.5								
		500	5								
		550	5.5								
		600	6								
		650	6.5								
		700	7								

Table 7: Vertical resolution of Cobra Probe traverses near the crest for Ren and Wu (2011) comparison.

x = 0, y = 0		x = 0.5h, y = 0		x = h, y = 0		x = 2h, y = 0	
z [mm]	z/h	z [mm]	z/h	z [mm]	z/h	z [mm]	z/h
5	0.05	5	0.05	5	0.05	5	0.05
10	0.1	10	0.1	10	0.1	10	0.1
12.5	0.125	20	0.2	20	0.2	20	0.2
15	0.15	22.5	0.225	30	0.3	22.5	0.225
17.5	0.175	25	0.25	31	0.31	25	0.25
20	0.2	27.5	0.275	32	0.32	27.5	0.275
22.5	0.225	30	0.3	33	0.33	30	0.3
25	0.25	32.5	0.325	34	0.34	32.5	0.325
27.5	0.275	35	0.35	35	0.35	35	0.35

x = 0, y = 0		x = 0.5h, y = 0		x = h, y = 0		x = 2h, y = 0	
z [mm]	z/h	z [mm]	z/h	z [mm]	z/h	z [mm]	z/h
30	0.3	37.5	0.375	36	0.36	37.5	0.375
32.5	0.325	40	0.4	37	0.37	40	0.4
35	0.35	42.5	0.425	38	0.38	42.5	0.425
37.5	0.375	45	0.45	39	0.39	45	0.45
40	0.4	47.5	0.475	40	0.4	47.5	0.475
42.5	0.425	50	0.5	41	0.41	50	0.5
45	0.45	52.5	0.525	42	0.42	52.5	0.525
47.5	0.475	55	0.55	43	0.43	55	0.55
50	0.5	57.5	0.575	44	0.44	57.5	0.575
52.5	0.525	60	0.6	45	0.45	60	0.6
55	0.55	80	0.8	46	0.46	62.5	0.625
57.5	0.575	120	1.2	47	0.47	65	0.65
60	0.6	160	1.6	48	0.48	67.5	0.675
80	0.8	200	2	49	0.49	70	0.7
120	1.2	250	2.5	50	0.5	72.5	0.725
160	1.6	300	3	52.5	0.525	75	0.75
200	2	350	3.5	55	0.55	77.5	0.775
250	2.5	400	4	57.5	0.575	80	0.8
300	3	450	4.5	60	0.6	82.5	0.825
350	3.5	500	5	62.5	0.625	85	0.85
400	4	550	5.5	65	0.65	87.5	0.875
450	4.5	600	6	67.5	0.675	90	0.9
500	5	650	6.5	70	0.7	92.5	0.925
550	5.5	700	7	72.5	0.725	95	0.95
600	6			75	0.75	97.5	0.975
650	6.5			77.5	0.775	100	1
700	7			80	0.8	102.5	1.025
				120	1.2	105	1.05
				160	1.6	107.5	1.075
				200	2	110	1.1
				250	2.5	112.5	1.125
				300	3	115	1.15
				350	3.5	117.5	1.175
				400	4	120	1.2
				450	4.5	160	1.6
				500	5	200	2
				550	5.5	250	2.5
				600	6	300	3
				650	6.5	350	3.5
				700	7	400	4
						450	4.5
						500	5
						550	5.5
						600	6
						650	6.5
						700	7

Table 8: Stream-wise resolution of traversing planes. For the yawed FFS cases, *x* is measured as the perpendicular distance from the crest.

Bowen & Lindley FFS Comparison		Ren & Wu FFS Comparison (Downstream)		Yawed FFS Cases		Sawtooth FFS: $A/\lambda = 0.325$		Sawtooth FFS: $A/\lambda = 0.5$		Sinusoid FFS: $A/\lambda = 0.325$	
x [mm]	x/h	x [mm]	x/h	x [mm]	x/h	x [mm]	x/h	x [mm]	x/h	x [mm]	x/h
0	0	0	0	0	0	-130	-2.6	100	2	-130	-2.6
50	0.5	50	0.5	25	0.5	-65	-1.3	150	3	-65	-1.3
100	1	100	1	50	1	0	0	200	4	0	0
200	2	200	2	75	1.5	100	2	550	11	100	2
300	3	300	3	100	2	500	10			500	10
400	4	400	4	125	2.5						
500	5	500	5	150	3						
700	7	700	7	200	4						
1000	10	1000	10	250	5						
				350	7						
				500	10						

3.4.4 Cobra Probe Post Processing Calibration

When traversing with multiple probes, as shown in Figure 26, there was found to be a small inherent yaw and pitch misalignment between the probes due to differences in alignment of the cylindrical probe in the jacket, due to some damage to the probe stem of two of the Cobra Probes (shown in Figure 27), and due to the vibration and wind load on the traversing system.

These issues imply uncertainty in pitch and yaw statistics as well as in the spatial position of the probes. The vibration of the traversing system was mitigated by damping the base of the vertical traverse, as shown in Figure 28. The structural vibration associated with the traversing system was at lower frequencies than the frequencies of interest associated with the flow structures that were being measured. Recalibration of the probes subsequent to the damage of the stems means that the problems with the Cobra Probes are merely cosmetic.

To mitigate the uncertainty of the velocity measurements, traverses were completed such that there were overlapping points when traversing laterally, allowing a manual correction of the raw data based on matching the mean pitch and yaw parameters and determining points where, for example, 0° yaw might be expected along lines of symmetry and where 0° pitch might be expected in the free-

stream. Thus it was possible to determine the relevant offsets, which were applied to the

instantaneous U, V and W components, from which corrected summary statistics could be

calculated. When traversing vertically and in a stream-wise direction with two probes, as shown in

Figure 28, the manual correction was applied based on the assumption that neither probe would

encounter pitch nor yaw in the free-stream flow. This configuration was implemented for the yawed

flow FFS cases and the rugged FFS cases. An example of the yaw angle correction is presented in

Figure 29.
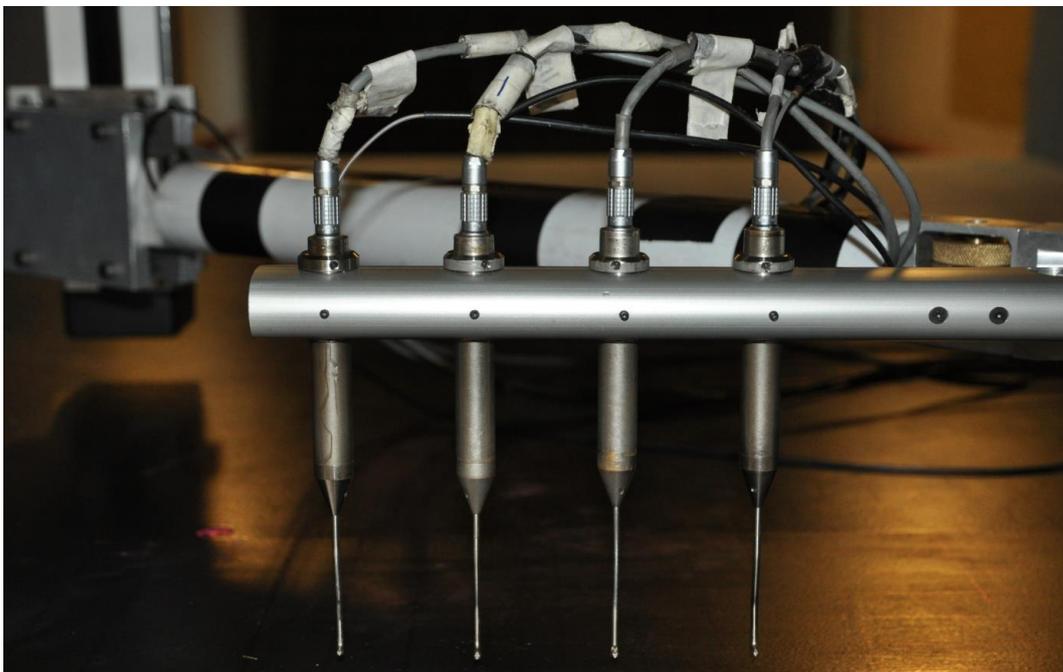
Figure 26: Four Cobra Probe configuration for two-dimensional traversing.

Figure 27: Slight skew of Cobra Probes with superimposed vertical lines.
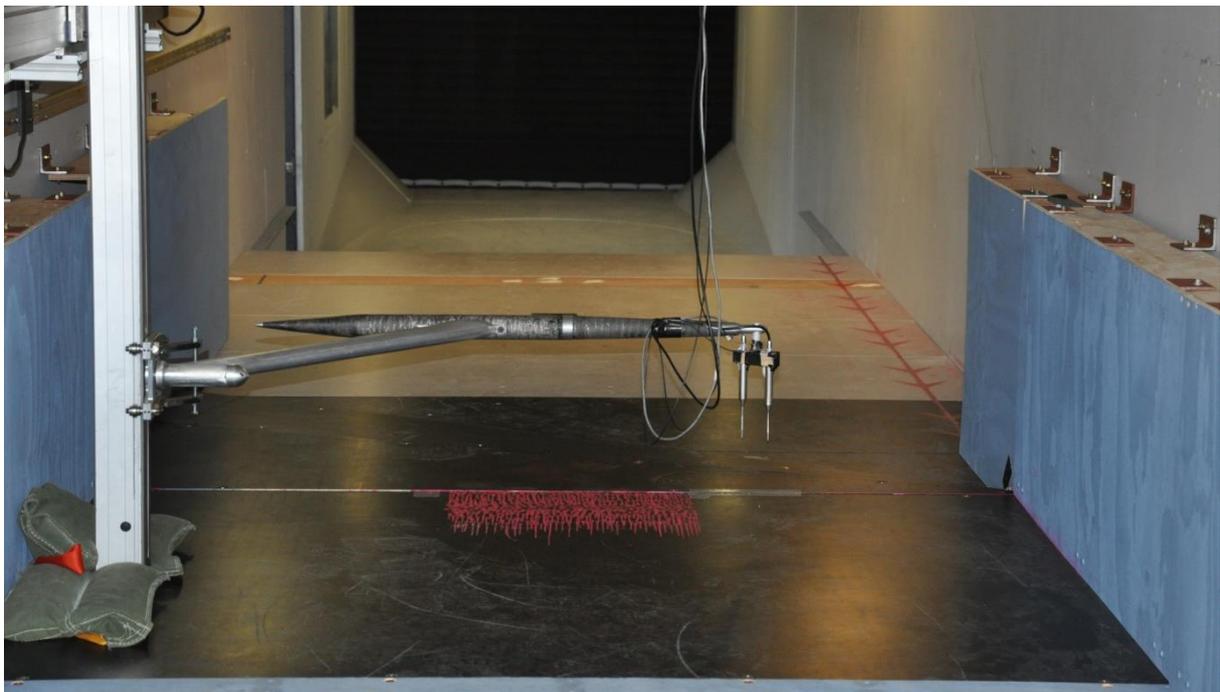
Figure 28: Two Cobra Probe configuration for two-dimensional traversing. Traversing vertically and in the stream-wise direction. Note the weight bags for vibration damping at the base of the vertical traverse on the left.
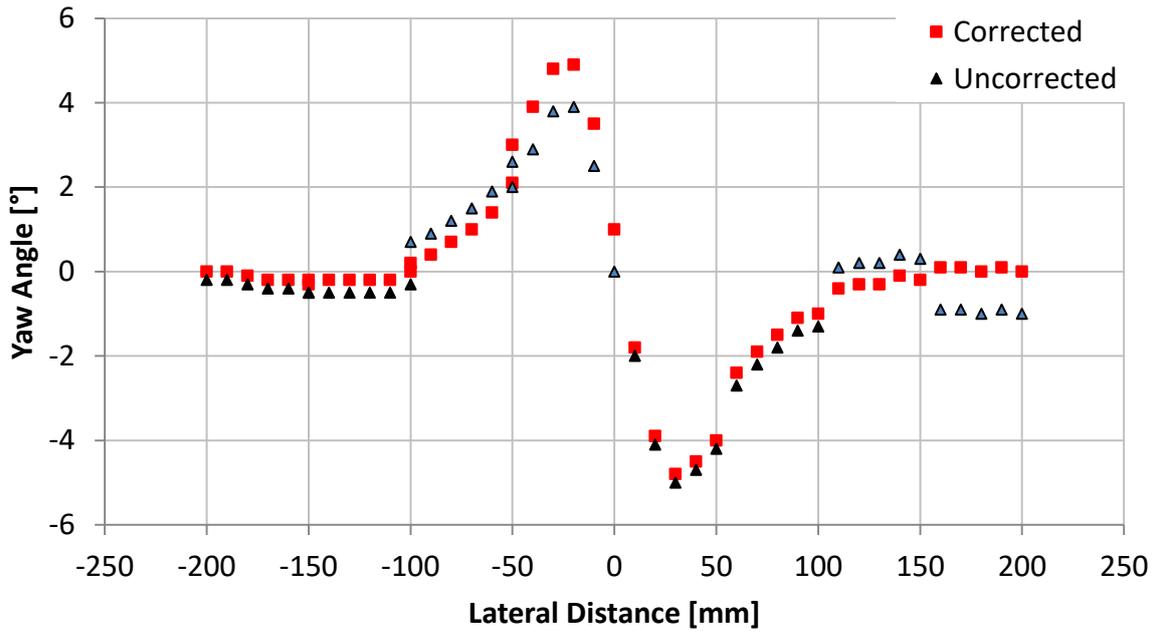
Figure 29: Example of post-processing correction of yaw angle data from Cobra Probes.
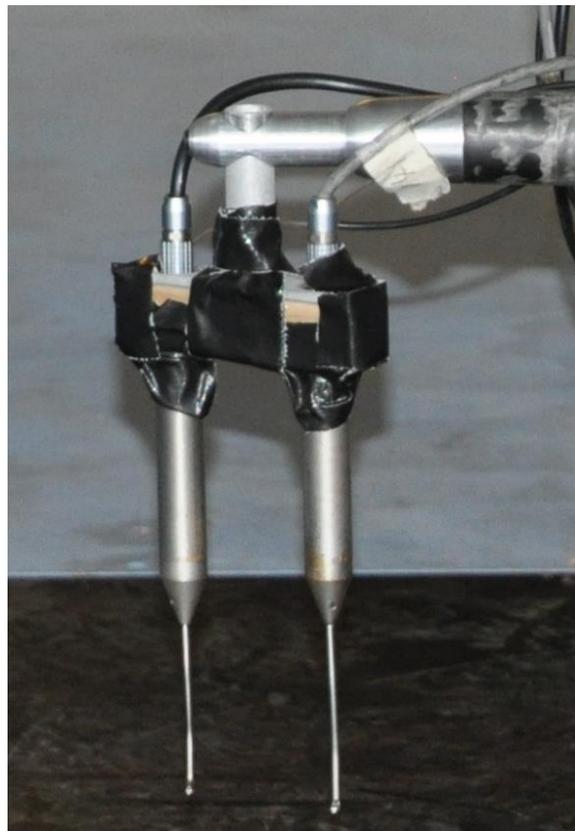
Figure 30: A close-up of the boom, mounting the two Cobra Probes. The central axis could be rotated to allow the probes to align along the datum (the crest of the FFS). The probes themselves could then be aligned such that they would face directly into the free-stream flow.

3.5 Paint Drop Surface Shear Stress Visualisation

The paint droplet visualisation technique was used to depict the surface shear stress vector field, giving an indication of the strength of the surface shear stress, but more importantly, the direction in which it acts. Two techniques have been implemented in this research: the first was to generate a grid of droplets and allow them to streak. The second was to gradually build up the number of droplets, running the wind tunnel between each group.

These techniques are an adaptation of more traditional oil film visualisations. In oil film visualisations, the surface is painted with an oil, typically seeded with a pigment, relying on the surface shear stress to be converted to momentum of the oil and the seeded pigment, resulting in streaky deposits of the pigment (Merzkirch 1974, Tropea et al. 2007). The experimental handbook of Tropea et al. (2007) also highlighted the oil-film interferometry technique, whereby the surface shear stress could be determined by measuring the thickness of the oil. Peake et al. (1972), in their investigations of flow around aircraft and missiles at flow speeds around Mach 0.7, also completed oil film visualisations. Rather than coating the surface with the seeded oil mixture, they used discrete point applications, enabling the direction of the streaking to be clearly identified, as well as using the length of the streaks to serve as an indicative measure of the surface shear stress in a particular location (Merzkirch 1974).

Ultimately, the streaky deposits from whichever method is used are for the purpose of characterising the mean flow structure over the region of interest using flow topology principles (Merzkirch 1974, Hunt et al. 1978, Tobak and Peake 1982, Perry and Chong 1987, Perry and Chong 1994, Tropea et al. 2007). The ability of the droplets to "capture" the flow structures is directly related to the viscosity of the paint mixture. Where the paint mixture was not sufficiently viscous, it had a tendency to splatter – forming into droplets; the resultant pattern represented the effect of the turbulent flow field, rather than remaining as a coherent streak, which is representative of the mean shear stress vector.

In this research, FFS models were prepared such that the surfaces were aerodynamically smooth, covered with black self-adhesive contact or black, semi-gloss enamel paint. This finish provided a

consistent surface, allowing the paint to streak easily over the surface. Magenta-coloured water-based paint was diluted with tap water. The magenta coloured paint contrasted strongly against the black models. The ratio of water-based paint to tap water was approximately 1:1, to provide a paint mixture with a viscosity such that the droplets would streak freely across the surface but not speckle when subjected to the wind tunnel flow. Obtaining this ideal viscosity required some trial and error. The mixture would flow easily across a smooth surface under the influence of gravity when the paint was sufficiently dilute. It was clear when the mixture was insufficiently diluted, and thus too viscous, as when the wind was applied, the droplets failed to fully streak. When the mixture was too dilute and hence insufficiently viscous, the droplets, rather than streaking, would splatter over the surface of the model.

The surfaces of the models were horizontal, meaning that gravitational effects did not need to be considered in the analysis of the data (Tropea et al. 2007).

The first method required an array of paint droplets over the downstream region of the FFS and in the boundary layer case, without the step in place.

For the 100 mm and 150 mm FFSs (at both zero and non-zero yaw), the grid had a lateral resolution of 100 mm and a stream-wise resolution of 50 mm. In these cases, the grid was aligned with the crest of the FFS. In the 50 mm cases, higher resolution was implemented. Lateral resolution of 25 mm and downstream resolution of 10 mm was used. The grid was aligned with the free-stream flow. This lateral array of droplets allowed lateral variations in the flow structure to become visible. The stream-wise resolution allowed measurement of the mean reattachment length accurate to one quarter of the step height for h = 100 mm step cases, and one sixth of the step height for h = 150 mm cases. For h = 50 mm step cases, the mean reattachment length could be measured accurately to one tenth of the step height. For the h = 100 mm and h = 150 mm cases, droplets were placed in the grid centres through the centre of the experimental domain, as shown in Figure 31, effectively doubling the resolution.

Hypodermic syringes were used to apply approximately 0.1 mL of the paint solution at each grid point in the 100 mm and 150 mm FFS cases. Further drops were also applied toward the edges of the experimental domain. This was done to increase the resolution so as to observe in more detail the edge effects. In the 50 mm case, 0.1 mL of paint was administered to one in every four grid points in a diagonal array. Both of these arrays are depicted in Figure 31. The application of paint was performed in still conditions.

To obtain the streaks, the wind tunnel was run up to a fan blade pitch angle of 30°, corresponding to a free-stream velocity of 34 ms^{-1}. The paint could typically be observed to begin streaking at a fan blade pitch of 25°. The wind tunnel was allowed to run at speed for approximately one to two minutes from the time the wind tunnel fan blade pitch had reached 30°. This allowed the streaks sufficient time to form.

The second method, referred to as the "build-up" method, was used in the sawtooth and sinusoidal cases to allow higher resolution, as well as to avoid paint droplets interacting. The method is demonstrated in Figure 32. An initial group of droplets were deposited on the model surface with a hypodermic syringe in such a way as to avoid the streaks from overlapping when the wind was applied. Additional droplets were then applied in the same manner, and the process repeated until the flow field could be described. As in the grid method, droplets were approximately 0.1 mL, though in regions where the flow structure was finer, smaller droplets were deposited.

Initial testing of the base FFS cases at a range of step heights resulted in good agreement with the literature, as presented in Chapter 4.
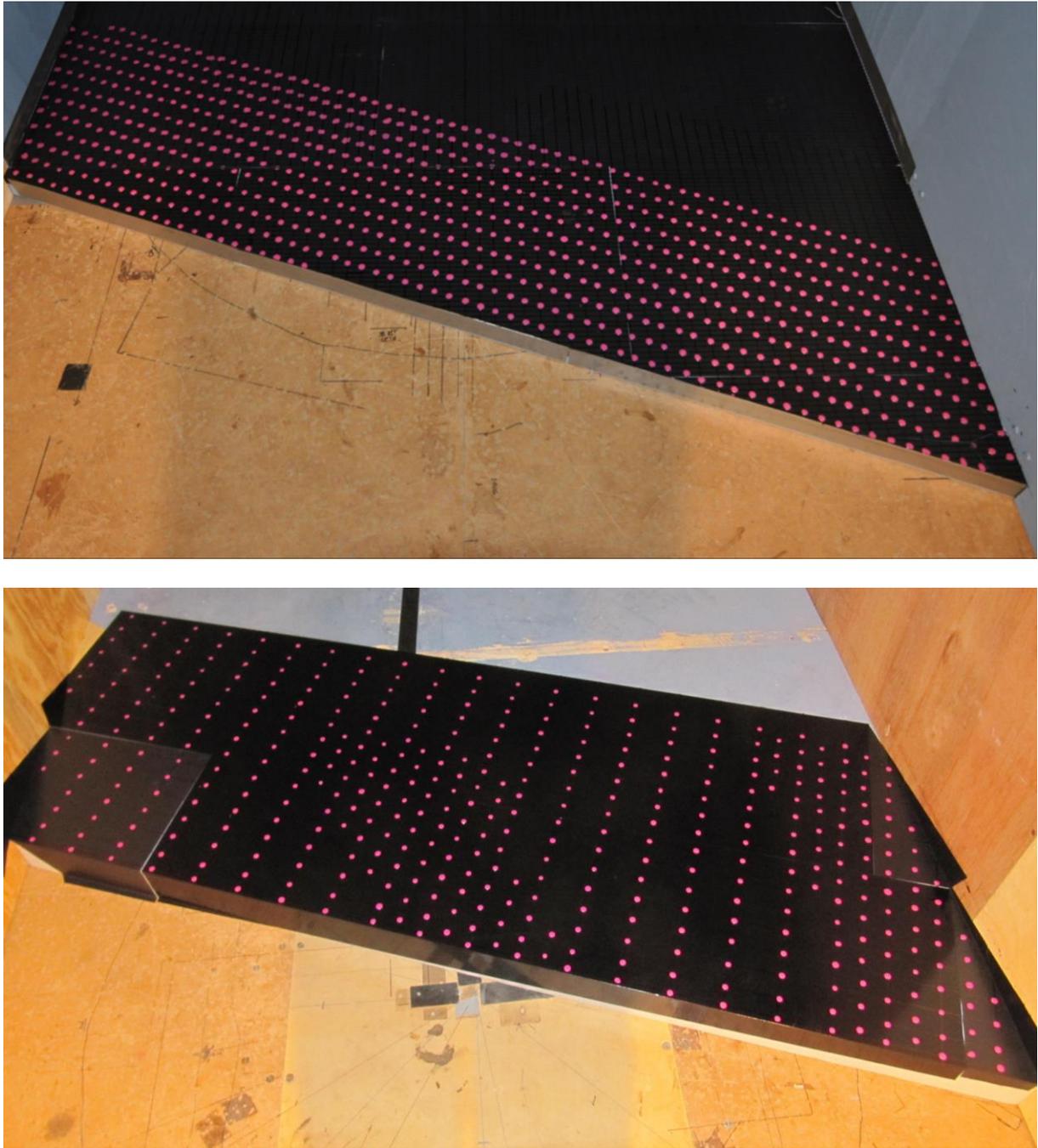
Figure 31: Grid configurations for *h* = 50 mm case (Top) and *h* = 100 mm and *h* = 150 mm case (Bottom).

3.5.1 Interpretation of Surface Shear Stress Visualisation

From these surface shear stress visualisation techniques, it is possible to deduce the mean flow

topology over the surface of the model. Flow topology is presented in the form of topological vortex

skeletons, where critical points are identified and the relationship between them is established

(Merzkirch 1974, Hunt et al. 1978, Tobak and Peake 1982, Perry and Chong 1987, Perry and Chong

1994, Tropea et al. 2007). Critical points are defined as points where the shear stress is equal to zero (Tropea et al. 2007). Based on these skeletons, flow structures can be characterised. In this research, these skeletons are constructed based on the surface shear stress visualisations described in Section 3.5 *Paint Drop Surface Shear Stress Visualisation*.
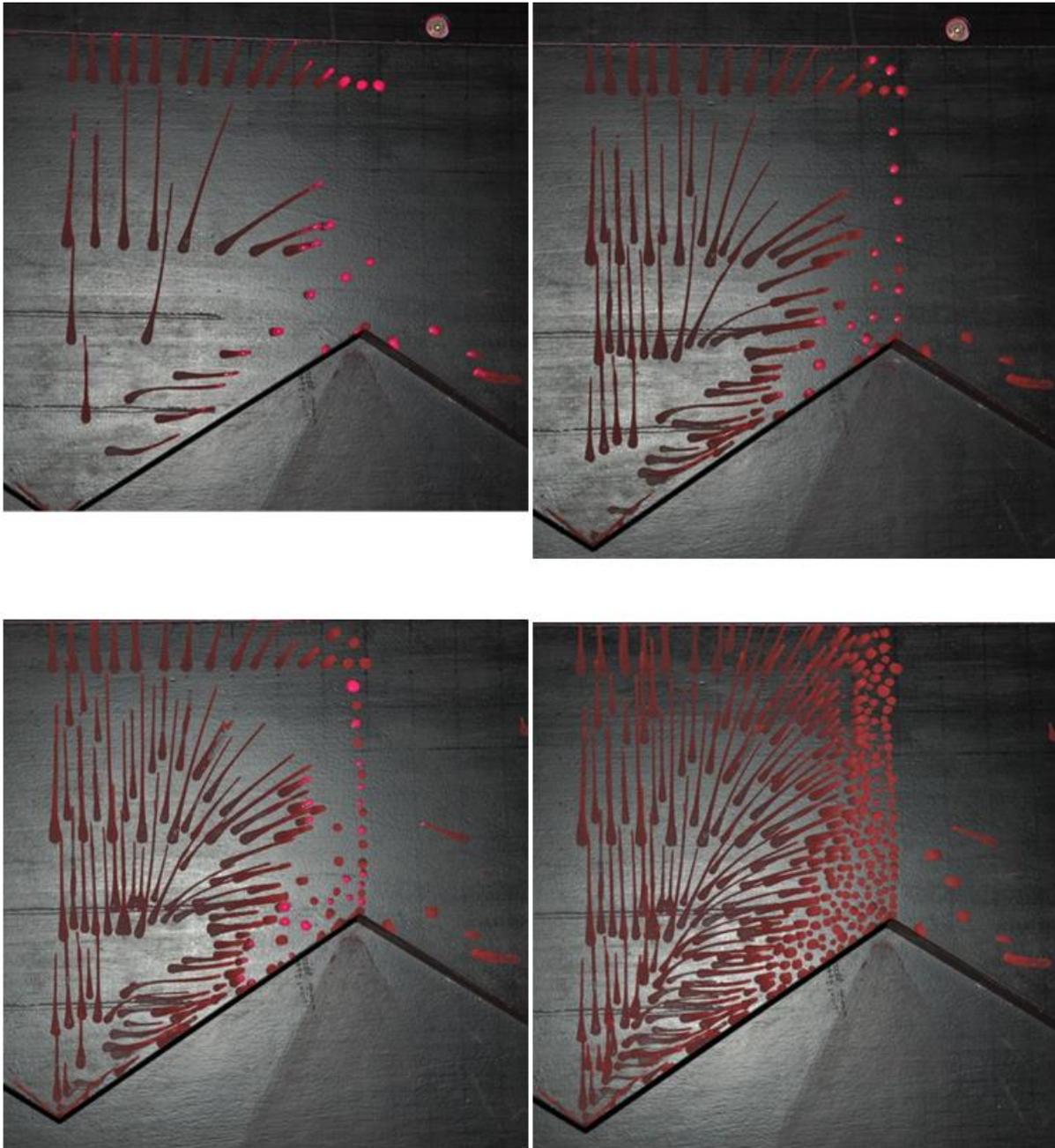
Figure 32: Demonstration of build-up technique. Four instances are shown. Intermediate steps are omitted for brevity.

Five different critical points are used to describe the flow topology in conjunction with two types of bifurcation lines. These critical points and lines, described by, amongst others, Perry and Chong

(1987, 1994) are shown in Figure 33 and Figure 34. The critical points represent vortex interactions in the plane on which they are located.

According to Hunt et al. (1978), the number of node points must equal the number of saddle points for a bluff body on a flat plane, which is the case in this body of work.

To convert the surface shear stress visualisations into the topological skeletons described, the following process was used.
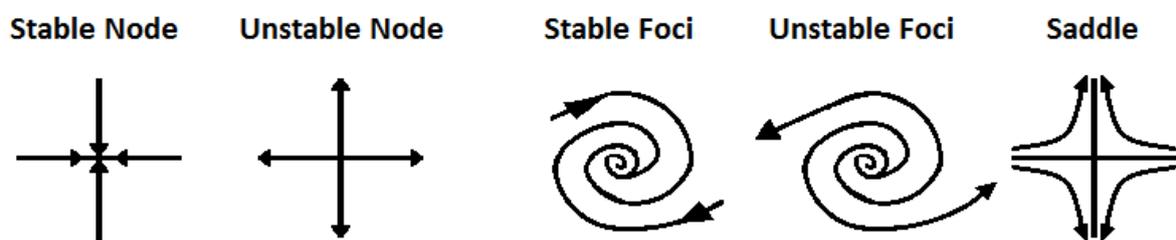
Figure 33: Five types of critical points. Illustrations based on those by Perry and Chong (1987).

First, the completed visualisation was photographed and each droplet was assigned a direction, as seen in Figure 35. In some instances the droplets may have been too large to properly capture the finer flow structures, implying that two directions needed to be assigned to a particular droplet for different parts of the droplet, as demonstrated in Figure 36. In regions of low shear stress, it was not always evident in which direction the paint had streaked, or if it had streaked at all, particularly when the droplets had completely dried. In this case the "build-up" technique was useful, as droplets were added in smaller quantities, gradually building up a picture of the shear stress field. After each run, most droplets would streak, while some of the droplets, in low flow regions, may not have streaked. In these instances, the bulk of the paint would accumulate on one side or other of the droplet, allowing a determination of the mean shear stress direction.

Secondly, using an overhead transparency, skeleton lines were fitted by eye over the photograph, using the assigned directions to determine the trajectory of the skeleton lines. The skeleton lines were drawn in, beginning with the easily identifiable critical points and moving onto the more

general flow structure including bifurcation lines. This would often leave a region containing one or

more critical points that were not immediately obvious, but could nonetheless be deduced from the

shear stress direction field. An example is presented in Figure 37.
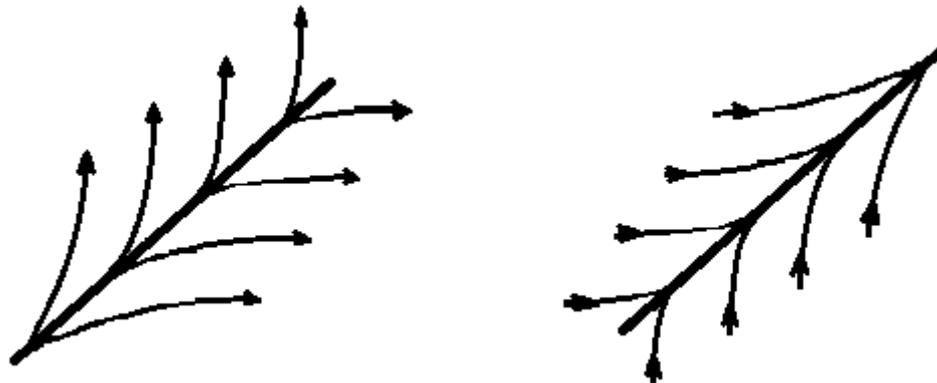
Figure 34: Positive bifurcation line (Left), negative bifurcation line (Right). Illustrations based on those by Perry and Chong (1994).

One means of verifying the topological solution was to ensure, as established above, that the

number of nodes was equal to the number of saddle points. In the sawtooth and sinusoidal cases it

was important to recognise the lines of symmetry. Thus, a node that was located on a line of

symmetry would account for half a node, as half of the node was in the experimental domain while

the other half was not. This is shown in Figure 37.

From this determination of the flow topology, the generation, interaction and decay of coherent

flow structures can be understood.
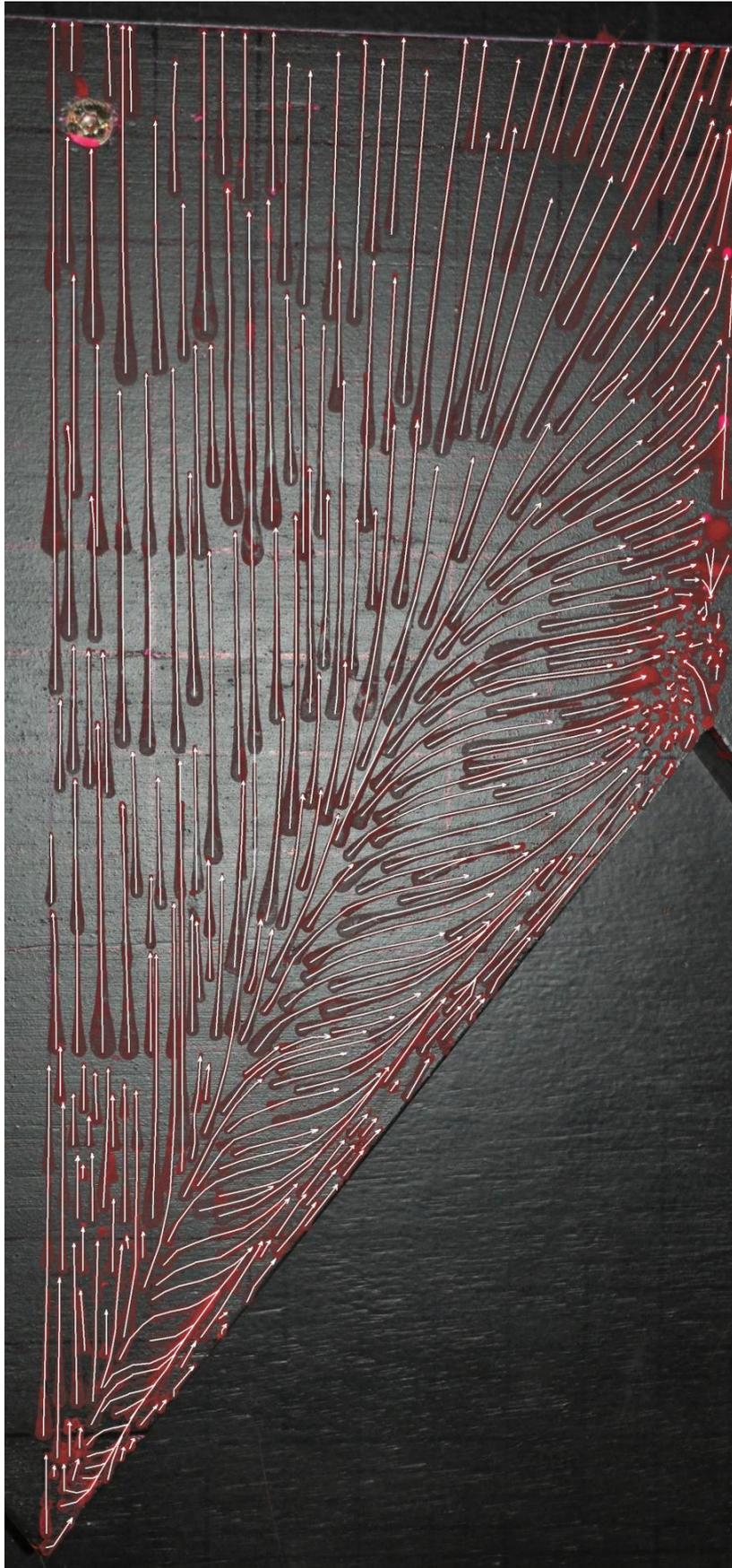
Figure 35: Assignment of direction to the streaks.
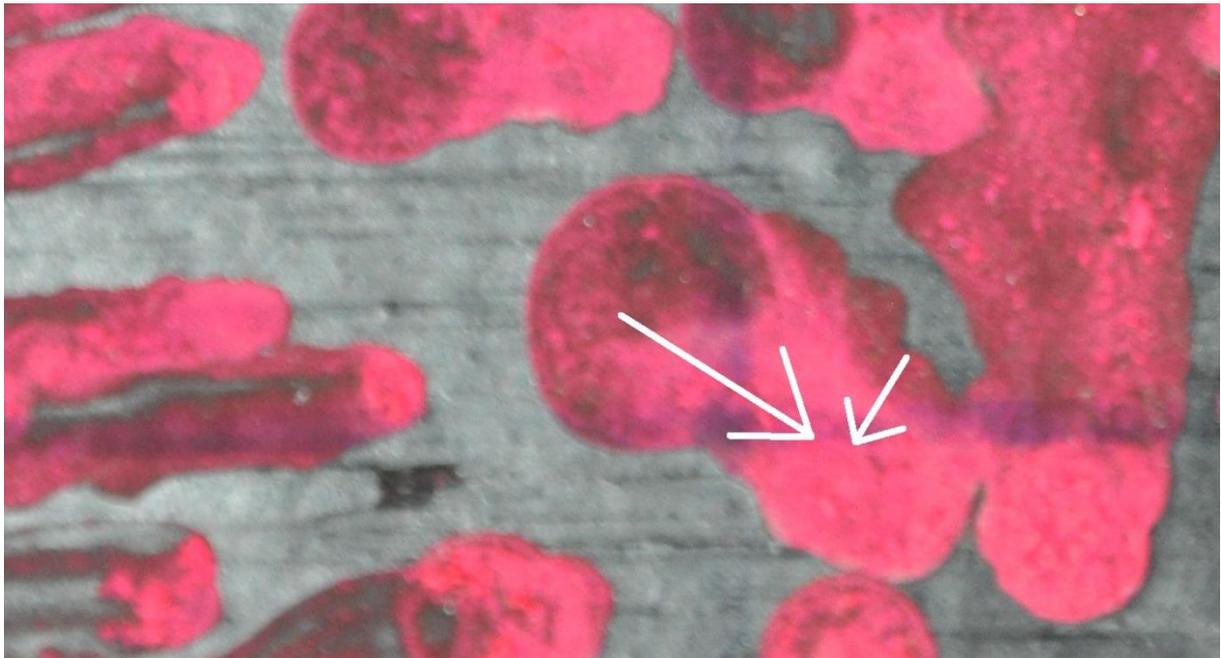
Figure 36: Example of a streak with multiple directions assigned.
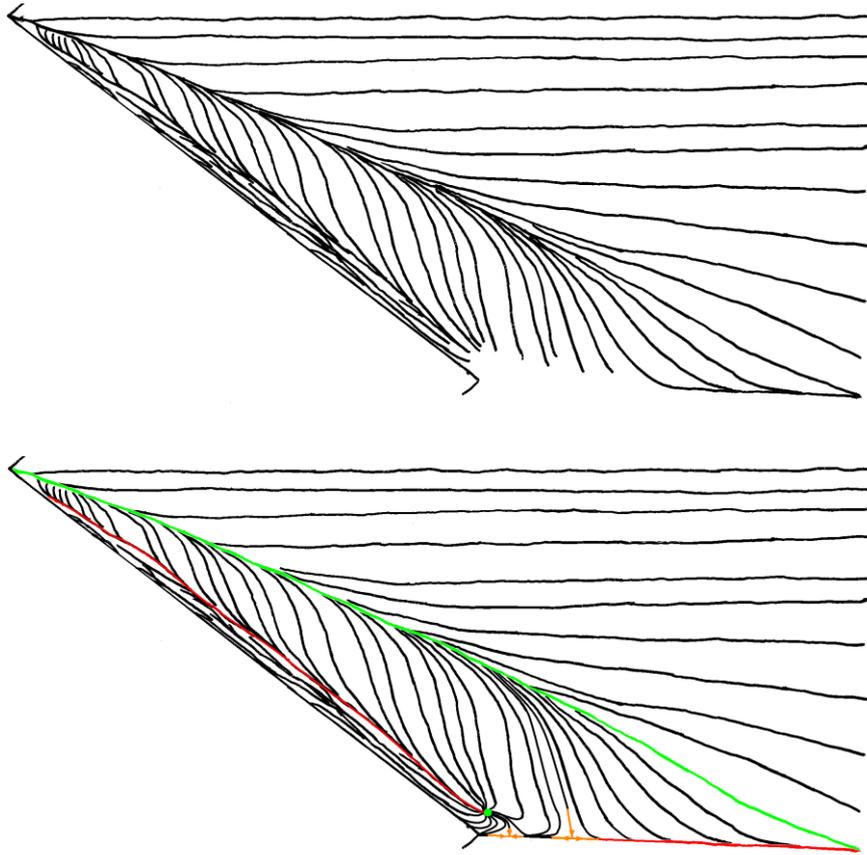
Figure 37: Basic topological detail is fitted first (top), before fitting determining location of critical points (bottom). Note the two saddle points on the line of symmetry in orange balanced by the positive node in green. Positive bifurcation line is in green and negative bifurcation lines are in red. Flow is from left to right.

3.6 Surface Pressure Taps

Surface pressure taps were used to capture transient surface pressure data over the surfaces of the

sawtooth and sinusoidal models to provide further quantification of the topological data obtained

with the surface shear stress visualisations. Between 120 and 125 pressure taps were used on each

model, allowing quantification of peak and mean pressures and instantaneous pressure distribution.

An example of a mean pressure distribution is given in Figure 38.

TFI's Dynamic Pressure Measurement System (DPMS) was used, providing 128 input channels, across

two DPMS units. Details of the system are available at the TFI website:

http://www.turbulentflow.com.au/Products/DPMS/DPMS.php (viewed 27 February 2013). Units

DPMS 1335 and DPMS 1336 were used, with DPMS 1335 having a range of ±3 kPa and DPMS 1336

having a range of ±7 kPa.

The DPMS units contain a pressure transducer for each channel. The pressure transducer has a diaphragm, which measures the force over its surface applied by the flow via the pressure taps and tubing using a strain gauge. The other side of the pressure transducer's diaphragm is common to each of the channels, and plumbed to the atmosphere using a reference pressure tube. Thus each channel measures a pressure relative to a common reference pressure.

A static calibration was performed on DPMS Unit 1335 and DPMS Unit 1336 to ensure that each of the channels was working within the manufacturer's specifications. The full calibration report is presented in Appendix: *Static Calibration of Dynamic Pressure Measurement System Units*. The report highlighted the fact that channels 40 and 56 were performing outside of the manufacturer's specifications, however the remainder of the channels were performing within the manufacturer's specifications. A further three channels exhibited a larger error than the remaining 123 channels, but still performed within the manufacturer's specifications. Channels 40 and 56 were not used in this research.

The raw dynamic pressure data is distorted by the amplitude damping and lag associated with the tube diameter and tube length. TFI implements a *Frequency Response Calculator* to linearise the tube response, correcting the dynamic pressure data, based on the known tube lengths and diameters. Their linearisation is based on the work of Bergh and Tijdeman (1965). The tube correction function is presented in Figure 41.

Validation of the frequency response was performed internally at Monash University (Chan 2012). For the calibration experiments, a fully enclosed speaker box was manufactured. The speaker box was instrumented with a Cyclone CS-120 subwoofer connected to a Hewlett Packard 3311A function generator via an amplifier in one wall. On the opposite wall, the speaker box was instrumented with pressure taps connected to the DPMS modules, a Kulite pressure transducer (*ULTRAMINIATURE XCQ-062*) and a G.R.A.S. ½" Free-Field microphone. Input signals from 10 Hz to 340 Hz were applied. The signals were sampled for 30 s at a sampling frequency of 1250 Hz.

The experiments compared the performance of experimentally determined tube correction functions against the theoretical functions derived by Bergh and Tijdeman (1965). Chan (2012) identified that the theoretical tube correction performed better than those determined experimentally, with good agreement in phase and amplitude over the frequency range measured.

The surface pressure measurements were conducted as follows. Each pressure tap was linked to the manifold connected to the DPMS unit with a 1 m PVC tube with inner diameter of 1.2 mm. The models were predrilled with the array of pressure taps. Tubes were cut to lengths of 1.005 m and the tubing was glued in place using *Araldite* superglue. The end of the tube protruding from the top of the model was sliced off with a razor blade, leaving the end of the tube flush with the model surface. The tubes were then purged with nitrogen gas, clearing any debris. An example of a pressure tapped model is shown in Figure 39. The pressure measurements were conducted at a sampling frequency of 1000 Hz for a sample length of 180.224 s. The data were logged using the TFI *Device Control* software. Further details of the logging regime are provided in Section 3.8 *Logging Regime*.
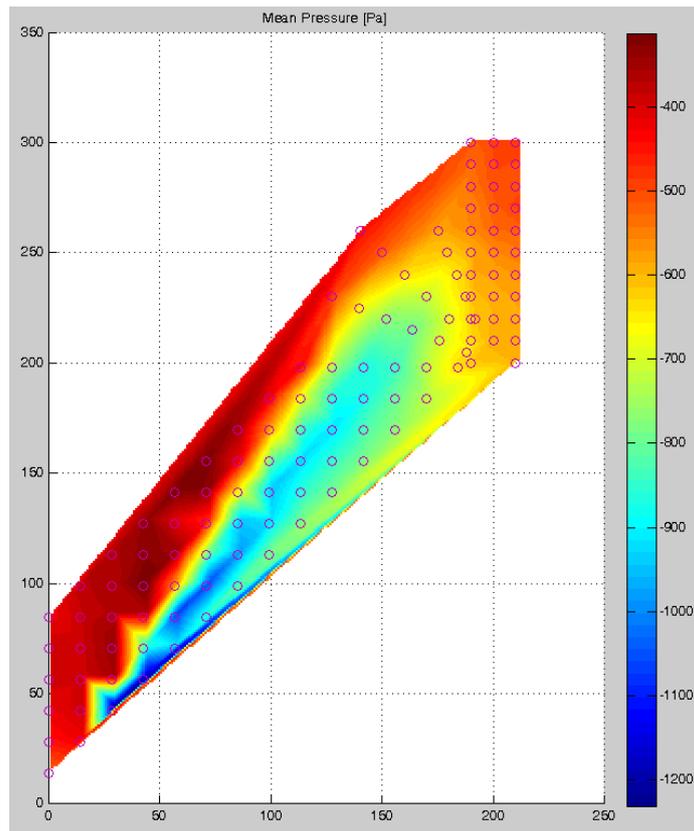
Figure 38: Example of output data from DPMS unit, interpolated using Matlab interpolation tools. Circles represent pressure tap locations. Colour scale represents pressure in units of Pascals. Spatial dimensions are in millimetres.
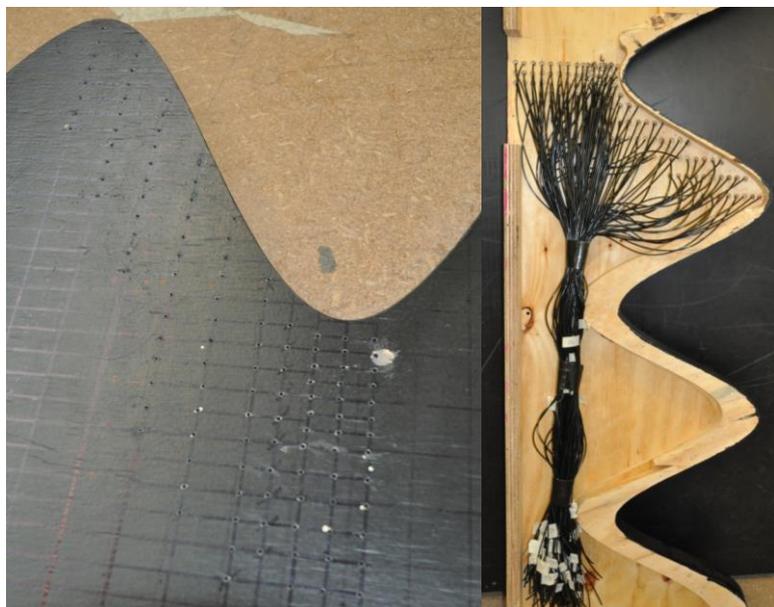
Figure 39: Surface of pressure tapped sinusoidal model (Left). Underside of pressure tapped model, showing 1 m long tubes (Right).

Figure 40: Manifolds for the DPMS (Left) and one DPMS unit with an attached manifold (Right).
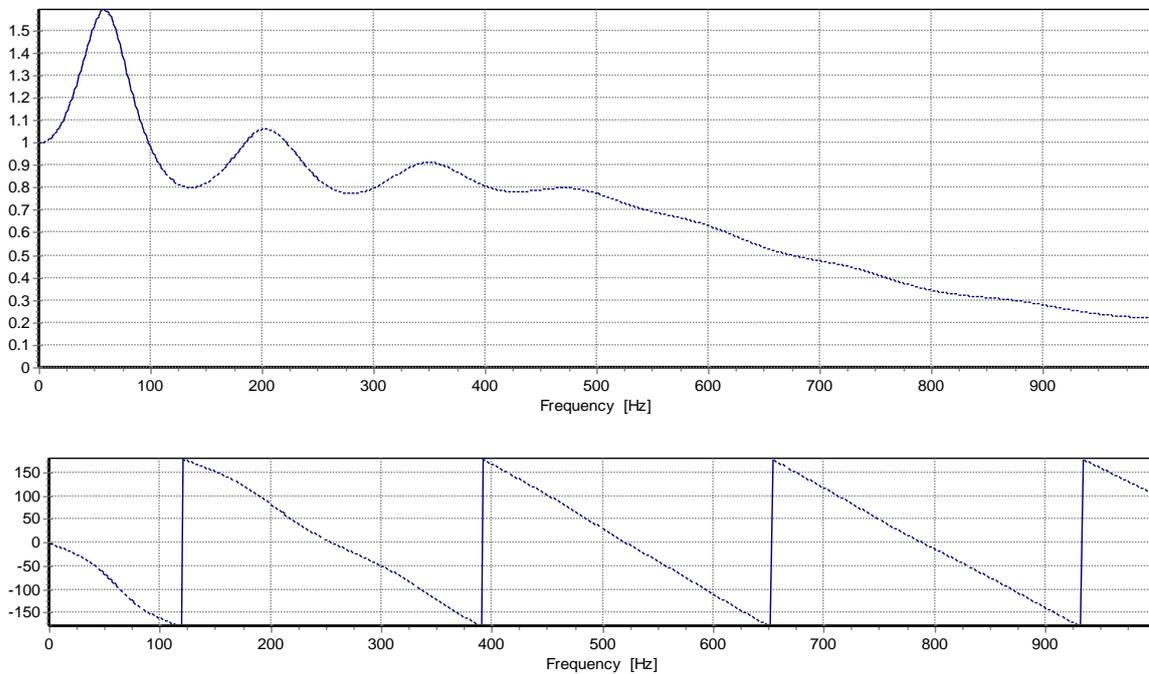
Figure 41: Amplitude and phase correction applied to DPMS results, calculated using TFI's frequency response calculator, which is based on the theoretical work of Bergh and Tijdeman (1965).

3.7 Wind Tunnel Flow Monitoring

Free-stream wind speed was logged with an upstream Pitot-static tube linked to a Honeywell

differential pressure transducer, giving a dynamic pressure reading. This was connected as an

analogue input to a TFI Data-acquisition Interface Unit (DIU). In the case of the upstream Pitot-static

tube, no signal corrections were applied, thus, the Pitot-static tube can be used only as a mean

reference, and not for instantaneous data.

The wind tunnel temperature was measured with a thermocouple, which was connected to a transducer, linked to a DIU. The output range was 0°C to 50°C. Logging hardware, acquisition rates, and sample times are described below.

The wind tunnel is pitch controlled, and controlled with a LabView application, however, the pitch is measured on a separate, analogue dial. Inflow conditions were setup based on the fan blade pitch, allowing repeatability. Atmospheric pressure was measured on a *Tief Hoch* barometer at the beginning of each testing session and manually input into the TFI software, for the calibration and zeroing of the Cobra probes. The logged temperature data was used in the calculation of air density in the conversion from dynamic pressure measured by the Pitot-static tube, to velocity.

3.8 Logging Regime

The setup for the logging is presented in Figure 42. In each case an analogue voltage signal is input to the DIU box, where the analogue signal is converted to a digital signal.

The DIU box contained a DT9836-12-0 Data Acquisition (DAQ) card with twelve analogue to digital channels with a ±10 V range, four Cobra Probe input channels and inputs for two DPMS modules of 64 channels. The total sample rate was 225 kHz. The computer ran a DT-OpenLayers (Version 6.7.3.1) DAQ driver.

When testing with the Cobra Probes, the sample rate was set at 5 kHz and down sampled to 2500 Hz, to reduce aliasing, except where stated otherwise. When testing with the DPMS, data was sampled at 1000 Hz.

Given that up to four Cobra Probes were operated at a time, with each probe consisting of four outputs, in addition to one analogue to digital channel for temperature and another analogue to digital channel for the upstream Pitot-Static tube, eighteen channels were used at a time. Thus the sampling rate of 5 kHz was half of the maximum recommended sample rate, set by the following equation provided by TFI (Mousley 2011):

$$f_{max} = \frac{0.8 \times f_{DAQ}}{Number\ of\ Channels}$$

(3-7)

Here, f_{max} is the maximum sample rate; f_{DAQ} is the maximum sample rate of the DAQ card.

The sampling frequency when using the DPMS was set at 1 kHz, with 128 pressure channels and a further two for temperature and the upstream Pitot-Static tube, which is less than the maximum recommended sampling frequency of 1384 Hz.
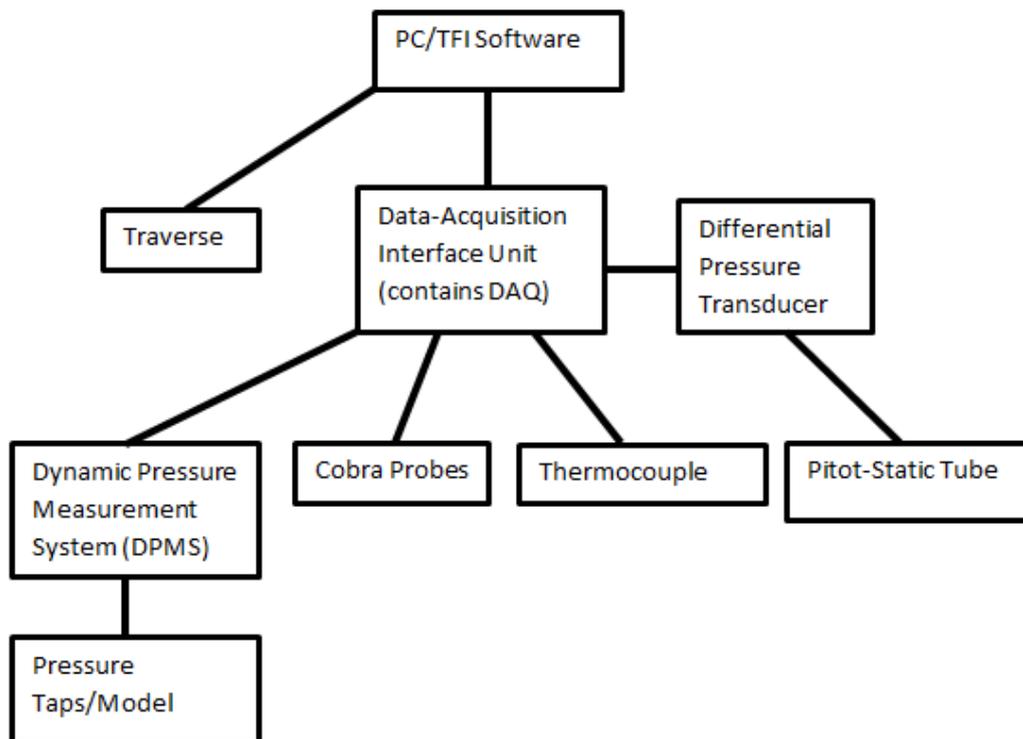
Figure 42: Configuration of logging equipment, showing Cobra Probe, surface pressure taps, upstream Pitot static tube, and thermocouple linked to the DIU where the data acquisition card is located, which then feeds data to the TFI software.

4. Forward Facing Step Validation Studies

The foundation of this thesis is the body of work addressing FFSs. In this chapter, results from the

Monash University 450 kW wind tunnel are validated against previous work.

In Section 4.1 *Cobra Probe Data* results from Cobra Probe data collected over an h = 100 mm FFS

case with Configuration 2 inflow conditions, as described in Section 3.3 *Inflow Conditions* are

presented. Flow speed was 20 ms^{-1}, resulting in a Reynolds number of 1.37×10^5. Mean data

statistics collected with Cobra Probes are presented in Section 4.1 *Cobra Probe Data*. These statistics

were compared against comparable studies from Bowen and Lindley (1977) and Ren and Wu (2011)

and the field study from Mann et al. (2012).

In Section 4.2 *Surface Shear Stress Visualisations*, surface shear stress visualisations are presented

for cliff heights of h = 50 mm, 100 mm and 150 mm, and with the three inflow configurations.

Reattachment lengths are compared with results from other researchers. Three-dimensionality is

identified.

4.1 Cobra Probe Data

The mean velocity and turbulence intensity statistics are first compared with the wind tunnel work

of Bowen and Lindley (1977), before the development of Reynolds Stresses are compared with the

work of Ren and Wu (2011). The results of correlation analysis are then shown, providing an insight

into the coherent structures that develop from the crest of the FFS. Finally, PSDs are examined, from

which peak Strouhal numbers can be determined and compared to the work of Camussi et al.

(2008).

4.1.1 Mean Velocity and Turbulence Intensity

The experimental configuration is shown in Figure 43. The development of normalised velocity,

turbulence intensity, speed up and normalised turbulence intensity of the flow as it passes over the

crest of the forward facing step are shown in Figure 44, Figure 45, Figure 46, Figure 48 and Figure 49.

In Figure 48 the speed-up is compared to the data from Bowen and Lindley (1977). The speed-up is

calculated as follows:

$$S = \frac{U_{Model}(x,z)/U_{Pitot,Model}}{U_{BL}(z)/U_{Pitot,BL}} \tag{4-1}$$

The speed-up, *S*, is a ratio of the normalised velocity above the model to the normalised velocity in the boundary layer without the model. $U_{Model}(x,z)$ denotes the flow speed as a function of distance downstream of the crest, *x*, and height above the step, *z*. $U_{BL}(z)$ denotes the flow speed without a model, as a function of height above the ground. U_{Pitot} denotes the flow speeds measured by the upstream Pitot-Static tube in the respective experiments.

The normalised turbulence intensity is calculated as follows:

$$TI\ Ratio = \frac{I_{uu,Model}(x,z)}{I_{uu,BL}(z)} \tag{4-2}$$

$I_{uu,Model}(x,z)$ is the longitudinal turbulence intensity as a function of distance downstream and height above the cliff. $I_{uu,BL}(z)$ is the longitudinal turbulence intensity as a function of height above the ground, with no model in place.

Figure 43 (Left) View of straight edged FFS case from upstream. Note four Cobra Probes traversing. (Right) View of 0° straight edged FFS case from downstream. Note trapezoidal tooth trip to promote mixing.
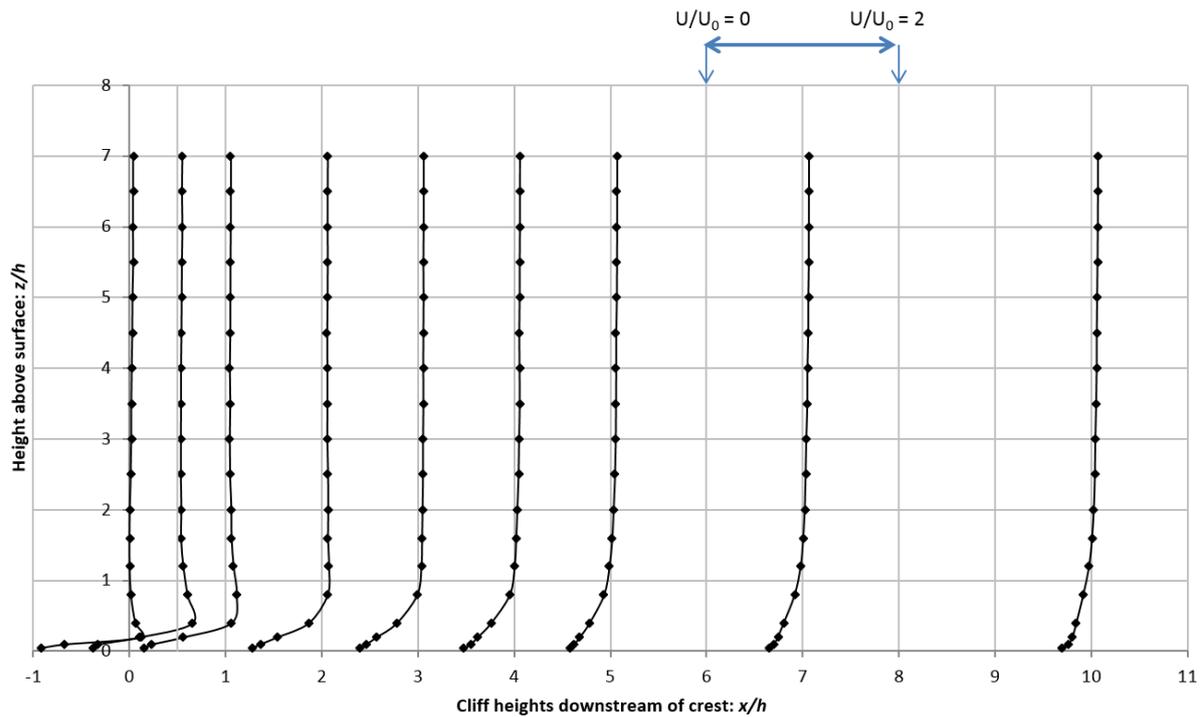
Figure 44: Development of normalised flow speed. Speed normalised against free-stream velocity for inflow configuration 2, described in Section 3.3 *Inflow Conditions*, at free-stream velocity of 20 ms^{-1}.

Careful examination of the first colour plots in both Figure 46 and Figure 49, at x = 0*h*, reveals a lateral inconsistency on the bottom left hand side of each of the plots; these are more clearly demonstrated in Figure 47 and Figure 50 where the four vertical profiles normalised speed and turbulence intensity are presented for the *x* = 0 location. This can be attributed to the large vertical velocity gradient in the shear layer and the experimental uncertainty in the height of the Cobra probes above the surface of the model, which is in the order of 1 mm. The remainder of the flow field has much smaller velocity gradients and hence is less sensitive to the uncertainty in probe height.

The colour maps of speed-up shown in Figure 46 indicate that the effect of the FFS persists downstream, beyond the 10*h* that was examined. Speed-up above 1.2 is observed between 0 and 3*h* downstream of the crest, though these regions also have the largest drop off in speed-up near the surface, associated with the recirculation region.
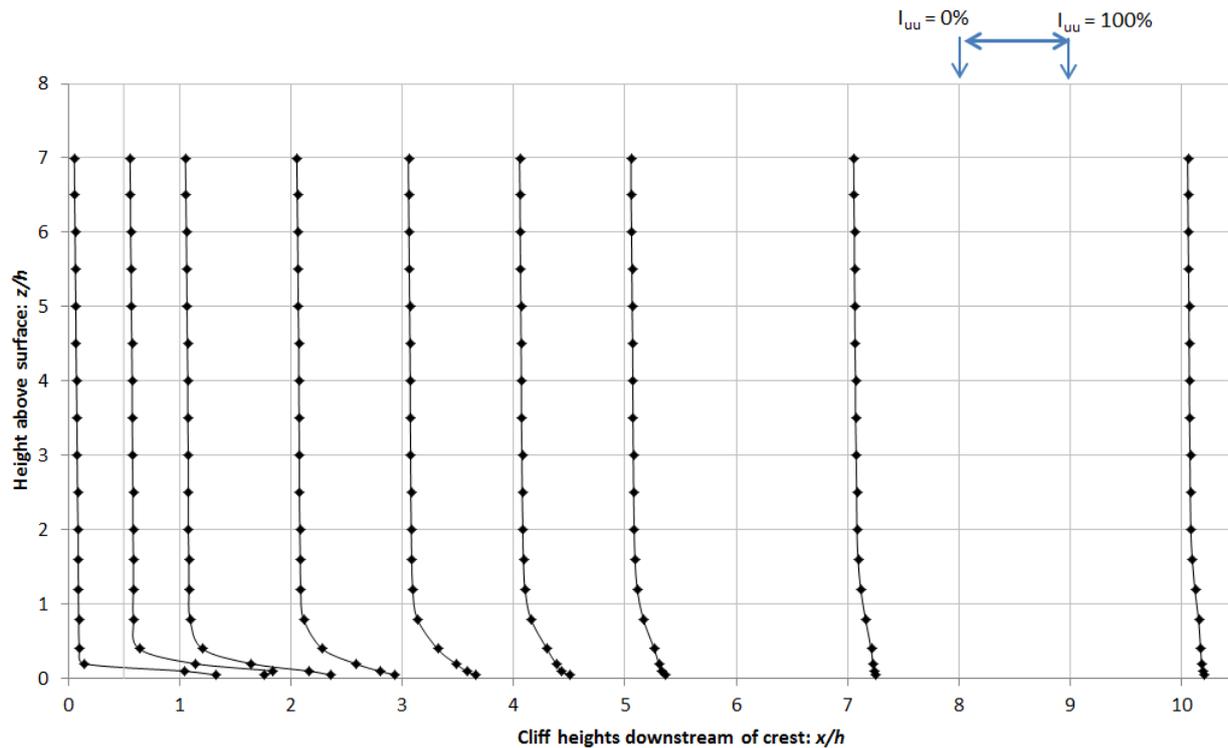
Figure 45: Development of longitudinal turbulence intensity over a FFS of height 100 mm using configuration 2 at 20 ms^{-1}.

There is some ambiguity in this near ground region in terms of the velocity/speed measurement, making comparison difficult between Cobra Probe data, hot-wire data and Particle Image Velocimetry (PIV) data. In the current study, the use of Cobra Probe results in a pseudo-velocity measurement: that is, the positive *U*-velocity component is accurately recorded, while the negative *U*-velocity component is recorded as either zero or incorrectly assigned a small positive value that might be induced by recirculation in the wake of the probe. Thus, the directional nature of the flow is partially captured by the Cobra Probes. In contrast, hot-wire anemometers make no distinction between forward flow and reversed flow, thus a large negative flow is assigned a positive value, causing the resulting reading to be more representative of a scalar speed than a vector velocity. PIV approaches are able to capture the recirculating eddies and are capable of providing the true velocity data, which would result in an even lower velocity value. Thus, it is expected that Cobra Probes will record lower mean velocity values than hot-wire anemometers in cases where recirculating flow exist.
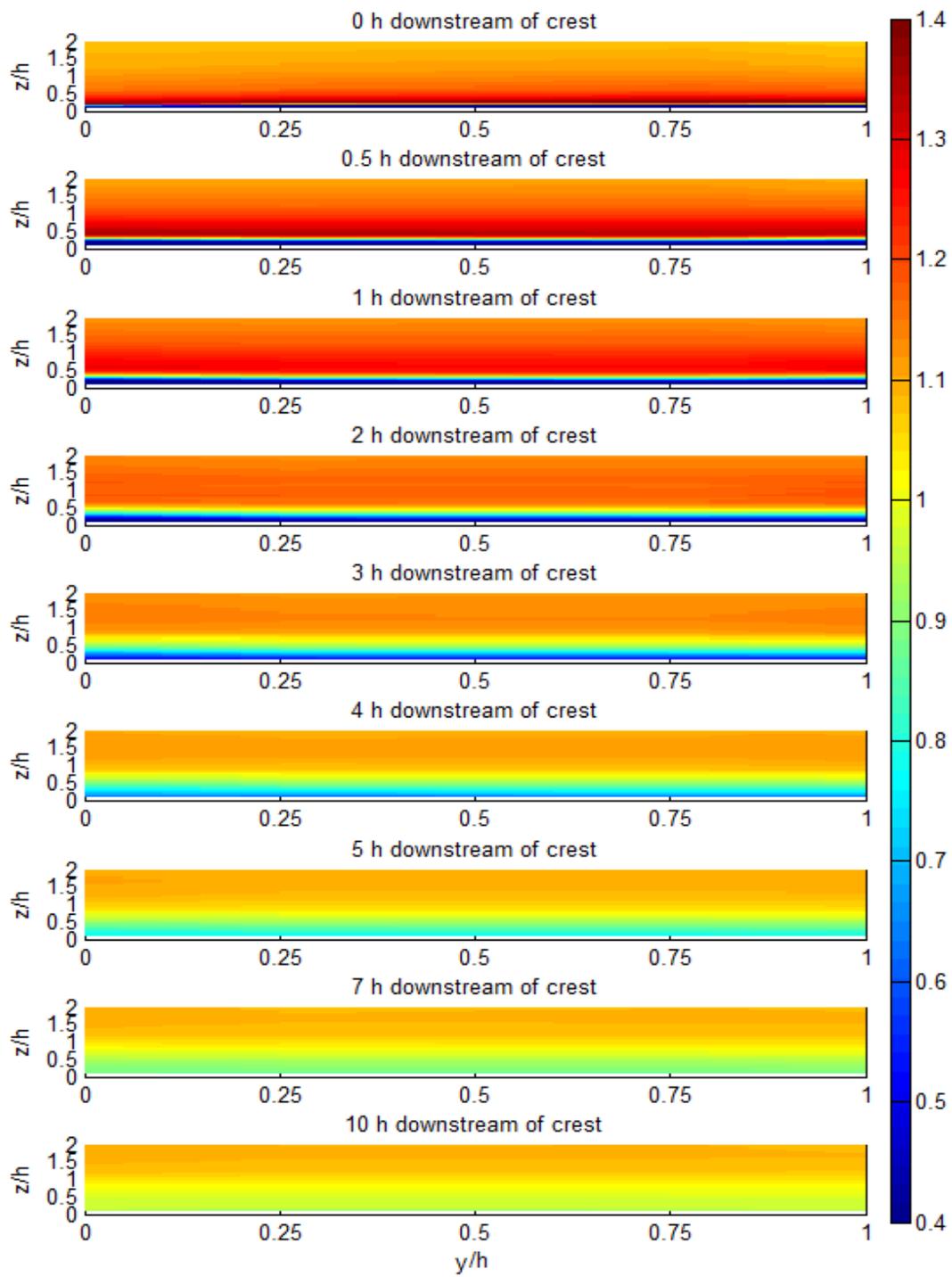
Figure 46: Flow development (speed-up) downstream of crest. From z = 0 to 2h above surface of step shown. Lateral measurement locations are y/h = 0, 0.25, 0.75, and 1.
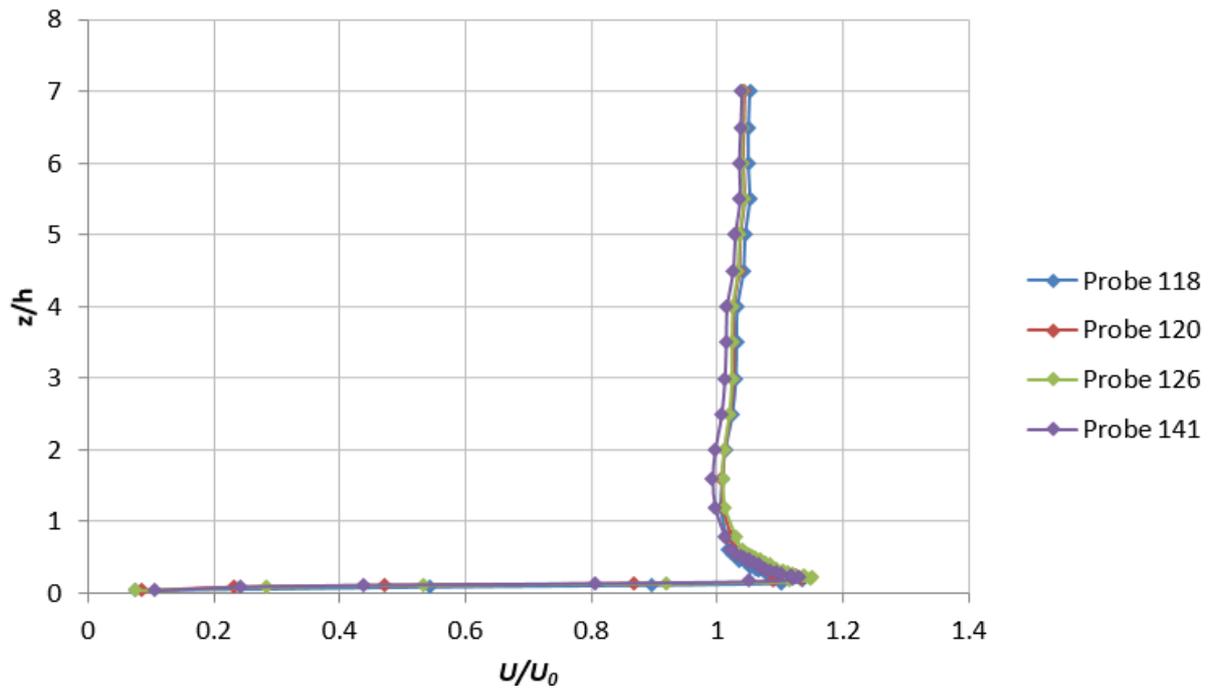
Figure 47: Normalised flow speed at *x* = 0. From *z* = 0.05*h* to 7*h* above surface of step shown. Lateral measurement locations are y/h = 0, 0.25, 0.75, and 1.

Nevertheless, above the region that the recirculation is likely to have an impact on, the speed-up reported by Bowen and Lindley is consistently higher than that reported in the current study. In particular, at the crest, no recirculation is expected; however, the speed-up remains noticeably higher in the work of Bowen and Lindley. This can be attributed to the difference in boundary layer thickness to step height ratio, δ/h. In the work of Bowen and Lindley, δ/h = 20; in the comparison dataset, δ/h = 7.15. With the larger value of δ/h, the crest height is located in a region of greater vertical wind shear when considering the undisturbed boundary layer. At a point at $z = h$ above the crest, which is above the recirculation region, but where there is a noticeable discrepancy between the current work and that of Bowen and Lindley, the flow is heavily influenced by the undisturbed boundary layer flow, $U_{BL}(z = 2h)$. The speed-up is caused by a combination of the increase in elevation due to the cliff height, as well as the increase induced by continuity – the flow being compressed and accelerated over the crest. The first of these effects is reduced in a thinner boundary layer.
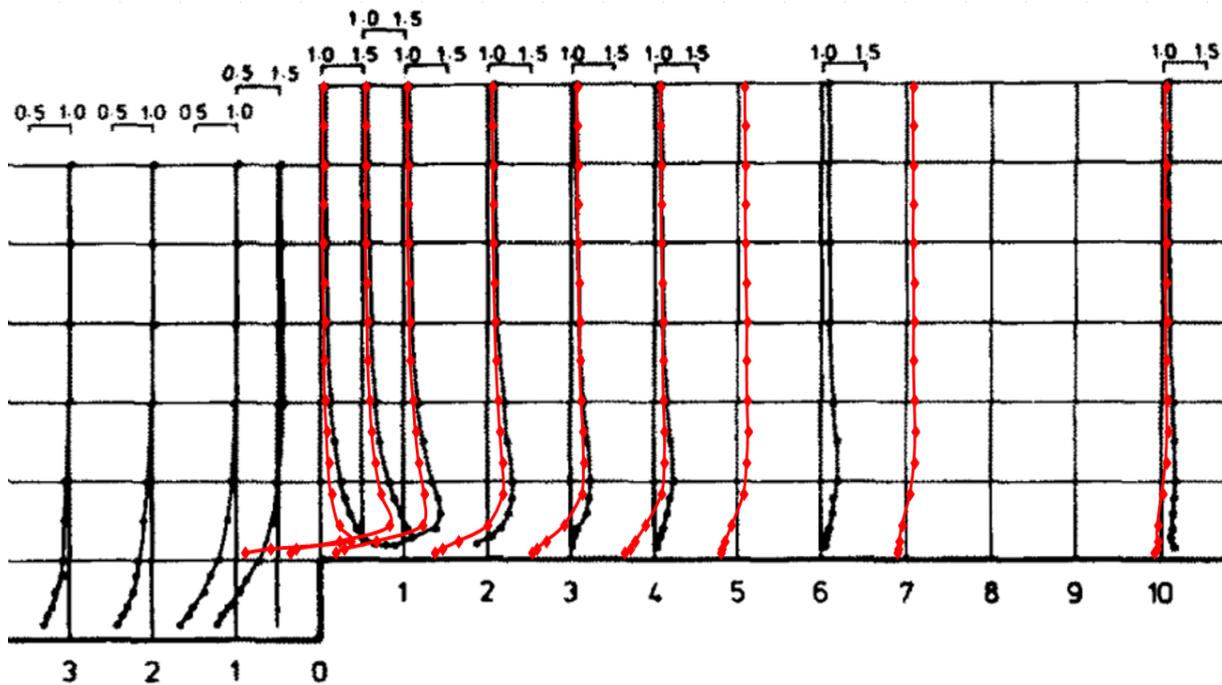
Figure 48: Speed-up over a FFS from Bowen and Lindley (1977), used with permission. Boundary layer to step height δ/h = 20. Experiment performed at nominally the same Reynolds number as the current experiment. Results from the current experiment are shown in red.

Thus, in comparing the speed-up, *S*, generated in this research with the research of Bowen and

Lindley (1977), who used hot-wire anemometry, it is important to understand the differences in

velocity data. The speed-up is consistently lower through the region that might be associated with

the separation bubble, where recirculating flow might be encountered. This can be attributed in

small part to the Reynolds number (Sherry et al. 2010): the current experiment was conducted at a

Reynolds number of 1.2×10^5, approximately double that used by Bowen and Lindley, with both

experiments using a free-stream velocity of 20 ms^{-1}, while in the current research, a step height of

0.1 m was used, while a step height of 0.05 m was used by Bowen and Lindley (1977). But the

primary causes for the discrepancy in speed-up magnitude are the measurement technique and the

thickness of the boundary layer.

The development of normalised turbulence intensity is presented in Figure 49. The development of

turbulence intensity is consistent with the flow structure described by Kiya and Sasaki (1983b) who

describe the weak vortex shedding from the separation bubble that is insufficient to stop an

accumulation of vorticity in the bubble, which periodically results in a large shedding event. The

weak shedding events lead to the increase in turbulence intensity near the surface that persists into the far wake, while the accumulation of vorticity drives the even greater increase in turbulence intensity in the separation bubble that was observed.

Above the separation bubble and the subsequent downstream ejections, the turbulence intensity shows a reduction from the undisturbed boundary layer state consistent with a slight increase in speed that has extended downstream, seen in Figure 46, while the turbulent eddies have remained unaffected by the topography.

A comparison between the turbulence intensity in the current study and the work of Bowen and Lindley (1977) is presented in Figure 51. The results from the current study are superimposed in red, using the same normalised scale. In this instance Bowen and Lindley calculated the turbulence intensity based on the standard deviation of local velocity divided by the mean free-stream velocity, rather than the standard deviation of local velocity divided by the mean of the local velocity. The turbulence intensity data from the current study has been recalculated to match this definition. Four step heights directly above the crest, a wind tunnel shutdown whilst traversing caused an outlying data point. This data point has been replaced by linear interpolation between the neighbouring points.

Given the higher δ/h ratio in the Bowen and Lindley work[4], combined with a lower Reynolds number, a slightly smaller recirculation region is expected compared to the current work (Sherry et al. 2010). Thus, it is unsurprising to observe that the region of elevated turbulence intensity extends further downstream in the current study than in the Bowen and Lindley work. The near surface points within 2-3h of the crest are dominated by recirculating flow, which, as pointed out, is treated differently by the two measurement techniques implemented. In this instance, the Cobra Probe should record

---

[4] Relationship between δ/h and the size of the downstream recirculation zone is established in the literature, e.g. Sherry et al. (2010). However, this is further expounded in the following section, as a range of δ/h cases are tested for the size of their reattachment length using paint droplet surface shear stress visualisation.

much higher turbulence intensity than a hot-wire probe as the reversed flow velocity components are assigned a zero value as opposed to a positive value.
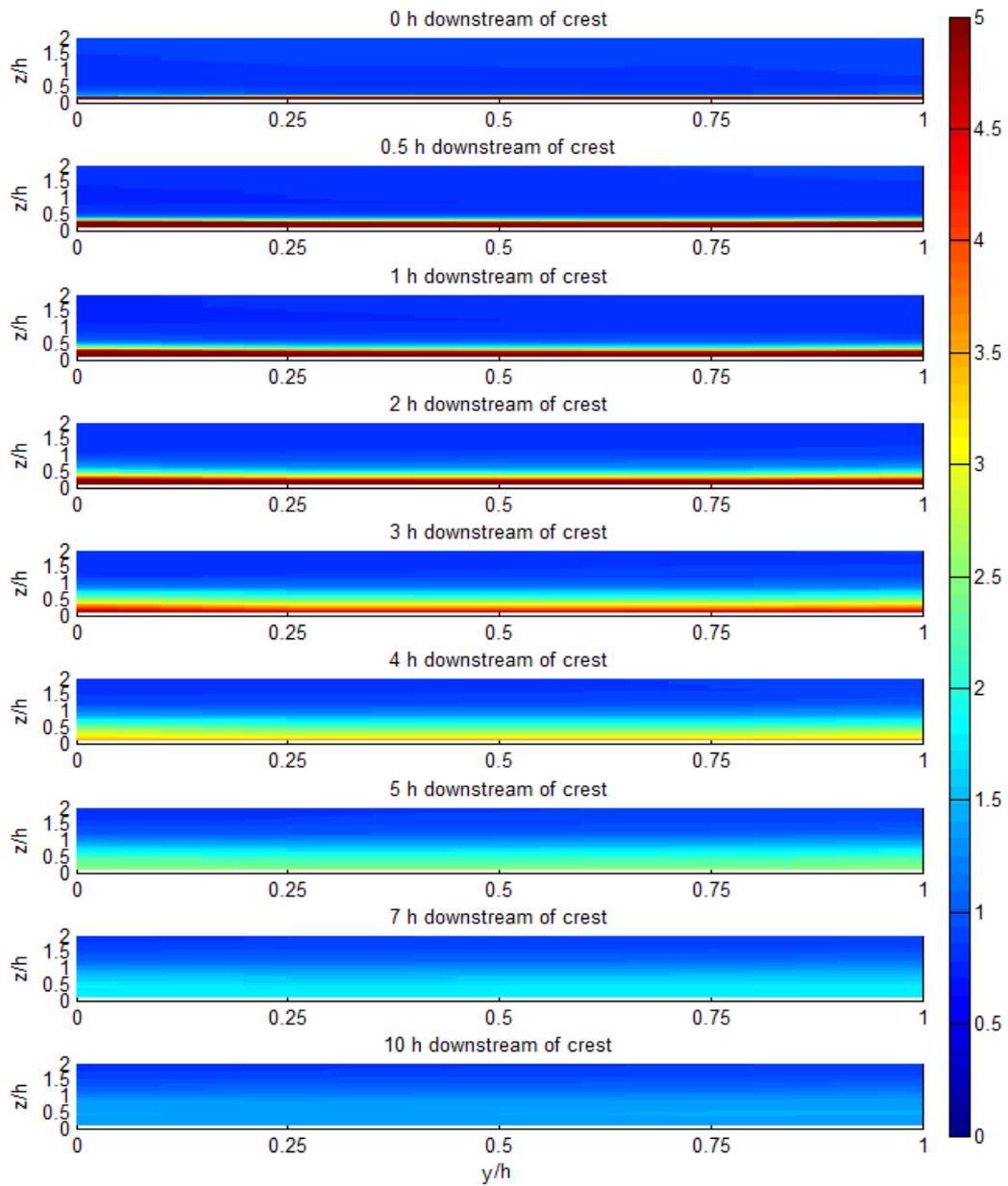
Figure 49: Flow development (normalised turbulence intensity) downstream of the crest. From z = 0 to 2*h* above surface of step shown. Lateral measurement locations are y/h = 0, 0.25, 0.75, and 1.
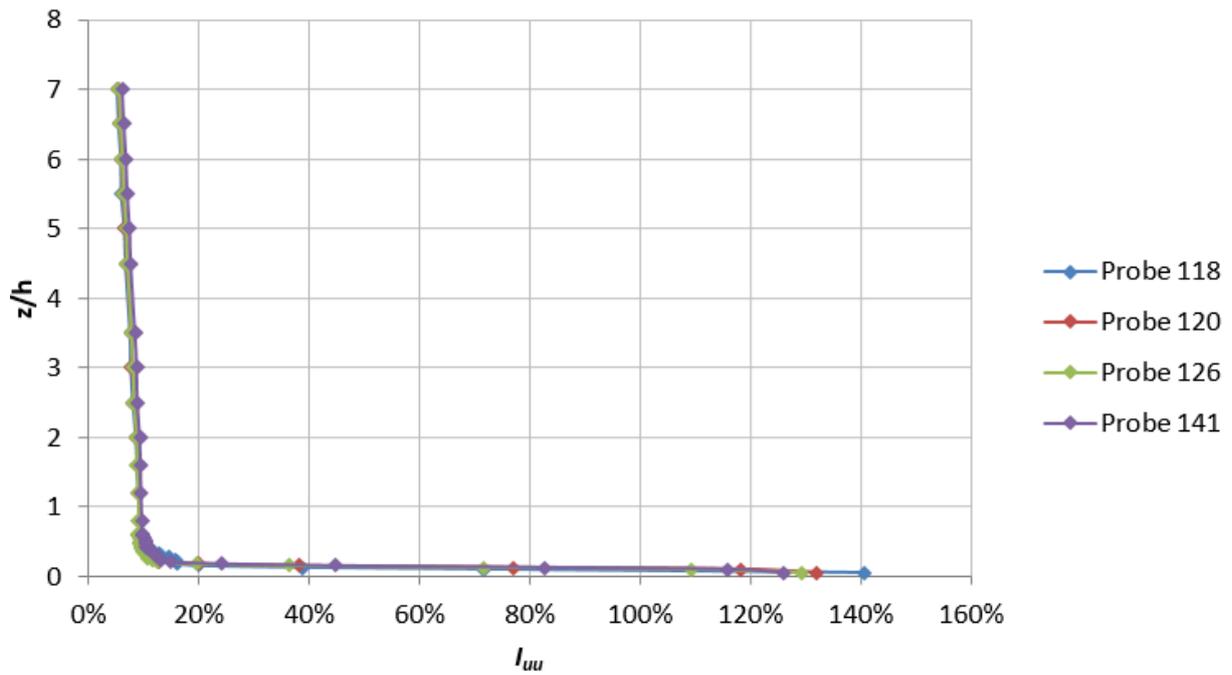
Figure 50: Turbulence intensity at *x* = 0. From z = 0.05*h* to 7*h* above surface of step shown. Lateral measurement locations are y/h = 0, 0.25, 0.75, and 1.
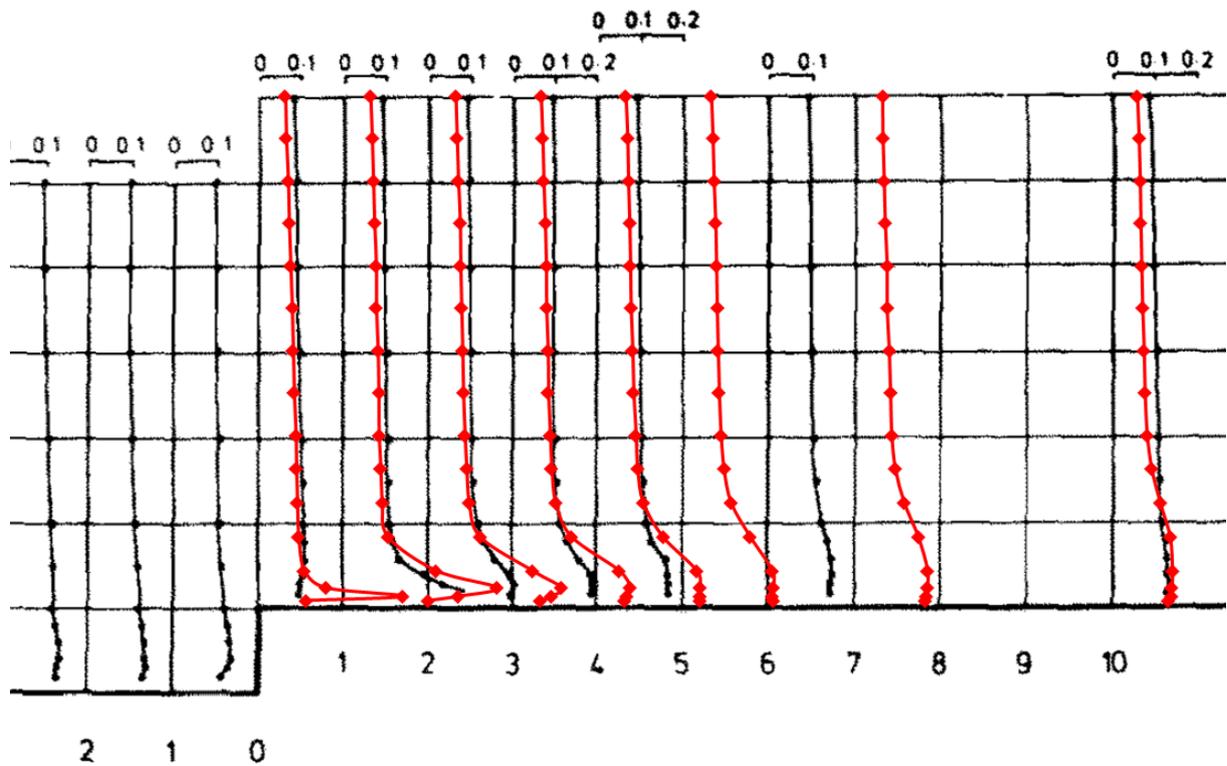
Figure 51: Turbulence intensity over a FFS from Bowen and Lindley (1977), used with permission. Boundary layer to step height *δ/h* = 20. Experiment performed at nominally the same Reynolds number as the current experiment. Results from the current experiment are shown in red.

The comparison between the results from the current research and the results from Bowen and

Lindley provides reasonable agreement of the trends observed in the development of speed-up and

turbulence intensity, within the limitations of the two measurement techniques that were implemented, and the differences in the inflow conditions.

A similar comparison is presented with the data presented by Mann et al. (2012). They used a Lidar anemometer to measure line of sight wind speed and standard deviation of wind speed over the crest of Bolund Hill in Denmark. Site and measurement details are provided in Mann et al. (2012). The profile of the hill is shown in Figure 52, and the data presented by Mann et al. (2012) is shown in Figure 53. For comparison with the current work, the data presented in Figure 53 was digitised, and three profiles are presented in Figure 54, at x/h = 0, 0.5, 1.

As with the comparison with Bowen and Lindley, it is of fundamental importance to understand the difference between the measurement techniques, and thus the difference in statistics that are presented. In this field data, line of sight velocity statistics were collected at a sampling rate of 390 Hz, with the ability to differentiate the direction of the velocity vector, thus enabling the capture of recirculating flow. This will result in lower mean velocity values than those recorded by the Cobra Probes. Similarly, because negative wind speeds can be recorded by the Lidar, the full range of wind speeds can be captured, implying that the standard deviation will be larger than that recorded by the Cobra Probes, which cannot account for the negative wind speeds.

Another important difference between the wind tunnel measurements and the field data is the difference between an idealised topography and the topographic profile shown in Figure 52. Discerning the precise effect of the topography from the variation induced by the difference in Reynolds number, the difference in boundary layer to cliff height ratio or topographic profile is not trivial. Nevertheless, the purpose of this research is to provide insight into wind turbine siting, which is ultimately a field exercise; thus, while the comparison is not ideal, it is significant in establishing the applicability of the research.
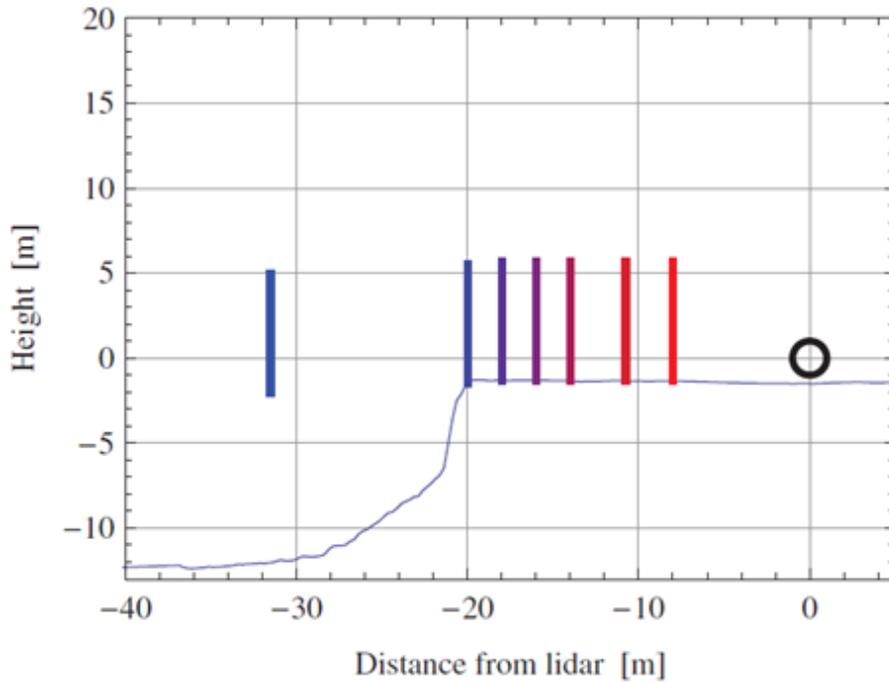
Figure 52: Bolund Hill topography and location of vertical profiles. Circle shows location of Lidar. Reproduced from Mann et al. (2012) with permission.
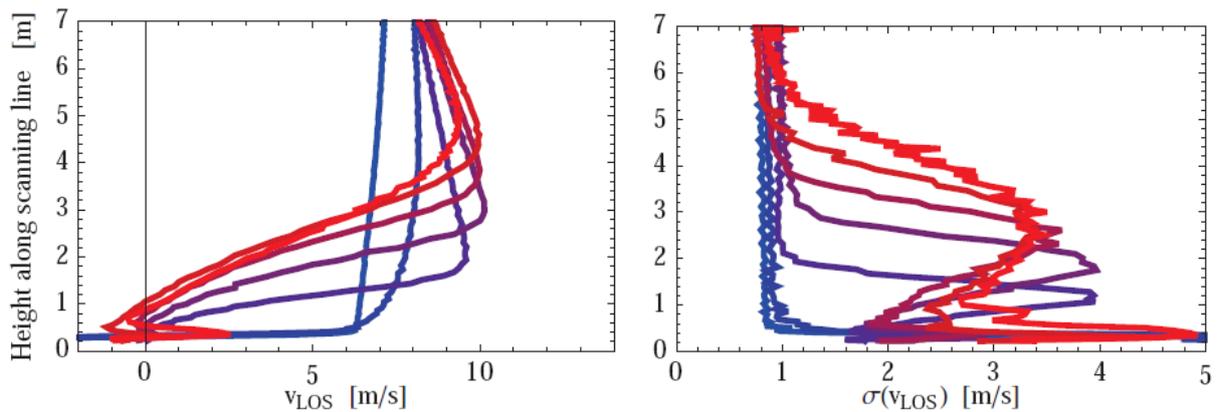
Figure 53: Vertical profiles of velocity profiles and standard deviation of wind speed over the Bolund Hill. Reproduced from Mann et al. (2012) with permission.

The set of plots on the left side of Figure 54 contains comparisons between the normalised velocity profiles measured on Bolund Hill, and the normalised velocity profile measured in the wind tunnel.

On the right side are the corresponding turbulence intensity values, calculated using the approach from Bowen and Lindley, that is, normalising the standard deviation by the free-stream wind speed.

The free-stream wind speed by which the field data has been normalised is 7 ms^{-1}, based on the highest measurement point upstream of the cliff.

In terms of the normalised wind speed data, the primary difference between the two datasets is that the wind tunnel data has a strong peak wind speed at a height of 0.2h at the crest, while the field data has a broader peak centred at a height of 0.35h at the crest. Downstream, the roles are reversed. At 0.5h and h downstream of the crest, the wind tunnel velocity profiles feature broader peaks; the vertical velocity profiles from the field data are much more defined. This may be attributable to the slight rounding of the crest of the Bolund Hill, as seen in Figure 52. A similar effect can be observed in the experimental work of Bowen and Lindley (1977) in their comparison of the FFS case with ramp cases. The regions of strongest speed-up are projected vertically, implying that a strong speed-up peak is observed at the peak in the FFS cases, while in the ramp cases the speed-up region is projected downstream, resulting in the distinct speed-up peak in the downstream profiles.

Consistent with the difference in the measurement techniques, the magnitude of the turbulence intensity measured in the field data are larger than those measured with the Cobra Probes in the wind tunnel. However, this is in fact distorted by the normalisation employed here. The free-stream wind speed from the field study is not published, and the use of 7 ms^{-1} is an underestimate of the wind speed, although the vertical velocity gradient appears small, as seen in Figure 53. Using unscaled standard deviation data is not appropriate because the scale of the turbulence varies with wind speed. Normalising the standard deviation with the mean wind speed at the measurement point gives the turbulence intensity statistic that is used through the remainder of this thesis. However, this approach skews the result because of the inability of Cobra Probes or, in the case of Bowen and Lindley, hot-wire anemometers to distinguish the direction of the flow. Thus, normalising the standard deviation with the free-stream velocity is the most appropriate approach.

The crest profile reveals the largest difference between the wind tunnel turbulence intensity data and the field data. A suggested reason for this divergence, presented in the paragraph above, is that the rounded crest alters the initial formation of the separation region. By x/h = 0.5 the shape of the vertical turbulence intensity profiles show good agreement between the field measurements and

the wind tunnel measurements. In the final comparable profile, at *x/h* = 1, the consistency in profile shape can again be observed, though some near-surface scatter affects both velocity and turbulence profiles, which Mann et al. (2012) attribute to "…a sharp and rapidly varying interface between fast and slowly moving air".
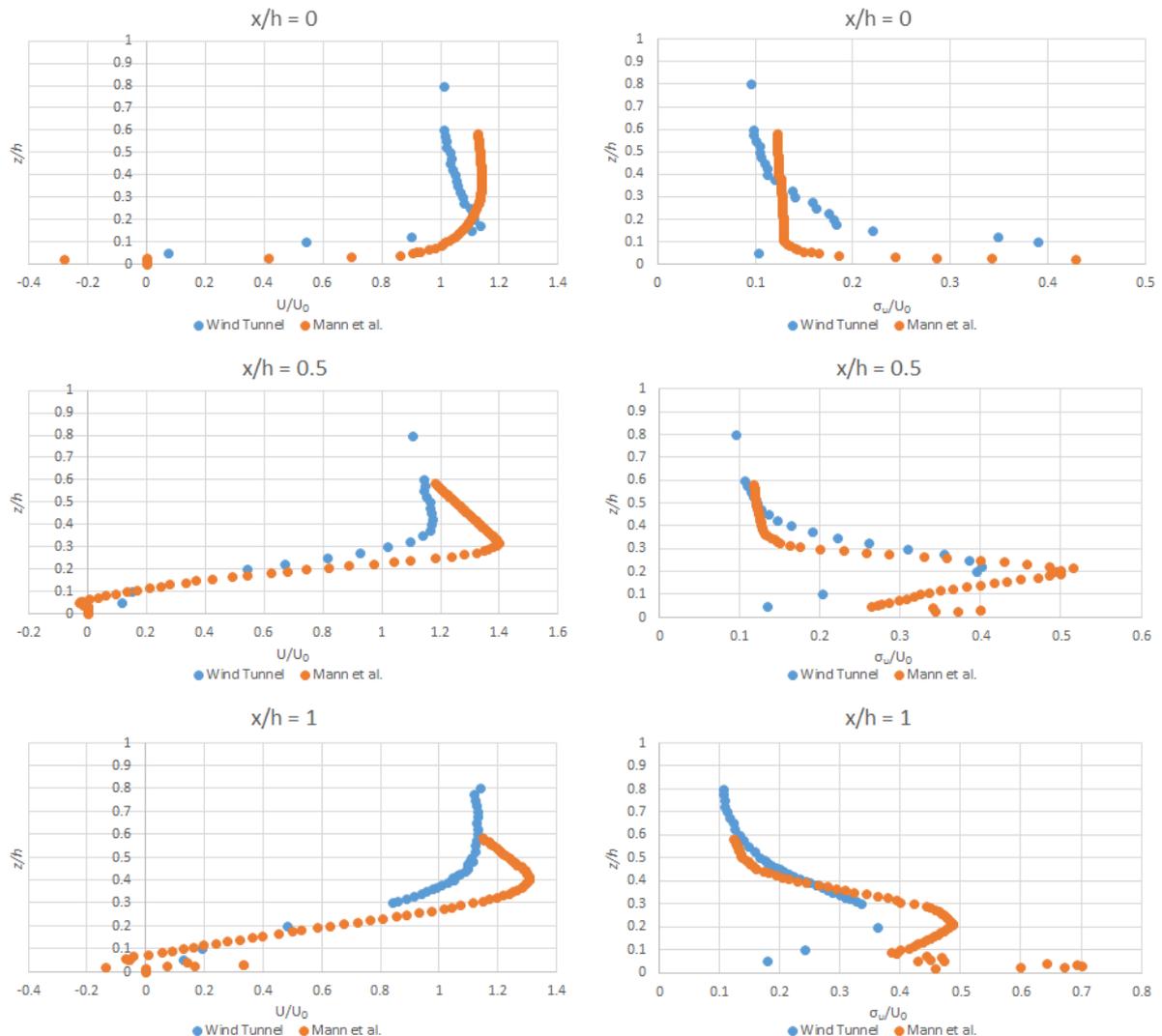
Figure 54: Comparison of normalised velocity and stream-wise turbulence intensity between the current study and the field study at the Bolund Hill in Denmark, performed by Mann et al. (2012).

4.1.2 Reynolds Stresses

In addition to the mean velocity and turbulence intensity statistics, analysis of the Reynolds Stresses provides an alternative perspective on the velocity fluctuations induced by the FFS as well as useful information regarding the flow structure. A form of the Reynolds Stress in which the variance is normalised against the square of the free-stream velocity is used: $(\sigma_u/U_0)^2$, also expressed as $<u'^2>/U_\infty^2$.

This provides a direct measurement of fluctuations relative to the overall flow regime. Similar information is available with the vertical component $<w'^2>/U_\infty^2$, and the cross component, $<u'w'>/U_\infty^2$.

The Cobra Probe traversing data are compared to the FFS analysis of Ren and Wu (2011). Using configuration 2 and an FFS of height $h = 0.1$ m gives a δ/h ratio equalling 7.3, which is near the δ/h ratio of 8 from Ren and Wu. Ren and Wu (2011) used PIV to capture velocity statistics over their FFS. As outlined in the previous section, the ability of PIV techniques to correctly capture recirculating flow will result in larger variances than will be captured by Cobra Probes. However, there is a significant discrepancy in Reynolds number, as the Ren and Wu experiment is conducted at a Reynolds number of 3450, compared to the Reynolds number for this configuration of 1.37×10^5. The work of Sherry et al. (2010) implies that at a Reynolds number of 3450, Reynolds number independence will not have been achieved, resulting in a smaller recirculation region in the Ren and Wu experiment. The second cause of difference is the inflow turbulence. While the inflow turbulence intensity is not fully characterised by Ren and Wu, they state that the free-stream turbulence intensity is 0.45%, compared to 5% in the current study. The elevated levels of turbulence intensity from the inflow act to break down the flow structures, limiting the size of the recirculation region.

Examination of the downstream development of longitudinal turbulence, shown in Figure 55, suggests that the downstream turbulence in the $\delta/h = 7.3$ case dissipates sooner than the $\delta/h = 8$ case investigated by Ren and Wu (2011), which is consistent with the inflow turbulence intensity differential between the two cases.

Specifically, at $x/h = 0.5$ (Figure 55b), it can be seen that the longitudinal turbulence intensity matches closely between the two cases. However, higher levels are recorded in the Ren and Wu study at $x/h = 1$, corresponding to a persistence of the turbulence levels associated with the flow structures generated off the crest, in contrast to the dissipation of the longitudinal Reynolds stresses observed in the current study. However, in Figure 55e, the longitudinal turbulence from the current study becomes larger than

that recorded by Ren and Wu (x/h = 3 onwards), which is attributable to the larger recirculation region caused by the Reynolds number difference between the two experiments.

The vertical Reynolds Stresses are presented in Figure 56. At the first comparison location, the vertical Reynolds Stresses are already 30% higher than the current work. This may be attributable to the means of turbulence generation – in Ren and Wu's case, a cylindrical bar was placed span-wise across their wind tunnel, just downstream of the leading edge of the splitter plate; in the current work, a truncated spire type vortex generator was used, as can be seen in Figure 14. In Ren and Wu's case, their means of turbulence generation will tend to generate vertical fluctuations. The vertical Reynolds Stresses provides a mean of momentum transport, which may explain the higher "nose" profiles in the downstream profiles in the other Reynolds Stress components.

The *u-w* component of Reynolds Stress presented in Figure 57 demonstrates an excellent match in the turbulence development downstream of the crest of the FFS in spite of the obvious discrepancy in Reynolds number, though from x/h = 1 onward, the peak value from Ren and Wu occurs at a height above that of the current experiment.

While the magnitude of the Reynolds Stresses in the current study are, for the most part, the same or less than those reported by Ren and Wu (2011), the two studies exhibit very similar characteristics, with peak values occurring at similar heights above the surface of the FFS, in spite of contrasting inflow conditions.

Ren and Wu (2011) also compared the maxima of σ_u relative to the free-stream velocity. The (σ_u/U_0) parameter is related to the step height to boundary layer thickness ratio, which in turn is a controlling parameter in determining the size of the downstream recirculation bubble. Various researchers, including Ren and Wu (2011) and Sherry et al. (2010), have shown that as the boundary layer thickness to step height ratio (δ/h) increases, the size of the separation bubble decreases because the top of the boundary layer, where flow speed is highest, interacts directly with the FFS, resulting in increased

turbulence generation and larger fluctuations. In the work of Ren and Wu (2011) the maximum σ_u/U_0 was 0.3. Leclercq et al. (2001) and Sherry et al. (2010), investigating δ/h values closer to unity, observed σ_u/U_0 ratios in the order of 0.35 – 0.45.

The maximum σ_u/U_0 recorded in the present study was approximately 0.25. Given the lower δ/h value of 7.3, (compared to $\delta/h = 8$ used by Ren and Wu), it was expected that the σ_u/U_0 ratio would increase. From the differences between experimental techniques used, it could be argued that the maximum σ_u/U_0 value has increased because, if the data were to include negative velocity values in the heart of the recirculation region, the standard deviation would be approximately doubled.

The variations in magnitude of the Reynolds Stresses and σ_u/U_0 peaks observed between the current study and the work of Ren and Wu are attributable to two things. First, the Reynolds number, which impacts on the relative size of the recirculation regions, and secondly, the limitations of the Cobra Probes, which are capable of only measuring the flow within the 45° cone of acceptance. The latter causes the magnitude of the variations to not be fully captured when flow recirculation occurs.
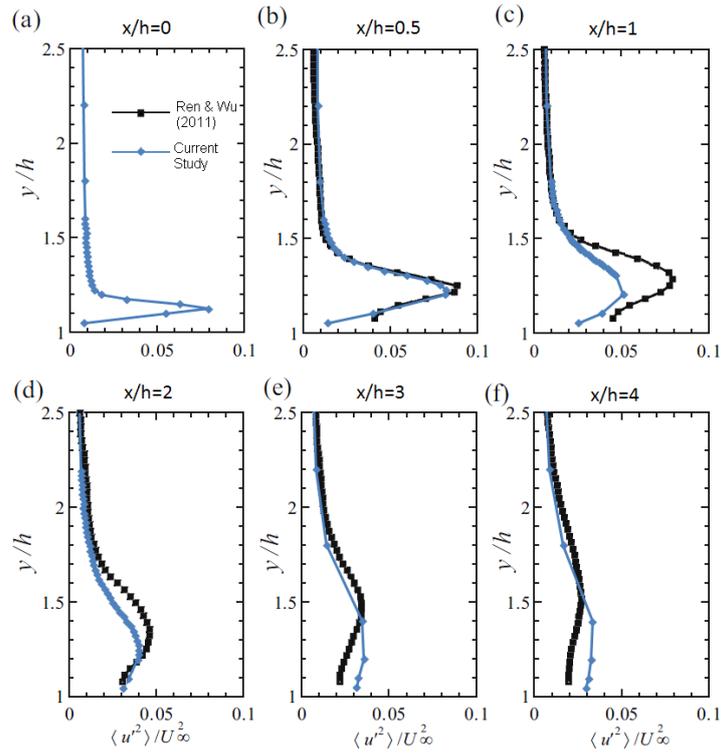
Figure 55: Longitudinal Reynolds Stress. Comparison between current study and Ren and Wu (2011). Note Ren and Wu did not report values for x/*h* = 0. Figure adapted from Ren and Wu (2011), and used with permission.
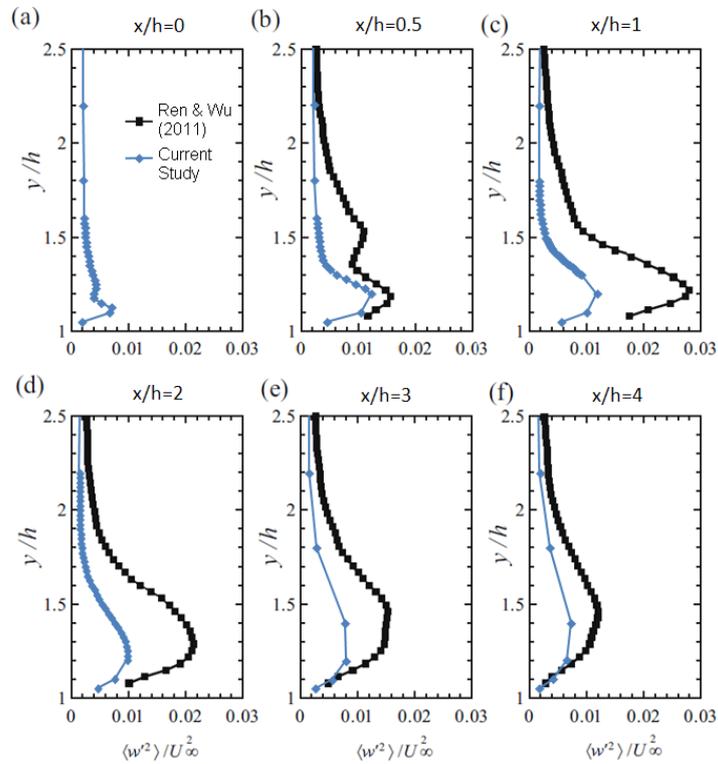
Figure 56: Vertical Reynolds Stress. Comparison between current study and Ren and Wu (2011). Note Ren and Wu did not report values for x/*h* = 0. Figure adapted from Ren and Wu (2011), and used with permission.

119
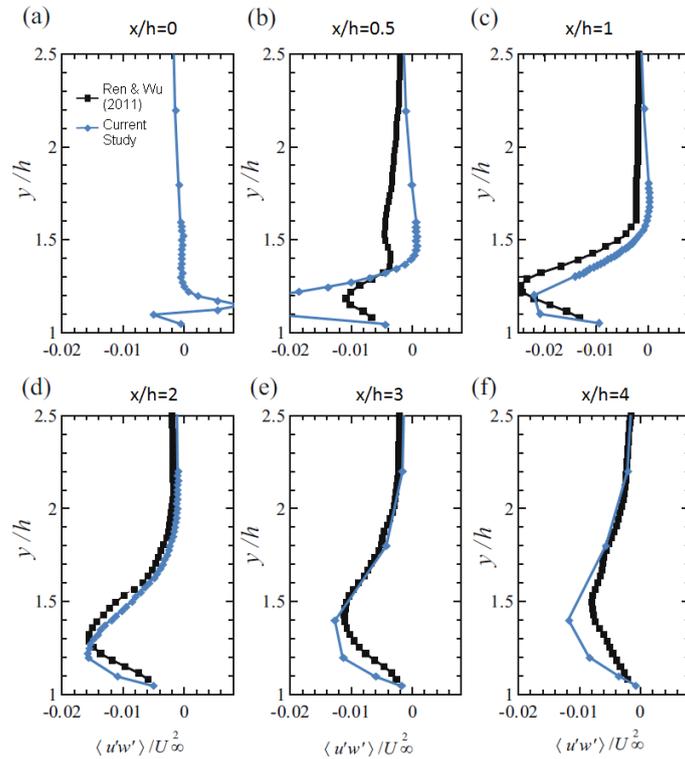
Figure 57: Stream-wise and vertical Reynolds stress. Comparison between current study and Ren and Wu (2011). Note Ren and Wu did not report values for x/h = 0. Figure adapted from Ren and Wu (2011), and used with permission.

4.1.3 Correlation Analysis

The cross-covariance is a measure of the correlation between two signals. The biased cross-covariance was implemented, implying that the cross-covariance was normalised by the number of points in the sample (Orfanidis 2007). As the number of samples is increased to infinity, the bias reduces asymptotically (Orfanidis 2007). The higher the cross-covariance, the more closely correlated are the two signals. Figure 58 presents the maximum biased cross-covariance of the stream-wise velocity measurements from two probes at 25 mm spacing, traversing vertically through the undisturbed boundary layer. This baseline measurement provides a comparison with the maximum cross-covariance of the stream-wise velocity signals from two probes traversing 0.25h apart over the h = 100 mm FFS, which is presented in Figure 59.

The strongest correlation is evident in the recirculation bubble, confirming the presence of a coherent vortex structure. From x = 2h to x = 5h a secondary region of high correlation can be observed near the surface, which highlights the presence of the coherence of the structures being

120

ejected from the recirculation bubble. This secondary structure is consistent with the ejection

described in Section 4.1.1 *Mean Velocity and Turbulence Intensity*, which was particularly evident in

the development of turbulence intensity, and linked to the work of Kiya and Sasaki (1983b) which

showed that an accumulation of fluid sheds off periodically downstream. The correlation was not as

strong in this downstream shedding region, as in the initial recirculation region.

The decay of the ejected structures is clearly illustrated in the plot in Figure 60, with the correlation

steadily dropping downstream. At 10h downstream, the maximum correlation was still 12.5 times

higher than that in the initial boundary layer conditions.
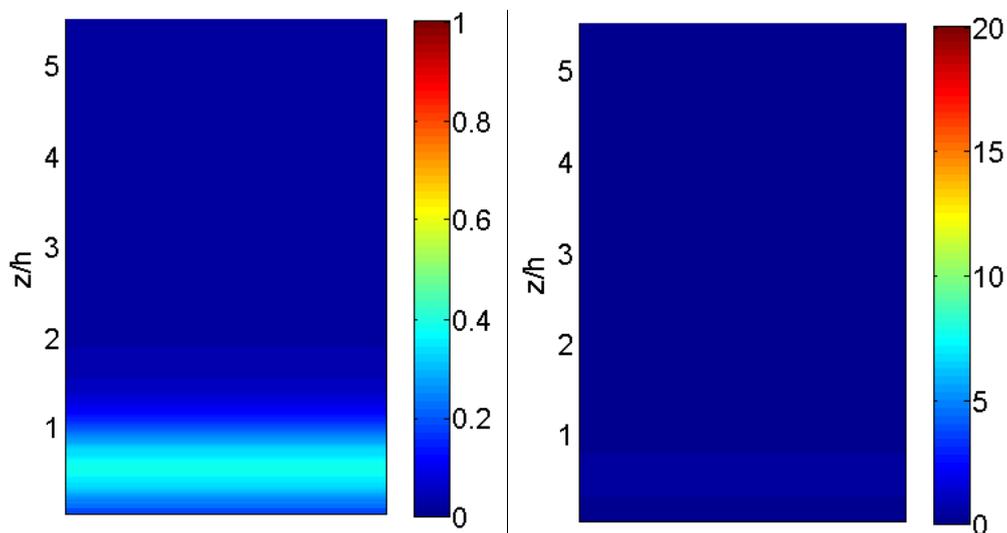
Figure 58: Colour plots of the maximum biased cross-covariance between two probes traversing 25 mm/0.25h apart through the undisturbed boundary layer. (Left) Colour bar range limited from 0 to 1. (Right) Colour bar based on range in Figure 59.
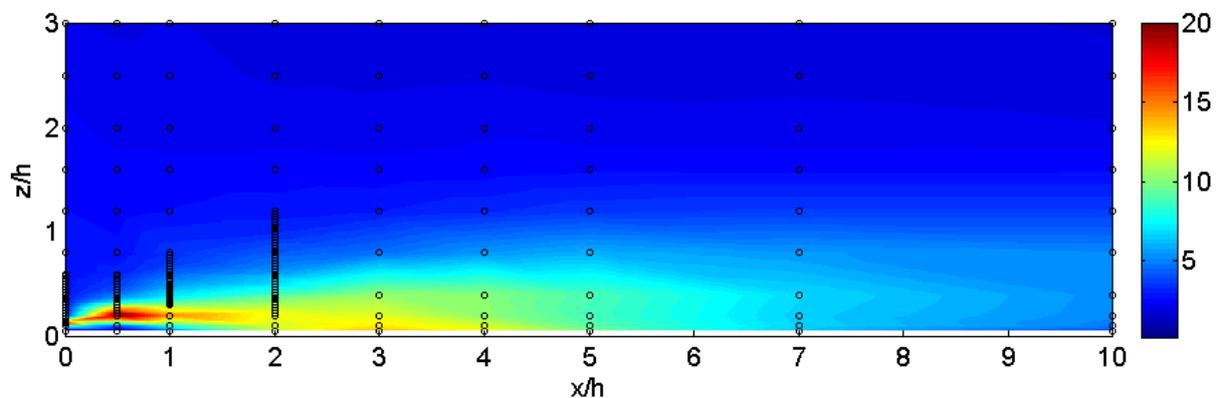
Figure 59: A colour plot of the maximum biased cross-covariance between two probes traversing 25 mm/0.25h apart over an FFS of height h = 100 mm. Measurement locations are shown by the black circles.
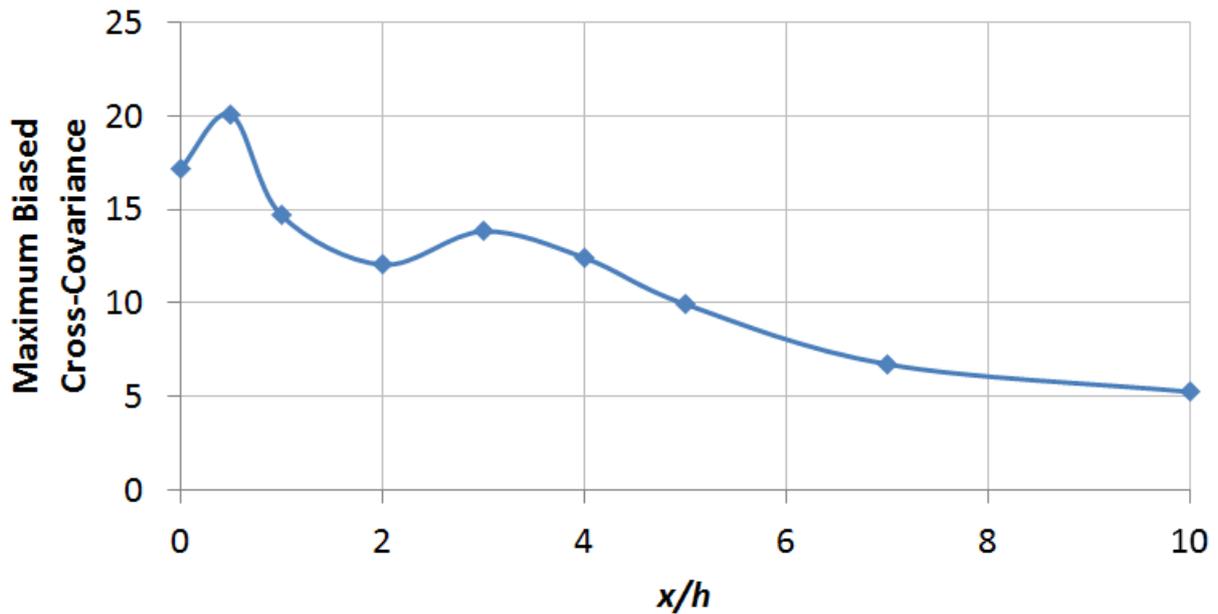
Figure 60: Maximum biased cross-covariance v Distance downstream. The maximum cross-covariance at each location downstream is normalised against the maximum cross-covariance in the undisturbed boundary layer.

4.1.4 Power Spectral Density

Having identified the regions of increased correlation, and attributed the increased correlation to

the existence of coherent structures, that is, vortices whose dominant axes extend in a span-wise

direction, it is anticipated that the shedding of these vortices downstream would occur at distinct

Strouhal numbers. However, given the turbulent nature of the inflow, one would expect a broad

spectral peak, extending over a range of Strouhal numbers. Thus, the frequency of occurrence of

such structures can be characterised through the consideration of the power spectral density (PSD).

Normalised PSDs presented here are calculated using Welch's method, as described in Section 3.4.1

Calculating Power Spectral Density and Integral Length Scale.
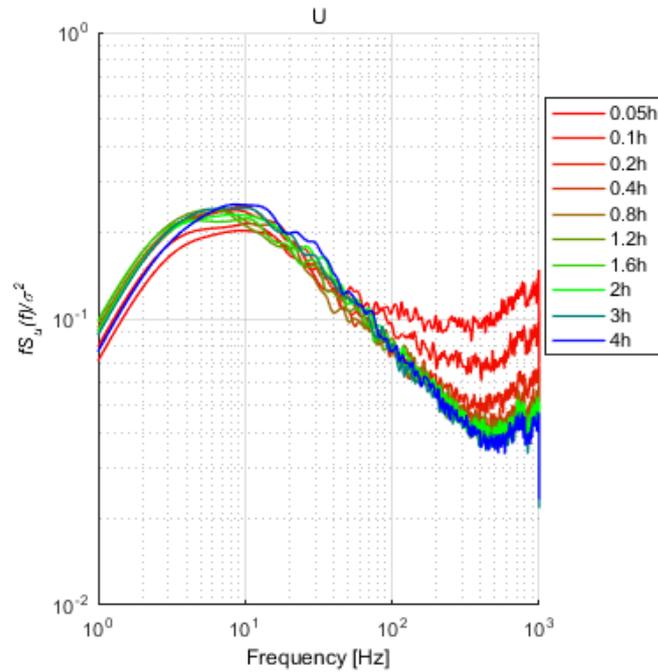
Figure 61: Vertical development of PSD of stream-wise velocity through the undisturbed boundary layer.

PSDs based on the stream-wise velocity data from the inflow conditions are presented in Figure 61, and provide a datum for comparison with the remainder of the PSDs. The vertical development of the PSD of the stream-wise velocity at $x = 0$, $0.5h$, h, $2h$ and, $4h$ are presented in Figure 62. The peak frequency values from each of the PSDs were converted to Strouhal numbers based on the height of the FFS and free-stream velocity, then collated and presented in Figure 63. The peaks were simply taken as the frequency associated with the highest relative power level in the PSDs. Thus, in measurement locations where the decay of the vortex structures and the fluid-surface interactions were evident, Strouhal numbers based on high frequencies were reported. The limitations of the Cobra Probes in characterising the energy cascade down to fine-scale turbulence are discussed later in this section.
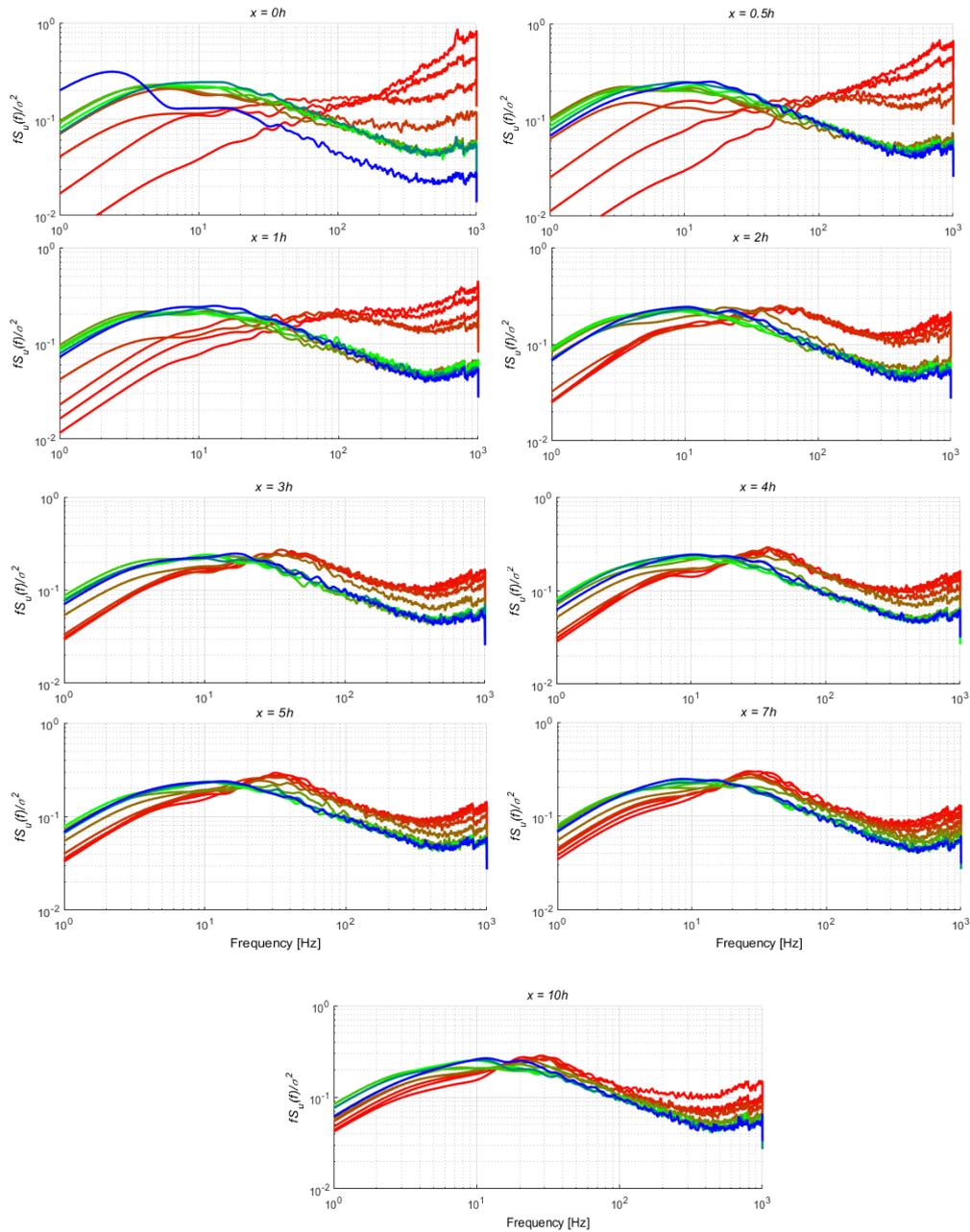
Figure 62: Stream-wise and vertical development of PSD of stream-wise velocity. Colour-coding based on legend in Figure 61.

Integral length scales in the undisturbed boundary layer were almost uniform with height above the ground, according to Figure 61. The peak frequencies corresponded to broad rises between 8 to 10 Hz, that is, Strouhal numbers between 0.04 and 0.05. In the near-surface measurements, an increase in the relative energy at higher frequencies is observed, though the relative amount of energy contained at these frequencies is still significantly less than at the peak frequency around 10 Hz. The increase in the relative energy in the high frequency range is attributable to the air-

surface interaction, though the normalisation, which multiplies the energy by the frequency, artificially amplifies the high frequency side of the spectrum.

The relative energy in the PSDs at $x = 0.5h$ in the region immediately downstream of the crest of the FFS is dominated by finer scale turbulence in the near surface measurements, associated with the chaotic flow in the recirculation region. This turbulence production differed from the flow through the undisturbed boundary layer, as the fine-scale turbulence production generated near the ground through the undisturbed boundary layer did not dominate the PSD, as seen in Figure 61.

From the crest through to $x = h$, there was a large percentage of rejected data due to the recirculation within the region affecting the PSDs. Sampling was conducted at 2000 Hz during this series of experiments, implying a Nyquist frequency of 1000 Hz. Thus there were limitations in identifying precisely how small the dominant fine turbulent eddies were. The frequency associated with these structures is discussed later in this section.

Between $x = h$ and $x = 2h$, dominant structures become apparent, distinct from the length scales observed in the undisturbed boundary layer conditions and the energy at high frequencies that dominates the spectra nearer to the crest of the FFS. At $x = h$, this was measured as peak Strouhal numbers of 0.6 (120 Hz) and reducing with increased height; the relative PSDs from $z = 0.2h$ and below were still dominated by the high frequency elements. By $x = 2h$, the peak Strouhal numbers are between 0.15 and 0.3 (30 – 60 Hz), and the small scale turbulence no longer dominate the spectra. By $z = 0.9h$, the PSDs are returning to their inlet conditions.

Downstream of the mean recirculation region, the peak Strouhal number associated with the stream-wise velocity component stabilised to a band between 0.15 and 0.2 above the surface region. This Strouhal number range was an excellent match with what was published by Camussi et al. (2008) who reported a value of 0.2 based on a broad peak in the PSD of surface pressure data. The broad peak in the spectrum measured by Camussi et al. (2008) compares well with the broad

peaks shown at *x* = 2*h* and *x* = 4*h*. From *x* = 5*h* onward, the Strouhal number range shifts down to 0.1 to 0.15.
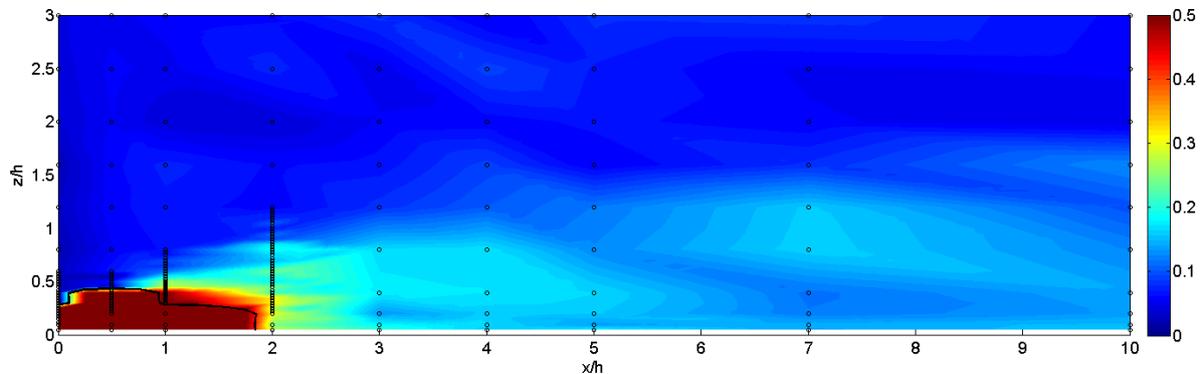
Figure 63: Peak Strouhal Number from U-component of PSD. Black circles represent measurement points. The colour bar is scaled to illustrate shedding in the wake at Strouhal numbers between 0.15 and 0.25.

The Cobra Probe traverses have successfully characterised the large scale structures as they shed from the recirculation region, as well as identifying that an intensification of high frequency fluctuations are associated with the recirculation region. In observing the elevated levels of relative energy at high frequency, one may question whether the underlying cause is associated with the energy cascade and decay, or whether the high frequency energy is driven by the vertical shear profile, resulting in a Kelvin-Helmholtz instability.

Stull (1997) provides a good description of the Kelvin-Helmholtz instability, or shear layer vortices. The Kelvin-Helmholtz instability occurs across a shear profile and is a convective instability. It is characterised by a wave-like disturbance across the shear layer. The waves grow in amplitude, and eventually roll up, and appear visually as breaking waves. These breaking waves diffuse and generate turbulence.

Various researchers have quantified the periodicity associated with the Kelvin-Helmholtz instability, particularly in the context of cylinder wakes (Bloor 1964, Wei and Smith 1986, Kourta et al. 1987, Sigurdson 1995, Brun et al. 2008). These researchers considered cases with Reynolds numbers below 6×10^4. Little research exists characterising the Kelvin-Helmholtz instability in flow over FFSs at

Reynolds numbers comparable to those used in the current study, though Abdalla et al. (2009) did complete DNS simulations over a FFS at a Reynolds number of 4500. They suggested that the shear layer vortices exhibited characteristic Strouhal numbers in a similar range to the large-scale shedding observed downstream of the recirculation region in the current investigation. This implies that there is a significant disconnect between the work of Abdalla et al. (2009) and the current study. The work of Bloor (1964), Wei and Smith (1986), and Kourta et al. (1987) suggested a power law relationship between the large-scale shedding, the Kelvin-Helmholtz instability and the Reynolds number. In contrast, Sigurdson (1995) suggested that frequency associated with the Kelvin-Helmholtz instability was ten to twenty times the frequency associating with the large-scale shedding, while Brun et al. (2008) observed a factor of forty.

Thus, based on Sigurdson (1995), the lowest frequency associated with the Kelvin-Helmholtz vortices is ten times the shedding frequency: 380 Hz. However, based on Kourta et al. (1987), a frequency of 10 kHz might be expected. This implies that, as well as limitations associated with the sampling frequency, the size of the Cobra Probe is of the same order of magnitude as the size of the structures it is measuring. Given a translation speed of the Kelvin-Helmholtz vortices of $U_{KH} = 0.67U$ (Moon et al. 2006), and the size of the Cobra Probe head, l, is 2.6 mm, the frequency, f, associated with vortices matching the size of the Cobra Probe head is as follows:

$$f = \frac{U}{l} = \frac{0.67 \times 20}{0.0026} = 5153 \text{ Hz} \tag{4-3}$$

Thus, the Cobra Probes are sufficient for establishing the presence of fine scale structures and the turbulent decay of the flow, however, their sampling capabilities are not sufficient to characterise these structures, with the size of the Cobra Probes being large compared to the size of any Kelvin-Helmholtz structures.

4.2 Surface Shear Stress Visualisations

Paint droplet visualisation of surface shear stress was performed on the 0° yaw angle FFS case. Photographs of these visualisations are presented in Appendix: *Surface Shear Stress Visualisations –*

Forward Facing Step from Figure 157 through to Figure 163. Based on Sherry et al. (2010) one of the key relationships is between δ/h and the mean reattachment length, X_L. The cases examined and the resulting reattachment lengths are presented in Table 9. These are then compared with results from the literature, shown in Figure 64. A discussion of the flow structure identified through the visualisations is then presented.

4.2.1 Mean Reattachment Length

The results of this study, presented in Figure 64, are presented as ranges, expressing the uncertainty associated with the quantification of X_L, due to the grid method that was used. Data from the current study are in good agreement with Farabee and Casarella (1986), Camussi et al. (2008) and Leclerq et al. (2001). Lower Reynolds numbers in other studies cause the reattachment lengths to be lower than those reported in this study and by other researchers at similar δ/h ratios. The current study investigates a broad range of δ/h ratios, broken up into high turbulence intensity and low turbulence intensity cases and the reattachment lengths generally increase as δ/h values decrease. This is consistent with the theory that at low δ/h values, the highest velocity flow interacts with the crest of the FFS, resulting in greater velocity fluctuations, inducing a larger separation region. The δ/h = 1.35 case does not follow the trend, and the reason for this is not clear.

The delineation between high turbulence intensity and low turbulence intensity cases proved to be useful. Reattachment lengths in the higher turbulence intensity cases are lower than in the low turbulence intensity cases. This is consistent with the work of Hillier and Cherry (1981), Kiya and Sasaki (1983a) and Saathoff and Melbourne (1996) who identified a similar relationship between the size of recirculation bubbles and the inflow turbulence intensity. Unfortunately turbulence intensity profiles were not published for most of the FFS cases in the literature, making the comparison of turbulence intensity with the current study and those in the literature impossible. The current study indicates that the turbulence intensity, alongside the δ/h parameter, is a strong indicator of the mean reattachment length. This is illustrated in Figure 65 where the high turbulence intensity cases all have a smaller mean reattachment length, while the low turbulence intensity cases each have a

larger mean reattachment length. The increased turbulence intensity acts to destabilise the crest vortex, reducing the amount of fluid that it can entrain, resulting in a smaller mean reattachment length.

Table 9: Summary of FFS results.

Boundary layer thickness: δ [mm]	FFS height: h [mm]	Boundary layer to FFS height: δ/h	Turbulence intensity at FFS height: I_h	Mean reattachment length: X_L/h
715	50	14.3	12.3 %	1.90
715	50	14.3	12.3 %	2.20
715	100	7.15	11.9 %	1.90
715	150	4.77	10.8 %	2.17
135	50	2.7	7.55 %	2.60
135	50	2.7	7.55 %	2.40
135	100	1.35	2.55 %	2.38
135	150	0.9	1.21 %	2.84
100	50	2	4.59 %	2.80
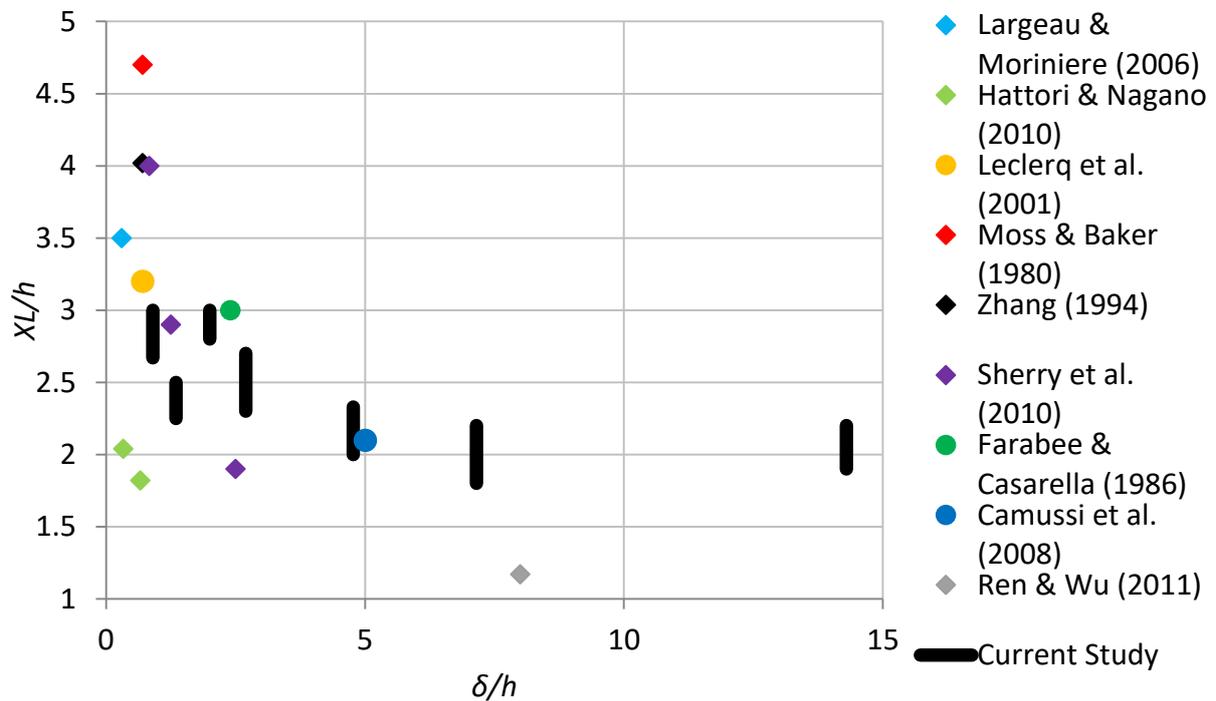
Figure 64: Comparison of 0° yaw FFS cases from this study with other cases in the literature.
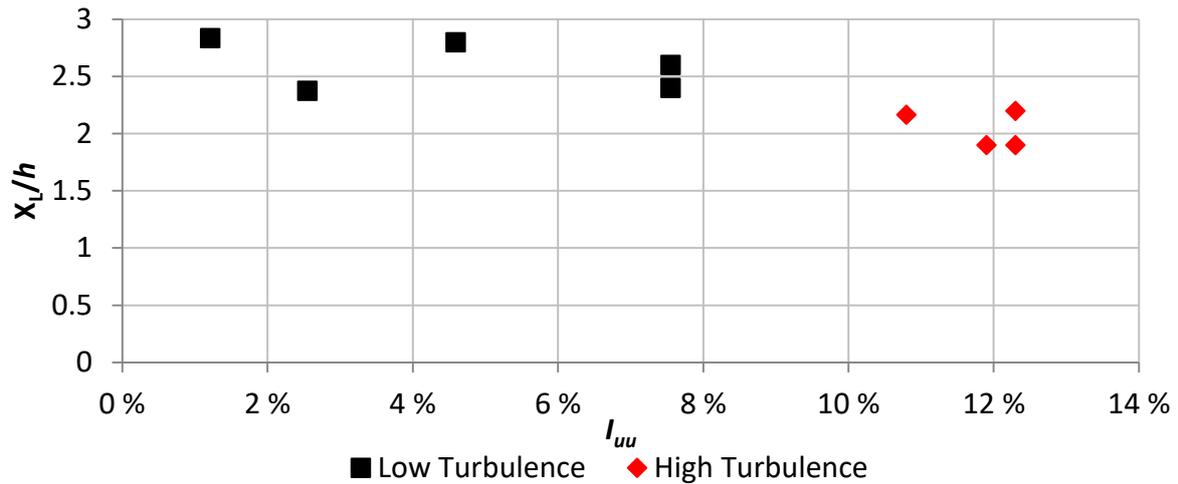
Figure 65: Reattachment length v Stream-wise Turbulence Intensity at cliff height.

4.2.2 Identification of Flow Features from Visualisations

Various researchers identify that, although the FFS is a two-dimensional topography, there are three-dimensional effects evident in the flow, beyond the obvious wall effects.

Castro and Dianat (1983), investigating surface flow topology over rectangular bodies in thick boundary layers at an aspect ratio of 9, observed saddle and node points in their topological analysis over various FFS geometries. They observed a line of symmetry along the model centreline as well as further saddle points relating to the edge effects. Largeau and Moriniere (2007) identified branched structures upstream of their FFS, which provided an inherent three-dimensionality to the flow over the two-dimensional geometry. The branched structures convected downstream over the crest of the FFS as the upstream vortex burst periodically. Largeau and Moriniere (2007) observed that these structures occurred symmetrically, and the number of branched structures related to their length, which was a function of the aspect ratio.
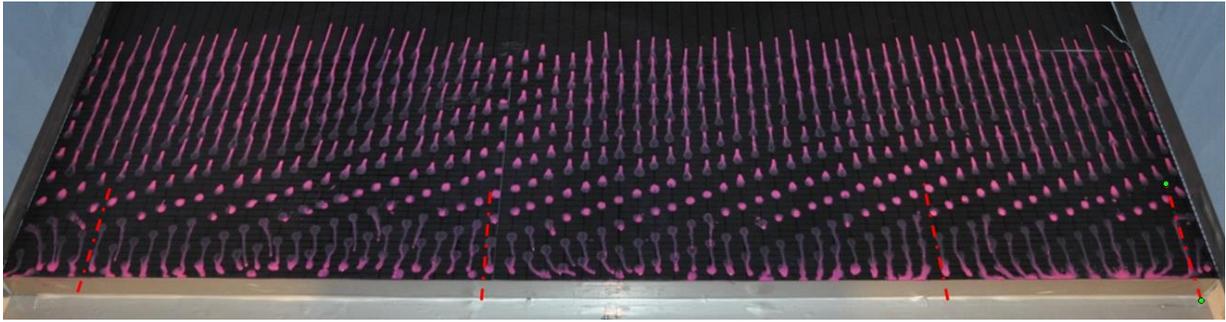
Figure 66: Surface shear stress visualisation of flow over a 50 mm FFS with δ/h = 2.7. Flow is from bottom to top. The cellular structure is highlighted with the red dashed lines.

Cell divisions were evident in the current study within the recirculation region and are highlighted by the red dashed lines in Figure 66; however the cellular division is more arbitrary in the example shown, with no cell boundary evident along the tunnel centreline. Other cases in this body of work exhibited cell boundaries closer to the tunnel centreline and fewer cells. In the work of Castro and Dianat (1983) and Largeau and Moriniere (2007) the flow tended to funnel towards the centre of the crest, which is similar to what was observed in the current work, though rather than converging on the centre of the crest, flow converged on the centre-line of each of the cells, as seen in Figure 66.

The clear distinguishing feature of the current work compared to the other researchers is the distinct cells that are formed. Two differences in methodology are evident: first, the presence of end-plates; and second, the use of higher aspect ratio in the current work. The lower pressure associated with the voids on either side of the models without endplates and the subsequent drainage flow induces the formation of an unstable node at the centre of the FFS. However, in the current research, rather than observing a line of symmetry, semi-regular cells are observed. These semi-regular cells were unable to occur in the work of Largeau and Moriniere (2007) and Castro and Dianat (1983) due to the unconstrained nature of the flow, which fails to imitate the constrained nature of an infinite step. While they were able to achieve a region through the centre of the flow where the end-effects were negligible, the aspect ratio of 9 used by Castro and Dianat (1983), and the aspect ratios between 9 and 15 used by Largeau and Moriniere (2007) were insufficient to allow span-wise structures to fully develop. This same criticism holds for the larger cliff heights used in this work,

131

particularly for the h = 150 mm cases, where the aspect ratio was only 13.3. The case in Figure 66 had an aspect ratio of 34. The largest cell in that experiment was 13h across, while the smallest was just under 7h across (excluding edge effects). Thus to capture the developed flow over an FFS imitating infinite aspect ratio, an aspect ratio of 10 is insufficient.

4.3 Summary

The straight-edged non-yawed FFS case has been analysed in the literature over a number of years and there is a general consensus on the flow structure over the FFS. Relationships between the geometric and flow properties have been identified, but the precise interactions have not been quantified. That is, the size of the recirculation region, measured through the proxy of the mean reattachment length, is known to vary with Reynolds number and with the boundary layer to step height ratio. But given a set of inflow conditions and a FFS, the ability to predict the size of the recirculation region remains based on "rule-of-thumb" estimates. The work presented in this section provides further support for those estimates, with speed-up, changes in turbulence intensity, Reynolds Stresses and flow topology all demonstrating common features with the analyses presented in the literature. Comparisons of speed up and turbulence intensity development with the wind tunnel tests of Bowen and Lindley (1977) and field measurements of Mann et al. (2012) and development of Reynolds Stress with Ren and Wu (2011) both provided reasonable quantitative agreement, despite differences in methodology between the experiments. The development of reattachment length as a function of δ/h also demonstrated consistency between this experimental work and that presented in the literature.

The presence of coherent structures was inferred from the correlation analysis, with a vortex being shed off the crest, resulting in a strong lateral correlation of stream-wise velocity in the region immediately downstream of the crest, corresponding with the region between the crest and the mean reattachment line. However, downstream of this, a region close to the surface of high lateral correlation persisted. While not as highly correlated as the crest vortex, the correlation indicated the presence of a coherent structure emanating downstream and slowly weakening. This flow structure

is consistent with the flow dynamics described by Kiya and Sasaki (1983b), where they described the entrainment and periodic shedding of the vortices. The shedding frequency of the vortices ejected from the recirculation region was also observed to be in agreement with that documented by Camussi et al. (2008).

A lateral structure was also identified in the surface visualisations. The width of these cell structures indicated that the aspect ratio of 10 recommended in the literature is insufficient to capture these three-dimensionalities.

Additionally, it was proposed that the turbulence intensity at the height of the crest of the FFS might prove to be a useful indicator of the size of the recirculation region, particularly in the context of wind turbine siting, where the boundary layer thickness is difficult to determine. It was noted that the turbulence intensity at cliff height was rarely documented in the literature. However, the proposed approach is similar to that used in AS/NZS1170.2, where the height of the building is used as a reference height.

The results presented in this section provide the foundation for the topographical developments that were examined in this research program. The level of agreement between these results and the published literature indicate that the methodology employed is sound. This gives confidence in the novel cases that have been examined, which cannot be compared with pre-existing literature.

5. Yawed Flow

This research focussed on the adjustment of the yaw angle, first in the low turbulence intensity

cases, covering a range of δ/h values from 0.9 to 2.7. The analysis identifies the changes to X_L as a

function of θ and δ/h, providing insight into the physical understanding of the flow processes. A

similar analysis examined the effect of inflow conditions comparable to an atmospheric boundary

layer, which more closely models real-world conditions. In these cases δ/h values are in the range

4.77 to 14.3. A comparison is made between the low and high turbulence intensity cases.

In addition to the flow visualisations, Cobra probe measurements were made above a FFS with a δ/h

value of 2, for θ = 0°, 20°, 30°, and 40°. To determine the optimal siting of wind turbines from a wind

resource perspective, maximum energy output needs to be balanced against wind turbine life-span

and wind turbine component life-span. Flow speed-up, turbulence intensity, pitch and yaw are

mapped to determine optimal siting regions. Additionally, the location and development of coherent

structures are shown.

In addition to providing insight into flow over FFSs that are more broadly applicable to wind turbine

siting than merely the 0° yaw case, the yawed flow experiments – in particular the Cobra probe

measurements – provide limiting cases for the ruggedness modelling presented in Chapters 6 and 7.

The yawed FFS cases provide fully developed half spans of sawtooth geometry, providing a gauge of

the vertical extent of the vortex structures.

5.1 Surface Shear Stress Visualisation Results

Photographs of results from surface shear stress visualisations are presented in Appendix: *Surface*

Shear Stress Visualisations – Yaw. The effect of yaw angle is broken down into the low turbulence

intensity cases and the high turbulence intensity cases. The comparison between the two regimes is

shown in Figure 67. The low turbulence intensity cases are shown in the left pane; the high

turbulence intensity cases are shown in the right pane. For each graph, comparisons can be made

based on values of δ/h. Comparisons between the two panes, however, need to be considered in

terms of a combination of both the turbulence intensity and δ/h.
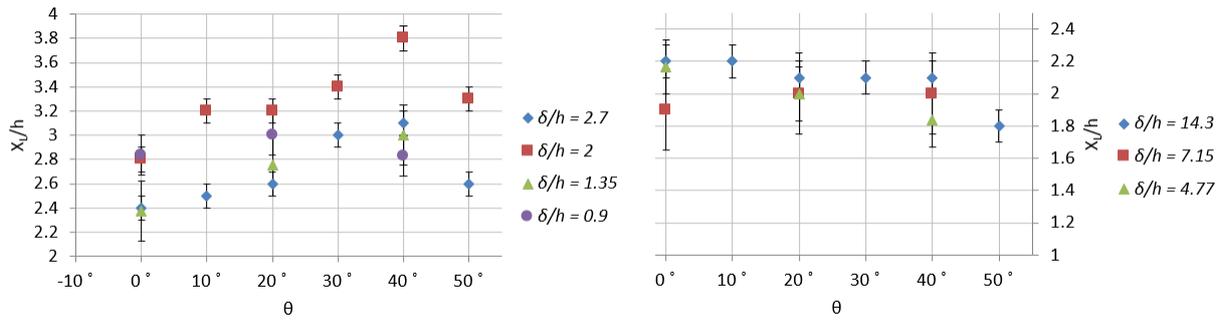
Figure 67: Mean reattachment length as a function of yaw angle for a range of δ/h ratios. Low turbulence intensity cases are shown in the left-hand pane; high turbulence intensity cases are shown in the right-hand pane. Note the difference in scale between the two plots in the X_L/h axis.

Considering first the low turbulence intensity cases, the δ/h = 2 and δ/h = 2.7 cases were sampled at 10° increments and a consistent trend of increasing X_L with increasing θ is observed. Beyond θ = 40°, a threshold appears to be exceeded, and X_L reduces sharply. The δ/h = 1.35 case exhibits a similar trend in X_L with increasing θ, albeit without an observable threshold, as the highest value of θ was 40° in this case. This trend indicates that the lateral flow along the crest increases the stability of the vortex, up to a critical yaw angle.

In addition to X_L, the visualisations give the direction of the surface shear stress lines. This is illustrated in Figure 68. The angle these lines make with the stream-wise direction is Ω, which varies linearly as a function of θ, as shown in Figure 69. Taking two theoretical points, the first at θ = 0°, the second at θ = 180°, the expected values of Ω are 180° and 0° respectively, corresponding to recirculation in the opposite direction of the free-stream flow in the first case, and no recirculation as the crest of the step is aligned parallel to the free-stream flow. Assuming a linear fit between the two theoretical points implies that Ω = 180 - 2θ. However, best fit for the data points resulted in the empirical relationship Ω = 180 - 2.4θ. This relationship was consistent across the low and high turbulence intensity cases. Extrapolating the observed data, the empirical relationship implies an earlier transition to a new topology, that is, as the yaw angle approaches θ = 75°, rather than at θ = 90°, when the theoretical change in topology was first anticipated.

The reduction in Ω with increased θ demonstrates that the orientation of the surface shear stress lines associated with the crest vortex are determined by a balance between the low pressure

135

generated by the crest separation and the dynamic pressure associated with the free-stream flow. Thus, there is a critical θ where the surface shear stress lines change from having a counter-stream-wise component (the most extreme case being the recirculation in the θ = 0° case) to no counter-stream-wise component, immediately before θ = 40°. At θ ≈ 40°, the low pressure from the flow separation balances against the pressure driven by the free-stream velocity, resulting in only a lateral component to the flow.

Lateral segmentation was observed in the recirculation region for θ = 0°, as previously established in the validation studies. By θ = 10°, this cellular structure in the recirculation region has broken down. However, Figure 70 shows there is a new cellular structure evident in the θ = 40° and θ = 50° cases, downstream of the separation region. The streaks delineate distinct regions where the surface shear stress is aligned at an angle of 13° to the direction of the free-stream flow from the regions where the flow is aligned at an angle of 0° to the free-stream flow. The orientation of the streaks indicates that the vortex propagating downstream in these regions is of the same sign as the primary vortex developed at the crest of the FFS. This implies that the vortex generated at the crest of the FFS detaches from the crest and propagates downstream as a coherent vortex structure. A new structure then begins to develop from the detachment point. The mean flow topology demonstrates the detachment and is presented in Figure 71. Because this observation was made in a time-averaged field the separation region appears to be a continuous structure along the length of the crest. The observable presence of the detachment in the flow visualisations indicates that there is a stable spatial periodicity in the detachment and shedding downstream of the primary vortex structure. The same spatial periodicity was not observed in the high turbulence intensity cases, indicating that the mean spatial periodicity is broken down by the increase in turbulence intensity.
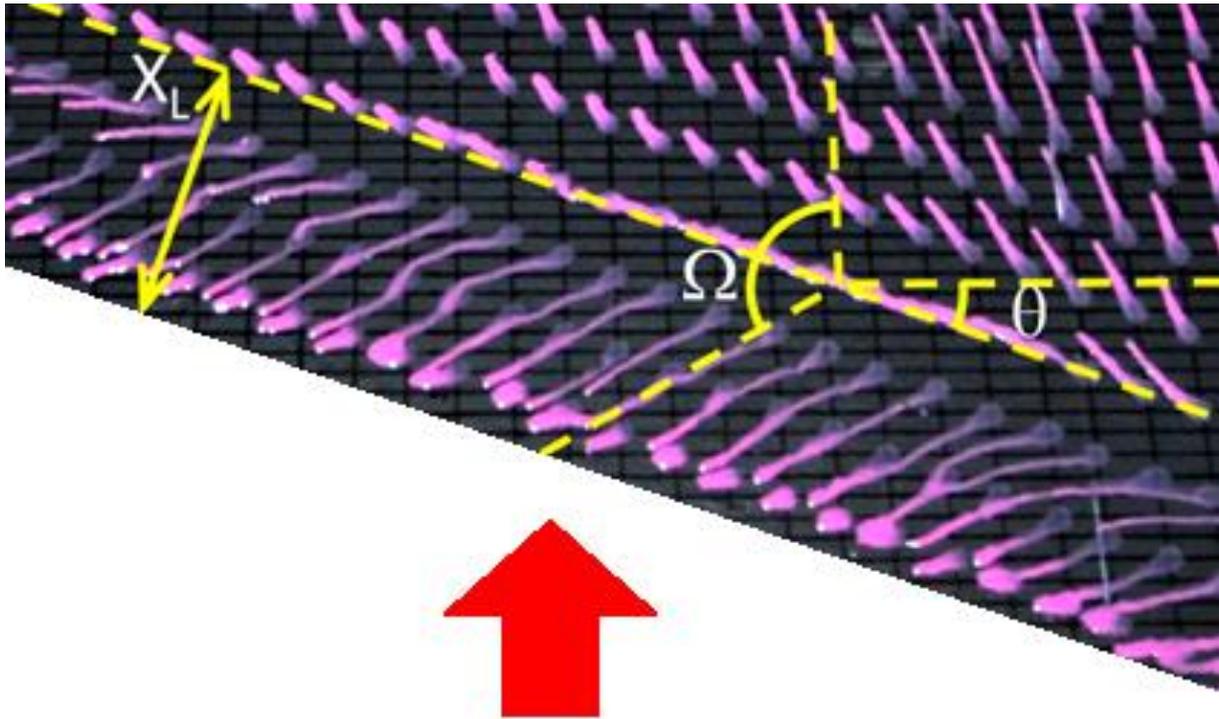
Figure 68: Angle at which vortex acts against surface, *Ω*, shown on a yawed FFS with paint droplet surface shear stress visualisation. Free-stream flow direction shown by red arrow; yaw angle denoted by θ; and reattachment length shown as *X$_L$*.

The high turbulence intensity cases, whose *X$_L$* values are plotted in the right-hand pane of Figure 67, exhibit weaker dependence on θ than the low turbulence intensity cases. In two of the three *δ/h* cases, a small reduction in *X$_L$* is observed, but the reduction is of a similar order to the magnitude of the uncertainty.

Each of the high turbulence intensity cases has smaller *X$_L$* values than the low turbulence intensity cases, as can be seen in Figure 67. Sherry et al. (2010) identified that the elevated levels of turbulence intensity associated with the lower portion of the boundary layer in the inflow leads to increased mixing between the free-stream flow and the recirculation region, driving reductions to *X$_L$*. While Sherry et al. (2010) applied this logic to the increase in turbulence intensity associated with the bottom portion of the inflow boundary layer, the same logic holds for turbulent inflow cases, such as the atmospheric boundary layer, where turbulence intensity levels in excess of 5% are observed at altitudes above 500 m (AS/NZS 2011). The reduced momentum and stronger vertical

shear at the step height at δ/h values greater than unity, as originally identified by Sherry et al.

(2010), compounds the effect.

The spatially periodic shedding that was observed through the surface shear stress visualisations in the low turbulence intensity inflows was not evident in the high turbulence intensity inflow cases. The increased turbulence intensity was the likely cause of the breaking down of the spatial periodicity.
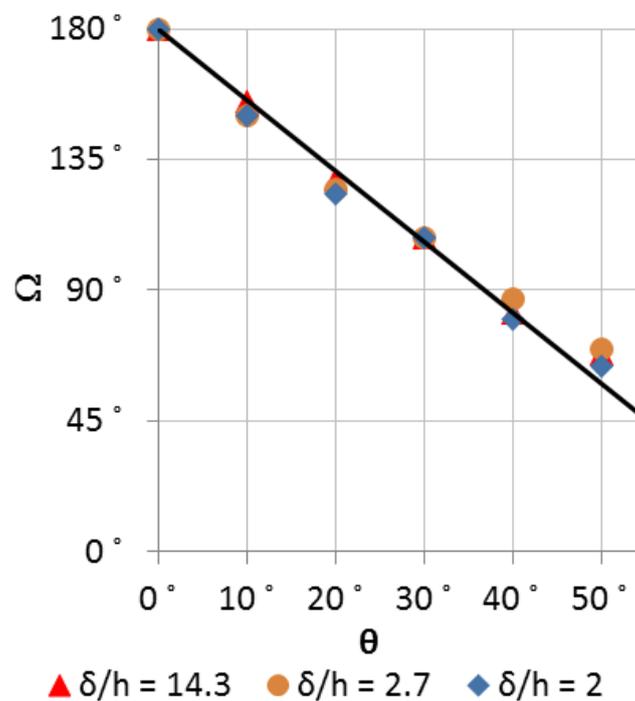
Figure 69: Direction of surface shear stress as a function of yaw angle. Black line corresponds to linear trend line.

Additionally, the end effects that were expected due to the lateral drainage, and presented diagrammatically in Figure 9, were clearly observed. Photographs from the θ = 30°, δ/h = 2 case are presented in Figure 72 and Figure 73. The region of flow accumulation associated with high pressure and low flow resulted in the accumulation of paint and short streaks, as shown in Figure 72. In contrast, the longest streaks were observed along the upstream edge, as shown in Figure 73.
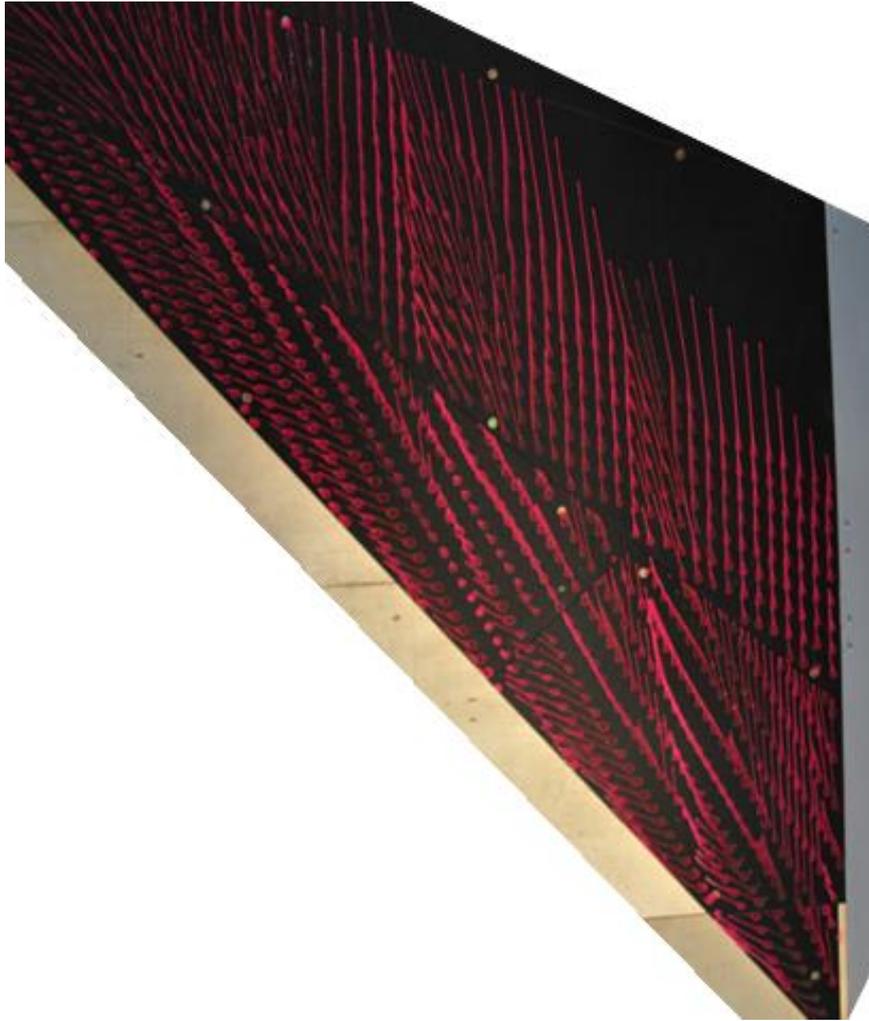
Figure 70: θ = 50°, *δ/h* = 2 case, showing the segmentation downstream of the separation region. Flow is from bottom of page to top of page.
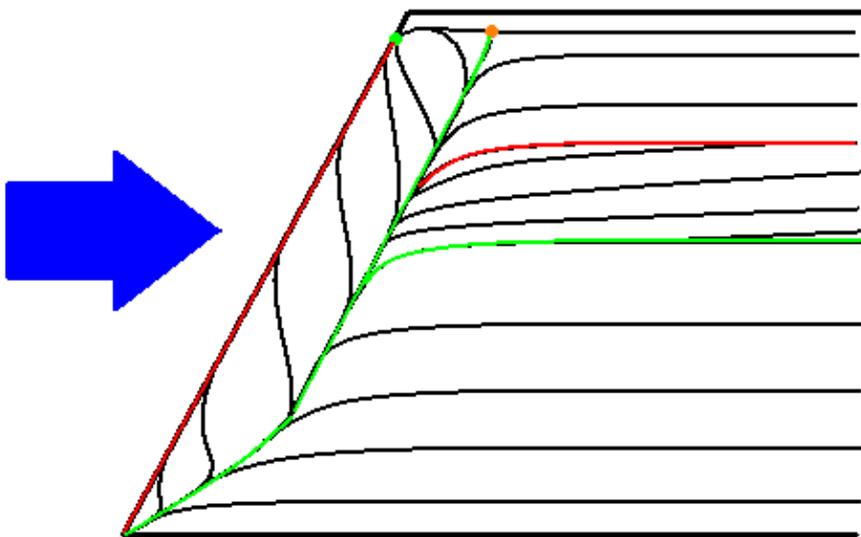
Figure 71: Topological skeleton for flow over a yawed FFS. Positive bifurcation lines are shown in green; negative bifurcation lines are shown in red. Saddle point indicated with an orange dot. Stable node indicated by green dot. Free-stream flow direction indicated by blue arrow. The skeleton presented here does not represent the number of segments observed in the actual experiments.
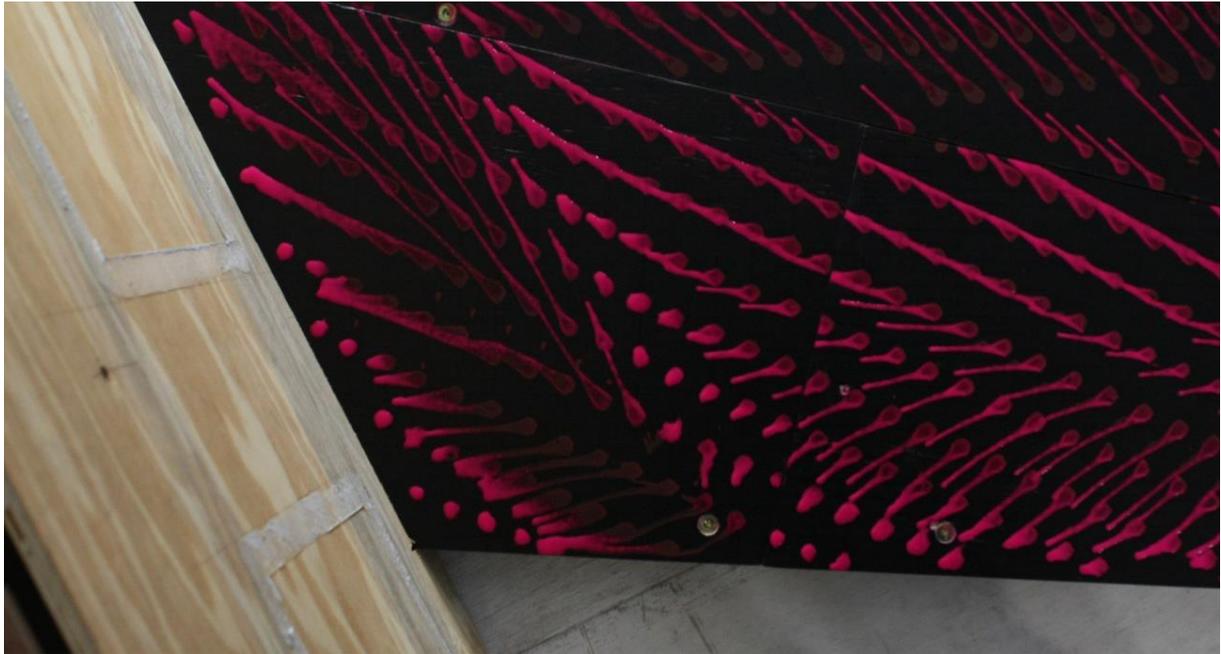
Figure 72: Flow accumulation, low flow, high pressure region at the downstream edge of the FFS, in the θ = 30°, *δ/h* = 2 case.
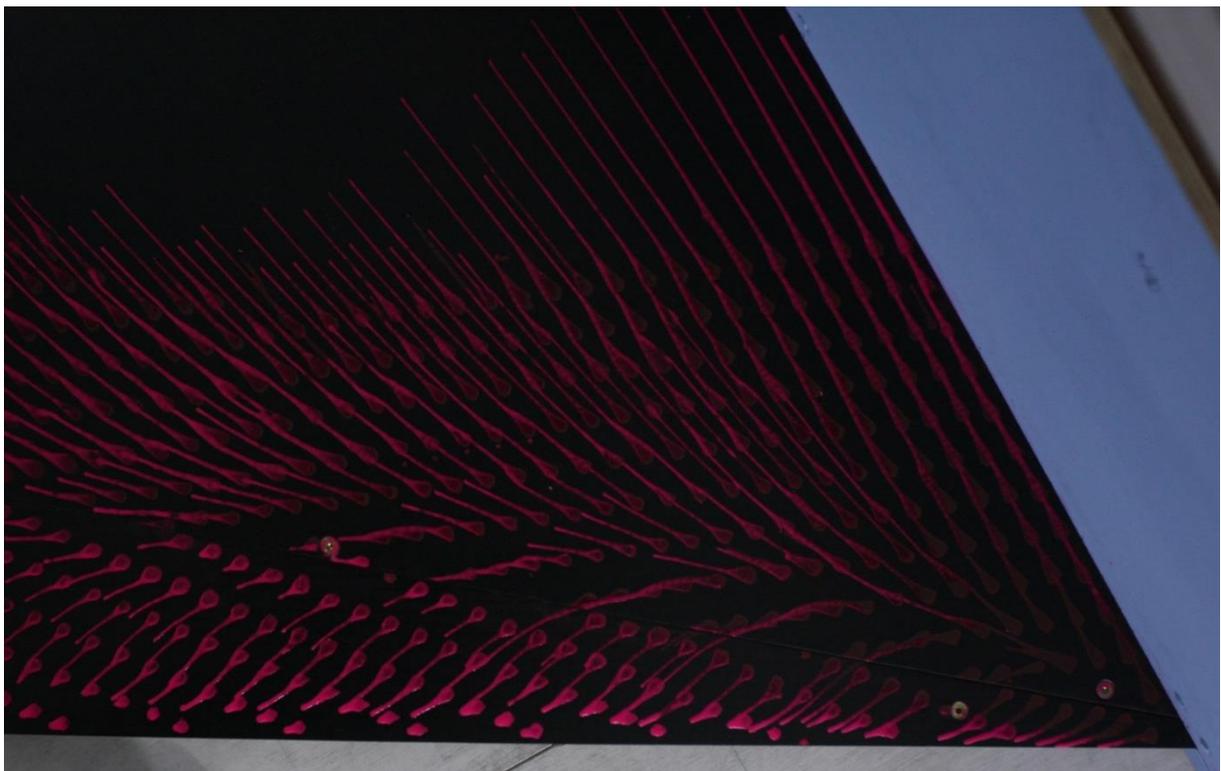
Figure 73: High flow, low pressure region at the upstream edge of the FFS, in the θ = 30°, *δ/h* = 2 case.

5.2 Cobra Probe Data

The results of the Cobra Probe measurements are presented in the following series of figures,

mapping mean speed-up, turbulence intensity ratio, pitch, yaw, and cross-correlation statistics for

four yaw angles: 0°, 20°, 30°, and 40°. A single step height and inflow were considered: the second

low turbulence intensity inflow case (Configuration 3, as described in Section 3.3.1 *Three Wind Tunnel Configurations*), and a step height, h = 0.050 m. Data were sampled at 5000 Hz, and down-sampled to 2500 Hz, for 180 s. This configuration was selected to maximise the difference between the low turbulence inflow and the coherent structures that are generated off the topography.

As shown in Figure 74, two sets of Cartesian co-ordinate systems are used. The global co-ordinate system relates to the orientation of the wind tunnel: x is the direction of the freestream flow, y is the direction perpendicular to the freestream flow, parallel to the ground plane, and z is the vertical direction. The magnitude of the wind speed is denoted by U, while the velocity fluctuations from the mean in the x, y, and z directions are u, v, and w, respectively. The local co-ordinates are based on the orientation of the FFS: x' is the direction perpendicular to the crest of the FFS, y' is the lateral direction along the crest of the FFS, and z' is the vertical direction, the same orientation as z.
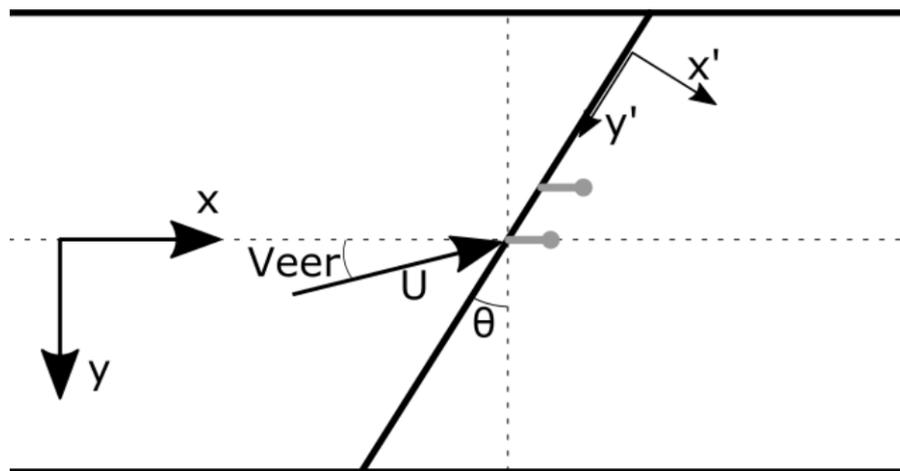
Figure 74: Plan view illustrating orientation of the co-ordinate systems. The orientations of the probes are shown in grey. The heads are facing in the x direction, but aligned laterally, parallel to the crest in the y' direction.

The probes were spaced 50 mm apart in the y' direction and their heads were aligned parallel to the crest of the FFS, whilst facing in the $-x$ direction. The orientation and spacing of the probes are shown on the right in Figure 74.

Speed-up, S, is visualised in Figure 75, and is defined according to Equation 4-1 and presented here again:

$$S = \frac{U(x',z')/U_P}{U_{BL}(x=0,z)/U_{P,BL}} \qquad (5\text{-}1)$$

$U(x',z')$ is the magnitude of the velocity vector at a point *(x',z')*, according to the previously defined

Cartesian co-ordinate system. U_P is the magnitude of the velocity vector measured at the up-stream

Pitot-Static tube, measured concurrently to *U(x',z')*. The Pitot-Static tube was located greater than

55*h* upstream of the centre of the crest of the FFS, 12.3 boundary layer heights above the surface of

the false floor. $U_{BL}(x=0, z)$ is the magnitude of the velocity vector in the undisturbed boundary layer,

that is, without the model in place, at *x* = 0. $U_{P,\ BL}$ is the magnitude of the velocity vector measured at

the up-stream Pitot-Static tube, measured concurrently to $U_{BL}(x=0, z)$.

Maximum speed-up in each of the cases occurs between the crest and 2*h* downstream and above

0.5*h* from the surface of the FFS, decreasing gradually with height. As the yaw angle increases, the

maximum speed-up is decreased, and the region where the speed-up is greater than one is also

decreased. This is illustrated by the contour lines presented in the colour maps of Figure 75, and the

vertical profiles presented for *x/h* = 0.5 in Figure 76.

Baker's hypothesis is that only the component of the flow perpendicular to the FFS is accelerated.

This assumption comes out of linear theory, which assumes simple terrain. Nevertheless, linear

theory is the basis of various commercial wind energy analysis packages, which are inevitably

applied to complex terrain. Thus, a comparison can be made with modelled estimates based on the

θ = 0° case with the actual speed-up measured at θ = 20°, 30°, and 40°. The predicted speed-up, S_{Pr},

based on Baker (1985) and Lubitz and White (2007), is shown below:

$$S_{Pr}(\theta) = \sqrt{S_0{}^2 \cos^2(\theta) + \sin^2(\theta)} \qquad (5\text{-}2)$$

In this equation, S_0 is the speed-up at θ = 0°. Thus, the deviation of the model from the measured

data is expressed as a percentage in the colour plots in Figure 77, according to the following

equation:

$$Variation = \frac{S_{Pr}(\theta) - S(\theta)}{S(\theta)} \times 100\% \qquad (5\text{-}3)$$

The deviation observed occur predominantly in the recirculation region and the shedding downstream of the recirculation region. These regions are associated with the well-documented problem of Cobra Probe measurements being subjected to reversed flow (see Appendix: *Performance of Cobra Probes in Recirculating Flow*). As the yaw angle is increased, the downstream region of over-prediction increases in size, in particular, the region of increased error widens in the vertical dimension. The 5% deviation contour is shown in the colour plots in Figure 77. In the θ = 20° case, the contour begins to decay at *x/h* = 4, and never reaches above 0.5*h* above the surface. At θ = 20°, the contour shows no sign of decay, and continues steadily downstream. By θ = 40° the 5% deviation contour continues to gain height through to the farthest downstream measurement plane at *x/h* = 10.

Thus, as yaw angle is increases, the deviation between the measured speed-up and the speed-up predicted by Baker's hypothesis, increases. However, the key area of interest is the bubble-like region where the greatest speed-up is observed. This area, which grows above the recirculation region through to 1.5*h* downstream in each case, exhibits consistent deviation, with the modelled data within 5% of the measured data.

Similar to *S*, the change in turbulence intensity, visualised in Figure 78, is expressed as a turbulence intensity ratio, and defined according to the following equation:

$$\text{TI Ratio} = \frac{I_{uvw}(x,z)}{I_{uvw,BL}(z)} \qquad (5\text{-}4)$$

I$_{uvw}$(x,z) is the turbulence intensity based on the three velocity components, with the BL subscript and the (*x,z*) location having the same meaning as in Equation (5-1). The region of highest turbulence intensity, as shown in Figure 78, is the recirculation zone for all yaw angles examined. Beyond the recirculation region, vortices are still ejected downstream. These vortices gradually weaken, resulting in a reduction of the turbulence intensity ratio. However, the turbulence intensity, even

10h downstream, is in the order of two to three times that measured in the inflow conditions up to a height of 1.5h above the surface, which is consistent with the ejection and diffusion of those vortices.
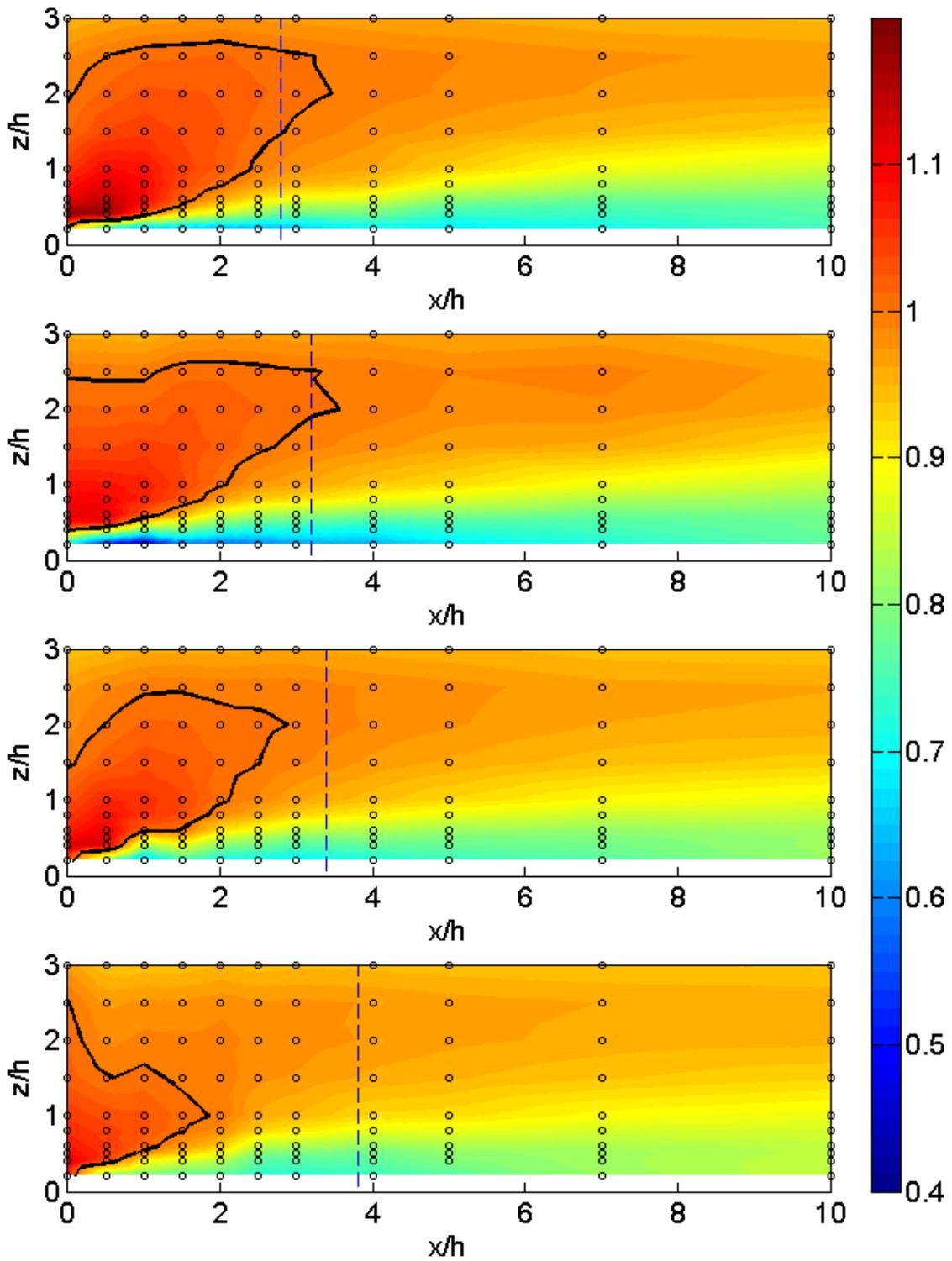
Figure 75: Map of speed-up down-stream of crest of FFS, as defined by Equation 5-1. From top to bottom, yaw angle is 0°, 20°, 30°, and 40°. Black circles represent measurement locations. Black trace represents $S = 1$ contour. Blue dashed line represents the mean reattachment length.
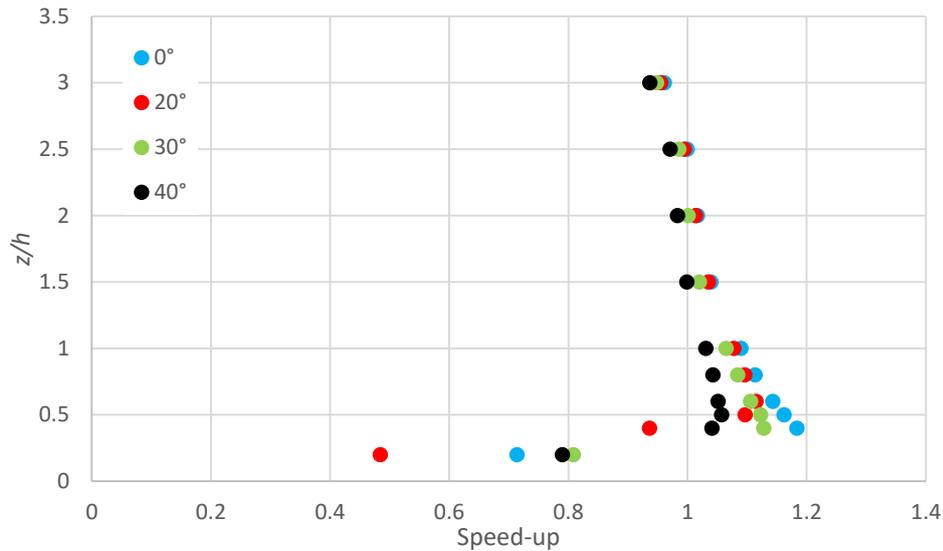
Figure 76: Vertical profiles of speed-up at _x/h_ = 0.5 for different yaw angles.

Wind veer, which results in yaw misalignment and imbalanced loads on wind turbine rotors, is

plotted in the colour plots in Figure 79, superimposed with a quiver plot depicting the pitch angles.

Contours representing a pitch angle of 8° are traced in red, while contours representing yaw angles

in excess of 10° are traced in black. Ideally, wind turbines are not subjected to large pitch angles, or

variations in yaw angle as a function of height above the ground. The primary standard used in the

wind energy industry to certify wind turbines is IEC61400-1 (2005), which requires that wind

turbines be capable of operating for inflows with pitch angle up to ±8°. At the crest and through the

recirculation region, the pitch falls outside of this design envelope in each model. However, in each

case, the measurements taken at $0.5h$ downstream of the crest, for $z > 0.5h$, were within the range

of $0° - 4°$.

145
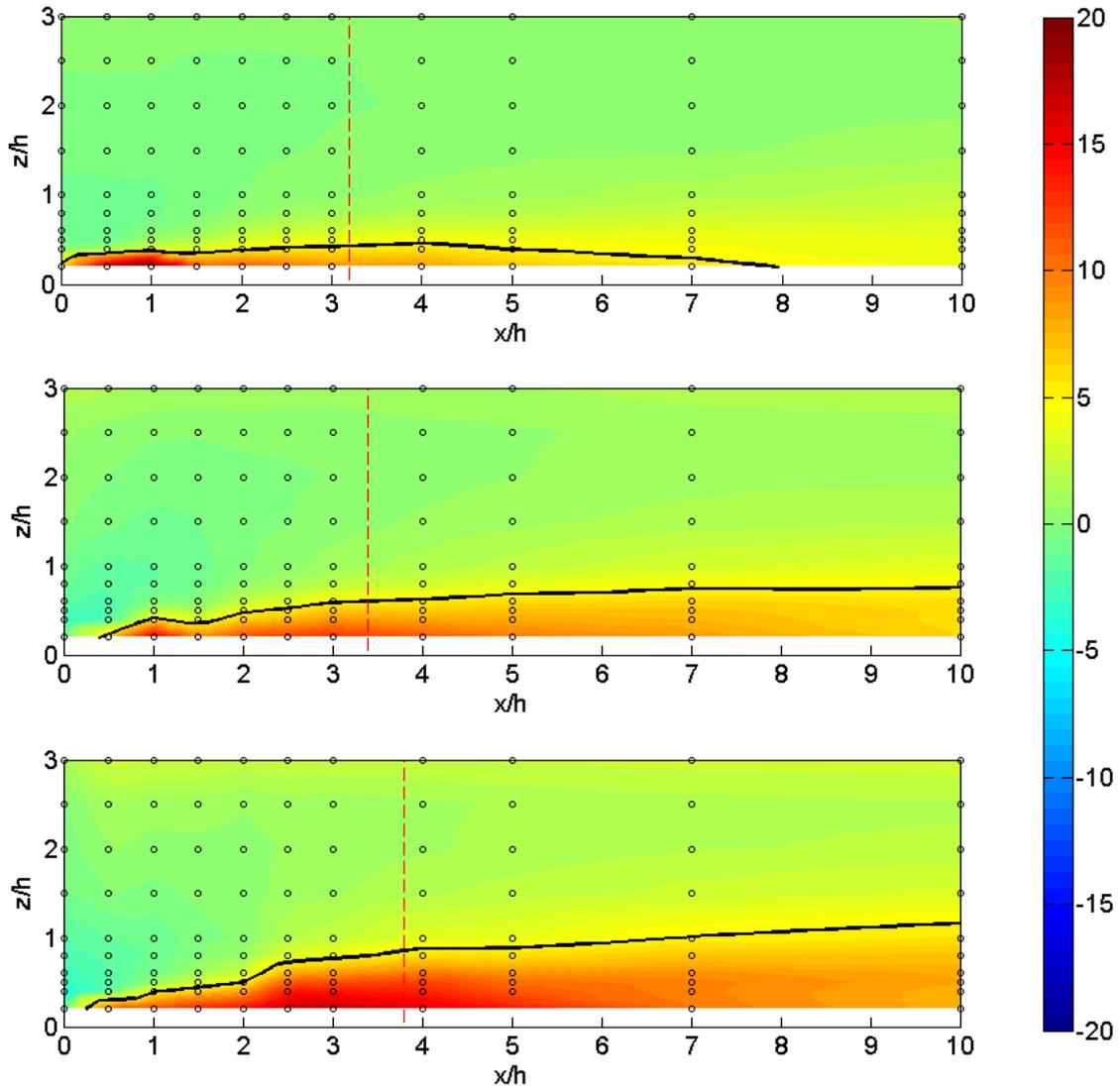
Figure 77: Comparison of speed-up with Baker's hypothesis. Variation expressed as a percentage, as describe in Equation 5-3. Model over-prediction is positive; model under-prediction is negative. Black circles represent measurement locations. Yaw angle, from top to bottom is 20°, 30°, and 40°. Black trace represents 5% error contour. Red dashed line represents the mean reattachment length.

The measured veer angle and its variation with height above the surface prove to be an issue

through the recirculation region, where speed-up is low, turbulence intensity is high and pitch angle

is high. In the wake region beyond the recirculation bubble, the veer remains significant. The region

up to 0.5h above the surface undergoes a veer of greater than 10°, which can be seen in the 20°, 30°,

and 40° models.

Figure 80 presents biased cross-covariances from the two traversing Cobra Probes. This means that

the cross-covariance is normalised by the number of samples in the signal. As described in Section

4.1.3 *Correlation Analysis*, the bias reduces asymptotically as the number of samples approaches

infinity (Orfanidis 2007). Given that the signals can be considered to be stationary, a 180 s sample length at 2500 Hz provides sufficient samples for the bias to be considered negligible. Within the recirculation region near the crest of the FFS there is clearly an increased correlation between the two Cobra Probes relative to the free-stream flow, independent of yaw angle.

However, this increase in correlation persists through to the last plane of measurement downstream in each case. This demonstrates, as Kiya and Sasaki (1983b) established, that the separation bubble entrains fluid until it bursts, giving the separation bubble a flapping appearance. The bursting separation bubble sheds a vortex down-stream, resulting in the increases in turbulence intensity and reduction in speed-up through the downstream region.

Increased yaw angle resulted in an increased size in the regions of correlated flow, and an increase in the magnitude of the correlation, for all the yaw angles tested. At $\theta = 0°$, the cross-covariance values decay rapidly from the high correlations associated with the separation region, though increased levels of correlation persisted through to the farthest downstream plane. By $\theta = 20°$ the reattachment length increased from the $\theta = 0°$ case, and the regions of increased cross-covariance are clearly visible around the mean reattachment line. From $\theta = 20°$, the size of the correlation region remains almost constant, as evidenced by the cross-covariance = 1 contour presented in each of the plots in Figure 80. However, the magnitude of the correlation continued to increase.
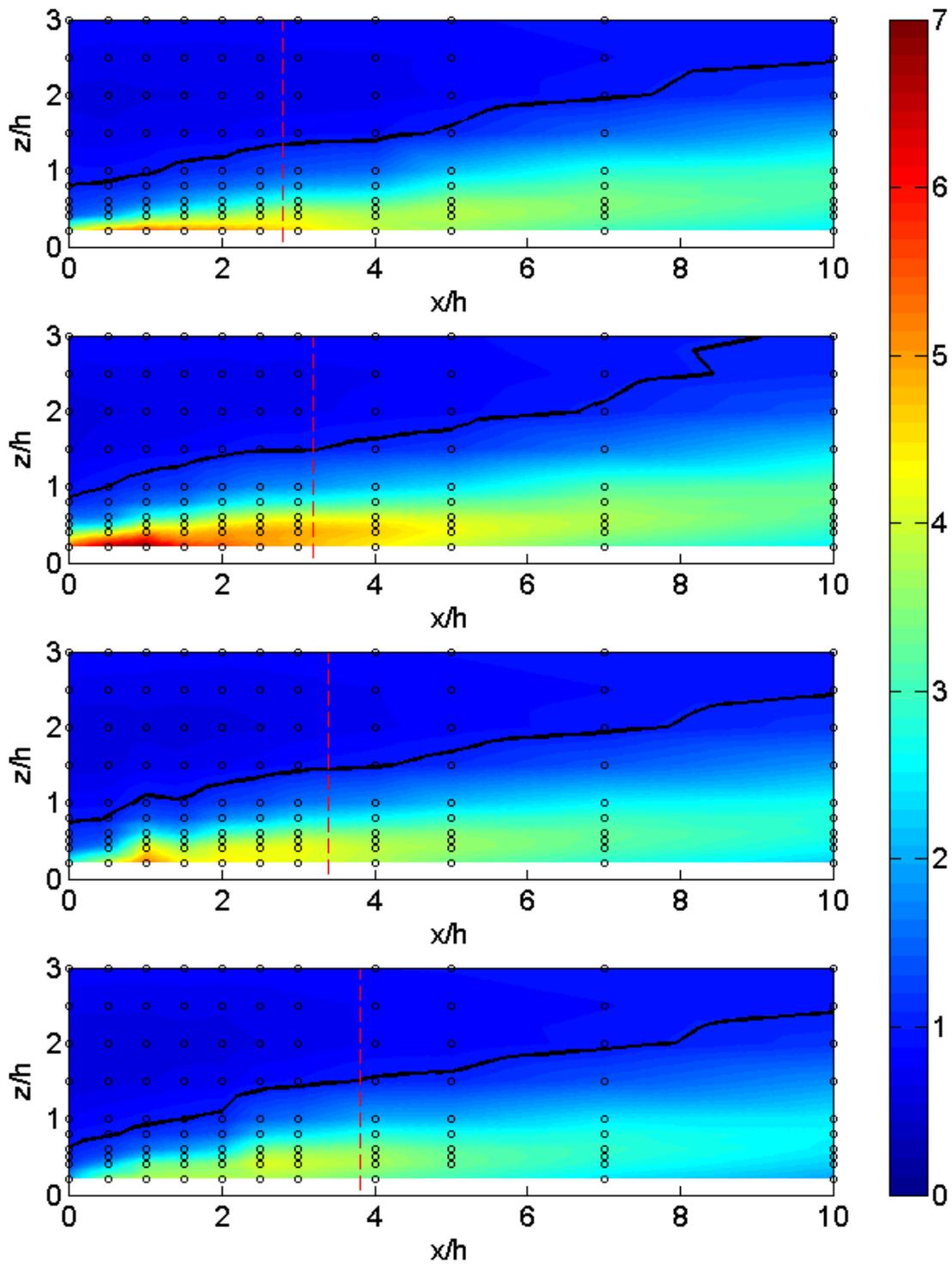
Figure 78: Map of turbulence intensity ratio down-stream of crest of FFS, as defined by Equation 5-4. From top to bottom, yaw angle is 0°, 20°, 30°, and 40°. Black circles represent measurement locations. Black trace represents TI Ratio = 1 contour. Red dashed line represents the mean reattachment length.
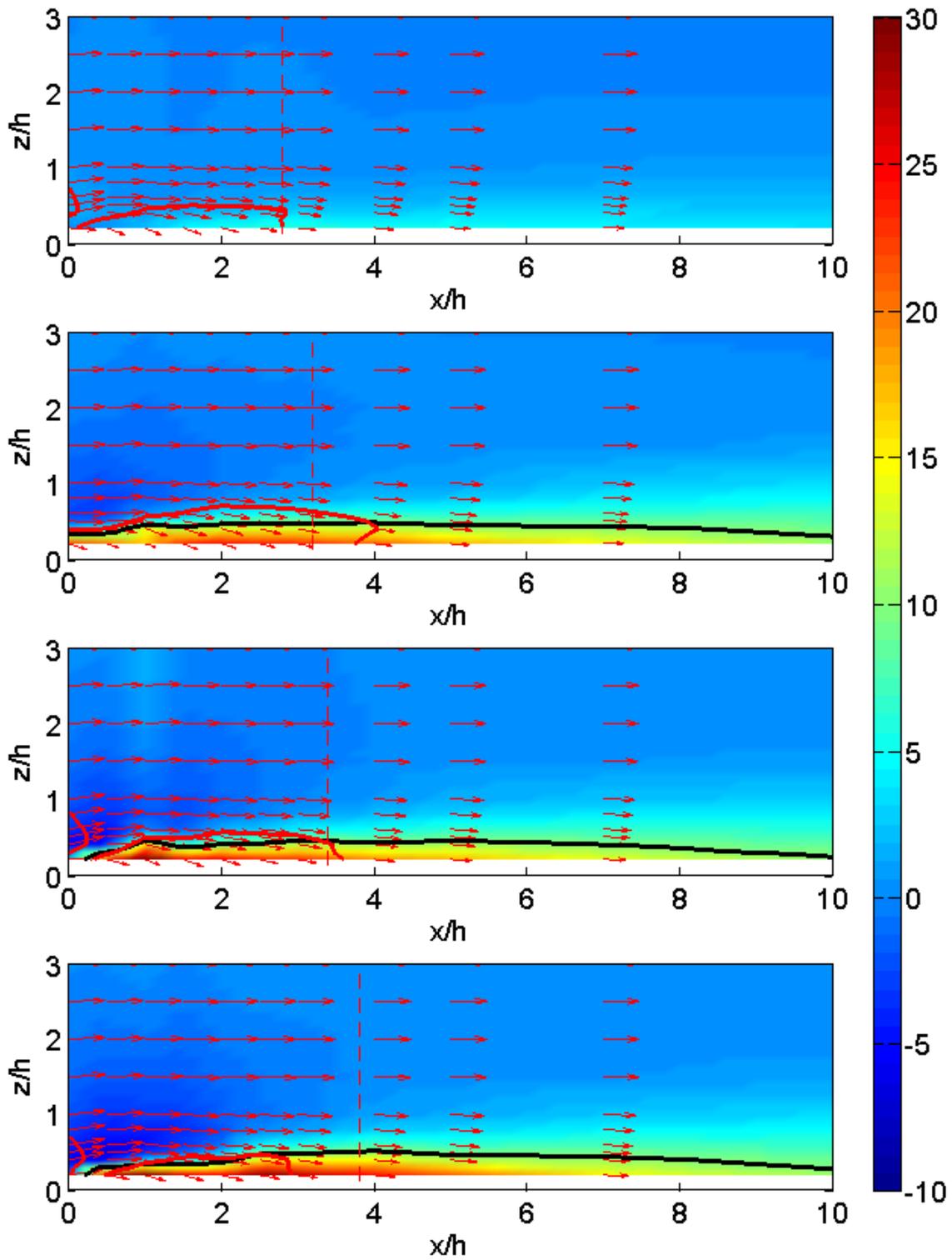
Figure 79: Map of flow veer angles down-stream of crest of FFS, superimposed with quiver plot of pitch angles. Yaw angle from top to bottom is 0°, 20°, 30°, and 40°. Black trace represents veer angle = 10° contour. Red trace represents pitch angle = 8° contour. Red dashed line represents the mean reattachment length.
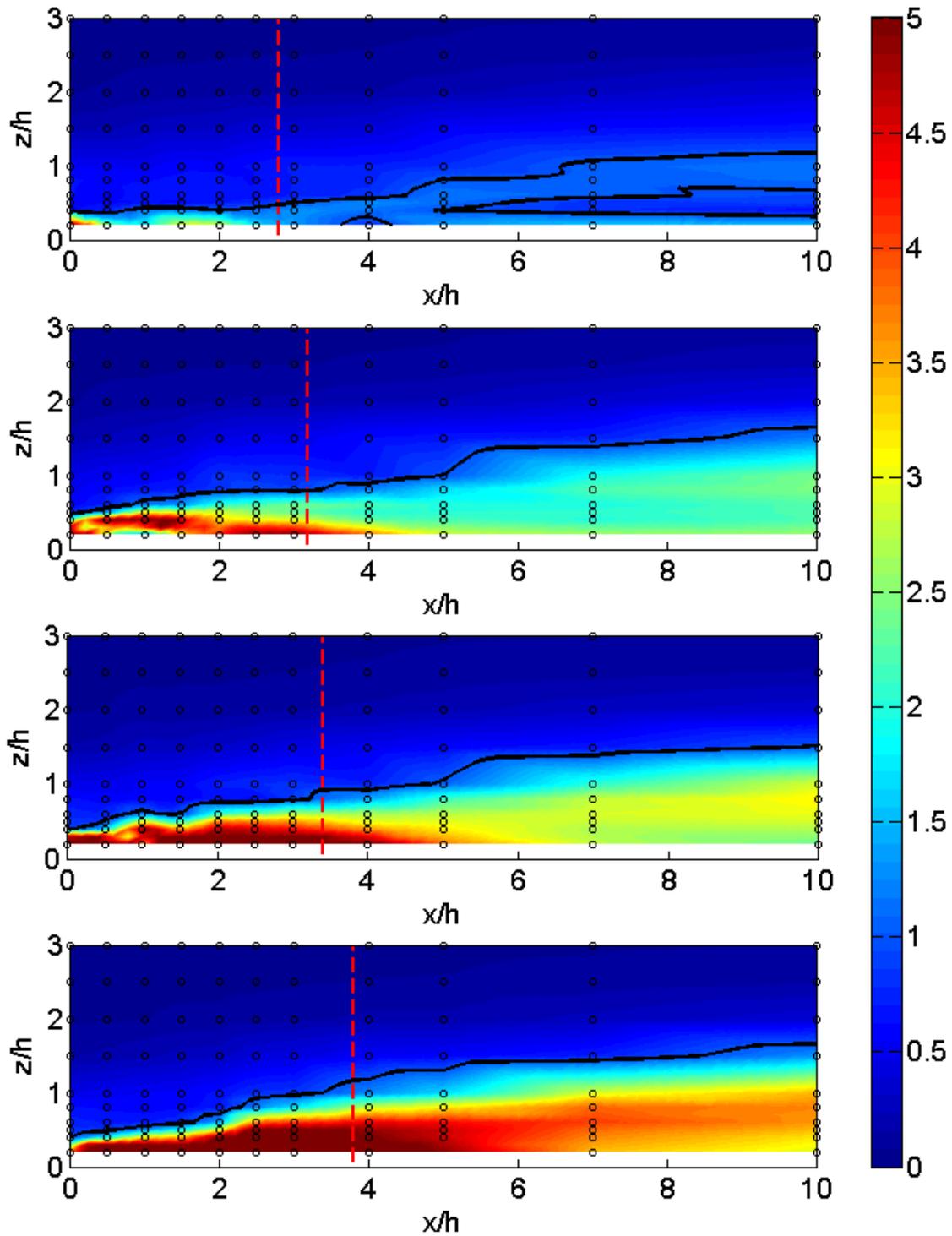
Figure 80: Plot of the biased cross-covariances between two probes traversing *h* = 50 mm apart in the y-direction over an FFS. From top to bottom, yaw angle is 0°, 20°, 30°, and 40°. Black circles represent measurement locations. Vertical red dashed lines represent the mean reattachment lengths. Black trace represents the cross-covariance = 1 contour.

From the 0° case to the 20° case, the vertical extent of the correlated region increases. In the 0°

case, at *x* = 0.5*h* downstream of the crest, the contour representing a cross-correlation of unity

passes below *z/h* = 0.4; through the centre of the recirculation region it remains below *z/h* = 0.5. In

150

the remaining yaw cases, the corresponding contour passed between z/h = 0.5 and z/h = 0.6 at

x = 0.5h; at x = 2h, approaching the centre of the recirculation region in each case, the contour

passes between z/h = 0.6 and z/h = 0.8. This development of cross-covariance as a function of yaw

angle provides further evidence that the effect of the increased yaw angle is to add stability to the

flow.

It is hypothesised that if the persistent downstream vortices could be broken down, the adverse

downstream turbulence intensity and veer conditions could be mitigated, but speed-up would not

increase above one.

The development of Strouhal number is presented in Figure 81. The Strouhal number was calculated

based on the free-stream velocity, the step height, and the highest relative energy containing

frequency from the PSD of the U-component of the time-series at each point. In the low energy

regions, for example in the undisturbed boundary layer, acoustic peaks were recorded by the Cobra

Probes at Strouhal numbers between 0.3 and 0.32. Thus, in the plots presented in Figure 81, where

these spikes were evident, the maximum Strouhal number was set to zero.

The colour plots in Figure 81 are scaled to capture Strouhal numbers in the range 0 to 0.5, identifying

the shedding from the separation bubble. The Cobra Probes are able to capture fluctuations of

frequencies up to the Nyquist frequency of 1250 Hz (St = 1.82). The maximum Strouhal numbers in

the colour plots has been limited to 0.5 because of the ambiguity between the shear layer vortices,

the decay of the shear layer vortices to fine-scale turbulence, and signal aliasing at the high

frequency end of the spectrum. Additionally, the recirculating flow associated with the flow

separation cannot be captured by the Cobra Probes. Regions where velocity fluctuations occur at

Strouhal numbers greater than 0.5, associated with the shear layer vortices and fine-scale

turbulence, are highlighted by the St = 1 contour. The regions affected by these flow regimes extend

between 1-1.5h vertically from the crest of the step, and from the crest to beyond the mean

reattachment line. Thus, the colour plots in Figure 81 show data from beyond the mean separation

region at *x* = 4*h* downstream of the crest, through to the final measurement plane at *x* = 10*h*.
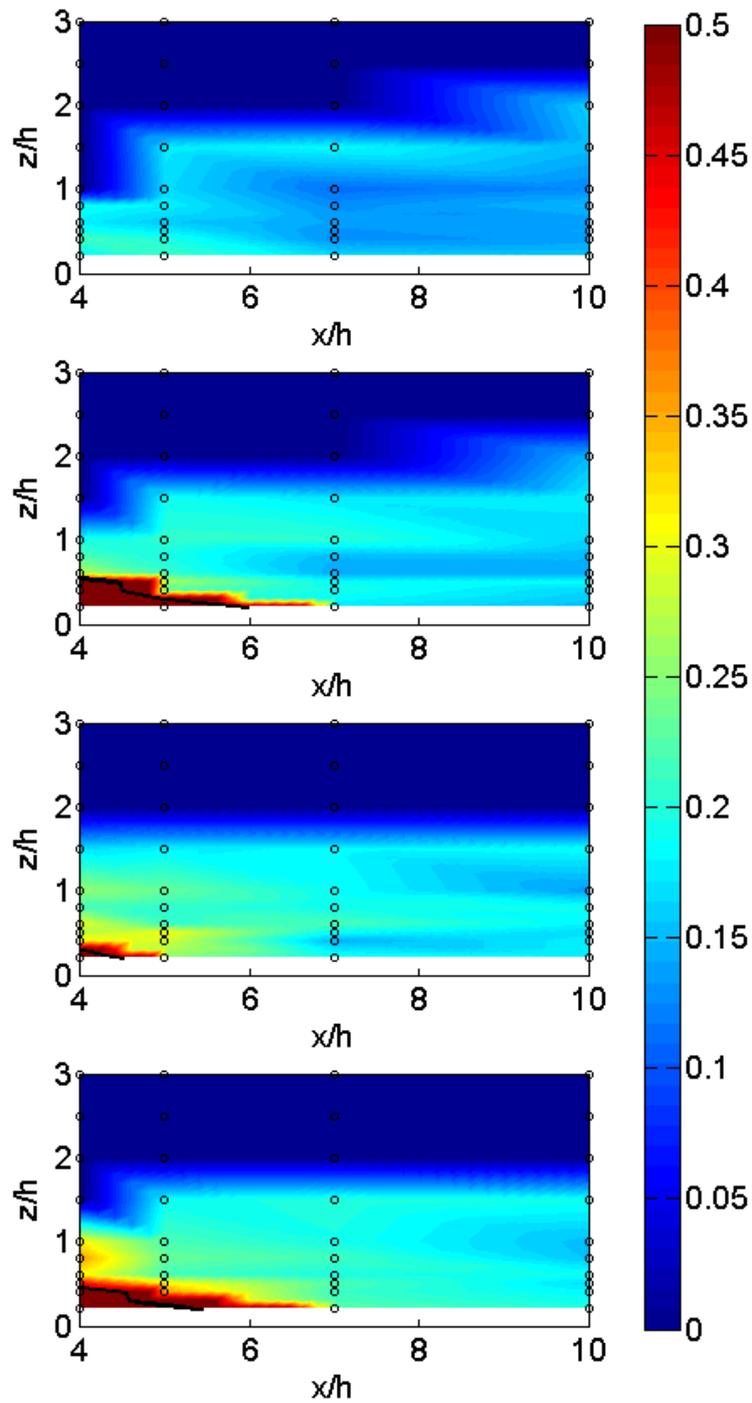
Figure 81: Development of Strouhal number from 4*h* downstream of crest. From top to bottom, yaw angle is 0°, 20°, 30°, and 40°. Black circles represent measurement locations. Black trace represents the St = 1 contour.

The low frequency shedding from the recirculation region is present for each of the yaw angle cases examined, illustrated in Figure 81. The peak Strouhal number in the downstream region is in the range 0.15 – 0.25, independent of yaw angle. This range is consistent with the initial validation study presented in Chapter 4, for a step of height h = 0.10 m, at a free-stream velocity of 20 ms^{-1}. It also agrees well with the work of Camussi et al. (2008).

The visualisations of the peak Strouhal numbers in Figure 81 present a decrease in Strouhal number with distance downstream. The precise cause of this is unclear. However, Winant and Browand (1974), in their seminal work on the growth of mixing layers identified that the underlying cause of this growth is the pairing mechanism of the vortices. Matsui and Okude (1983), investigating low Reynolds number wakes of circular cylinders, reported the case where some, but not all of the convecting vortices pair, resulting in a new shedding frequency that was not a harmonic of the original shedding frequency. Ho and Huerre (1984) reviewed many cases where span-wise vortices of the same sign were seen to amalgamate and merge. Ho and Huang (1982), again, investigating the merging of vortices in mixing layers, compared cases with and without forcing functions, and found that without forcing functions the merging of vortices tended to occur randomly, as opposed to under forcing conditions where the location of vortex merging could be accurately predicted.

In contrast Cimbala et al. (1988), based on their own wake visualisations, measurements and stability analyses behind cylinders and porous plates, validating the work of Taneda (1959), concluded that the reduction in dominant frequency with distance downstream was attributable to the hydrodynamic instability, whereby a most probable frequency as a function of distance downstream could be predicted by linear stability theory. This "most probable frequency", Cimbala et al. (1988) and Taneda (1959) postulate, is caused by the vortex street rearranging at various distances downstream as the dominant vortex structure decays, and other structures are amplified. Again, Cimbala et al. (1988) state that this is due to the instability and the subsequent rearranging of the structures rather than a merging of the structures.

However, as Simpson (1989) observes, the FFS case is more closely paralleled to the mixing layer case, where the vortices are of the same sign. In the current study no forcing is applied, hence the gradual reduction in Strouhal number is consistent with the hypothesis that the span-wise vortices merge sporadically. Similarly, the increase in vertical extent of the elevated *TI Ratio* is consistent with the increase in size of the merged vortices. Thus the passing frequency of the shed vortices decreases and their size increases, but the convection speed of the structures and any change to that is not characterised. As the yaw angle is increased, the decrease in Strouhal number is delayed. This is consistent with the increasing stability in the vortex structure induced by the yaw angle.

5.3 Summary

This work described the effect of yaw angle on flow over an FFS. The mean reattachment length was shown to vary as a function of θ, δ/h and upstream turbulence intensity. Lateral flow induced by the yaw angle as it passes over the FFS was shown to increase the stability of the crest vortex up to a critical value of θ, beyond which the effect diminished. When turbulence intensity was increased and combined with an increase in δ/h, a general decrease in X_L/h was observed. The relationship between θ and X_L/h was shown to break down in these cases. The increased turbulence intensity and increase in thickness of the shear layer both promote instability, reducing the ability of the crest vortex to entrain flow and assisting in the breakdown of the crest vortex, with stability referring to the crest vortex's ability to continue to accumulate fluid before shedding.

Vortices generated off the crest of the FFS at different yaw angles were shown to act at an angle relative to the surface, varying linearly with yaw angle, demonstrating a gradual dominance of the lateral flow over the recirculation as the yaw angle is increased. This effect was consistent, being independent of the inflow turbulence intensity and $\delta/h.$

Distinct segmentation of the flow was observed in the wake of the low turbulence intensity regimes in the $\theta = 40°$ and 50° cases examined. The angle at which the flow acted against the surface, relative to the direction of the free-stream was 13°, demonstrating the presence of a vortex propagating

downstream, with the vortex axis becoming aligned with the free-stream flow. The orientation of the streaks showed that the vortex was of the same sign as the crest vortex. Thus, it was concluded that the segmentation was caused by the separation of the crest vortex from the crest. At higher turbulence intensities and δ/h values, the segmentation was not observed, indicating the spatial periodicity is broken down by the increase in turbulence intensity. End effects induced by the funnelling of the flow to one side of the wind tunnel were also observed.

The Cobra Probe measurements provided more specific insight into optimal wind turbine siting locations, as well as providing an opportunity to test Baker's hypothesis. The following statistics were considered through a range of inflow yaw angles: speed-up, turbulence intensity, pitch and yaw angles, as well as the identification of vortices shedding from the recirculation region at the crest of the FFS.

Outside of the recirculation region, Baker's hypothesis was shown to be a good approximation to determine the speed-up as a function of yaw angle. Baker's hypothesis can be readily applied as a large number of studies have reported speed-up or velocity measurements for the θ = 0° FFS cases (Bowen and Lindley 1977, Largeau and Moriniere 2007, Sherry et al. 2010, Ren and Wu 2011, Cochard et al. 2012). Discrepancies observed outside of the recirculation and wake regions were of the order of 5%.

Large pitch angles were observed at the crest of the cliff. These were outside the design envelope specified in the standard IEC61400-1 (2005).

Wind turbine rotors will encounter high veer, high turbulence intensity, lower wind speeds, and unfavourable shear profiles should they pass through the recirculation bubble – between the crest and three to four step heights down-stream.

Beyond 10h downstream of the crest, a wake profile still exists. If sited in this region, rotors will be subjected to reduced wind speeds, increased turbulence intensity, wind veer, and low frequency

buffeting from vortex ejections from the recirculation bubble. The Strouhal number of the buffeting was measured in the range of 0.15 – 0.25, and was found to be independent of the yaw angle.

A region approximately 0.5h downstream of the crest, and above 0.5h above the surface provides a region with the following characteristics: increased wind speed; lowest turbulence intensity at that height, and reducing with increased height; pitch angles within the design envelope defined by the standard IEC61400-1 (2005); low wind veer; and away from the low frequency buffeting associated with shedding vortices. This location maximises energy output, whilst minimising fatigue loading across the inflow conditions investigated.

This work did not consider the lateral variations along the crest of the FFS, which might be encountered due to the inherent ruggedness of cliffs. However, the FFS at the various yaw angles can be considered to be elements of the sawtooth crest, which are considered in the following chapter.

6. Ruggedness Modelling: Sawtooth Approximation

Investigating the effect of the ruggedness on the flow over escarpments is a natural progression

from the straight-edged FFSs investigated in Chapter 5. Ruggedness can be constructed by piecing

together finite segments from the yawed FFS cases to form a sawtooth crest. The sawtooth crest is

an approximation of the ruggedness associated with sites such as the Cathedral Rocks Wind Farm,

shown in Figure 82.

Figure 82: Cathedral Rocks Wind Farm in South Australia sited above sheer cliffs. Photo taken from the Port Lincoln Times and used with permission[5].

The results presented in Chapter 5 demonstrate the extent of the fully developed vortex structures

as they are generated from the crests of FFSs at various wind directions. The effect of piecing

segments together is to limit the development of those structures. Thus, the fully developed crest

structures identified in Chapter 5 can be considered as limiting cases for the ruggedness being

investigated in this chapter, as well as for yawed ruggedness cases, which are not explicitly

investigated.

---

[5] http://www.portlincolntimes.com.au/story/1779866/record-wind-energy-production/ viewed 24 April 2014

This has, until recently, not been extensively researched. Cochard et al. (2012) and Montlaur et al. (2012) completed complementary wind tunnel and computational work on FFSs with sawtooth lateral variation. They identified delta wing styled vortices developing over the sawtooth elements, and documented fractional speed-up and turbulence intensity above a sawtooth element over a range of yaw angles. While their research did not focus on the amplitude of the sawtooth, they did investigate an alternative geometry where the triangular sawtooth elements were rotated around their vertical axes, providing a second amplitude to wavelength case for comparison. Their observation of delta wing styled vortices suggests that the research surrounding flow over delta wing shapes will provide a useful comparison with flow over sawtooth FFSs.

In this chapter the flow over a FFS with a range of sawtooth lateral variations is considered. This was done using surface shear stress visualisations, from which the flow topology was derived. These results are compared against surface pressure measurements, velocity statistics from Cobra Probe traverses, and CFD simulations.

6.1 Model Details

Experiments were performed using Inflow Configuration 3, as specified in Section 3.3.1 *Three Wind Tunnel Configurations* at a free-stream speed of 34 ms^{-1}, over forward facing steps of height, h = 0.050 m. As with the probe investigation of the yawed FFS case, this inflow configuration was chosen to maximise the effect of the topography relative to the inflow conditions. The experiments were completed at Reynolds Numbers of 1×10^5, using the step height, h, as the reference length. End plates extended 12h upstream of the models. The models resulted in 2.5% blockage and extended beyond 10h downstream, and can be thus considered isolated cliffs according to Moss and Baker (1980). The aspect ratio was 34, resulting in four complete wavelengths of the geometry being modelled. The experimental domain is shown in Figure 83. The models were painted with semi-gloss enamel paint, and were aerodynamically smooth. The geometric parameters are presented in Table 10.

Table 10: Geometric parameters of sawtooth FFS configurations.

Height: h	A/λ	Amplitude: A	Wavelength: λ	Yaw /Sweep Angle: θ	Extent downstream	Aspect ratio (width/height)
0.050 m	0.325	0.130 m	0.400 m	33°	2.6 m/52h	34
0.050 m	0.5	0.200 m	0.400 m	45°	2.6 m/52h	34
0.050 m	0.65	0.260 m	0.400 m	52°	2.6 m/52h	34
0.050 m	1	0.400 m	0.400 m	63°	2.6 m/52h	34
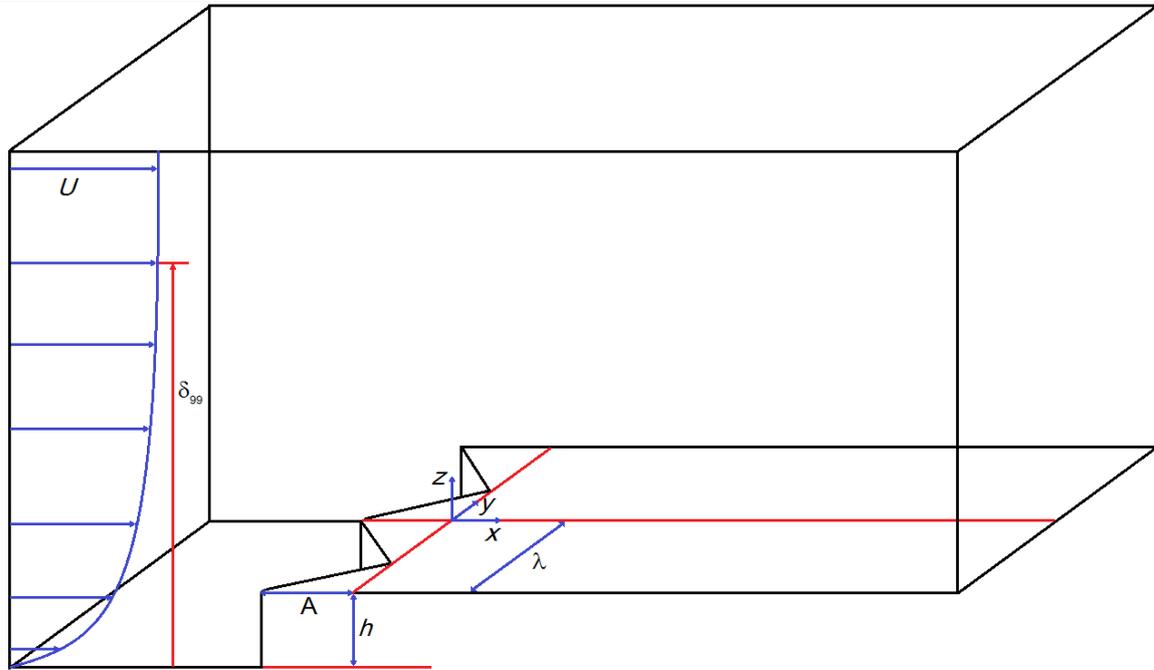
Figure 83: Experimental domain.

6.2 Results and Discussion

The surface shear stress flow visualisations were able to capture the mean surface shear stress fields, as shown in Figure 84 through to Figure 87. Dominant vortex structures are clearly visible; however some of the finer detail requires closer examination, particularly in the trough region. Surface shear stress visualisations were compared with surface pressure measurements and Cobra Probe measurements for the shallowest case: A/λ = 0.325. The analysis first focusses on the mean flow structure, before considering the development of Strouhal number over the surface of the FFS.

In each of the cases, the mean flow topology was deduced based on the surface shear stress visualisations and compared with the CFD analysis performed by Harbig (2013).
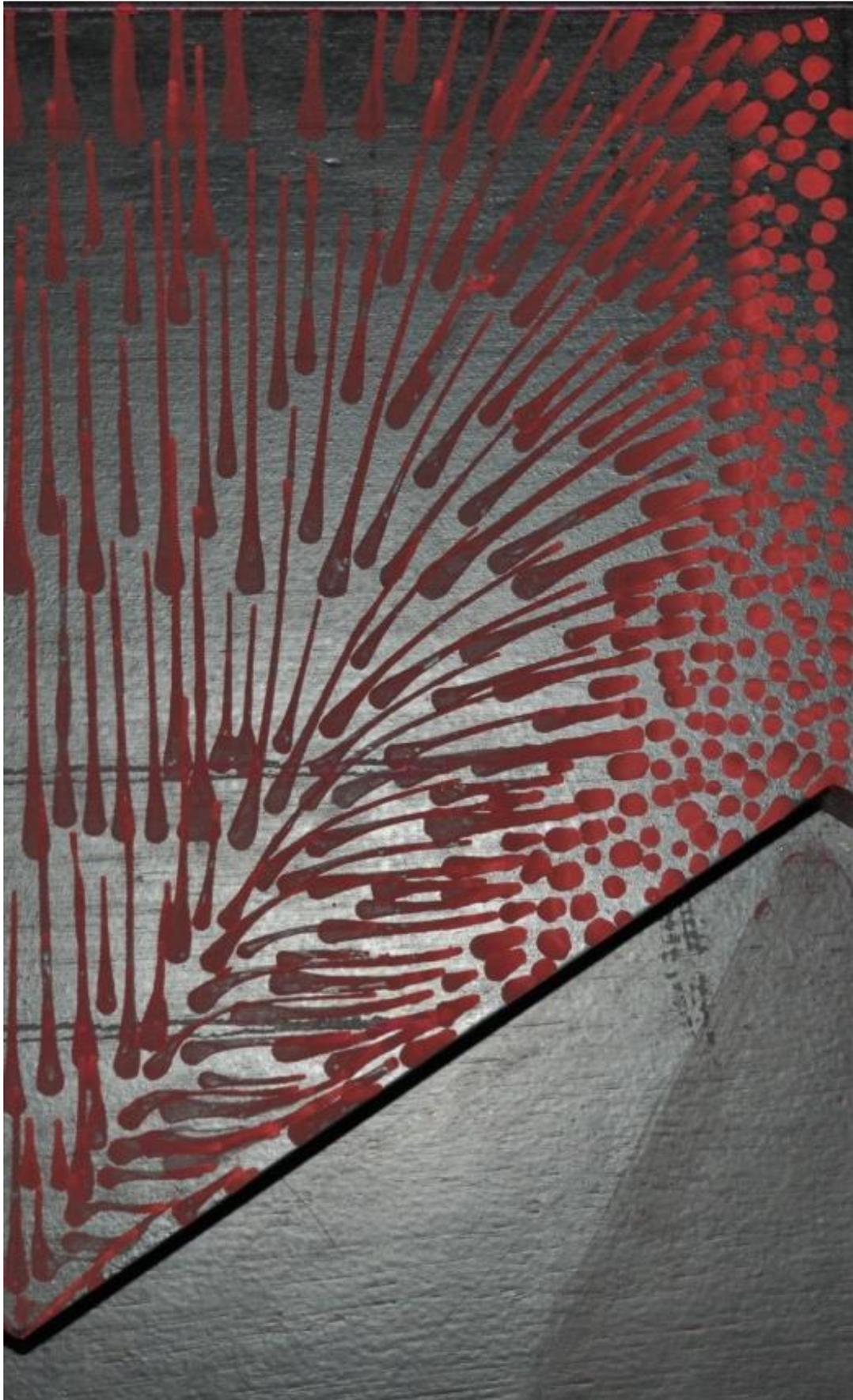
Figure 84: Paint droplet surface shear stress visualisation for *A/λ* = 0.325 case.
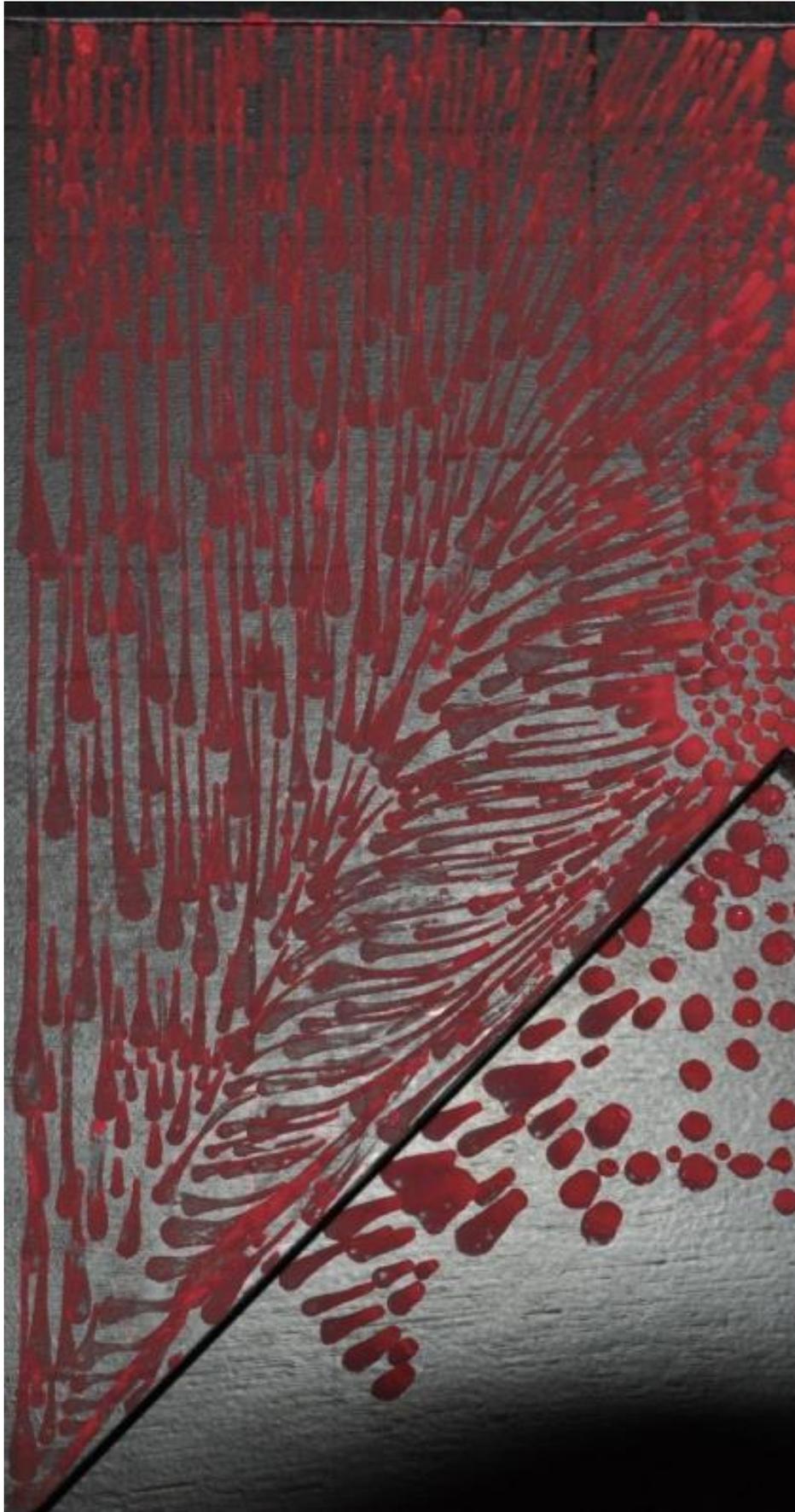
Figure 85: Paint droplet surface shear stress visualisation for *A/λ* = 0.5 case.
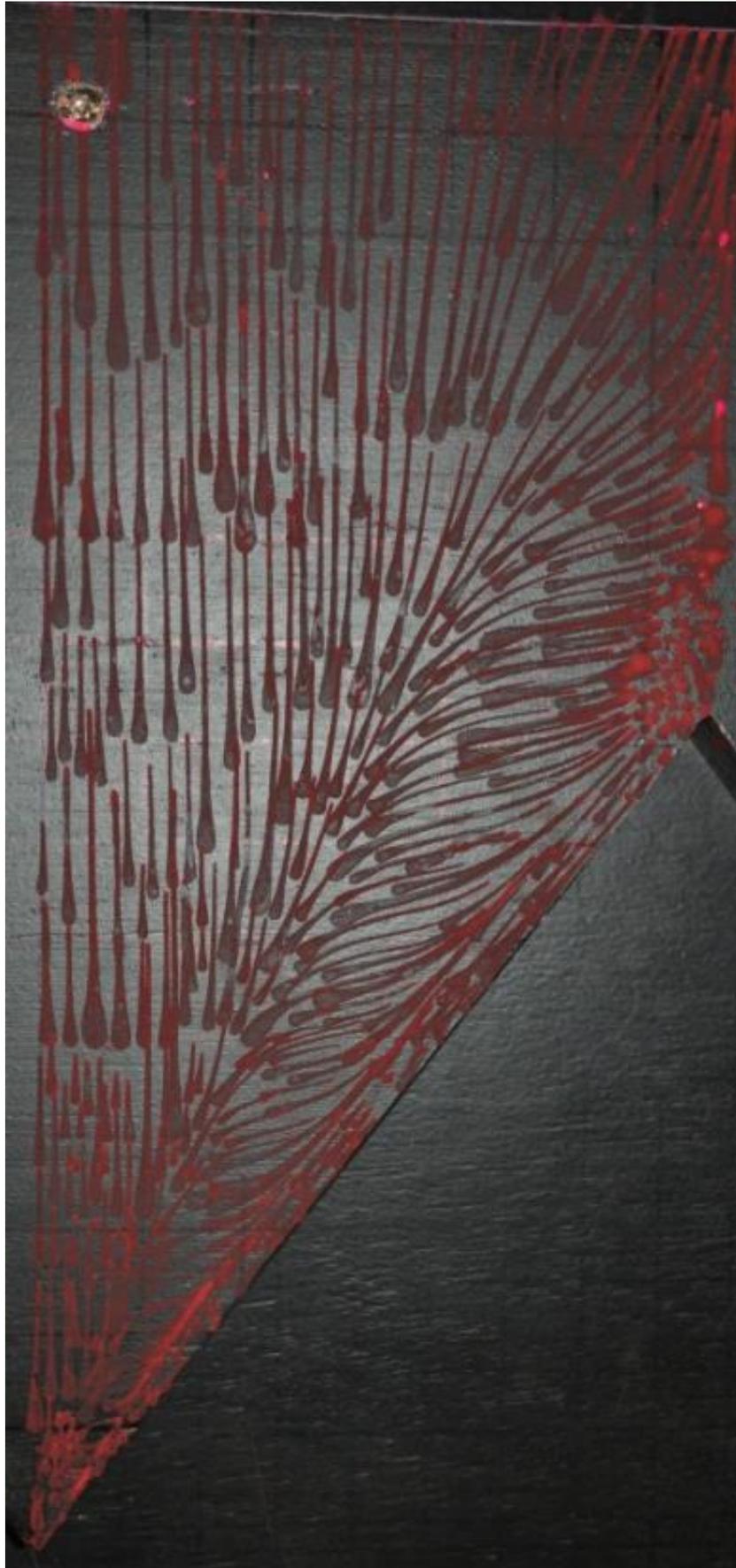
Figure 86: Paint droplet surface shear stress visualisation for *A/λ* = 0.65 case.
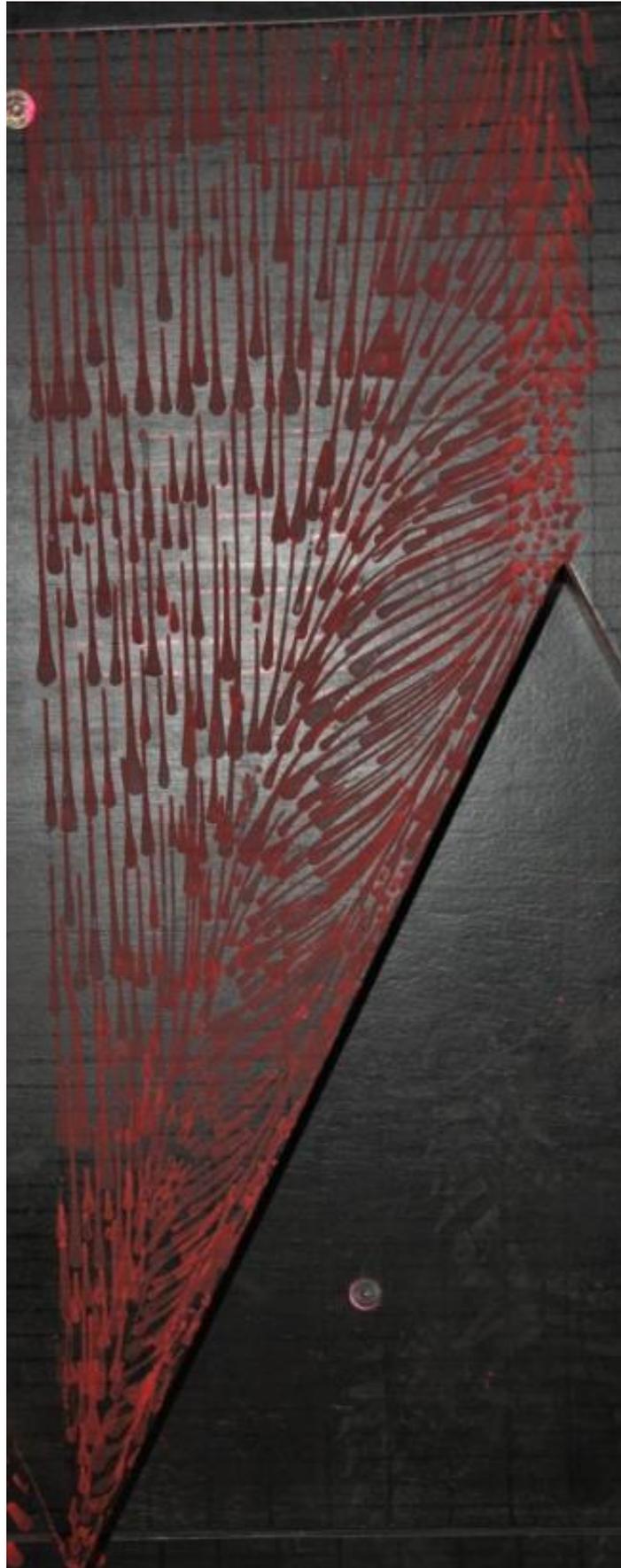
Figure 87: Paint droplet surface shear stress visualisation for *A/λ* = 1 case.

From the surface shear stress visualisations shown in Figure 84 to Figure 87, surface flow topology

can be determined, identifying critical lines and points. These are subject to the constraint

determined by the Poincaré-Bendixson Theorem that $\sum N - \sum S = \frac{\epsilon}{2\pi}$, where N denotes the

number of node points on the plane and S denotes the number of saddle points on the plane and ϵ

denotes the angle through which the shear stress vector passes over the plane relative to the

incoming flow (Hunt et al. 1978). Over this FFS geometry ϵ = 0° thus, the number of node points

must equal the number of saddle points.

Examining first the visualisations in Figure 84 through to Figure 87, it is clear in each case that the

peak of the sawtooth can be considered the distinct shedding point, with the vortex diameter

approaching zero at the peak. However, Verhaagen and Van Bossuyt (2006) demonstrated that a

complex vortex interaction exists at the peak at a microscopic level. They observed the interaction

by magnifying the radius of curvature of the nose of their delta wing. In the current research the

diameter of the vortex grows linearly for a period along the crest before turning downstream, with a

positive bifurcation line clearly evident in each of the cases. As A/λ varies, the topology over the

front half of the sawtooth remains largely unchanged. Immediately downstream of the vortex the

flow is slightly entrained by the vortex before straightening and continuing downstream. The vortex

itself channels flow along the crest. This is consistent in each of the A/λ cases observed.

To understand the flow it is useful to consider the straight edge FFS as a sawtooth FFS with A/λ = 0.

In that case, a straight reattachment line is evident parallel to the crest. If the amplitude of the

sawtooth increases above zero, but remains small, the reattachment line will remain largely

unaffected. At some A/λ, between A/λ = 0 and A/λ = 0.325, a transition occurs whereby the sharp

peak of the sawtooth dislocates the span-wise vortex shed from the crest. As described above, the

vortex entrains flow, resulting in it growing in diameter along the crest. The vortex detaches from

the crest near the trough. The transition from a straight FFS topology is not captured in this set of

experiments, however a transition in the location of the detachment of the delta wing style vortex

from the crest of the sawtooth FFS is observed as a function of A/λ, remaining attached farther

downstream along the crest as A/λ increases.

Including the A/λ = 0 case, four stages of development are observed, induced by geometric changes.

The first case is the straight edged FFS case, inclusive of very small A/λ such that the primary

separation off the crest and the ensuing recirculation region downstream of the crest is not broken

down by an increase in lateral flow or a secondary separation from the geometry. The remaining

three cases are considered in the following sections.

6.2.1 A/λ = 0.325

The second stage of development (following from the straight-edged FFS), presented by the

topology in Figure 88 where A/λ = 0.325, is characterised by three flow features. The first

distinguishing feature is the interruption to the continuous separation line at the geometric peaks

and troughs, compared to the A/λ = 0 case, where the mean reattachment line runs continuously,

parallel to the crest. Secondly, the vortex, growing from the peak, detaches from the crest before

the trough, changing direction, with the vortex axis aligning itself with the stream-wise x-axis. This is

highlighted in the close-up of the visualisation, shown in Figure 89. This vortex is similar to a delta

wing vortex. Thirdly, flow recirculation is clearly evident; flow is redirected from the vortex,

recirculating back past the trough, from the farther upstream of the two saddle points, back toward

each of the stable nodes located along the crest, which is also clearly evident in the close-up in

Figure 89, highlighted by the green arrow. This recirculation is reflected in the topology in Figure 88.

Flow near the trough experiences low surface shear stress, with droplets only streaking marginally.

In the remaining three cases (A/λ = 0.5, 0.65, and 1) the vortex remains attached along the length of

the crest. Additionally, a secondary vortex structure within the delta wing style vortex is observable

in the paint droplets, and is represented by the fine red line near the crest in Figure 88. This

secondary structure is smaller than in the other three cases, but is clearly observable along the crest

in the visualisation presented in Figure 84.
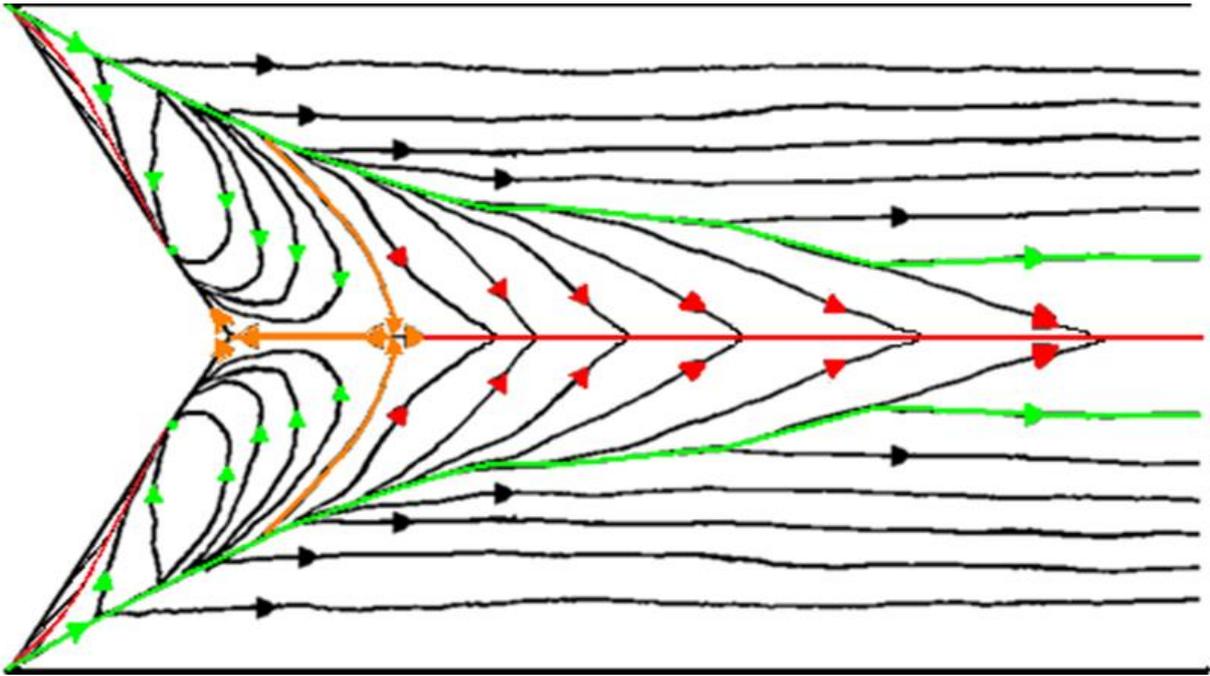
Figure 88: Flow topology over a FFS with sawtooth leading edge. *A/λ* = 0.325. **Flow is from left to right. Positive bifurcation lines are shown in green; negative bifurcation lines are shown in red. Saddle points are indicated with orange direction arrows. Stable nodes are indicated by green dots and arrows. Dividing streamlines are shown in orange.**
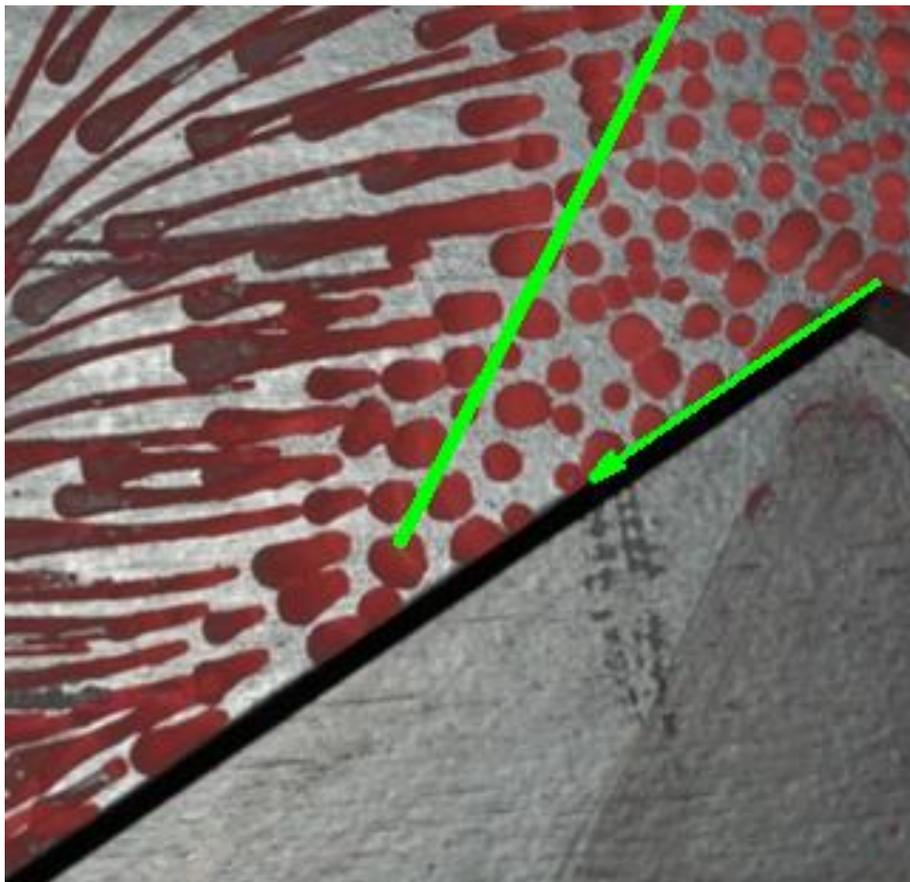
Figure 89: Close-up of the trough region from the *A/λ* = 0.325 case. Flow is from top to bottom. Separation of the vortex structure from the crest is highlighted by the green line, and recirculation from the trough point back along the crest is highlighted by the green arrow.
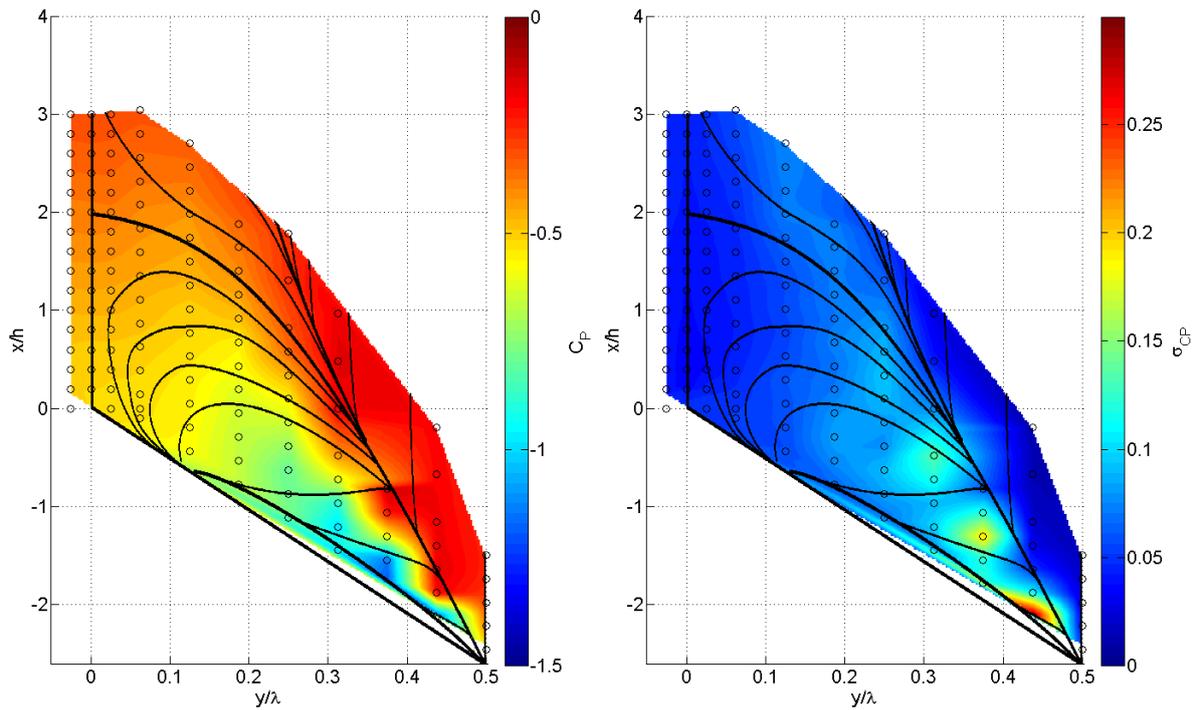
Figure 90: Mean surface pressure (left) and standard deviation (right) expressed as a pressure coefficient C_P over A/λ = 0.325 case, overlayed with flow topology and pressure tap locations. Circles represent measurement locations. Flow is from bottom of page to top.
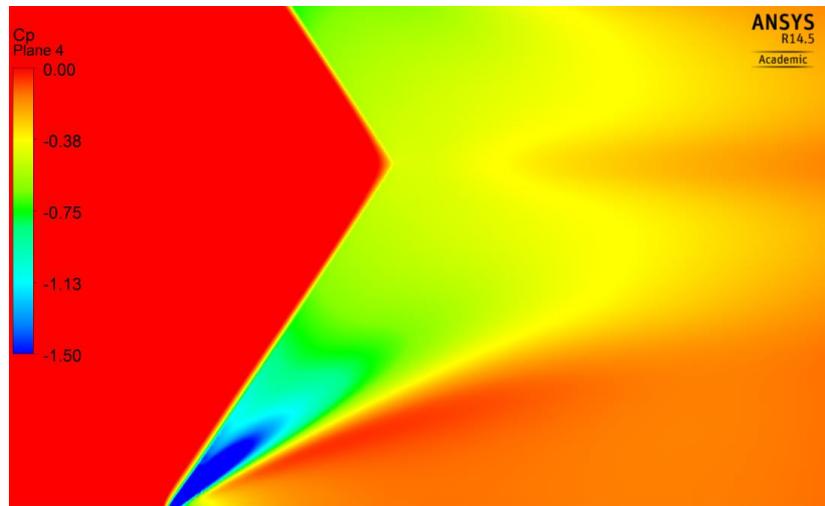
Figure 91: Mean pressure coefficient from the CFD investigation conducted by Harbig (2013). Flow is from left to right. A/λ = 0.325.

The mean and standard deviation of the surface pressure data are presented in Figure 90, while a CFD comparison is presented in Figure 91. The pressure is expressed as a pressure coefficient, C_P, defined as:

$$C_P = \frac{P - P_\infty}{0.5\rho V_\infty^2} \tag{6-1}$$

167

The standard deviation of pressure is normalised in a similar manner:

$$\sigma_{C_P} = \frac{\sigma_P}{0.5\rho V_\infty^2} \tag{6-2}$$

P_∞ is the surface pressure measured in the undisturbed region upstream of the step; P is the mean surface pressure; σ_P is the standard deviation of the surface pressure; ρ is the air density; and V_∞ is the free-stream velocity.

An RSS analysis of the uncertainty, considering the manufacturer's specification of the DPMS units (0.1% of full-scale) and the uncertainty of the free-stream dynamic pressure suggests an uncertainty of 4% for typical values of the pressure coefficients. The calibration of the DPMS units, presented in *Appendix: Static Calibration of Dynamic Pressure Measurement System Units*, demonstrated that the units performed well within the manufacturer's specifications.

The pressure tap locations are denoted by the small circles in Figure 90. Because of the irregular nature of the grid of pressure taps, the two-dimensional interpolation fails to capture the exact delineation between different parts of the flow, however the overlay of the topology demonstrates good agreement between the surface shear stress visualisation and the surface pressure taps, attributing pressure measurements to the different flow regimes associated with the delta wing style vortices. The peak negative pressure coefficients are associated with the largest fluctuations, located near the peak of the geometry. Higher pressure coefficients are observed along the bifurcation line that was derived from the surface shear stress visualisations. The standard deviation, however, remains elevated along this line. These pressure extrema are associated with the vortex structures as they cause flow to impinge on the surface.

Mean Cobra Probe measurements are presented in Figure 92 through Figure 94. The mean static pressure is presented in Figure 92; Figure 93 presents the speed-up ratio, *S*, defined in Equation 4-1 and 5-1. Figure 94 presents the turbulence intensity ratio, previously defined in Equation 5-4. The plots are centred on the peak of the sawtooth protrusion.

168

The Cobra Probe measurements help to paint a clearer picture of the flow structure over the sawtooth FFS. The static pressure measurements show that two vortex cores persist downstream, whereas the speed-up and turbulence intensity ratios fail to separate the structures. The speed-up and turbulence intensity ratios highlight the persistence downstream of the vortices, with the flow speed reduced to sixty percent of the inflow conditions, and the turbulence intensity increased up to tenfold in the farthest downstream of the measurement panes, 10h downstream.

The speed-up data, presented in Figure 93, show that the highest speed-up ratios occur at x/h = -1.35. This high speed region is clearly associated with the vortex structure, seen also as a low pressure region Figure 92. The high turbulence intensity region only becomes noticeable at x/h = 0, in Figure 94, due to the scale of the colour bar, with much larger increases in turbulence intensity observed downstream. The low turbulence intensity measurements at the z/h value of 0.5 indicate that the top half of the delta wing style vortex, as it is generated off the crest of the FFS, is quite stable. This is also consistent with the delta wing literature, which identifies delta wing vortex bursting as a distinct change from jet-like behaviour, with a dominant axial flow, to a wake-like behaviour with flow approaching stagnation (Gursul et al. 2005). It is clear that the delta wing style vortices persist downstream. The sudden expansion in the diameter of the vortex beyond the trough region with a corresponding decrease in the velocity is consistent with vortex bursting, as described by Hall (1972). A positive pressure gradient can also be observed in the top panel of Figure 94, consistent with the flow requirements identified for vortex bursting (Hall 1972).

CFD modelling provides further detail of the flow structure. Agreement between the CFD model and the wind tunnel modelling is established through the consistency of flow topology, velocity fields, and surface pressure. There is good agreement between surface pressure, compared in Figure 90 and Figure 91; and surface shear stress lines, presented in Figure 95, and the topological skeleton derived experimentally in Figure 88. Similarly, consistency is observed in the velocity field comparison provided in Figure 96 at various planes downstream of the peak, though the vortex

structures appear more diffuse in the computational work, which may be attributable to the vertical

profile of TI, which was set at 5%, compared to the wind tunnel inflow conditions, which varied

between 9% near the surface, and 0.8% in the free-stream. These points of comparison provide

sufficient confidence in the validity of the CFD model. Thus, because of the reasonable comparison

between the CFD and the experimental work, there is confidence that the visualisation presented in

Figure 99 provides a similarly reasonable visualisation of the mean vorticity over the FFS. The

structure shown in Figure 99 illustrates the dominant vortex generated from the crest of the FFS

encapsulating a secondary vortex generated from the trough point.

It was established in the literature review that large Reynolds Stress magnitudes correlate strongly

with the largest loads on the wind turbines (Hand et al. 2003). Selected plots of Reynolds Stress, in

particular the stream-wise vertical component, R_{uw}, are presented in Figure 97. Results from three

planes are presented: x/h = -1.3, 2, and 10. In each plane, five lateral traverses are presented:

y/λ = 0, ±0.25, and ±0.5. Remembering that y/λ = 0 is aligned with the peak, it is expected that the

magnitude of those Reynolds Stress peaks would be minimal, compared to the peak values aligned

with the trough points, which correspond to the propagation of the delta wing style vortices. This is

confirmed in the three profiles presented in Figure 97. The remaining profiles demonstrate good

symmetry about y/λ = 0. Lateral profiles through regions of Reynolds Stress maxima are also

presented in Figure 98. While Figure 97 highlights the vertical extent of the elevated levels of the

peak values of R_{uw}, Figure 98 illustrates their lateral extent.

The peak values observed at x/h = -1.3, are significantly lower than the peaks observed downstream,

which is likely to do with the bursting of the vortex structures. By z/h = 0.5 the elevated stresses are

beginning to subside. In contrast, the large peak values of R_{uw} observed downstream, which occur

through the vortex in its burst form, highlights the presence of significant instantaneous velocity

variations either side of the stagnated mean velocity.
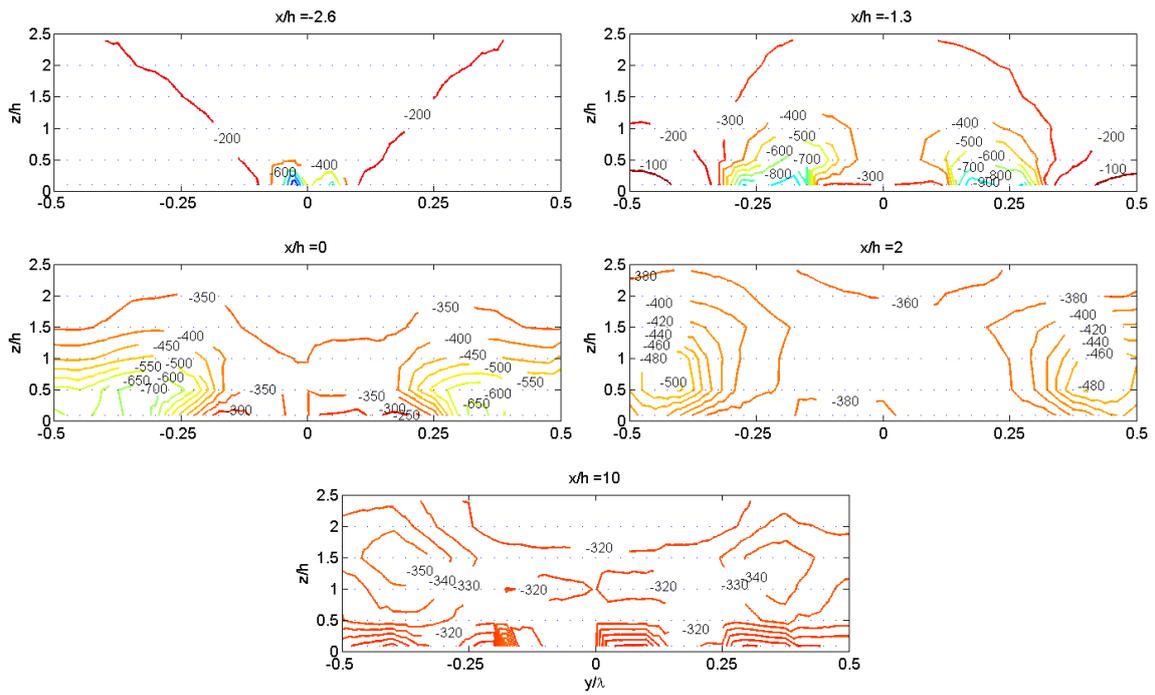
Figure 92: Mean static pressure from Cobra Probe measurements over _A/λ_ = 0.325 case.
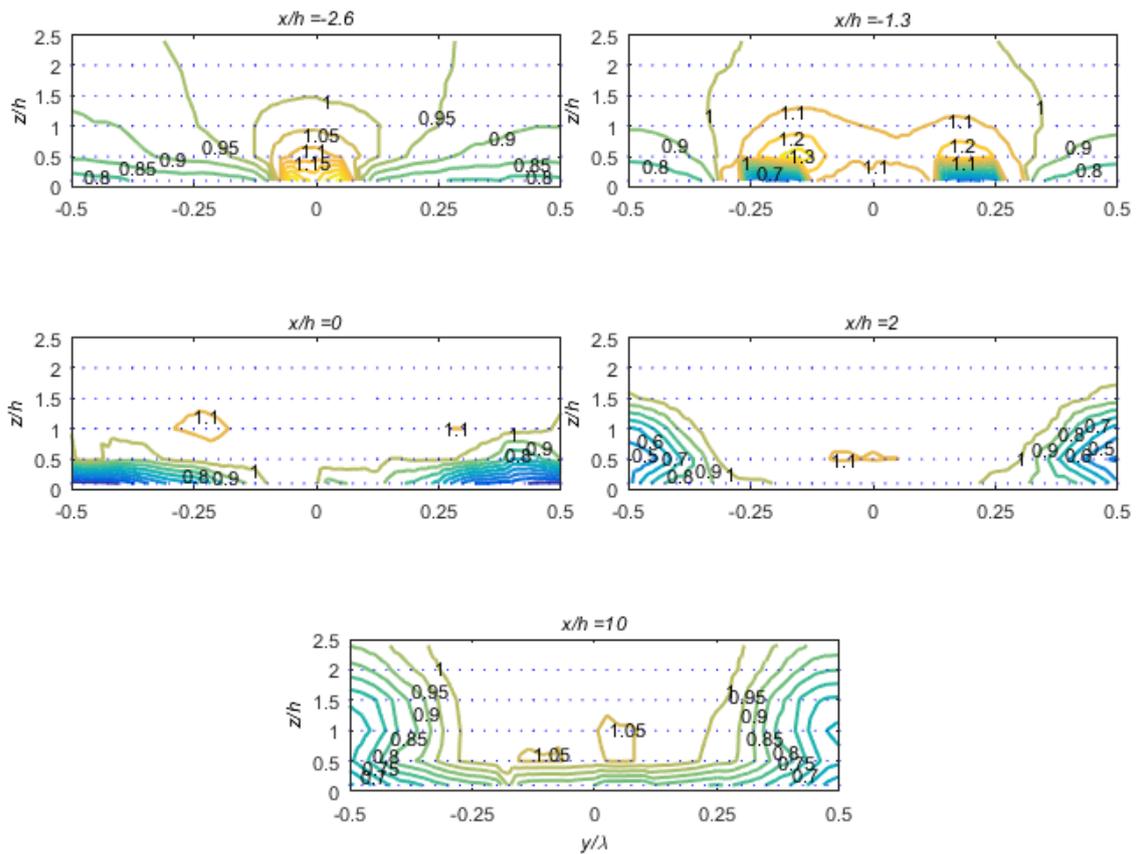
Figure 93: Mean speed-up from Cobra Probe measurements over _A/λ_ = 0.325 case.

171
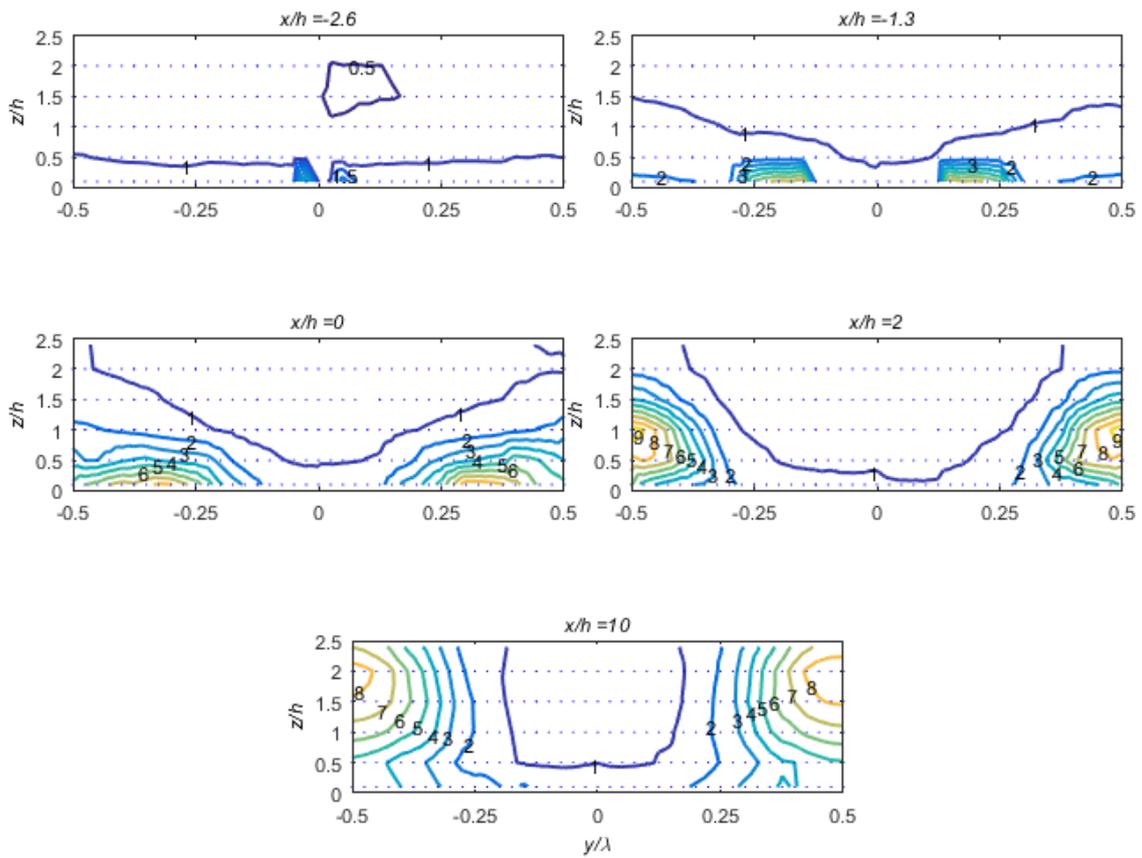
**Figure 94: Mean turbulence intensity ratios from Cobra Probe measurements over *A/λ* = 0.325 case.**
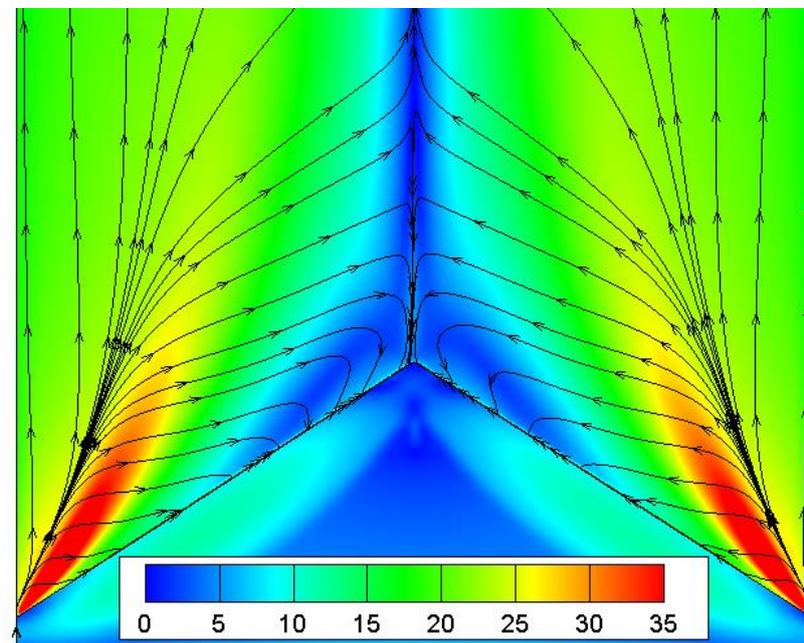
Figure 95: Surface shear stress lines based on CFD modelling of a FFS with sawtooth lateral variation, courtesy of Robert Harbig. *A/λ* = 0.325. Colouring represents near surface flow speed in ms⁻¹.
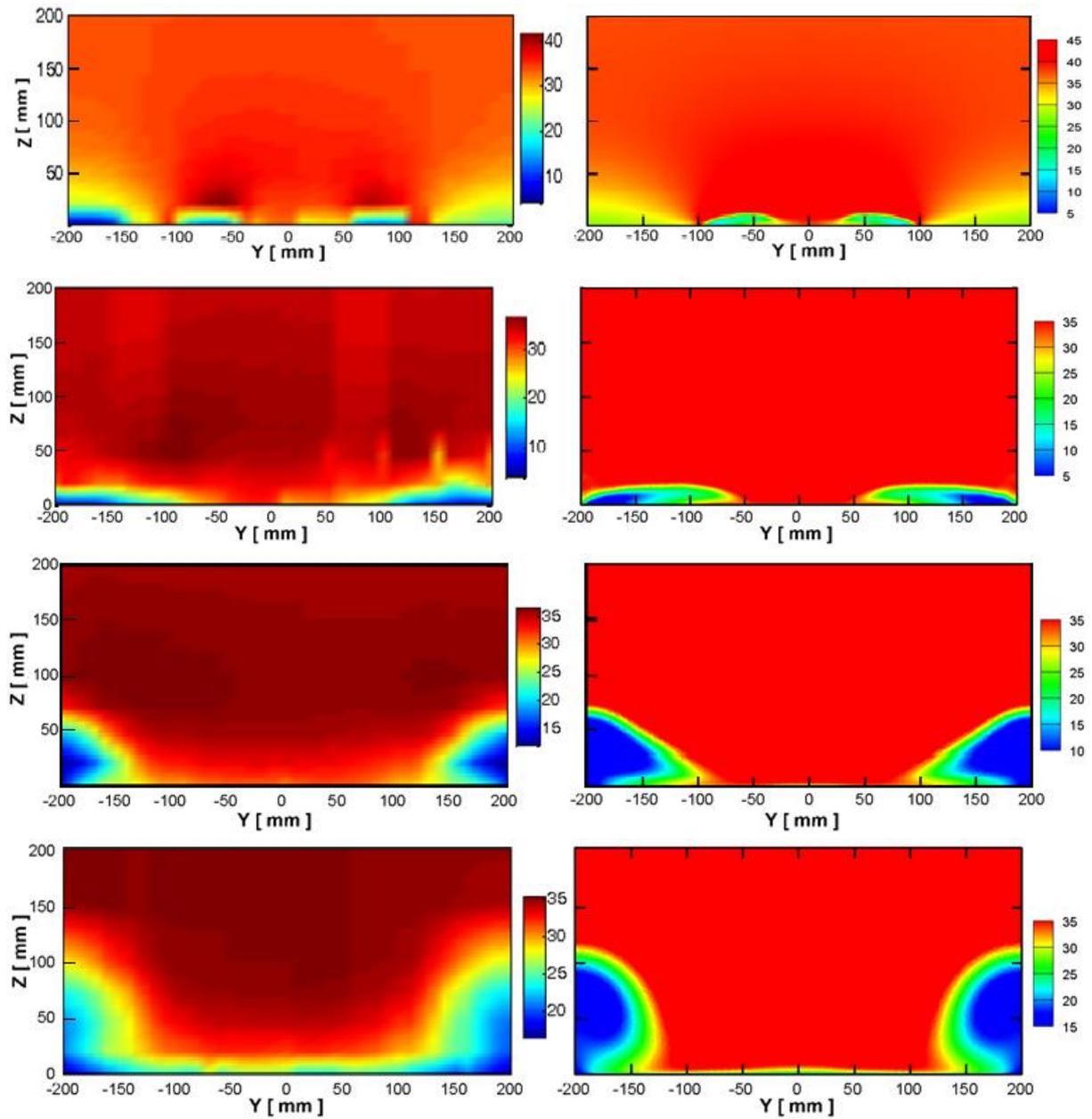
Figure 96: Velocity comparison between wind tunnel measurements (left) and CFD (right). Y-Z planes from top to bottom are *x* = -67 mm, 0 mm, 100 mm, 500 mm. Note that the colour scales vary in each pane. Colour units are ms⁻¹.
***A/λ* = 0.325.**
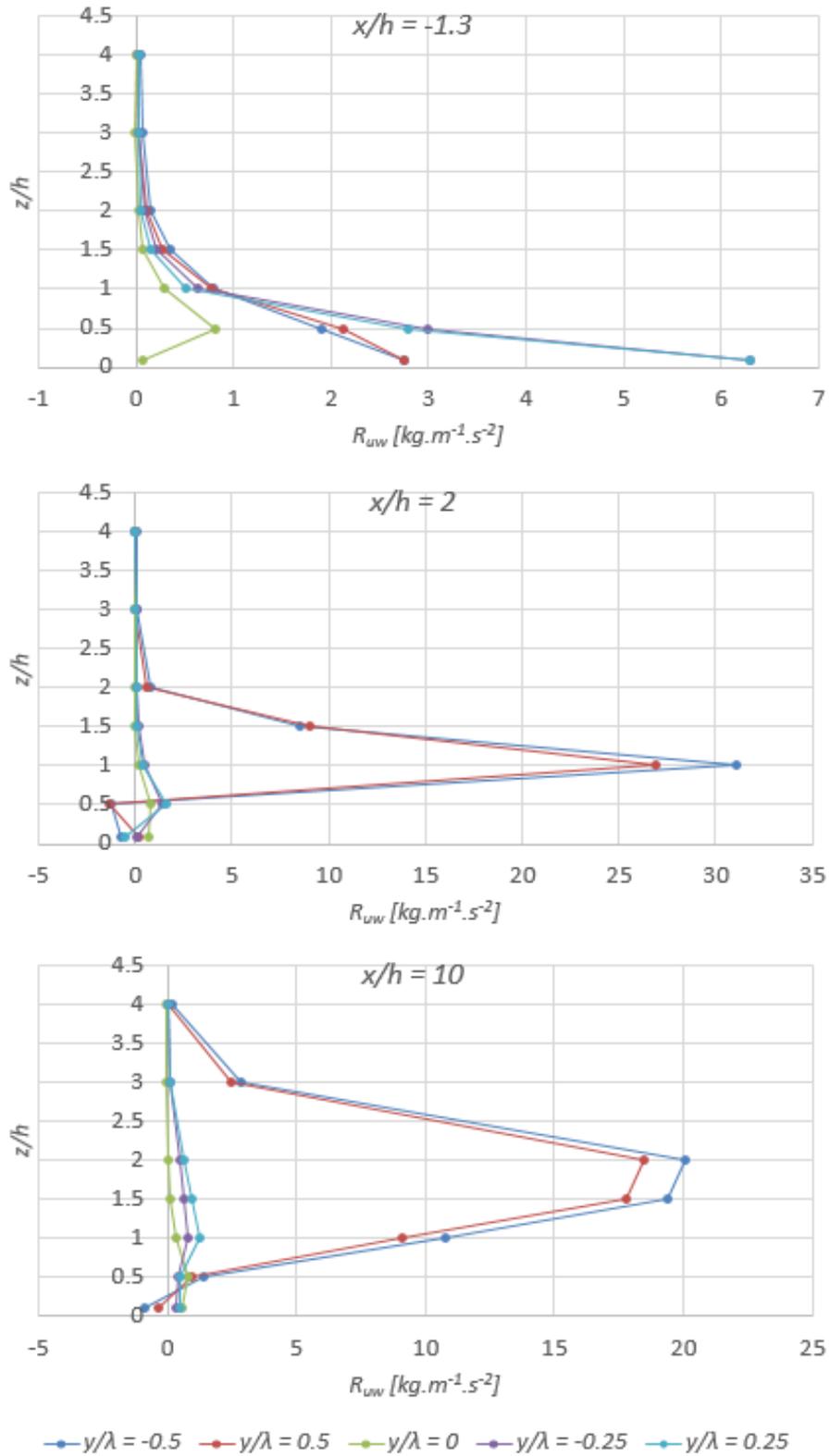
Figure 97: Development of stream-wise-vertical Reynolds Stress, R_{uw}. Note the different horizontal axis scale in each case.
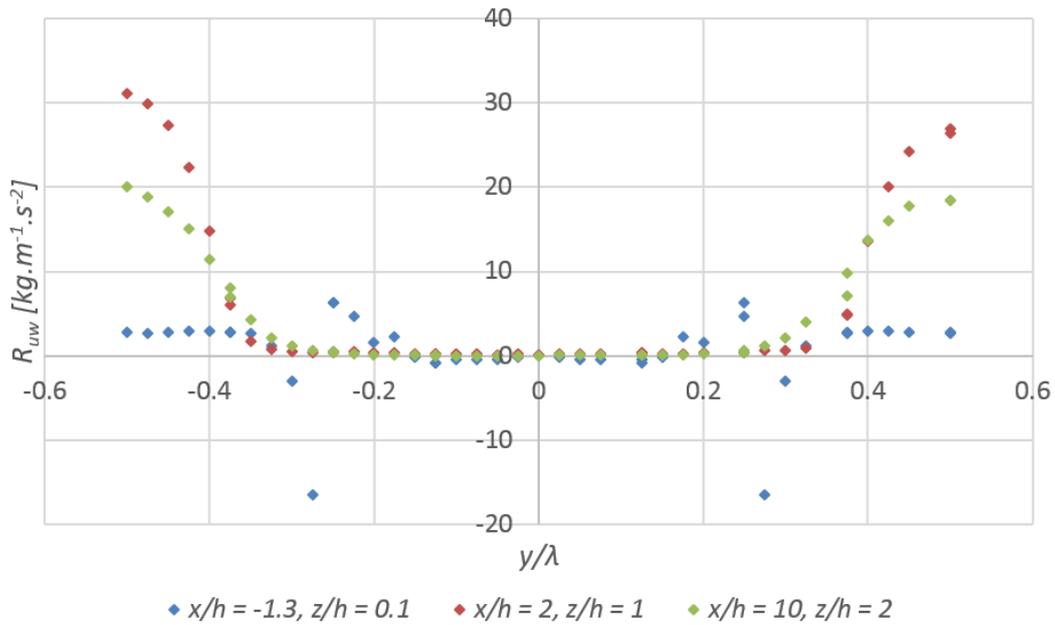
Figure 98: Lateral profiles of stream-wise-vertical Reynolds Stress, R_{uw} through the region of peak Reynolds Stress.

A statistical analysis of the flow dynamics was also conducted for the A/λ = 0.325 case. A map of the peak Strouhal numbers is presented in Figure 100 for this case. This plot illustrates the development of Strouhal number over the geometry, providing a measurement of how strong the shedding signal is at various spatial locations, whilst providing comparison with the surface shear stress visualisation data. This figure presents maximal relative power values from the PSDs, where the PSD is plotted against Strouhal number. The Strouhal numbers are binned in increments of 0.05. Thus, the relative power, $fS_u(f)/\sigma^2$, is a function of Strouhal number, St = fh/U, and normalised spatial position, x/h and y/λ. The maxima are averaged across the line y/λ = 0, which, in this case, corresponds to the geometric peak of the sawtooth, and a line of symmetry. The peaks in the spectral data correlate remarkably well with the visualisation data. The data is presented again as a set of individual plots for clarity from Figure 101 through to Figure 105. The following paragraphs describe the flow development in terms of three phases before comparing the measurements to measurements of peak shedding frequencies found in the literature. The locations of these phases are presented in Figure 106, represented as three shaded regions.
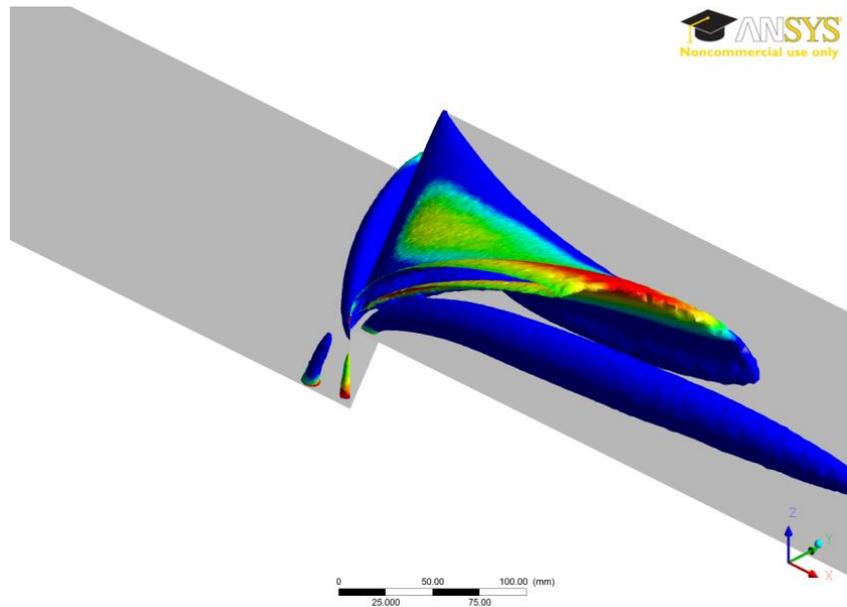
Figure 99: Iso-Q surfaces coloured by stream-wise vorticity based on CFD modelling of a FFS with sawtooth lateral variation, courtesy of Robert Harbig. *A/λ* = 0.325.

Figure 101 depicts the upstream tip of the model, at *x/h* = -2.6, and as such, is largely unaffected by the topography, with only minor lateral deviations in the PSD.

At *x/h* = -1.3, midway along the sawtooth protuberance, the development of the PSD is much more pronounced, and this is well illustrated in Figure 102, where the plot is dominated by the high Strouhal number bins (St > 0.61), corresponding to the regions associated with the delta wing vortices. The increase in energy content is first observed in the 0.41 < St < 0.45 bin. Measurements along this plane passed above the stable node located on the crest of the sawtooth, which was previously identified in the flow visualisation. Thus the data collected are representative of the flow structure – that is, the delta wing style vortex – before it has developed significantly or interacted with other flow structures or burst; in effect it is representative of the first phase of the flow development. This phase is depicted as the grey region in Figure 106.
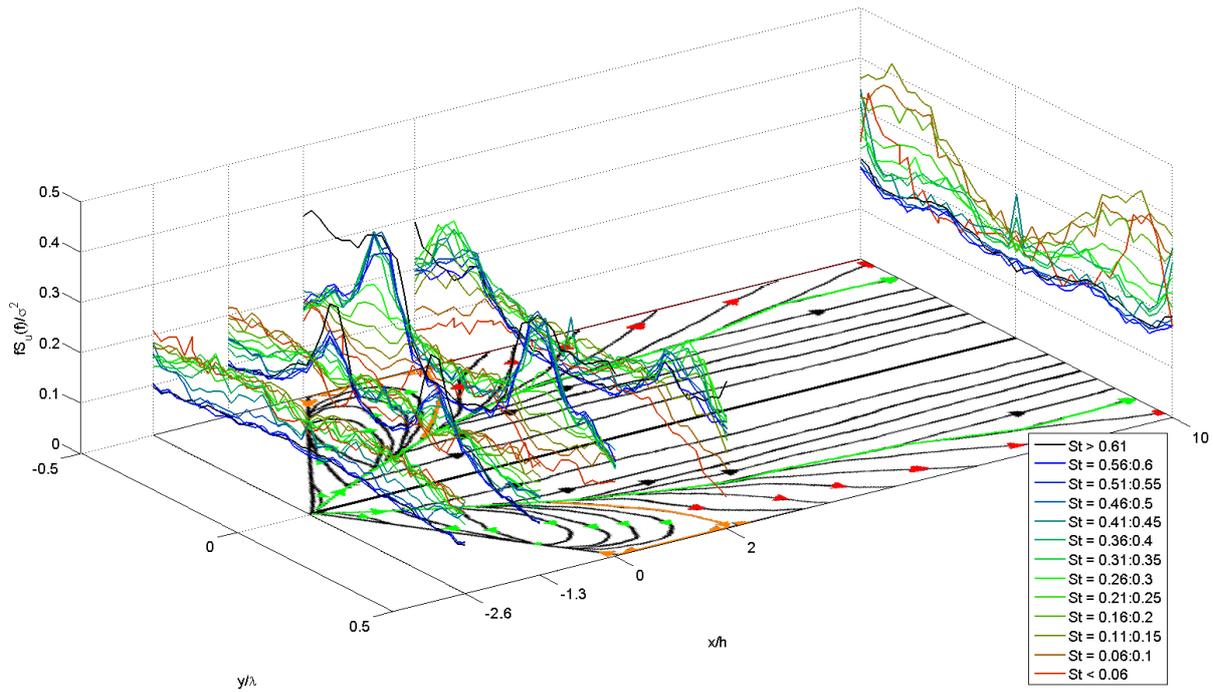
Figure 100: Power maxima from each Strouhal number bin, shown at each spatial location over the topological skeleton for a single height, *z/h* = 0.5. *A/λ* = 0.325.

Given the dominance of the high Strouhal numbers in this plane, and the limitations of the probes, it is more appropriate to say that the flow in this region is dominated by high frequency fluctuations, than to assign a characteristic Strouhal number. This high frequency spectral dominance is consistent with a constant entrainment of flow into the crest vortex. The notion of a constant entrainment is consistent with the measurements, that is, the lack of a distinct Strouhal number. The measurements instead record the shear layer vortices within the larger vortex structure. This is consistent with the dynamic flow structure over delta wings. Various researchers have identified the presence of Kelvin-Helmholtz vortices within delta wing vortices, despite noting that characterising their distinct frequency was difficult (Gad-el-Hak and Blackwelder 1985, Gordnier and Visbal 1994, Gursul 2005). Within the vortex there is also a discernible reduction to the relative energy contained in the low Strouhal number bins, remembering that the PSD is normalised by the local variance, with the relative energy content increasing through to the highest Strouhal number bin. The regions on either side of the high Strouhal number peaks are quite consistent with the results observed in the upstream plane at *x/h* = -2.6, which are associated with the free-stream flow.

At *x/h* = 0, the traverse aligns with the trough points, and the vortex signature on the PSD is just as pronounced as in the *x/h* = -1.3 case. This is illustrated in Figure 103. There are, however, some notable developments.

This traverse measures a persistence of the primary delta wing style vortex. The spectrum is dominated by the higher frequency fluctuations, denoted by the black trace in Figure 103. The energy gradient, that is, the increase in relative energy with Strouhal number, is largely consistent with the *x/h* = -1.3 case through the primary vortex region (the light green area in Figure 106). The slight divergence between the two traverses can be observed by comparing the Strouhal number bins where the normalised PSD begins to peak. In the *x/h* = 0 case, the normalised PSD begins to peak in the Strouhal number bin of 0.31 < St < 0.35, as opposed to the 0.41 < St < 0.45 bin in the *x/h* = -1.3 traverse. This shift indicates a transition to the phases measured at *x/h* = 2 and *x/h* = 10 where the PSDs are dominated by the lower Strouhal numbers, and the relative power in the high frequency side of the spectra has diminished to be almost insignificant. The shift between the two regimes is associated with the bursting of the delta wing style vortex.
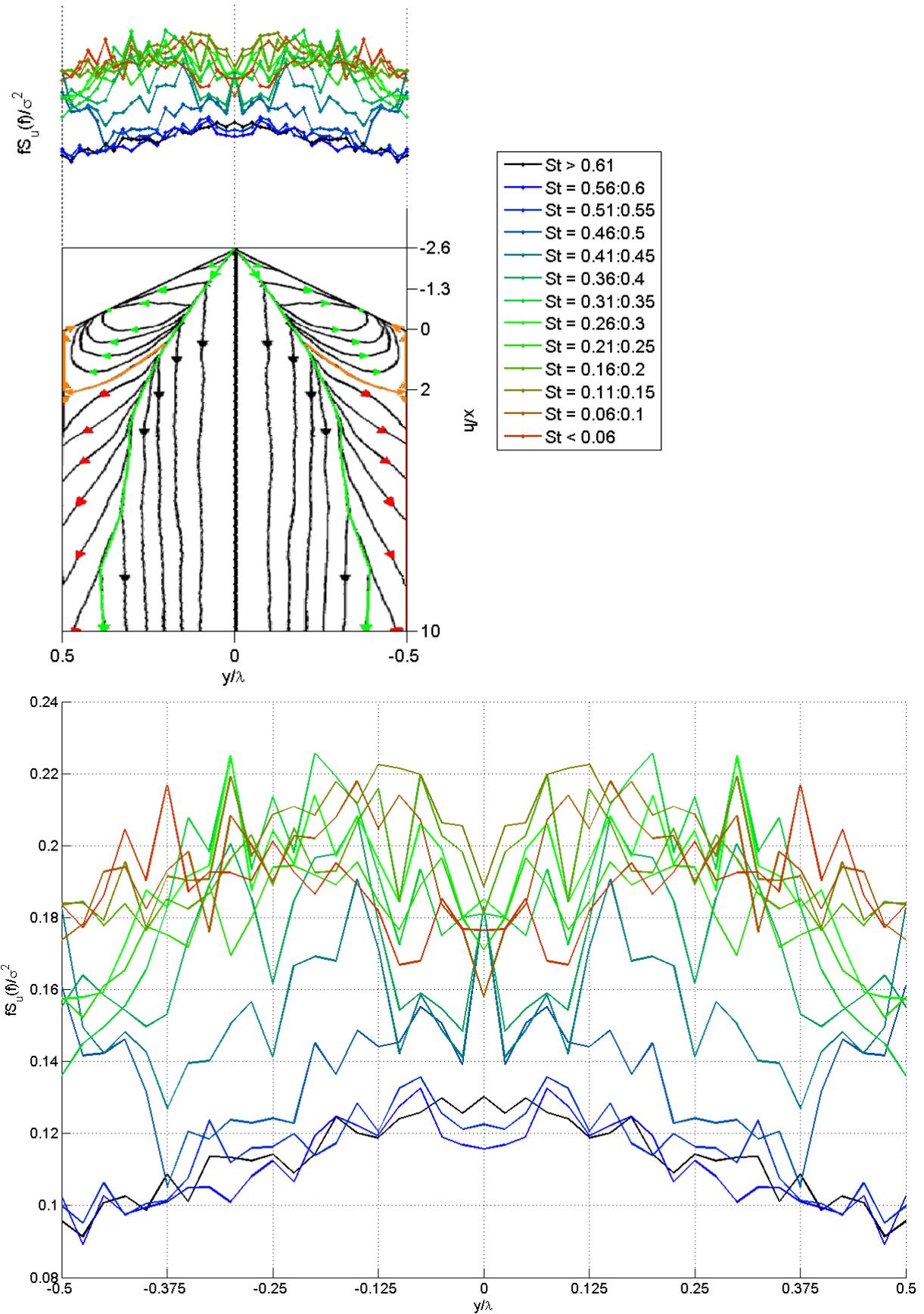
Figure 101: Power maxima from each Strouhal number bin, shown at lateral locations, centred on the peak of the sawtooth with *A/λ* = 0.325 and *z/h* = 0.5. Plot shown corresponds to *x/h* = -2.7. Top figure places Strouhal numbers and power values in the context of the geometry and flow topology.
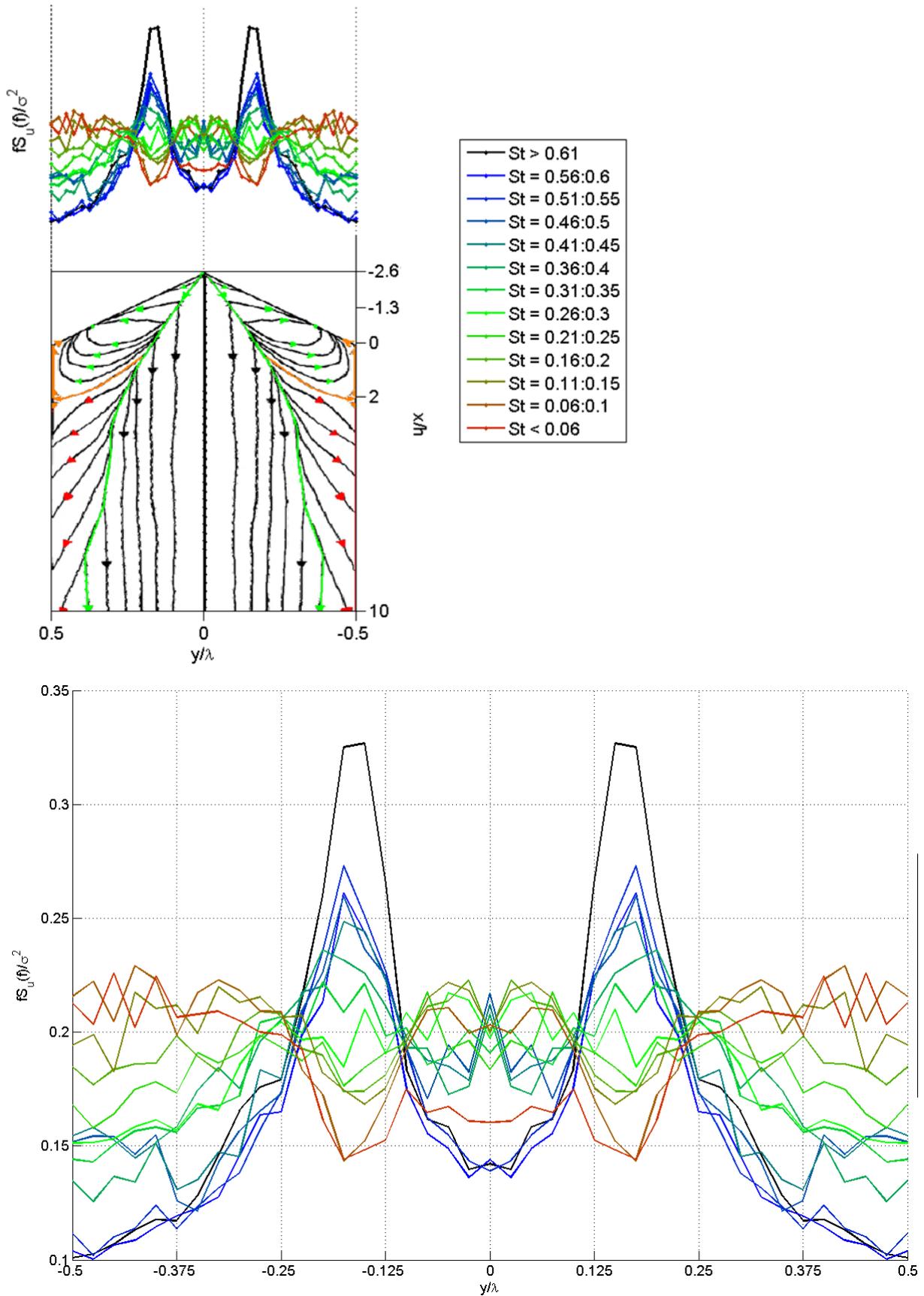
Figure 102: Power maxima from each Strouhal number bin, shown at lateral locations, centred on the peak of the sawtooth with *A/λ* = 0.325 and *z/h* = 0.5. Plot shown corresponds to *x/h* = -1.3. Top figure places Strouhal numbers and power values in the context of the geometry and flow topology.
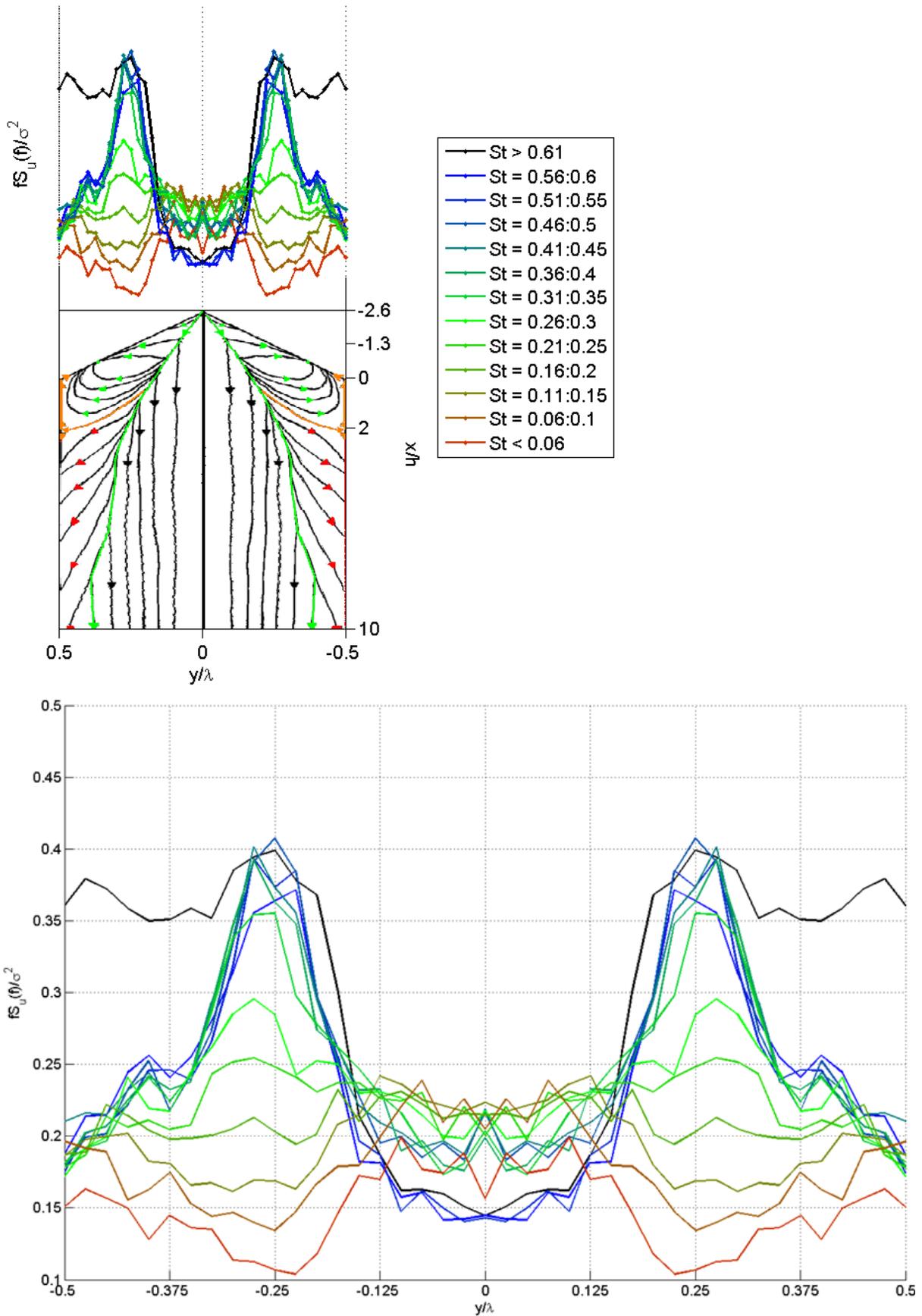
Figure 103: Power maxima from each Strouhal number bin, shown at lateral locations, centred on the peak of the sawtooth with _A/λ_ = 0.325 and _z/h_ = 0.5. Plot shown corresponds to _x/h_ = 0. Top figure places Strouhal numbers and power values in the context of the geometry and flow topology.

This traverse also measures a secondary phase of the flow regime, across the lateral spatial range of approximately 0.375 < |y/λ| < 0.5. This is done in an attempt to measure the flow phase where the flow recirculates in a counter-stream-wise direction, from the farthest downstream of the saddle nodes at x/h = 2, back down to the stable node at x/h = -1.3. Visualisation with paint droplets in this region was difficult because there was minimal streaking of the paint. Assuming a strong correlation between surface shear stress and flow velocity, it can be concluded that this region experiences very low flow. The surface shear stress visualisation also reveals a mean flow direction that is counter-stream-wise. Thus, it is reasonable to expect measurement difficulties associated with the Cobra Probes, which are unable to measure flow from outside of the 45° cone of acceptance, and are thus unable to give a realistic picture of the flow. Nonetheless, the dominance of only the black St > 0.61 trace in this region of recirculation, as shown in Figure 103, indicates that there are pressure fluctuations in that Strouhal number range. This is consistent with decay into chaotic turbulent motion.

The fourth traverse, 2h downstream of the trough points, is presented in Figure 104. The measurements display a strong transition to a regime dominated by low frequency shedding, though there are still some remnants of the finer scale structures that were observed in the previous traverses farther upstream.

The strongest shedding signal is associated with the Strouhal number range 0.26 < St < 0.3 across the region 0.325 ≤ |$y/λ$| ≤ 0.475, which is a further reduction in peak frequency from the x/h = 0 traverse. Compared to the upstream measurements, the high frequency component associated with shear layer vortices and fine scales of turbulence is diminished, resulting in a distinct Strouhal number peak across the stated Strouhal number range. Through the region 0.275 ≤ |$y/λ$| ≤ 0.3 the strongest peak is still attributable to the 0.36 < St < 0.4 bin, but this is a weaker shedding signal than the previously described region.
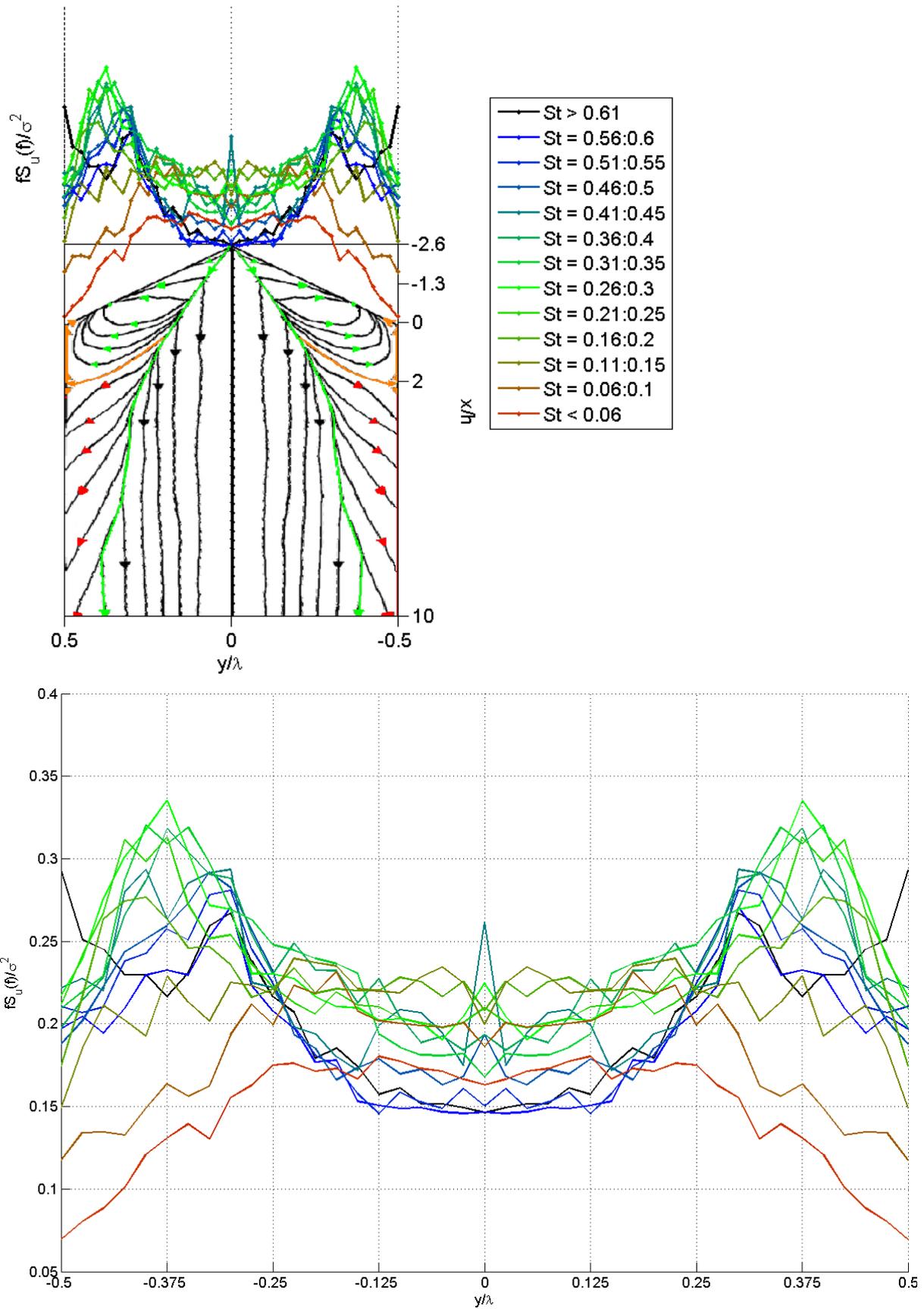
Figure 104: Power maxima from each Strouhal number bin, shown at lateral locations, centred on the peak of the sawtooth with *A/λ* = 0.325 and *z/h* = 0.5. Plot shown corresponds to *x/h* = 2. Top figure places Strouhal numbers and power values in the context of the geometry and flow topology.

183
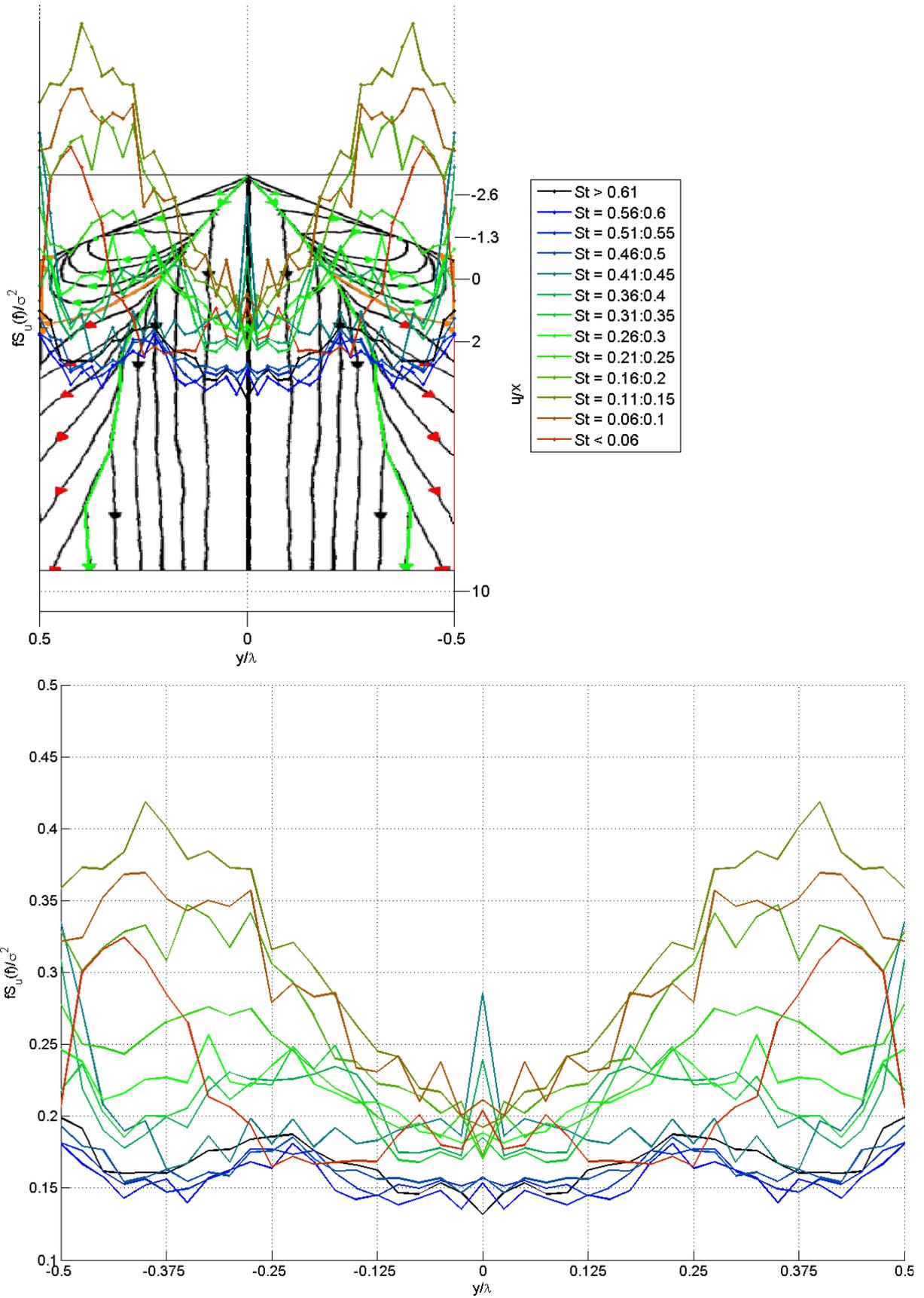
Figure 105: Power maxima from each Strouhal number bin, shown at lateral locations, centred on the peak of the sawtooth with *A/λ* = 0.325 and *z/h* = 0.5. Plot shown corresponds to *x/h* = 10. Top figure places Strouhal numbers and power values in the context of the geometry and flow topology.

184

The region around $|y/\lambda| = 0.5$ exhibits a reduction in power in all but the St > 0.61 range. This indicates that the two vortices being ejected are not yet interacting. They exist as counter-rotating vortex pairs propagating downstream.

The traverse farthest downstream is presented in Figure 105. The dominant Strouhal number is again reduced from the previous traversing plane. This implies that the vortex ejections emanating from the upstream phases tend to slow down relative to the free-stream velocity, which results in a merging of the vortices as they travel downstream.

In this downstream plane, the dip in peak power of the normalised PSD at $|y/\lambda| = 0.5$, that is, along the trough line, might indicate a persistent separation of the counter-rotating vortex pair. However, in this trough region there is a significant secondary peak in the range of Strouhal numbers: 0.41 < St < 0.45. This range corresponds to a higher frequency than the first harmonic of the dominant peak, which is within the Strouhal number bin of 0.11 < St < 0.15. This would indicate that while there is a vortex pair shedding downstream, in the course of its dissipation the two vortices interact across the plane of symmetry. While the vortices interact, it is not an interaction that hastens the vortex decay or annihilation. If this were the case, the high Strouhal number bins would contain a large portion of the energy as the two vortices would cross-annihilate resulting in a large amount of chaotic motion, characterised by small scales of turbulence; instead, it is clear from Figure 105 that the high Strouhal number bins remain at very low energy levels.

Thus, three phases of flow development are identified across the five measurement planes. The first phase being the initial generation of the delta wing style vortex which is associated with an almost constant entrainment, characterised by a jump in energy from Strouhal numbers of 0.3 to 0.4 and remaining at that elevated state through to the Nyquist frequency. This is represented by the pale green shaded region in Figure 106. The second phase represents a recirculation region, driven by the separation of the delta wing vortex from the crest and is represented by the grey shaded region in Figure 106. This region is characterised by a shift in energy to the high Strouhal number bins, where

the measurements are limited by the Nyquist frequency and the inability of the probe to capture the recirculating flow. The third phase is characterised by vortex ejections from the previous two phases. It is represented by the blue shaded region in Figure 106. In this region, minimal energy is contained within the high Strouhal number ranges. Instead, the majority of the energy is contained within the 0.11 < St < 0.15 bin.
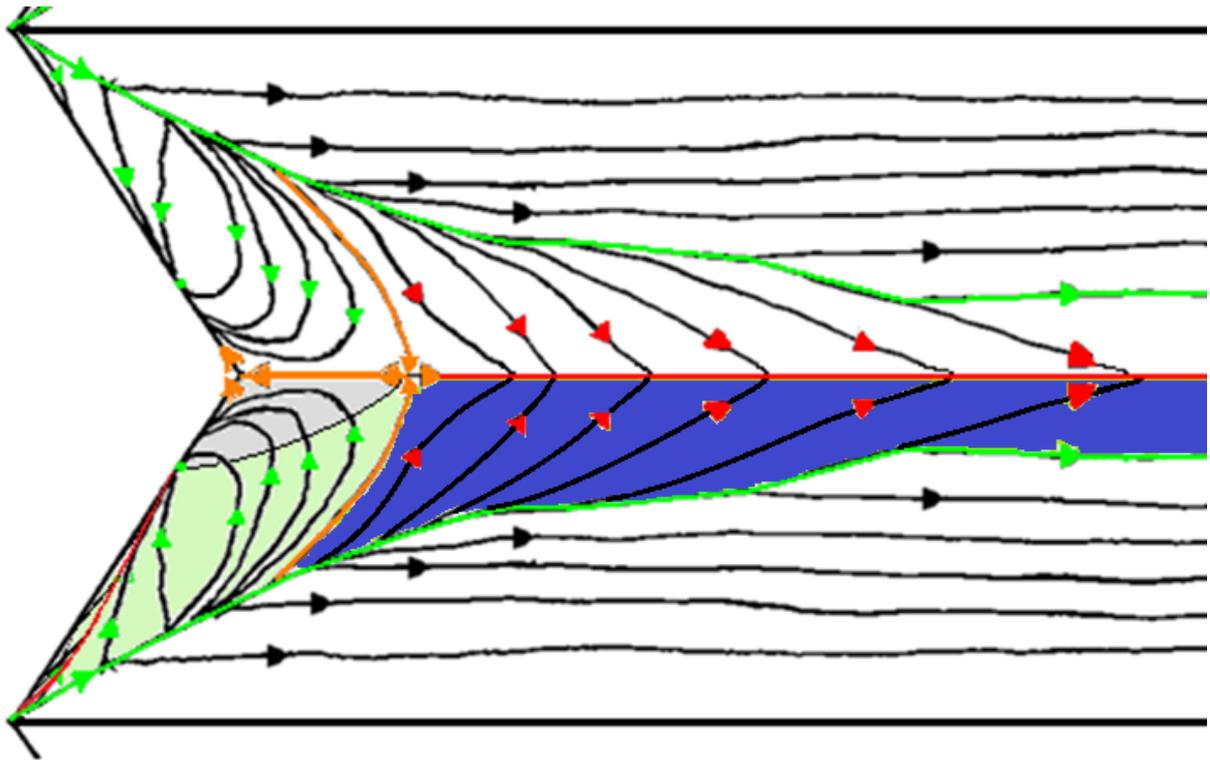

Figure 106: Topology of *A/λ* = 0.325 sawtooth case, showing three phases of development, based on PSD development. Flow is from left to right.

6.2.2 *A/λ* = 0.5

The third stage of development is identified in the *A/λ* = 0.5 case, where the stable node shifts from the crest to the surface proper. The flow topology is shown in Figure 107. The flow can be described with three bifurcation lines. The positive bifurcation line begins at the peak and continues downstream in the same manner as the *A/λ* = 0.325 case. The negative bifurcation line is aligned with the trough, beginning beyond the trough and continuing downstream. The third bifurcation line is the negative bifurcation line associated with the secondary vortex structure along the crest. Thus, the two saddle points are pushed downstream on the same trough line and the stable node points are shifted from the crest to a location closer to the trough line, and downstream of the trough

point, but not beyond the nearest of the two saddle points. Furthermore, it is observed that the secondary vortex feeds directly into the stable node. It would be correctly argued that the A/λ = 0.325 case and the A/λ = 0.5 case are topologically equivalent, given that the critical points are simply shifted downstream. The reason for the delineation is to highlight the shift of the stable node from the crest onto the surface-proper of the step; to point out the significant increase in the size of the secondary vortex structure within the delta wing vortex and its new relationship with the saddle point; and to show that the vortex remains attached for the entire length of the crest, from the peak to the trough.

Above the surface, the flow structure is further verified with the Cobra Probe measurements. Measurements were focussed downstream of the trough region, capturing the persisting delta wing style vortices. The stream-wise vorticity and y-z component of velocity, depicted in Figure 108 illustrate the highly structured nature of the flow in the first three panes. By 11h downstream the vortex has undergone significant diffusion, however, the speed-up and turbulence intensity ratio presented in Figure 109 illustrates that there is not a complete dissipation of the vorticity, and breakdown of the wake.

As with the A/λ = 0.325 case, an analysis of the Strouhal number development is presented from Figure 110 to Figure 114.

The development of the PSD through four planes downstream of the trough point is illustrated in Figure 110. At each measurement location, the PSD of the stream-wise velocity component was calculated. The normalised power values from the PSD were then binned according to Strouhal number. The peak power value associated with each Strouhal number bin was then plotted as a colour, representing the Strouhal number bin. This was superimposed over the topological skeleton, with the vertical, z axis, representing the normalised power from the PSD. Figure 110 presents the four planes of measurements all on the same plot, illustrating the relative proximity of the planes, however, because of their proximity, the data in the first three planes are overlapped and difficult to

187

interpret. Each plane is then presented individually in Figure 111 through Figure 114, allowing closer

inspection of the spectral data. The sequence of figures highlights the presence of notable dynamic

components.
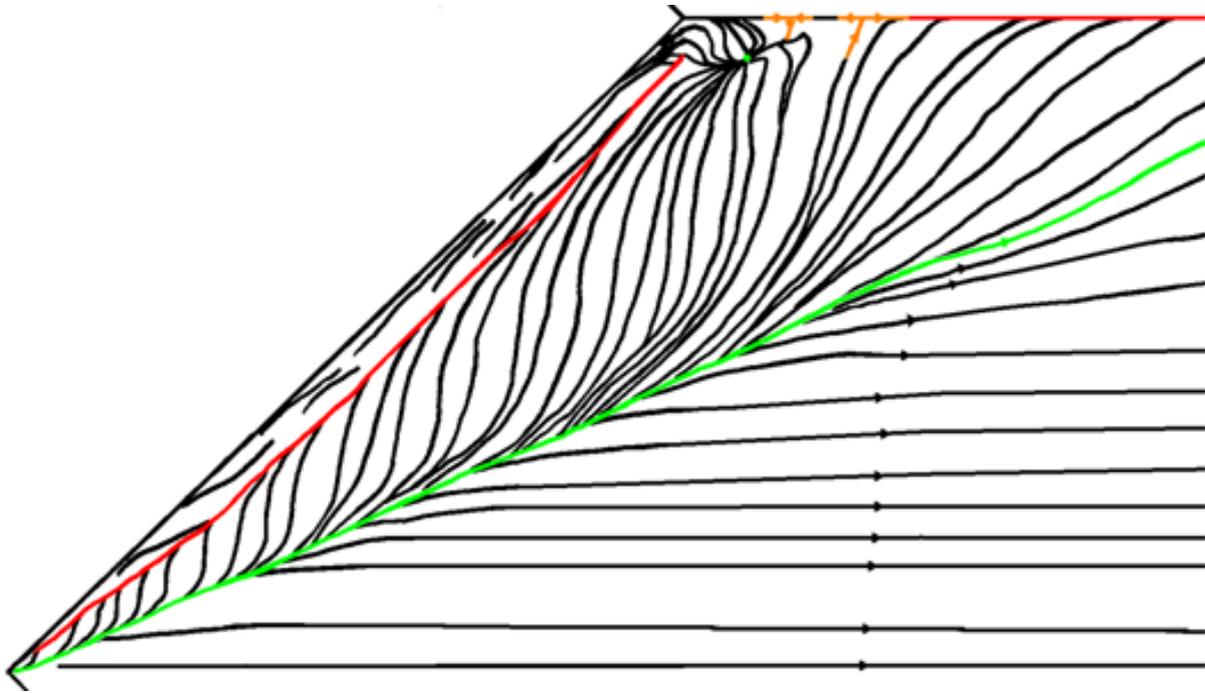
Figure 107: Flow topology over a FFS with sawtooth leading edge. *A/λ* = 0.5. Positive bifurcation lines are shown in green; negative bifurcation lines are shown in red. Saddle points are indicated with orange direction arrows. Stable nodes are indicated by green dots and arrows. Flow is from left to right.
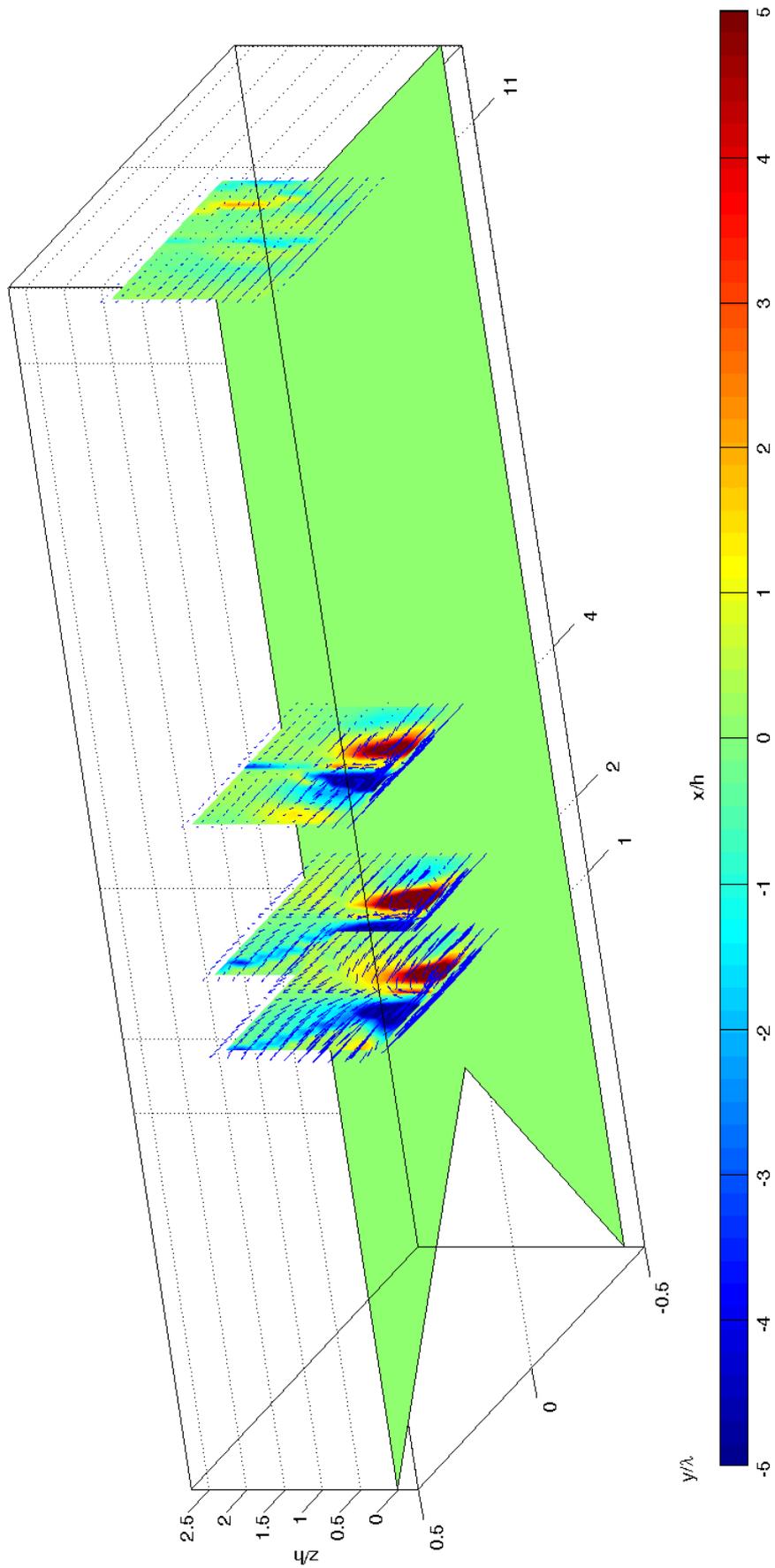
Figure 108: Normalised vorticity overlaid with lateral and vertical velocity components from Cobra Probe measurements over *A/λ* = 0.5 case.

189
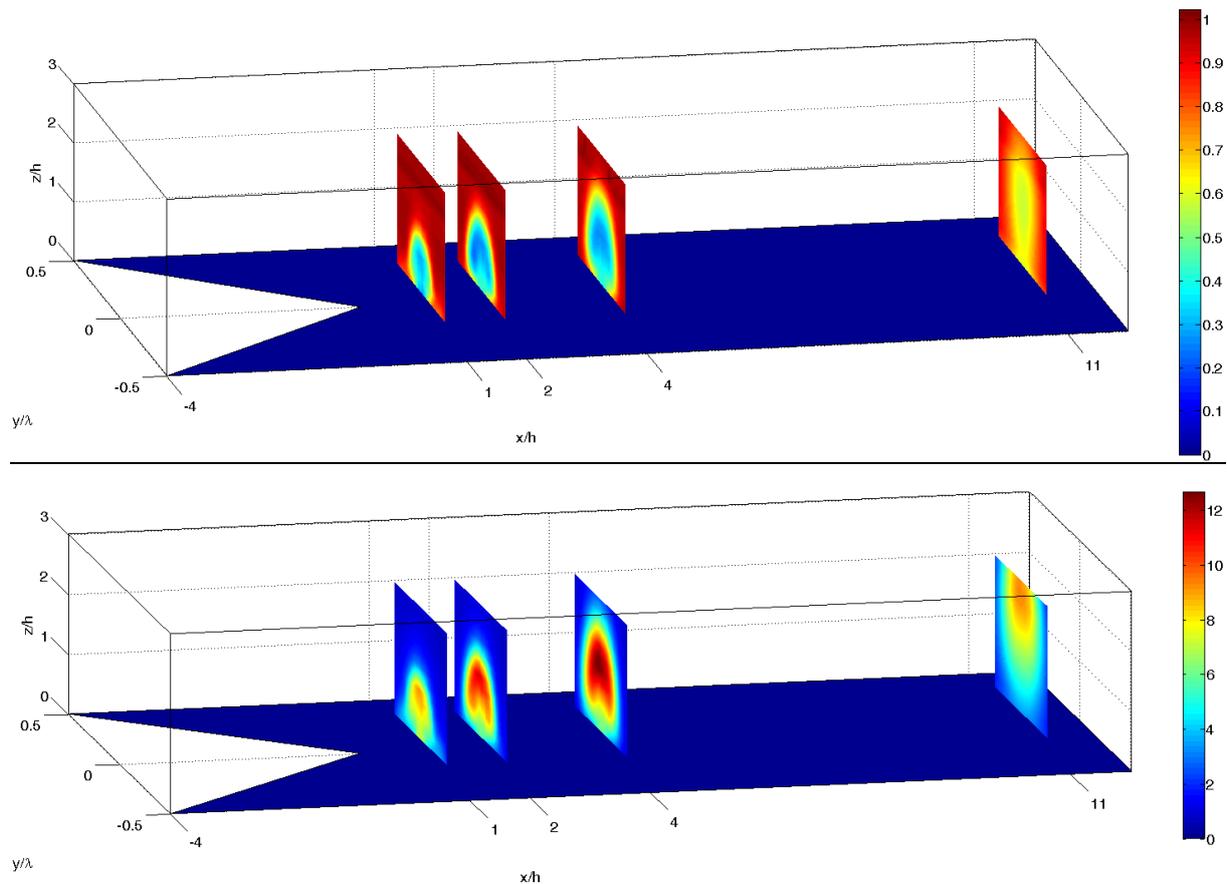
Figure 109: Speed-up (top) and Turbulence Intensity Ratio (bottom) over sawtooth FFS with *A/λ* = 0.5.

The aim of the Cobra Probe measurements was to better understand the interaction between the delta wing style vortices propagating downstream either side of the trough line. Thus, the measurement planes are all downstream of the trough, and the lateral variation is limited to -0.25 < *y/λ* < 0.25, where *y/λ* = 0 corresponds to the trough line. The Strouhal number bins have a width of 0.05, except at either end of the Strouhal number range. Strouhal numbers below St < 0.06 are considered as a single, low frequency bin. Strouhal numbers above St > 0.61 are considered as a single, high frequency bin. This range incorporates all data at Strouhal number values greater than one-third of the Nyquist frequency. The high frequency bins are associated with shear layer vortices as well as the chaotic breakdown of the coherent structures.

 At *x/h* = 1 the spectrum is dominated by the St > 0.61 bin, as shown in Figure 111. The limitations of the Cobra Probe in terms of its ability to capture the high frequency fluctuations is discussed in Section 6.2.1 *A/λ = 0.325*. Shear layer vortices can occur within the delta wing vortex structure (Gad-

190

el-Hak and Blackwelder 1985, Gordnier and Visbal 1994, Gursul 2005), as was highlighted in Section 6.2.1 *A/λ = 0.325*. Identifying that there are high frequency fluctuations is consistent with the presence of fine scale, shear layer vortices, as well as the decay of the coherent vortex structures into fine scale turbulence.

While there is clearly a dominant high frequency component across the *x/h* = 1 plane, secondary fluctuations can also be identified. At the lateral extents of the measurement domain, while the peak frequency is associated with the St > 0.61 bin, it is a low frequency bin (0.06 < St < 0.1) that contains the next highest energy levels. However, in the region associated with the vortex core, no such low frequency secondary fluctuation is observed.

The reason for the low frequency fluctuation at the lateral extremes of the measurement regime is unknown, but it may be associated with the vortex wandering that Gursul and Xie (2000) describe over delta wings. Gursul and Xie (2000) ascribe the wandering to the interaction between the shear layer vortices and the primary vortex core, an observation subsequently recorded by various researchers (Gordnier and Visbal 2003, Yaniktepe and Rockwell 2004). This theory is consistent with the spectral observations, though Gursul and Xie (2000) observed this phenomenon upstream of vortex breakdown. The values of speed-up observed in Figure 109 indicate that vortex breakdown had already occurred, having already transitioned from a jet-like flow to a wake-like flow.

In the *x/h* = 2 plane shown in Figure 112, there is a strong shedding signal across three Strouhal number bins covering the range 0.11 < St < 0.25. Additionally, along the trough line the St > 0.61 bin becomes dominant. This is indicative of the continuing decay of the wake-like flow. The St > 0.61 bin is dominant on each side of each of the propagating vortices; the peak in the St > 0.61 bin in the outer layer is driven by the shear between the free-stream flow and the vortex.
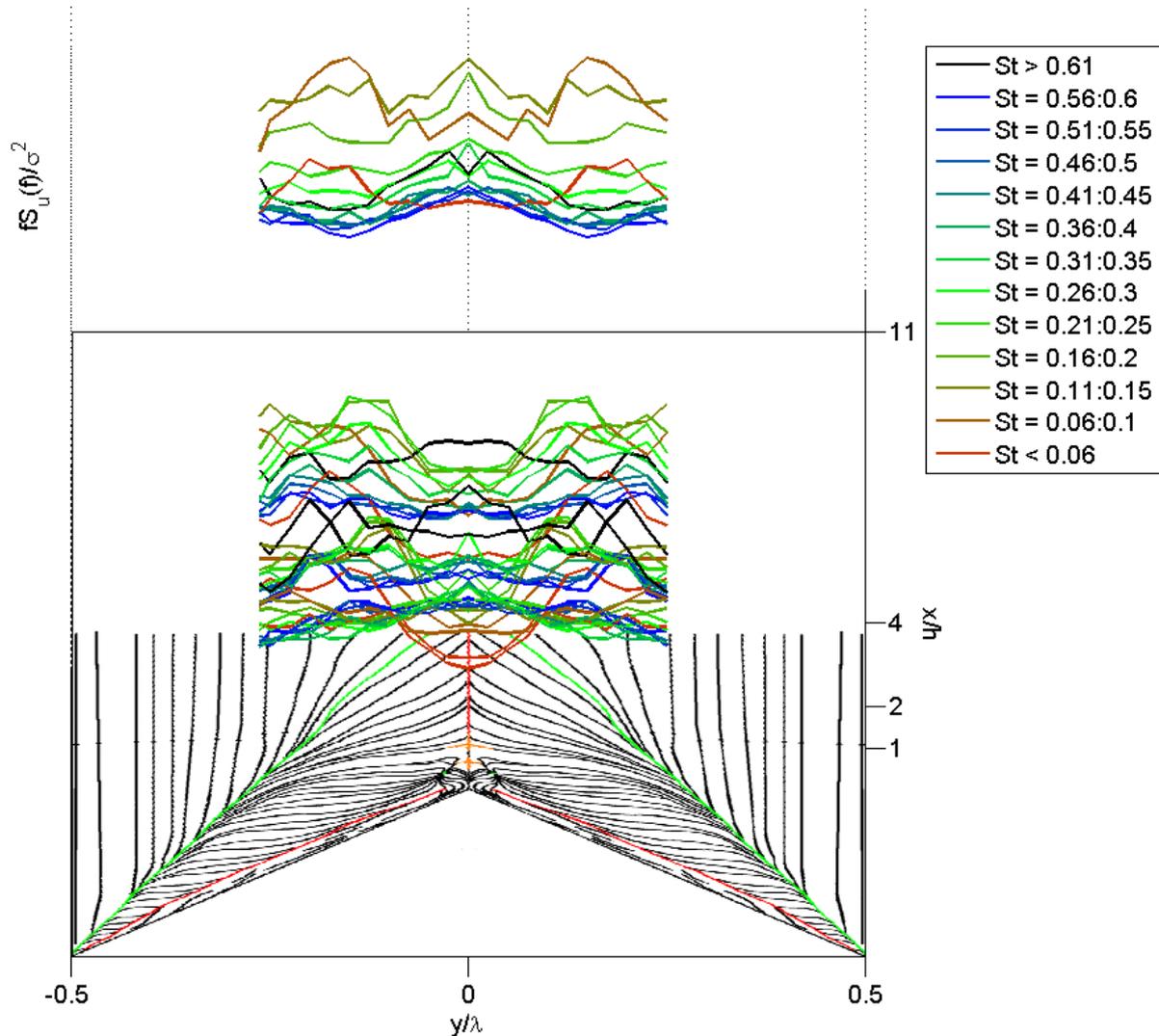
Figure 110: Normalised PSD maxima from each Strouhal number bin, shown at each spatial location over the topological skeleton for a single height, *z/h* = 1. *A/λ* = 0.5.

By *x/h* = 4, shown in Figure 113, the dominance of the St > 0.61 bin is only observed along the trough line. However, the relative energy content in the St > 0.61 bin does increase marginally at the outer extremities of the traverse, which is consistent with the vortex-free-stream interaction, with the dissipating vortex resulting in a reduction in shear.

The low frequency shedding can still be observed. However, it is distinct from what was observed at *x/h* = 2, the dominant Strouhal number is consigned to only two bins, within the Strouhal number range 0.16 < St < 0.25. This reduction of range is noteworthy. Gursul (1994) observed that the

breakdown of the burst vortex results in a growth in the radius of the vortex core, which is associated with a decrease in Strouhal number. Between x/h = 2 and x/h = 4, this observation does not hold. However, by x/h = 11, shown in Figure 114, there is, once again, a reduction in the Strouhal number associated with the most relative energy, with the St < 0.06 bin containing the most energy. Further discussion of this point is presented in Section 6.2.5 *Comparison with Flow over Delta* Wings.
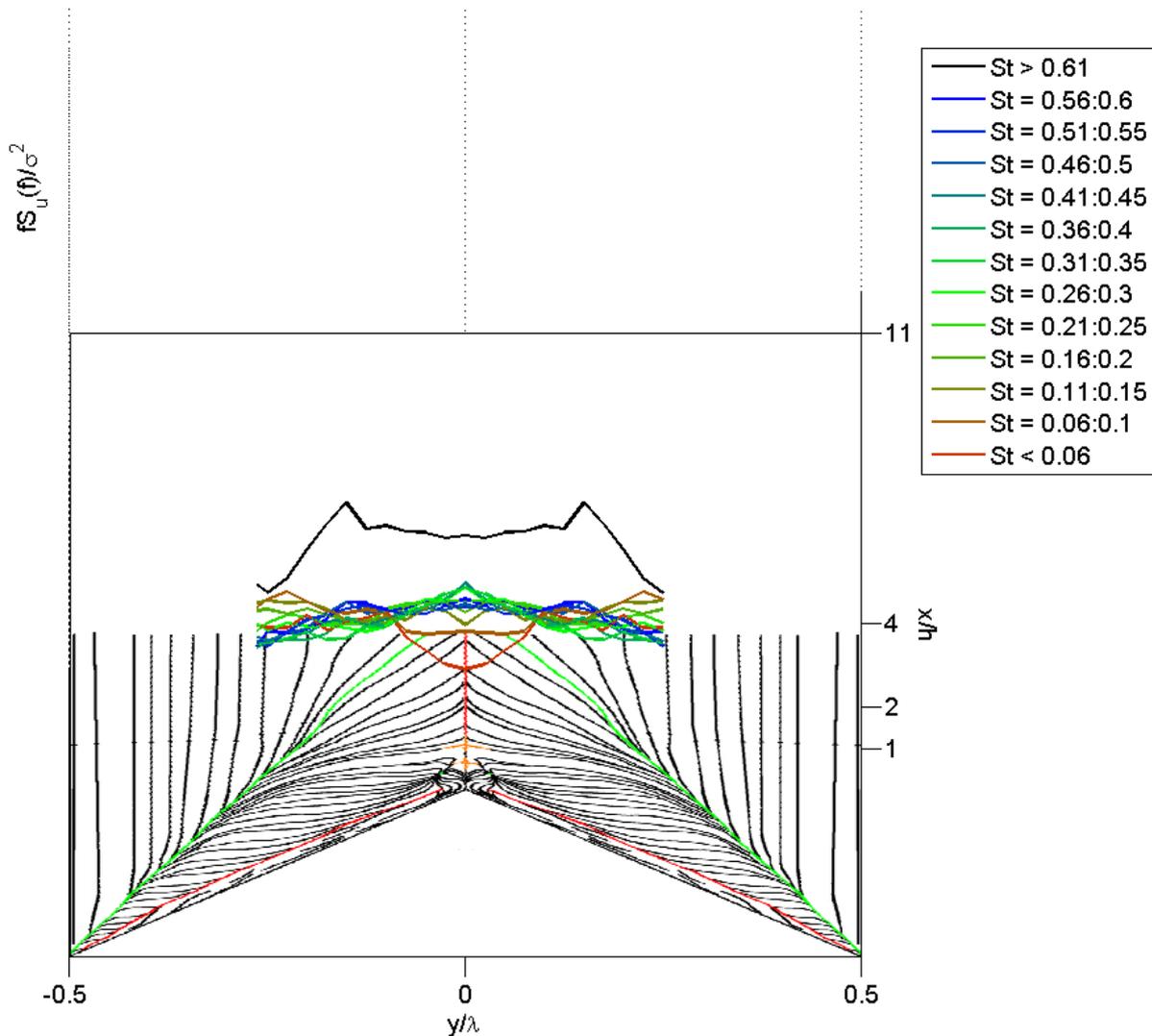

Figure 111: Normalised PSD maxima from each Strouhal number bin, shown at lateral locations, centred on the trough point of the sawtooth with *A/λ* = 0.5 and *z/h* = 1. Plot shown corresponds to *x/h* = 1.

The model configuration was also examined numerically. The simulation was run as a transient model (Harbig 2013). The mean surface shear stress lines generated by the CFD model are presented in Figure 118.
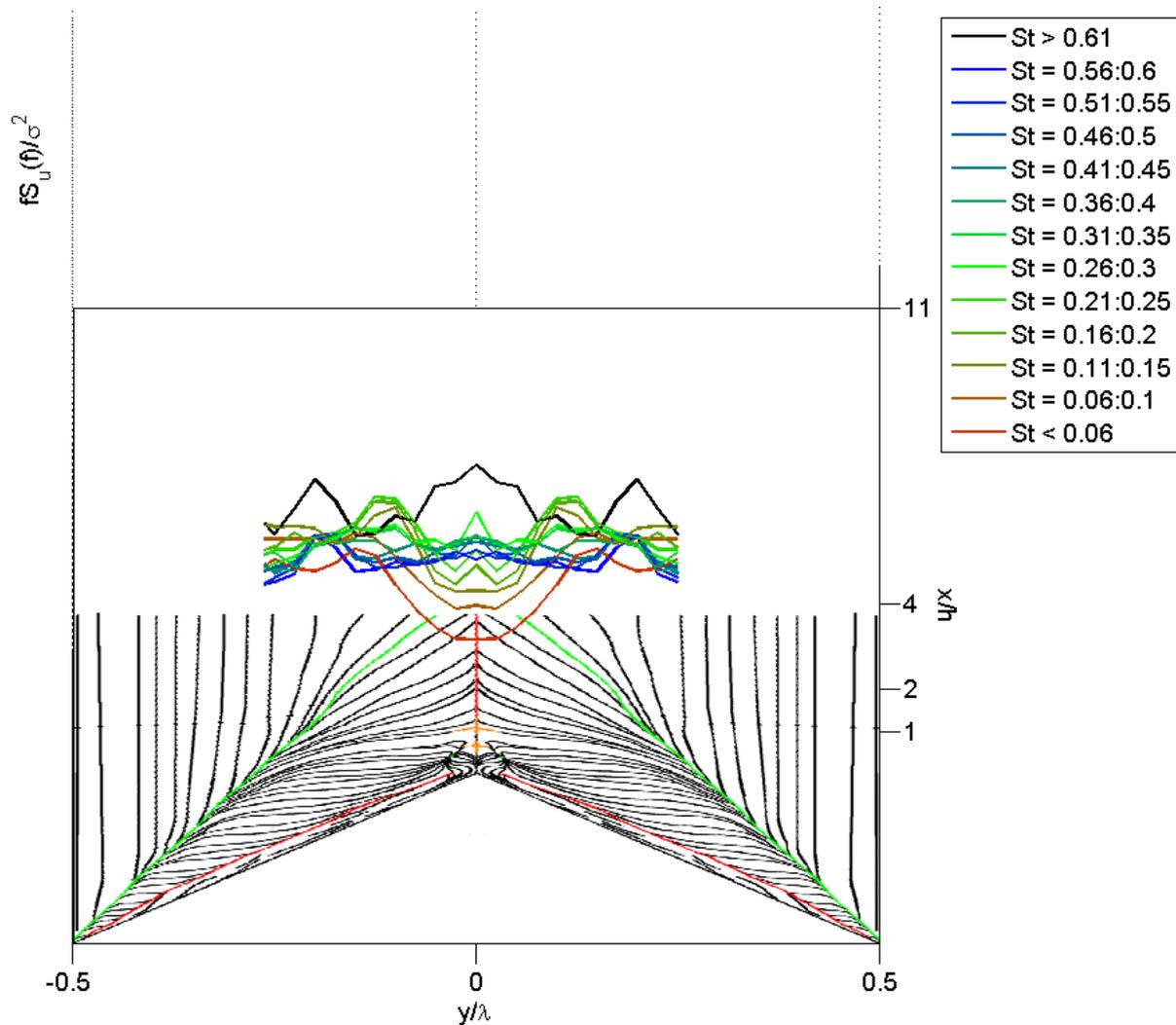
Figure 112: Normalised PSD maxima from each Strouhal number bin, shown at lateral locations, centred on the trough point of the sawtooth with *A/λ* = 0.5 and *z/h* = 1. Plot shown corresponds to *x/h* = 2.

The agreement between the numerical work and the experimental work is evident only on the broad scale. For example, the angle between the positive bifurcation line, shown in green in Figure 107, and the crest, is 20° in both the experimental and the numerical work. Further agreement is seen in the presence of the secondary structures that run along the crest. The initial visualisations suggested that there might be more than one secondary structure in this region, but the determination of the exact topology would have required resolution in excess of what the visualisation technique was

capable. In contrast the mean topology from the numerical work, shown in Figure 118, reveals the

primary structure, as well as clearly revealing two secondary structures. A comparison of the raw

velocity fields is presented in Figure 115. While the twin structures are clearly depicted in the CFD

results, they are not as obvious in the wind tunnel results. The velocity magnitudes and the sizes of

the vortex structures are, nevertheless, similar.
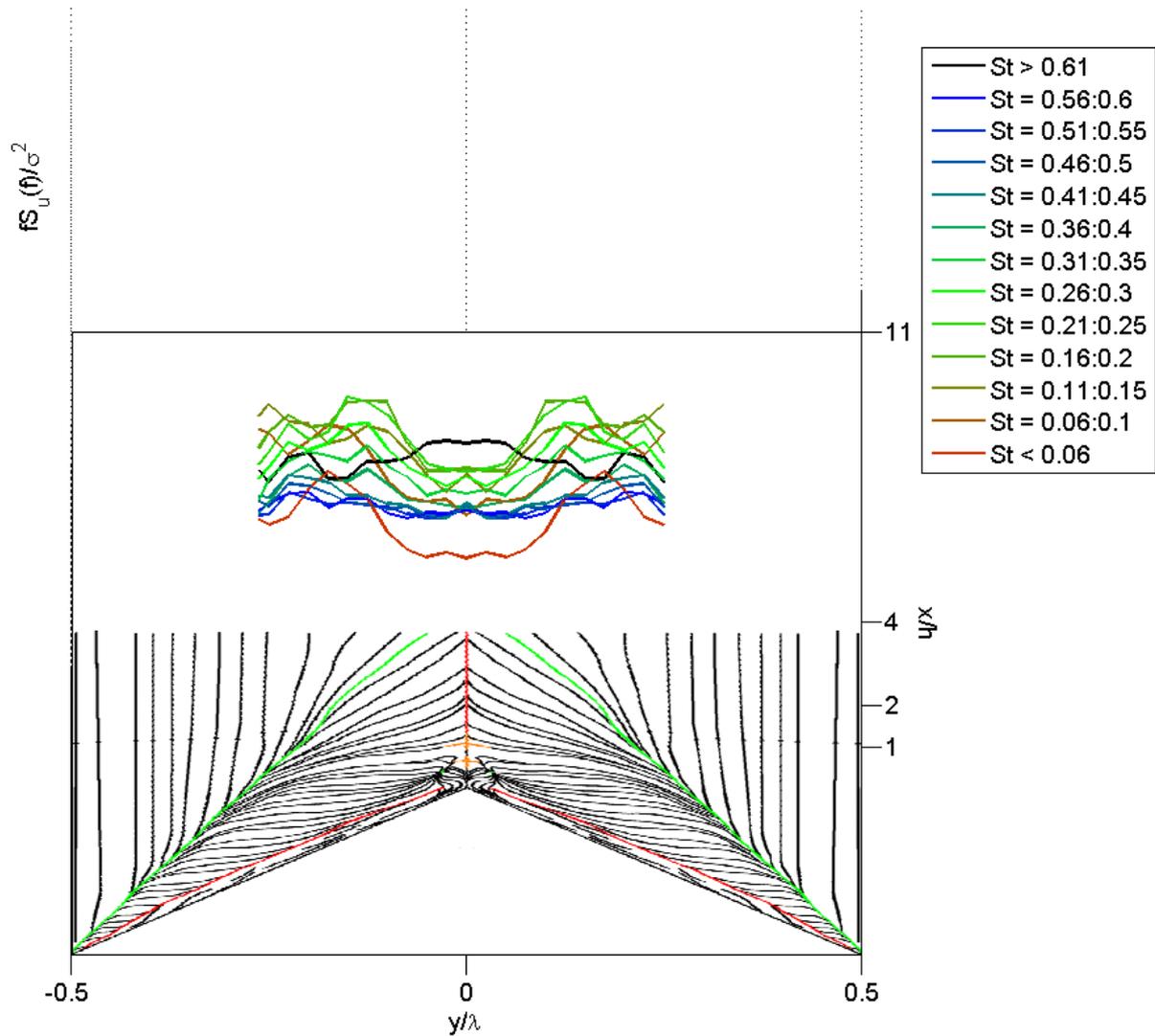
Figure 113: Normalised PSD maxima from each Strouhal number bin, shown at lateral locations, centred on the trough point of the sawtooth with *A/λ* = 0.5 and *z/h* = 1. Plot shown corresponds to *x/h* = 4.
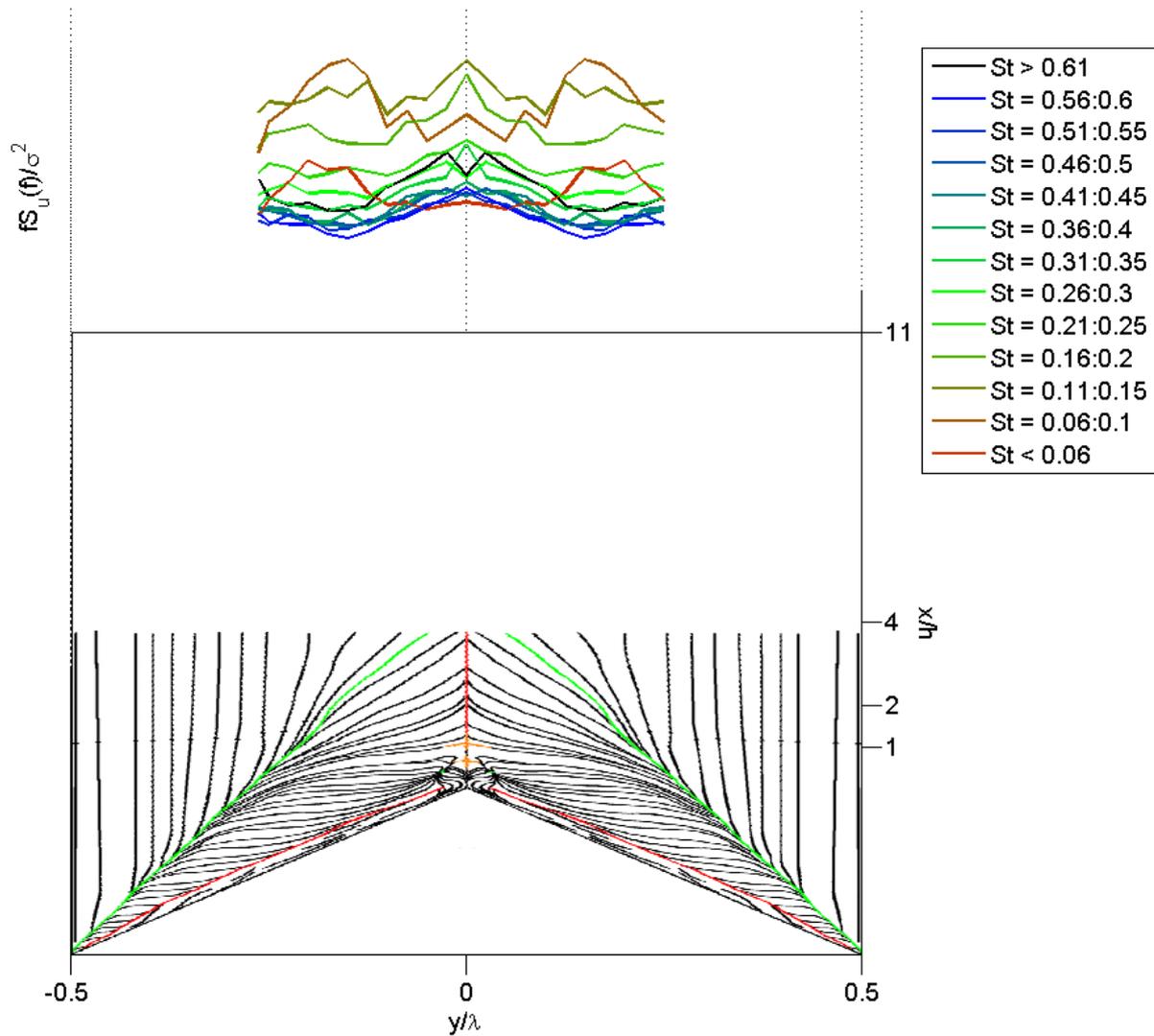
Figure 114: Normalised PSD maxima from each Strouhal number bin, shown at lateral locations, centred on the trough point of the sawtooth with *A/λ* = 0.5 and *z/h* = 1. Plot shown corresponds to *x/h* = 11.

A direct comparison of the surface pressure coefficients with those obtained in the wind tunnel tests of Cochard et al. (2012) is possible. The surface pressure over a sawtooth element from Cochard et al. (2012) is presented in Figure 116. The magnitude of the pressure coefficients are extremely similar, in both cases they are in the vicinity of unity in the region associated with the vortex. The size of the vortex region in each of these cases is also closely comparable.

There is, however, significant divergence in the topology itself with the two techniques generating non-equivalent shear stress fields. The numerical work suggests that a stable node exists on the trough point, and its saddle node is located just downstream. In looking at the surface shear stress in this region, it must be remembered that the mean shear stress is very close to zero, implying that

196

there is uncertainty in terms of the streak direction. The CFD is also not immune from such issues. Given the transient nature of the model, the mean is the accumulation of the snapshots at each time-step. The topology in Figure 118 exhibits an asymmetry along the trough axis, just downstream of the trough, indicating that there is some lateral flapping as the vortices develop downstream, requiring more time-steps to fully resolve.

The transient model revealed instability in the downstream wake. The surface shear stress appeared to flap in a manner similar to a von Kármán vortex street. Snapshots of the instantaneous wall shear stress, shown in Figure 119, exhibited a semi-periodic switching, as stable foci were formed, alternatively on either side of the trough, and shedding downstream, morphing into the dominant vortex. Snapshots from the surface pressure measurement of the corresponding model, shown in Figure 120, present a similar swirling in the trough region, which is consistent with the observations from the snapshots produced by the transient CFD modelling. Thus, a significant contrast can be drawn between the delta wing literature and what is observed here. In the delta wing literature, above a threshold angle of attack the two vortices shed from the two leading edges are observed to interact, with an alternating shedding pattern (Rediniotis et al. 1993, Katz 1999). In this case, the alternating shedding is observed, but it occurs between vortices formed on either side of the trough – which might be considered analogous to the situation where two delta wings are placed side-by-side. The current experiments could not determine the surface pressure at a resolution capable of resolving the flow topology of such detailed flow structures.

The Cobra Probe measurements, which are collected only downstream of the trough for this case, provide clear evidence of vortex bursting, as described in the delta wing literature, with low values of speed-up associated with the wake-like flow described by Gursul et al. (2005).
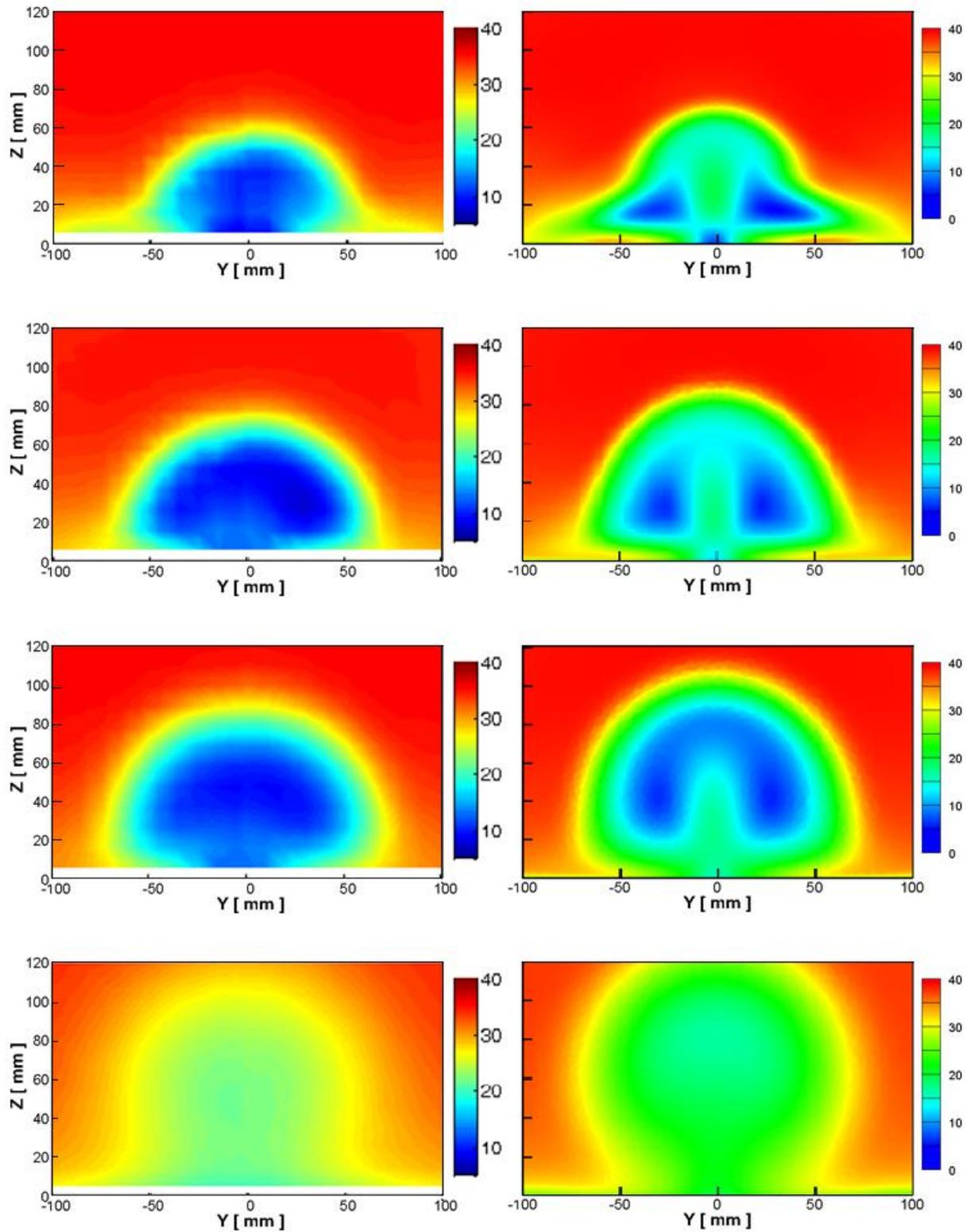
Figure 115: Velocity comparison between wind tunnel measurements (left) and CFD (right). *Y-Z* **planes from top to bottom are** *x* **= 50 mm, 100 mm, 200 mm, 550 mm. Note that the colour scales vary in each pane. Colour units are ms⁻¹.** *A/λ* **= 0.5.**
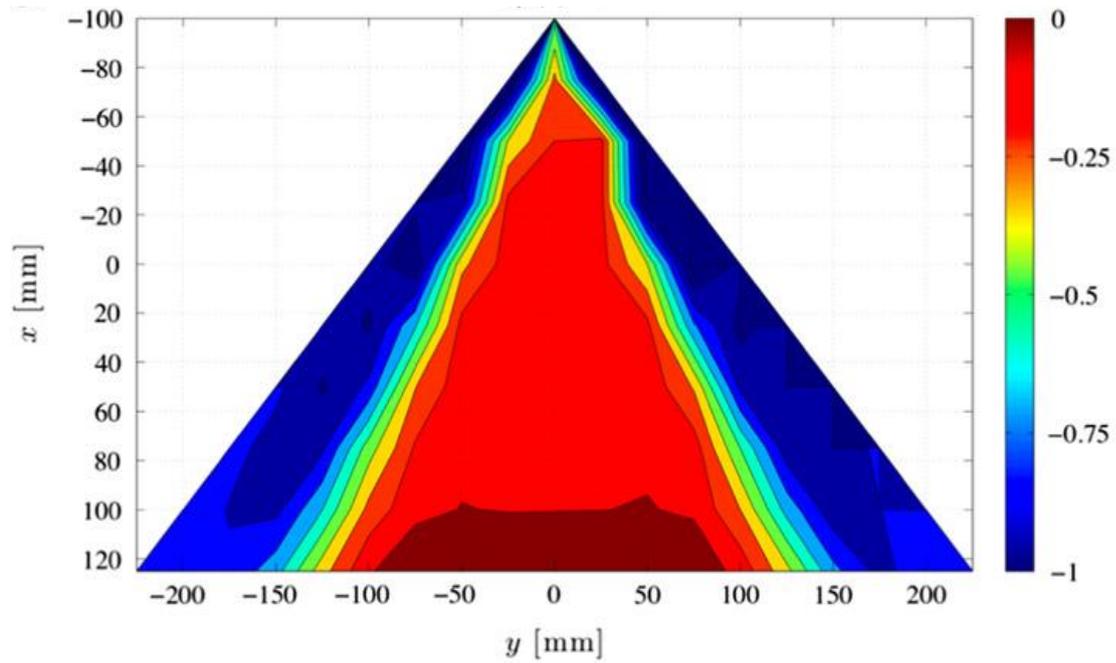
Figure 116: Surface pressure coefficients from the sawtooth FFS investigated by Cochard et al. (2012) and used with permission. Flow is from top of page to bottom. *A/λ* **= 0.5.**
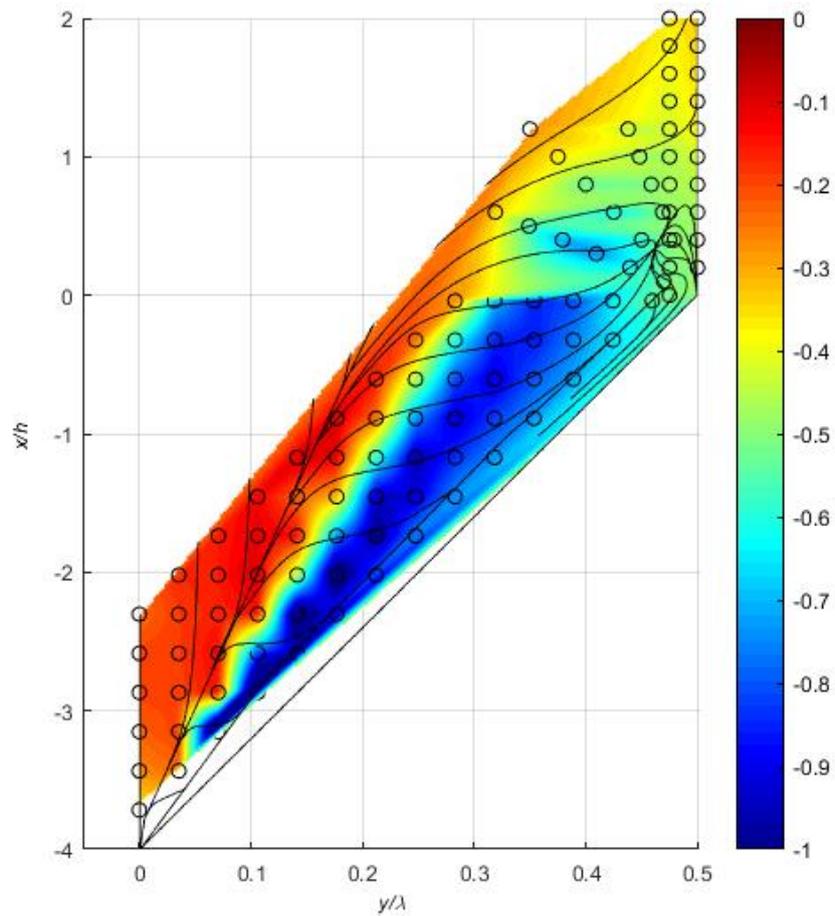

Figure 117: Surface pressure, presented as pressure coefficients, overlaid with the flow topology. Flow is from bottom of page to top. Black circles represent pressure tap locations. *A/λ* **= 0.5.**
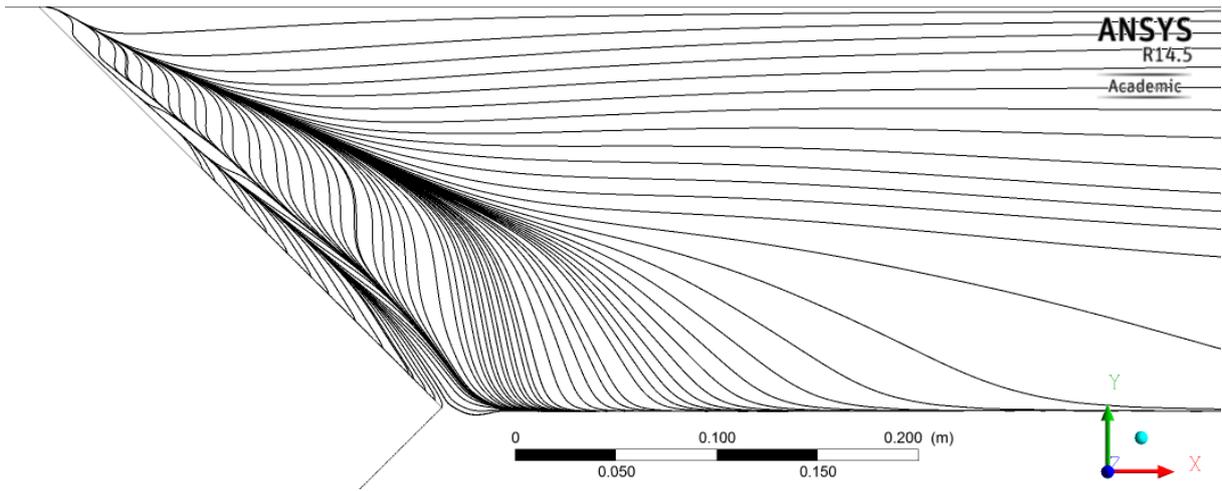
Figure 118: Mean surface shear stress lines from transient CFD model, for sawtooth FFS with *A/λ* = 0.5. Modelling courtesy of Robert Harbig (2013).
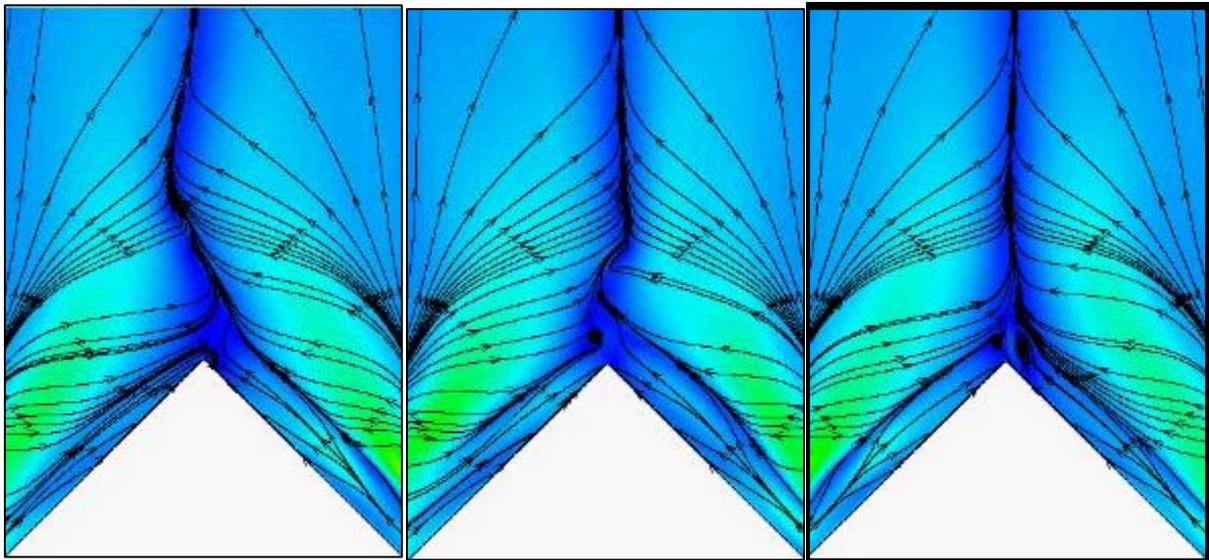

Figure 119: Instantaneous snapshots of the surface shear stress from the transient CFD model of the sawtooth FFS with *A/λ* = 0.5. Modelling courtesy of Robert Harbig (2013).
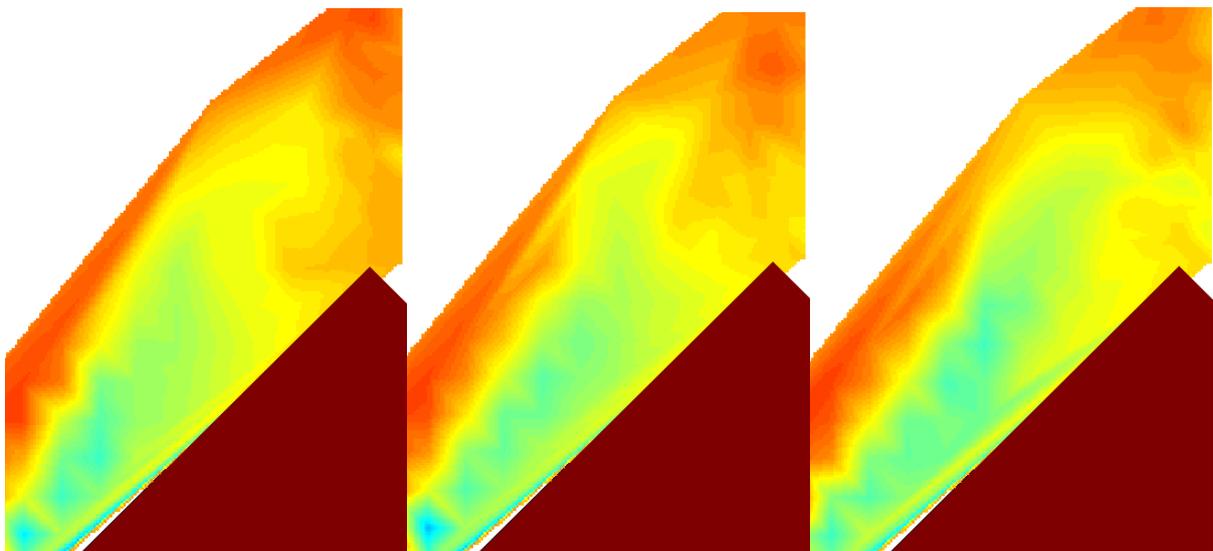

Figure 120: Instantaneous snapshots of surface pressure over the sawtooth FFS with *A/λ* = 0.5.

200

6.2.3 A/λ = 0.65

The A/λ = 0.65 case exhibited topological equivalence to the A/λ = 0.5 case and the A/λ = 0.325 case based on the experimental surface shear stress visualisations. That is, the flow topologies over these cases are of the same structure, albeit stretched or skewed relative to each other. The topology shows much greater similarity to the A/λ = 0.5 case. The topology is illustrated in Figure 121. The visualisations indicated a strong vortex structure drawing paint to the trough line, and a much weaker recirculation back to the stable node. This is almost identical to the layout of the A/λ = 0.5 case, but the upstream saddle point was pulled closer to the trough, together with the stable node. Also, as A/λ increased, the effective yaw angle of the sawtooth increased. The effect was that the shear stress lines in the vortex regions were rotated through a smaller angle, indicating that they were increasingly influenced by the free-stream flow.

The comparison CFD case behaved in a more stable manner than the A/λ = 0.5 case, with the RANS solution converging (Harbig 2013). Surface pressure, presented as pressure coefficients, from the wind tunnel measurements and CFD, are shown in Figure 122 and Figure 123, respectively. This comparison of surface pressure indicates good agreement between the wind tunnel testing and the CFD modelling; with comparable magnitude of pressure coefficients and growth in diameter of the vortex structures observed in both cases. The fine-scale detail, including the secondary vortex structures along the crest that are observed in the CFD analysis, is not captured in the pressure measurements due to the low resolution associated with the surface pressure measurements.

The surface shear stress lines and near surface velocity are presented in Figure 124. While there are inconsistencies between the CFD topology and the experimental solution, the near surface velocities agree well. The regions identified in the CFD analysis with mean velocity approaching zero correspond well with the critical points identified in the experimental visualisations.

The near surface velocity field generated by the CFD modelling indicates four regions where the velocity approaches zero, as shown in Figure 124. The Iso-Q surfaces are presented in Figure 125 to help visualise the mean vortex structure.
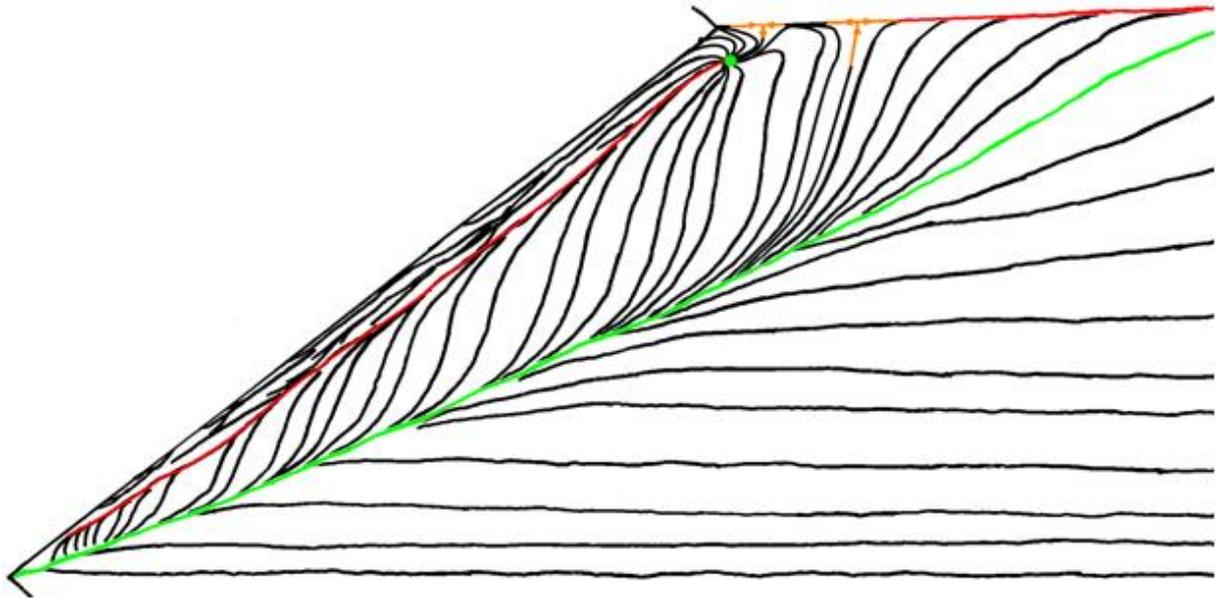

Figure 121: Flow topology over a FFS with sawtooth leading edge. *A/λ* = 0.65. Critical points defined as in Figure 107. Flow is from left to right.
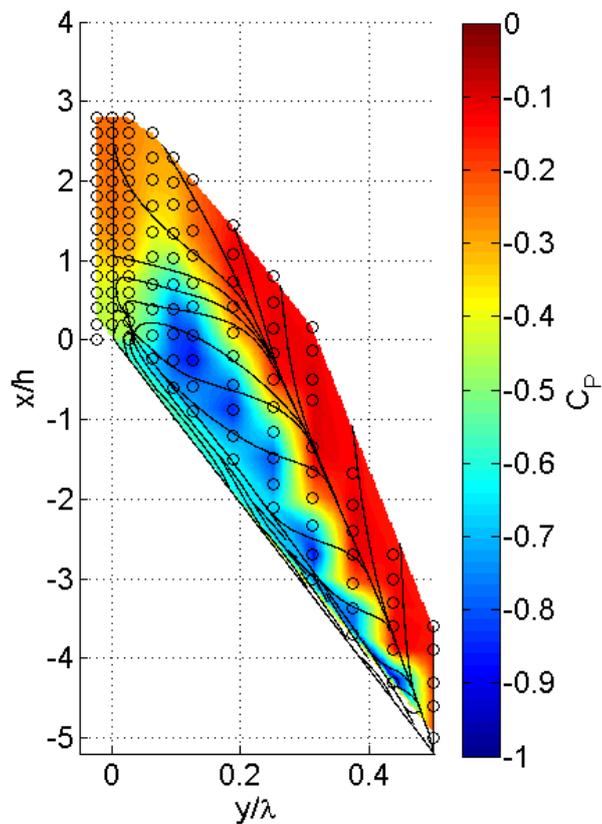

Figure 122: Surface pressure, presented as pressure coefficients, overlaid with the flow topology. Flow is from bottom of page to top. Black circles represent pressure tap locations. *A/λ* = 0.65.
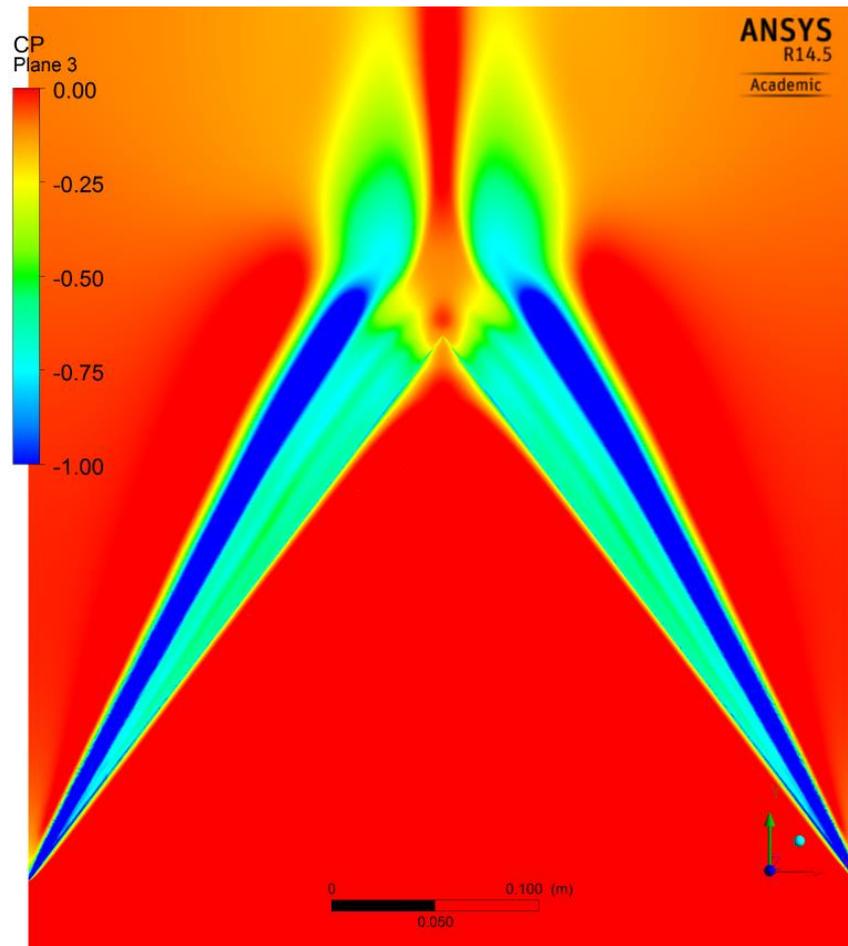
Figure 123: Mean pressure coefficient from the CFD investigation conducted by Harbig (2013). Flow is from bottom to top. A/λ **= 0.65.**

The surface visualisation from the experimental work identified two saddle nodes along the trough

line. These are shown in orange in Figure 121. The upstream of the two saddle points is downstream

of the trough point, dividing the streamlines from the primary structure from those of the secondary

structures along the crest. Turning the flow from the secondary structures toward the stable node,

denoted by the green point in Figure 121 induces some rotation in the trough region around the

stable node. In the shear stress visualisations generated by the CFD model in Figure 124, the

stagnant regions coloured in blue, either side of the trough axis are farther downstream than the

stable node in the experimental topology presented in Figure 121. They appear to be caused by the

rotation induced by the interaction between the primary vortex and the persistence of the

secondary structures along the crest through to the trough and slightly beyond. The CFD results

allow the reader to better visualise the secondary structures along the crest, however they exhibit

some discrepancies with the experimental work, with the computational model predicting a larger diameter secondary vortex region in both the A/λ = 0.5 case, and the A/λ = 0.625 case, explaining the discrepancy in how far downstream the stagnation regions occur.

The differences in the secondary structures between the experimental and numerical results also affect the topology in the immediate vicinity of the crest. In the surface shear stress lines generated by the CFD in Figure 124, stable nodes appear on either side of the trough point, on the crest. Thus, a saddle point is located on the trough, in much the same way as in the A/λ = 0.325 case. To satisfy the Poincaré-Bendixson Theorem a second saddle point is located immediately downstream of the first, in the same location as the upstream of the two saddle points that were located in the experimental work. However, this corresponding saddle point in the CFD result is of the opposite type, being rotated by 90°, and does not provide the same interaction with the primary vortex as is seen in the experimental work.

The farthest downstream of the low velocity regions in the left pane of Figure 124 also corresponds in spatial location with the downstream saddle node observed in the experiments. The Iso-Q surfaces in Figure 125 and Figure 126 indicate that this is where the primary vortex lifts off the surface, leaving a pair of counter-rotating vortices persisting downstream. While the role of the saddle node in each case is slightly different, they both signal the downstream limit of the interactions between the secondary structures, the primary structures and the trough. Downstream of that point, there is only the interaction between the pair of counter rotating vortices.
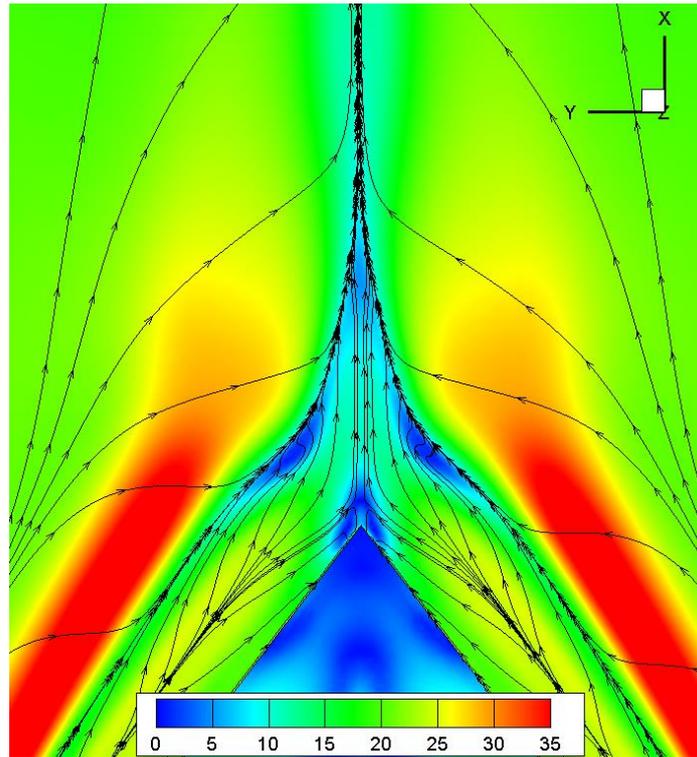
Figure 124: Surface shear stress lines based on CFD modelling for a FFS with sawtooth lateral variation, courtesy of Robert Harbig (2013). A/λ = 0.65. Colouring represents near surface flow speed in ms^{-1}.
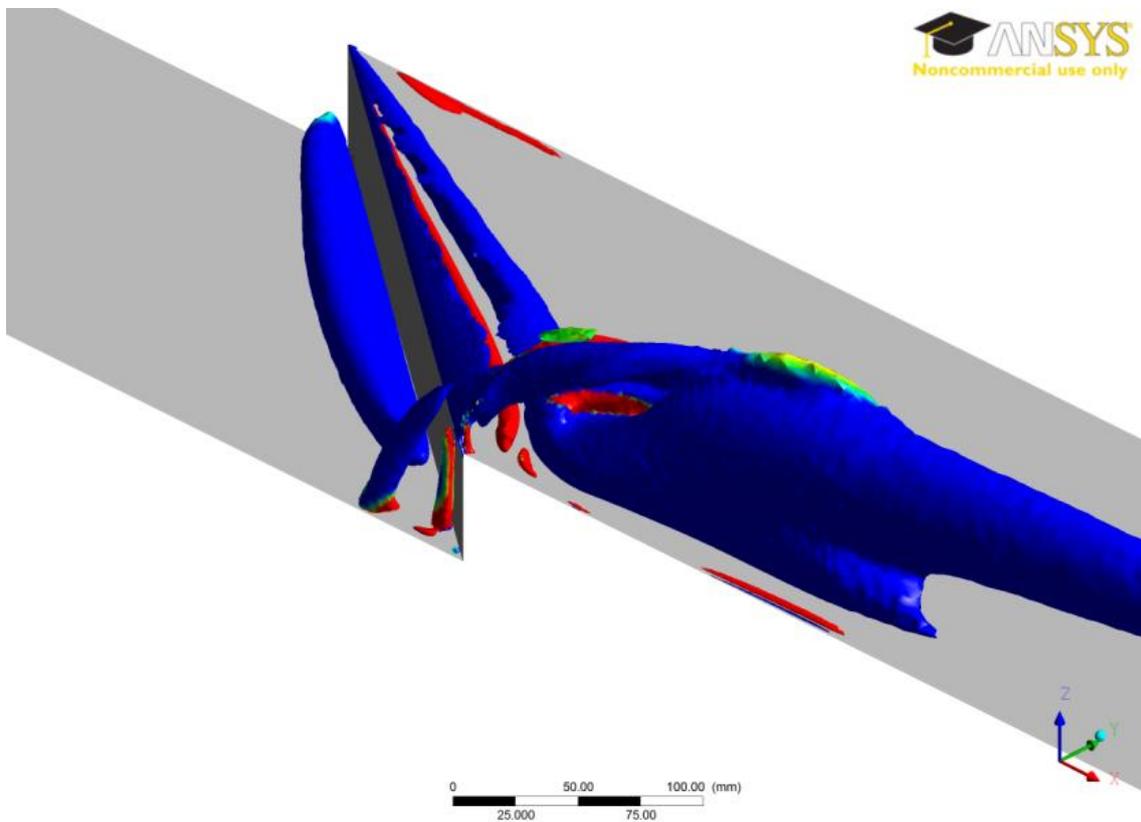
**Figure 125: Iso-Q surfaces coloured by stream-wise vorticity, courtesy of Robert Harbig (2013).** A/λ = 0.65.

205
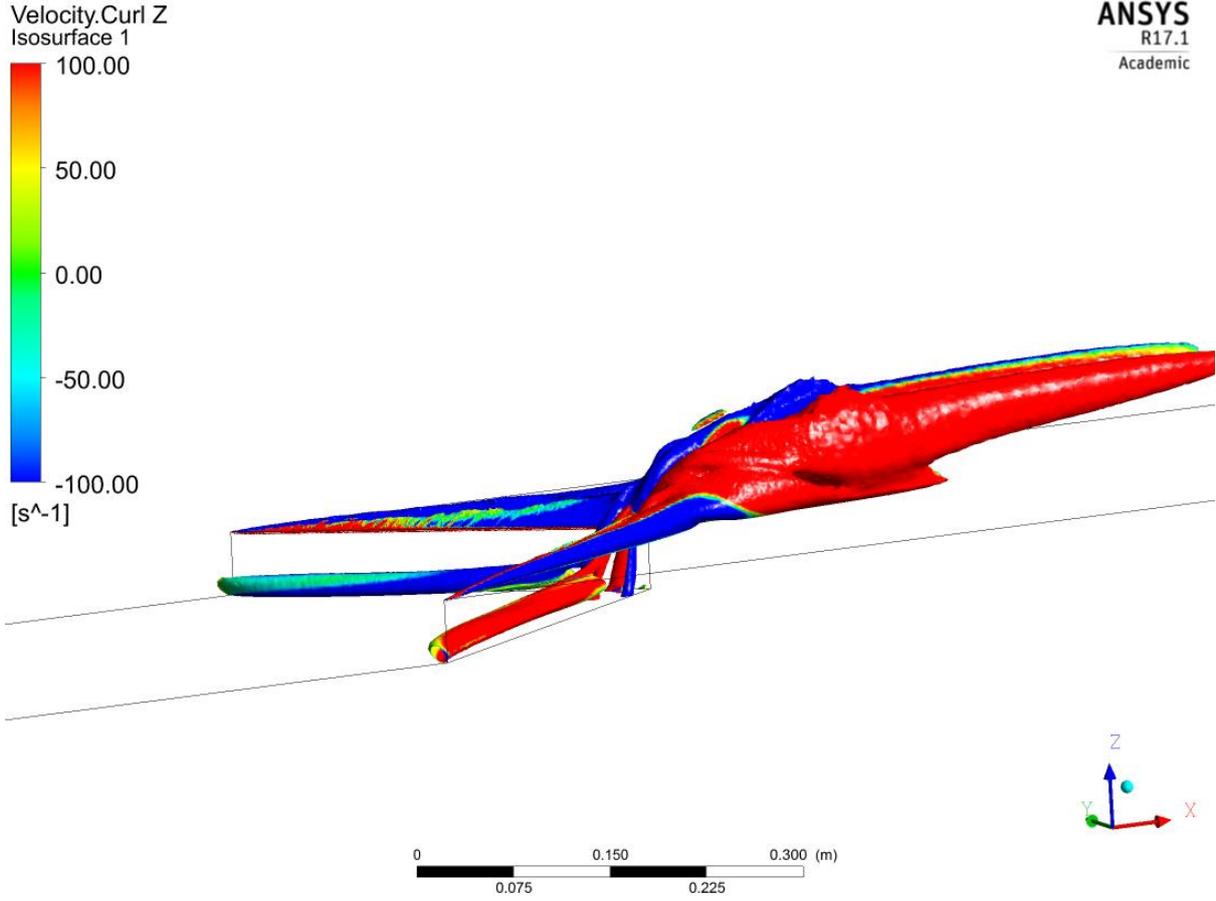
Figure 126: Alternative view of Iso-Q surfaces coloured by stream-wise vorticity, courtesy of Robert Harbig (2013). *A/λ* **= 0.65.**

6.2.4 A/λ = 1

In the *A/λ* = 1 case, a fourth stage of flow development was observed in the experimental work. The

mean topology is more complex than the previous cases. The delta wing vortex structure generated

from the peak is unchanged, complete with the secondary structure generated along the crest.

However, the interaction between the two vortices at the trough region generated finer scale

vortices, which lifted off the surface. In the half cycle shown in Figure 127, this is seen as one-and-a-

half counter-rotating vortex pairs lifting off the surface, resulting in foci on the surface. This mean

topology is similar to some of the instantaneous snapshots observed in the *A/λ* = 0.5 case.
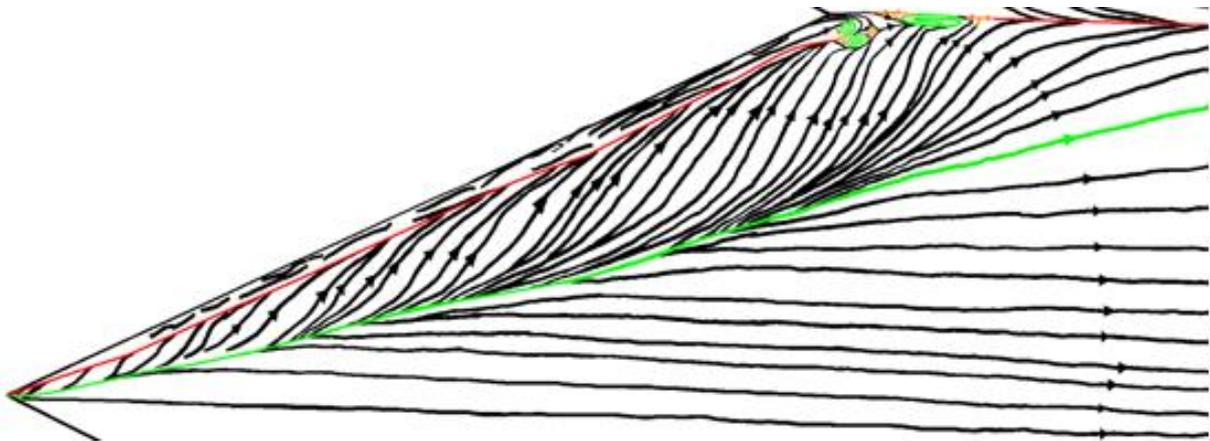
Figure 127: Flow topology over a FFS with sawtooth leading edge. *A/λ* = 1. Critical points as in Figure 107. Green swirls represent stable foci.

Figure 128: Close-up view of trough region of topological skeleton presented in Figure 127. *A/λ* = 1.

The development of the two counter-rotating foci in a similar location to the stable node in the

A/λ = 0.65 case is consistent with the curvature of the skeleton lines approaching the stable node in

that shallower case. In generating the two foci, two extra saddle points are, by necessity, created.

These junctions must exist to facilitate flow between the nodes. The two new saddle points are

more clearly presented in the close-up in Figure 128. With the development of the new saddle

points, a stable critical point must then exist to satisfy by the Poincaré-Bendixson Theorem. This new

207

critical point is the stable foci adjacent to the trough line. The pair of vortices located either side of the trough line result in a powerful, swirling updraft.
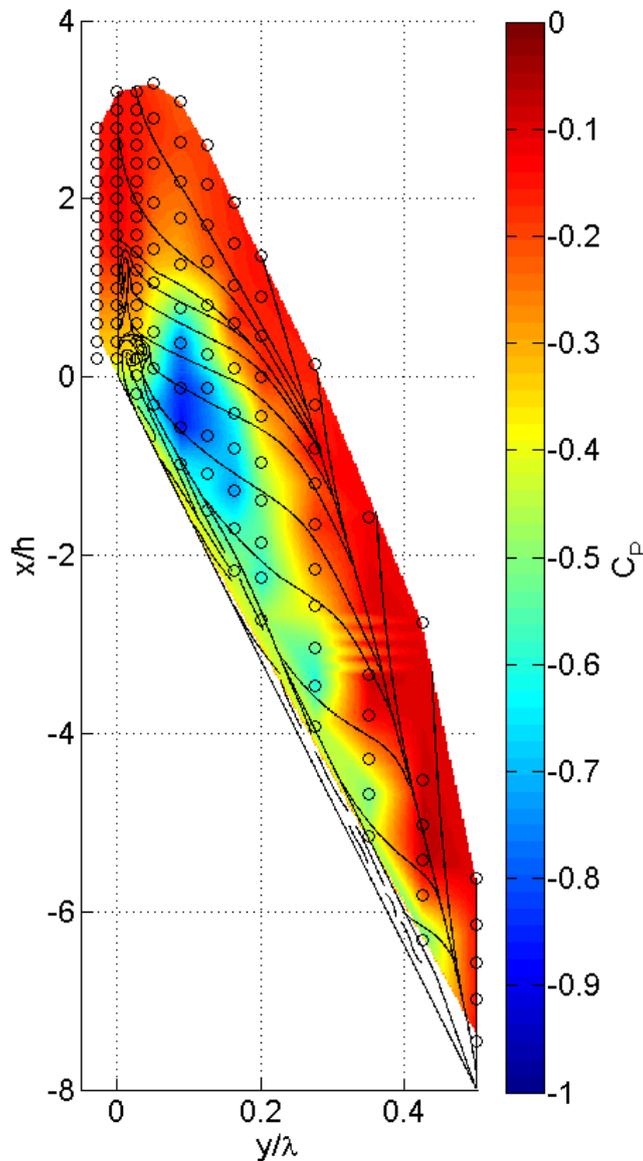
Figure 129: Surface pressure, presented as pressure coefficients, overlaid with the flow topology. Flow is from bottom of page to top. Black circles represent pressure tap locations. *A/λ* = 1.

Surface pressure measurements are compared with modelled surface pressure coefficients in Figure 129 and Figure 130, with reasonable agreement in the magnitude and distribution of the pressure coefficients. While the pressure taps give an indication of the magnitude of the surface pressure coefficients, the resolution is not sufficient to capture the fine structure that was observed in the surface shear stress visualisations, or the CFD modelling. Nevertheless, the largest regions of peak negative pressures are observed alongside the trough point. The near surface velocity overlayed

with the surface shear stress lines derived from the CFD modelling is presented in Figure 131, while

the Iso-Q surfaces are shown in Figure 132. The Iso-Q surfaces provide a useful visualisation of the

flow structure, in particular, the vertical up-flow structures are evident, consistent with the foci

identified in the surface shear stress visualisation experiments. Topological equivalence between the

CFD modelling and the topology derived from the experimental work was also observed.
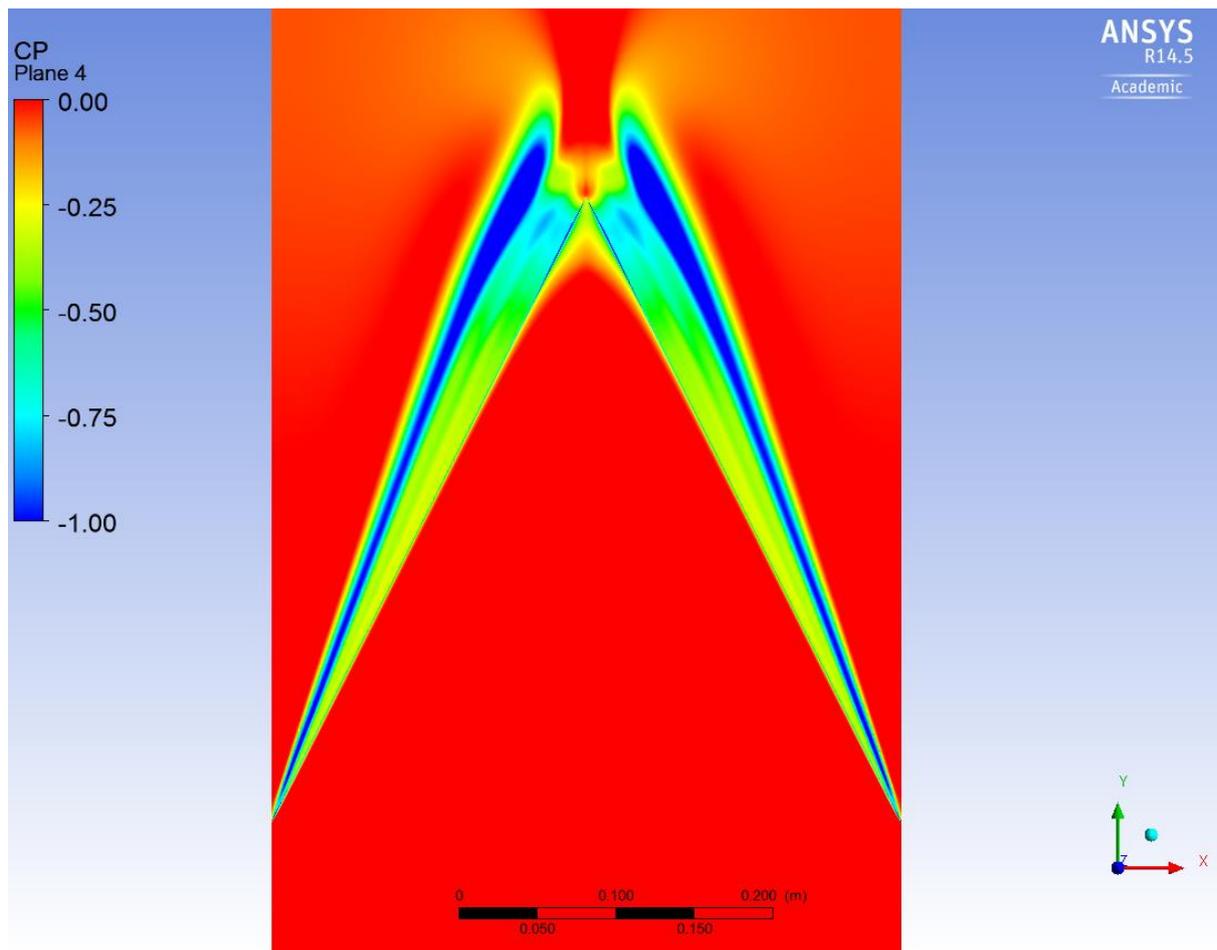
Figure 130: Mean pressure coefficient from the CFD investigation conducted by Harbig (2013). Flow is from bottom to top. A/λ = 1.
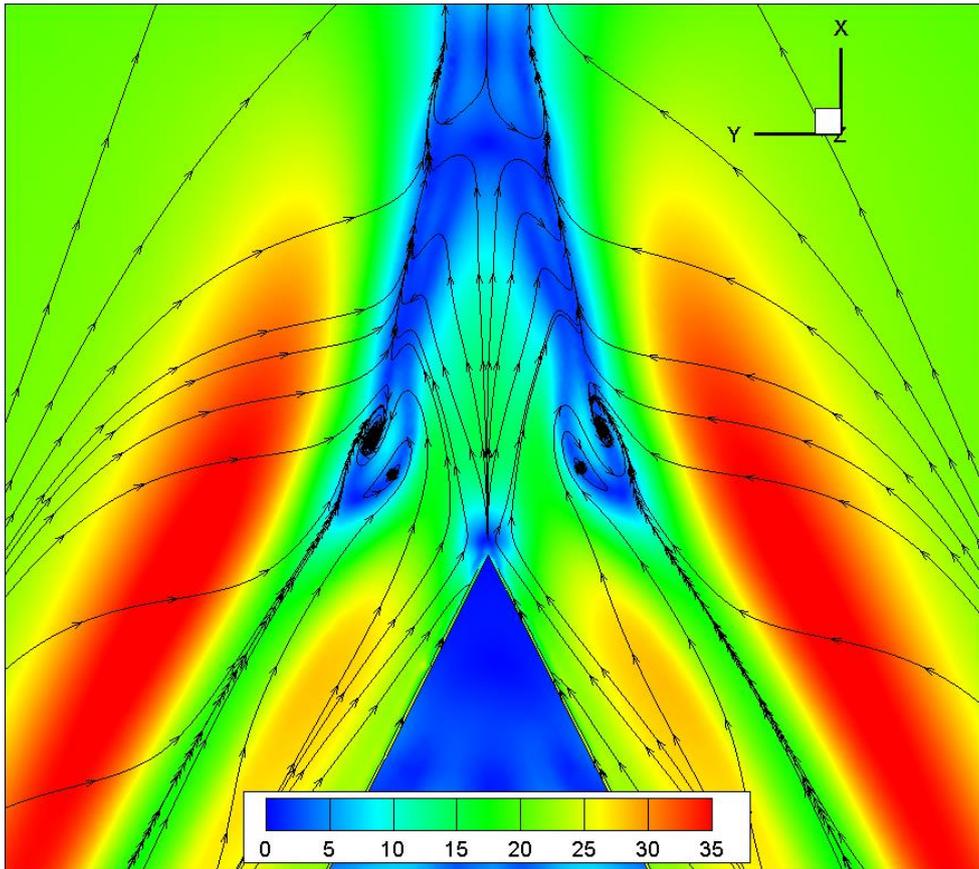
Figure 131: Surface shear stress lines based on CFD modelling for a FFS with sawtooth lateral variation, courtesy of Robert Harbig. A/λ = 1. **Colouring represents near surface flow speed in ms^{-1}.**
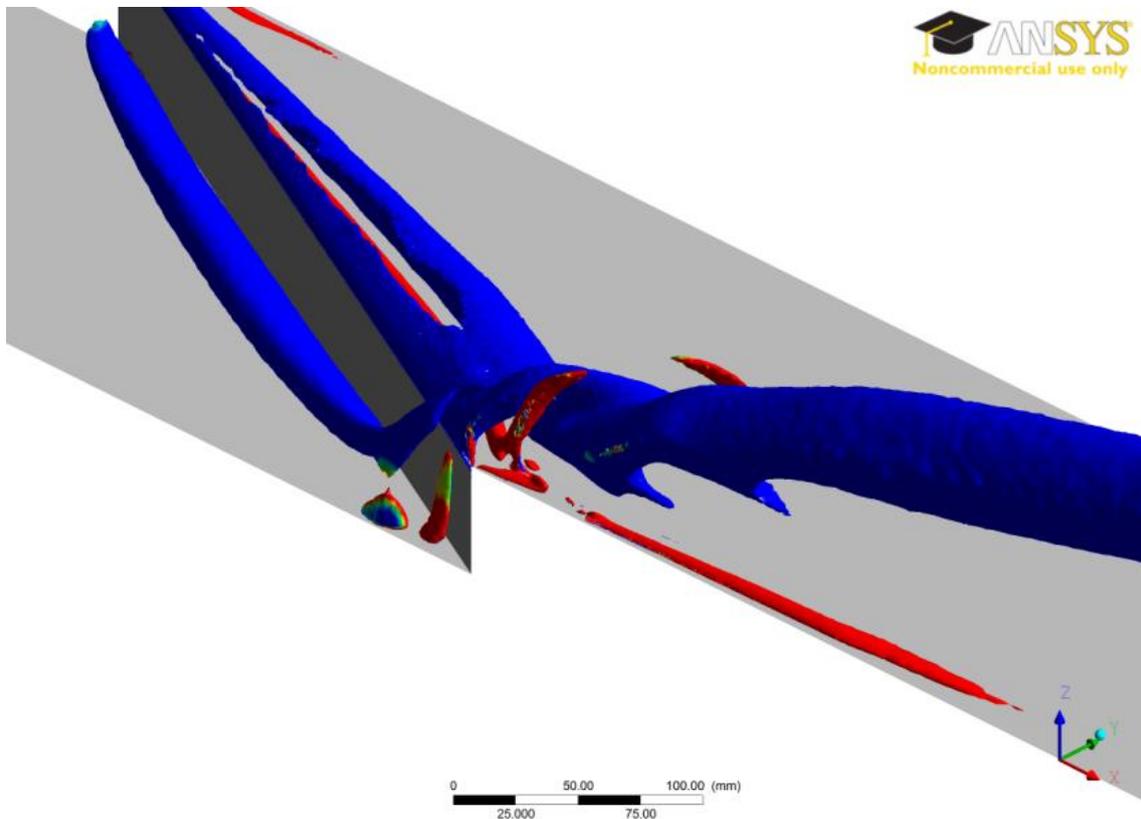

Figure 132: Iso-Q surfaces coloured by stream-wise vorticity, courtesy of Robert Harbig. A/λ = 1.

6.2.5 Comparison with Flow over Delta Wings

As noted previously, a comparison can be made with the results found here and results published in the literature on delta wings. In Section 2.4.2.2 *A Brief Review of Flow over Delta* Wings, the structure of flow over delta wings was described. References have already been made to the breakdown of the delta wing style vortices observed and the comparison was made with the vortices bursting over delta wings, as described in the literature. For these observations Cobra Probes were used to measure the velocities in the two shallowest cases: A/λ = 0.325 and A/λ = 0.5. These Cobra Probe measurements also made it possible to analyse how the Strouhal numbers developed through the flow structures. This means the Strouhal numbers could be compared against the various characteristic Strouhal numbers recorded in the literature, which are associated with the different parts of the delta wing vortex development and breakdown.

In the initial descriptions of the flow over the A/λ = 0.325 sawtooth element, the vortex regions are observed to be dominated by fine scale flow structures, consistent with Kelvin-Helmholtz vortices. The normalised PSDs associated with these regions are dominated by the energy in the high frequency side of the spectrum. This is consistent with results presented in the review of Gursul et al. (2005), who reported the presence of Kelvin-Helmholtz structures upstream of vortex bursting.

Gursul et al. (2005), comparing the experimental work of Yaniktepe and Rockwell (2004) with the numerical work of Gordnier and Visbal (2003), observed broad spectral peaks at chord-based Strouhal numbers around 3, downstream of vortex bursting over a delta wing. The former used a delta wing with a sweep angle of 39° at 7° angle of attack at chord-based Reynolds numbers less than 5×10^4, while the latter used a delta wing with a sweep angle of 50° at 5° angle of attack at a chord-based Reynolds number of 1000.

As is already well established, in the A/λ = 0.325 case, which corresponds to a sweep angle of 33°, broad spectral peaks were also observed. At x/h = 0, which is the location comparable to the observations of Yaniktepe and Rockwell (2004), and Gordnier and Visbal (2003), the majority of the

energy in the spectrum was contained above Strouhal numbers of 0.31, based on the step height, or 0.81, based on the amplitude, remaining relatively constant at the elevated energy levels through to the Nyquist frequency. Thus some consistency can be observed inasmuch as the peak Strouhal number of 3 observed in the literature is indeed greater than 0.81. In the $A/\lambda = 0.5$ case, at $x = h$ downstream, it is the St > 0.61 bin that dominates over all the others, as shown in Figure 111. Converting this height-based Strouhal number to an amplitude-based Strouhal number, or in the language of delta wings, chord-based Strouhal number, the equivalent bin range is St > 2.44. This is in much closer agreement to the Strouhal numbers observed by Yaniktepe and Rockwell (2004), and Gordnier and Visbal (2003), and the equivalent sweep angle of 45° in the $A/\lambda = 0.5$ case lies between the sweep angles of the delta wings that they implemented. Thus, the flow over sawtooth FFSs compares well with the flow over non-slender delta wings.

In both the $A/\lambda = 0.325$ case and the $A/\lambda = 0.5$ case the Strouhal numbers at which spectral peaks were observed decreased with increased distance downstream. This is consistent with the observations of Gursul (1994), who identified that the dominant Strouhal number decreases as a function of distance downstream. Gursul (1994) observed that the reduction in Strouhal number was linearly proportional to the distance downstream, implying that using the distance downstream as the length scale in the Strouhal number would result in a constant value, as the radius of the burst vortex core increased linearly with distance downstream. In this research, measurements beyond the sawtooth section could be compared (i.e. for $A/\lambda = 0.325$, $x/h = 0, 2, 10$; and $A/\lambda = 0.5$, $x/h = 1, 2, 4, 11$), and the results are shown in Figure 133. Note that for comparison with the work of Gursul (1994) that the distance downstream is measured from the peak of the sawtooth, and normalised against the amplitude of the sawtooth, which is equivalent to the chord length of a delta wing. The range exhibited at $x/A = 1$ for the $A/\lambda = 0.325$ case illustrates the fact that the spectrum first reaches its peak energy at a height-based Strouhal number of 0.31, but the peak in the spectrum is maintained through to the Nyquist frequency. The same thing is represented at $x/A = 1.25$ in the $A/\lambda = 0.5$ case. At $x/A = 3.75$, in the $A/\lambda = 0.5$ case, the range is representative of the height-based

Strouhal number range St < 0.06 and the minimum shown on the plot is a nominal minimum value rather than a precise minima. In the other cases, the ranges indicate the bin size associated with the dominant Strouhal number.

The A/λ = 0.325 case generated data consistent with a linear increase in radius of the vortex core with distance downstream, resulting in an overlap of the fx/U values for the three measurement planes. One key difference remains: Gursul (1994) measured data only from above the delta wing (x/A < 1), whereas, in this case, only measurements downstream of the sawtooth element are considered (x/A >1).
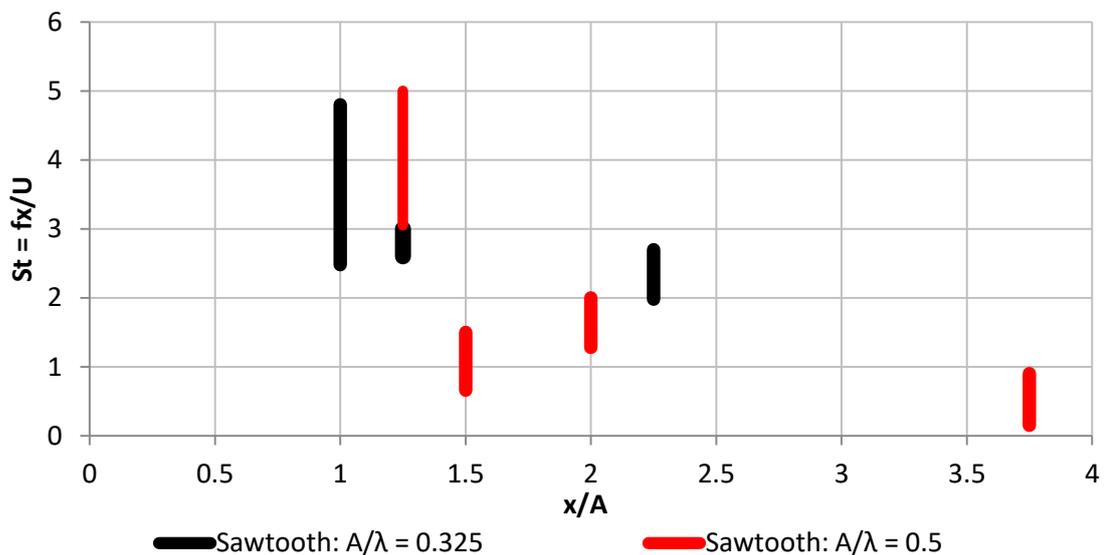
Figure 133: Ranges of dominant Strouhal numbers versus distance downstream of apex for the A/λ = 0.325 case and the A/λ = 0.5 case. Note that the Strouhal number is calculated based on distance downstream of the peak or apex, as is the distance downstream, *x*. The distance downstream, *x*, is normalised by the amplitude, A.

In the A/λ = 0.5 case, four planes were considered, and the spectral development fails to match up to the aforementioned theory from Gursul (1994). What is consistent, however, is the general decrease in the dominant Strouhal number with distance downstream, as seen in Figure 133. While the dominant downstream distance-based Strouhal number ought to remain constant to maintain consistency with Gursul (1994), a decrease in this value indicates vortex expansion in excess of linear growth. With respect to the A/λ = 0.5 case, the relevant points are summarised as follows:

- Vortex interaction is pushed downstream of the trough point

- Dynamically, alternating shedding is observed

- A sudden decrease in dominant Strouhal number is observed between $x = h$ and $x = 2h$ downstream

- A slight increase in dominant Strouhal number is observed between $x = 2h$ and $x = 4h$ downstream

- By $x = 11h$ downstream the dominant Strouhal number is at its lowest level

These points can be contrasted with the performance of delta wings:

- No vortex interaction exists either side of the trough point for a delta wing

- Alternating shedding is only observed at high angle of attack across either side of the delta wing apex

- Development of Strouhal number follows a linear trend over a delta wing: fx/U = constant, as dominant frequency is inversely proportional to the radius of vortex core, which increases linearly with distance downstream (Gursul 1994)

Thus, positive comparisons between the sawtooth FFS and the delta wing can be made. In the two cases observed (A/λ = 0.325 and A/λ = 0.5) the vortex structure was shown to burst, consistent with vortex bursting over a delta wing. Similarities in the spectral peaks and the associated Strouhal numbers were also observed. Evidence supporting the presence of shear layer vortices within the vortex structure was recorded, again in agreement with the literature. The growth of the diameter of the vortex and the subsequent reduction in Strouhal number was also measured. However, closer inspection revealed that the vortex interactions across the trough line, combined with the presence of the extended ground plane associated with the sawtooth FFS resulted in vortex structures forming that were not observed in the delta wing related literature. These points of divergence can be explained by the differences in topography between the two cases.

Three topographic differences exist between the sawtooth FFS and a delta wing: the extended ground plane beyond the sawtooth element; the thickness of the FFS and the resultant lack of angle of attack; and the lateral repetition of the sawtooth geometry compared to the isolated delta wing. These topographic differences to the delta wing topography drive the differences between the delta wing topology and the topology presented in this research. Of particular note is the vortex interaction downstream of the trough point. While in the A/λ = 0.325 case much of the vortex breakdown occurs over the sawtooth element, in the A/λ = 0.5 case the breakdown occurs farther downstream, as evidenced by the location of the critical points in the topological analysis. Furthermore, instantaneous snapshots of the surface pressure over the A/λ = 0.5 case, shown earlier experimentally in Figure 120 and numerically in Figure 119, reveal an alternating swirling dynamic structure limited to the region just downstream of the trough.

The analogy between the flows over delta wings compared to the flows over the sawtooth FFSs contains some useful parallels, in particular relating to the general structure of the vortex generation and the subsequent vortex bursting.

6.3 Summary

Using a range of experimental and numerical techniques, the mean flow topology over FFSs with sawtooth lateral variation has been investigated for a range of amplitude to wavelength ratios. Development of the mean flow topology was observed, particularly in the trough region, with the secondary vortex structures playing a significant part in determining the location of critical points. In each of the four cases, the topology was dominated by a delta wing style vortex with secondary structures generated along the crest.

In the shallowest case (A/λ = 0.325), the primary vortex structure separated from the crest. Increases to the amplitude to wavelength ratio resulted in the primary vortex remaining attached to the length of the crest, and the secondary structures becoming more important in determining the flow topology.

The A/λ = 0.5 case exhibited asymmetry driven by an instability when modelled with a RANS technique. Transient modelling revealed a vortex street developing downstream of the trough. This lateral flapping was observed both numerically and experimentally.

The topology observed experimentally in the A/λ = 0.65 case was shown to be equivalent to the A/λ = 0.5 case, whilst the numerical results indicated that it was an intermediate step between the lateral flapping of the A/λ = 0.5 case and the stable, but more complex mean topology exhibited in the A/λ = 1 case.

The A/λ = 1 case had the highest sweep angle of the models. Its mean topology indicated that pairs of counter rotating vortices rise from the surface in a stable manner and become entwined with the primary vortex.

Comparisons with the published literature associated with delta wings indicated that many aspects of the flow over sawtooth FFSs could be considered analogous to the flow over delta wings, particularly with respect to vortex bursting, which results in a near stagnation of the axial flow through the primary vortex structures.

In establishing the effect that the sawtooth ruggedness has on wind turbine siting, it is a question of maximising yield and minimising fatigue loads on the turbines.

Downstream of the trough region is the most straightforward region for consideration, with the growth of the delta wing style vortices; the vortex bursting phenomenon making the extents of the vortices extend vertically, with increases in turbulence intensity and reductions in wind speed observable up to $2h$ above the surface and beyond $10h$ downstream of the trough point, while Reynolds Stresses peaked between h and $2h$ above the surface. In the context of 100 m high cliffs, this implies that these adverse flow effects will be prominent with even a 1 km setback from such cliffs.

The peak of the sawtooth has regions amenable to the siting of wind turbines, provided the vortex structure can be avoided – which, in the vortices' pre-burst state, may be possible by allowing the rotor to pass above the vortex structure. This structure in its pre-burst state appear to be concentrated in a region below 0.5h above the surface. In this context, it is worth noting that the sawtooth FFSs can be considered as yawed FFS elements, implying that similar siting techniques apply.

7. Ruggedness Modelling: Sinusoidal Approximation

This chapter further refines the ruggedness model presented in Section 6 *Ruggedness Modelling: Sawtooth Approximation* by changing the shape of the lateral variation from a sawtooth to a sinusoidal variation. The sinusoidal geometries provide a stronger parallel to many naturally occurring cliffs than do the sawtooth geometries, for example, the rugged cliffs of the Cathedral Rocks Wind Farm, shown in Figure 82.

Four sinusoidal models, defined by their A/λ ratio, were investigated through a series of surface shear stress flow visualisations. Based on these visualisations the flow topology could be derived. Further validation of the flow structure is provided through Cobra Probe traverses and surface pressure mapping of the shallowest, A/λ = 0.325, case. Through an understanding of the flow topology, insight is gained into how best to model real world cliffs when designing wind farms.

While some previous work has been completed on sinusoidal lateral variations of leading and trailing edges of aerofoils (Dropkin et al. 2012), to the best of the author's knowledge, no previous work has been completed on FFSs with sinusoidal lateral variations. The closest analogies to the sinusoidal FFS are the sawtooth FFSs and blunt nose delta wings.

7.1 Model Details

As with the sawtooth cases presented in Chapter 6, experiments were performed using Inflow Configuration 3, as specified in Section 3.3.1 *Three Wind Tunnel Configurations* at a free-stream speed of 34 ms^{-1}, over forward facing steps of height, h = 0.050 m. The experiments were completed at Reynolds Numbers of 1×10^5, using the step height, h, as the reference length. End plates extended 12h upstream of the models. The models resulted in 2.5% blockage and extended beyond 10h downstream, and can thus be considered isolated cliffs according to Moss and Baker (1980). The aspect ratio was 34, resulting in four complete periods of the geometry being modelled. The experimental domain is presented in Figure 134. The models were painted with semi-gloss enamel paint, and were aerodynamically smooth. The geometric parameters are presented in Table 11.

Sinusoidal sections of various amplitudes were appended to straight-edged FFSs, as illustrated in Figure 135. Note that only the amplitude of the sinusoids was varied.

Table 11: Geometric parameters of sinusoidal FFS configurations.

Height: h	A/λ	Amplitude: A	Wavelength: λ	Maximum Yaw Angle	Extent downstream	Aspect ratio (width/height)
0.050 m	0.325	0.130 m	0.400 m	47°	2.6 m/52h	34
0.050 m	0.5	0.200 m	0.400 m	58°	2.6 m/52h	34
0.050 m	0.65	0.260 m	0.400 m	64°	2.6 m/52h	34
0.050 m	1	0.400 m	0.400 m	72°	2.6 m/52h	34
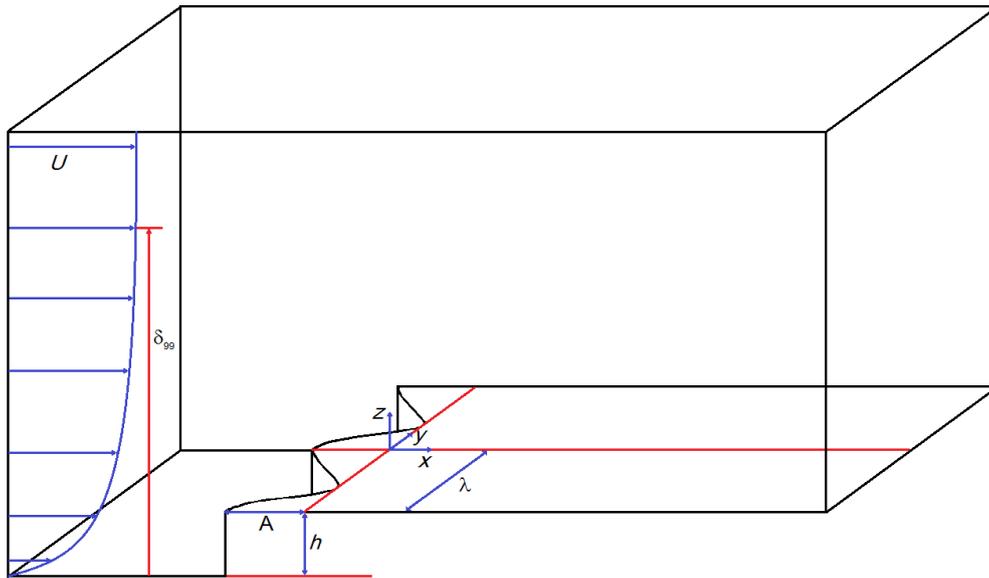
Figure 134: Experimental domain of the sinusoidal FFS.
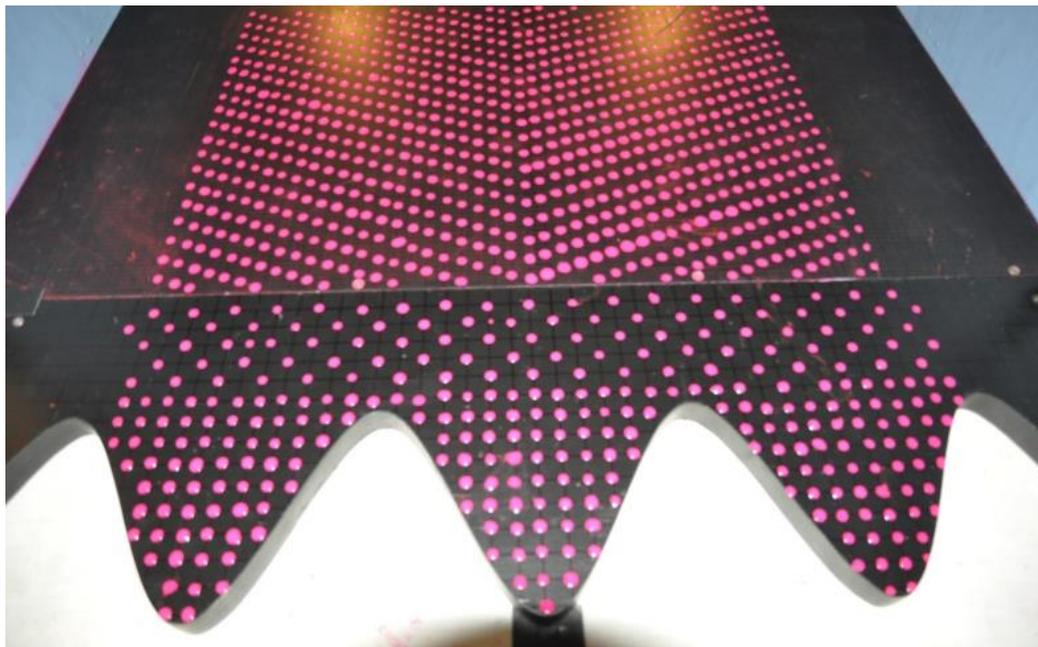
Figure 135: Sinusoidal section is appended to the front of the straight-edged FFS geometry.

7.2 Results and Discussion

The surface shear stress visualisations are presented in Figure 136 through Figure 139. In each of the cases the free-stream flow is from the bottom of the page to the top of the page. The streaks in each of the four visualisations highlight four regions of flow, illustrated in the top pane of Figure 140. The first region is the free-stream flow (I), where the streaks are aligned with the free-stream flow. The second region is the dominant vortex region (II), which follows the crest, and is only discontinuous near the trough points, where the vortex separates from the crest and persists downstream. The third region is the secondary vortex region (III), between the dominant vortex and the crest. The fourth region is the trough region (IV), where the flow approaches stagnation. This is the void created between the points either side of the crest where the dominant vortices separate from the crest. This region reduces in size as A/λ increases, until it is imperceptible in the A/λ = 1 case.

In the same way as in the sawtooth cases, these regions can be understood in the context of the mean flow topology, which have been derived from each of the visualisations and are presented in Figure 140. These topologies are derived based on the Poincaré-Bendixson Theorem whereby $\sum N - \sum S = \frac{\epsilon}{2\pi}$, where N denotes the number of node points on the plane and S denotes the number of saddle points on the plane and ϵ denotes the angle through which the shear stress vector passes over the plane (Hunt et al. 1978). Over the sinusoidal FFS geometry ϵ = 0°, thus, the number of node points must equal the number of saddle points. Two systems are topologically equivalent when the connections between critical points are the same.

For all but the A/λ = 1 case, topological equivalence is observed. The A/λ = 1 case appears to differ slightly in the trough region, with a stable node located on the trough point. There is enough uncertainty to question whether that critical point is on the trough point itself, or merely "close" to the trough point, which would imply topological equivalence across all of the systems.

The flow structure is dominated by a delta wing style vortex, similar to that described first by Cochard et al. (2012) while investigating sawtooth lateral variations to the FFS. The more detailed

flow structure including the development of swirl around the stable nodes and the development of the secondary vortex region evolving as a function of A/λ, as observed in Chapter 6: *Ruggedness Modelling: Sawtooth Approximation* is, however, not observed.

In contrast to the sawtooth cases where each of the delta wing style vortices has a genesis at the peak, the sinusoidal FFS cases exhibit continuity of the vortex structure around the peak, in each of the cases examined. The peak region develops its own cell, in a similar manner to a straight-edged FFS, as observed by Largeau and Morinere (2007) and again in the current work in Chapter 5, with the cells on either side of the peak forming the delta wing vortex structure.

7.2.1 Topology Comparison with Sawtooth Geometry

The flow structure of the FFS with sawtooth lateral variation with A/λ = 0.325, taken from Chapter 6 is shown for comparison in Figure 141. This case has many parallels with the sinusoidal A/λ = 0.325 case. In both cases, the flow structure is dominated by the delta wing style vortex, and in both cases, the dominant vortex separates from the crest some distance from the trough point, resulting in a large stagnation region in the vicinity of the trough. As in each of the cases examined, the secondary vortex structure is also evident, feeding the stable node. The most obvious difference between the two cases is that in the sawtooth case, the vortex generates from a point at the peak, whilst in the sinusoidal case, the vortex line is continuous around the curve of the peak.

While there are strong parallels between the sawtooth and the sinusoidal cases for A/λ = 0.325, the similarities in the finer structure do not extend to the steeper cases. In Chapter 6 it was observed that the sawtooth cases exhibited a topological development that was driven by the growth of the secondary structures. The growth of the secondary structures induced increased vorticity around the stable nodes, and shifted the stable nodes from the crest onto the surface proper of the step. Ultimately, the stable nodes developed into pairs of stable foci, which were interpreted as pairs of vortices rising from the surface of the step, encased by the primary structure.

Figure 136: Surface shear stress visualisation over Sinusoidal FFS: *A/λ* = 0.325.

Figure 137: Surface shear stress visualisation over Sinusoidal FFS: *A/λ* = 0.5.

Figure 138: Surface shear stress visualisation over Sinusoidal FFS: *A/λ* = 0.65.
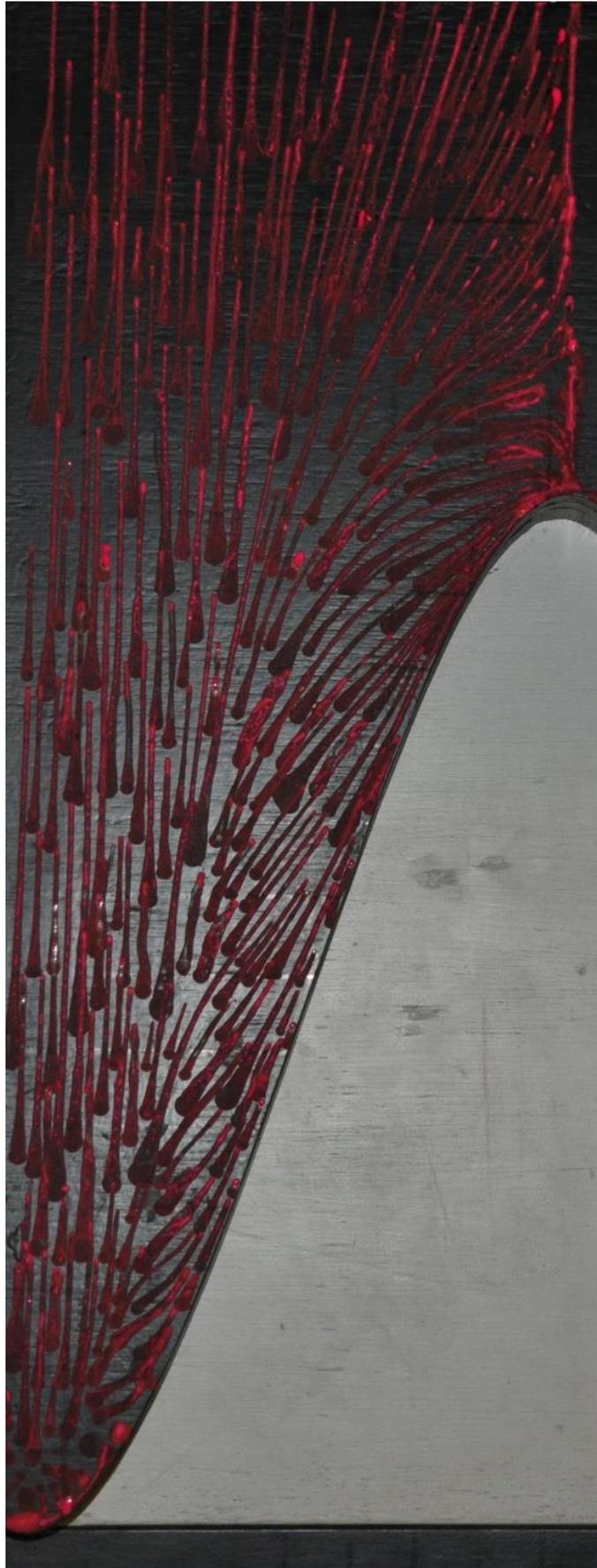
**Figure 139: Surface shear stress visualisation over Sinusoidal FFS:** *A/λ* **= 1.**
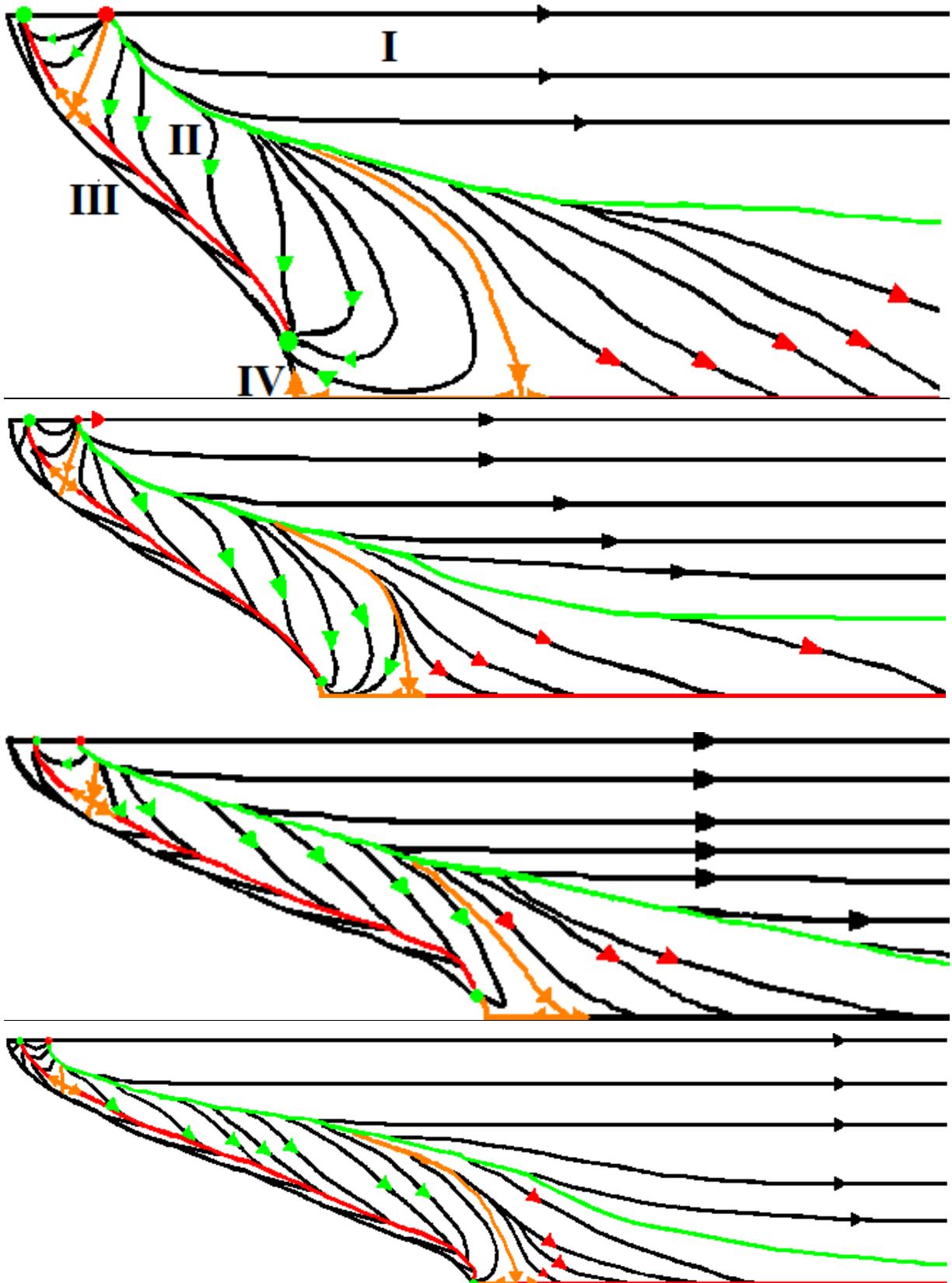
Figure 140: Surface topology for sinusoidal cases. From top to bottom, _A/λ_ = 0.325, 0.5, 0.65, and 1. Flow is from left to right. Positive bifurcation lines are shown in green; negative bifurcation lines are shown in red. Saddle points are indicated with orange direction arrows. Stable nodes are indicated by green dots and arrows. Dividing streamlines are shown in orange. Red dots indicate unstable nodes.
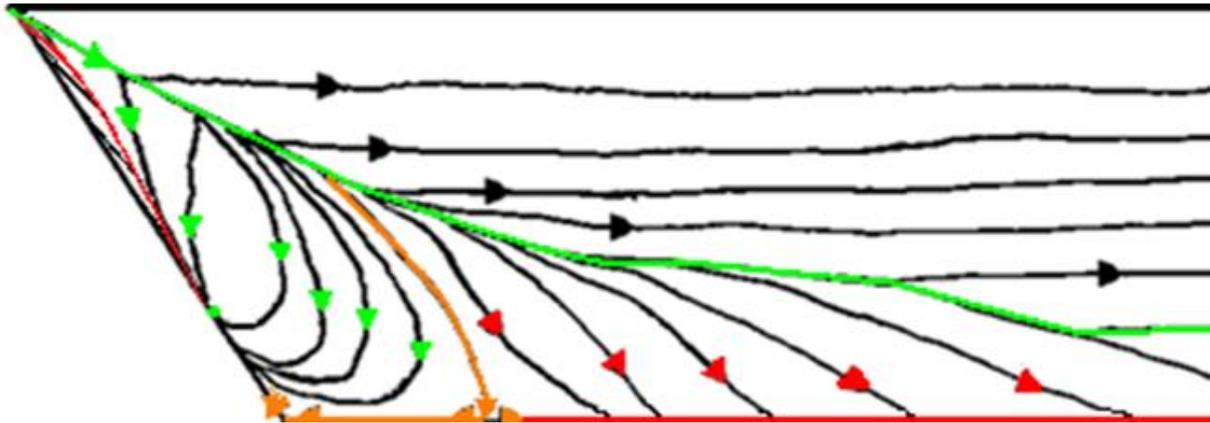
Figure 141: Flow topology over a FFS with sawtooth leading edge with *A/λ* = 0.325. Flow is from left to right. Critical points and colouring as in Figure 140.

Given the distinct vertices and the sharp-edged nature of the sawtooth geometry, the lack of stable topology was surprising. It was initially hypothesised that the topology would be more variable in the sinusoidal geometries because of the imprecise separation points associated with the sinusoidal curvature. However, the opposite was found to be true. The secondary structures in each case were found to remain relatively constant in size, as evidenced by the photographs in Figure 140. The only difference between the sawtooth cases investigated in Chapter 6 and the sinusoidal cases in this section is the constant curvature introduced by making the lateral variation of the FFS a sinusoid. Thus, the secondary structures, which were observed to increase in diameter along the crest in the sawtooth cases, are controlled by the curvature of the crest.

7.2.2 Comparison of Visualisation Data with Surface Pressure Measurements

Surface pressure measurements were conducted on each of the geometries, providing a comparison with the topological skeletons derived from the surface shear stress visualisations. The measurement system is described in Section 3.6 *Surface Pressure Taps*. The sampling frequency was 1000 Hz, with a sample length of 180 s.

The mean surface pressure is presented as a pressure coefficient, as defined in Equation 6-1. The pressure coefficients are presented in Figure 142, with the derived flow topology superimposed. In each case, there is good agreement between the surface pressure measurements and the flow structure that is identified with the surface shear stress visualisations.

While there is a consistent flow topology between the four cases, the visualisation of the surface pressure highlights a number of developments that occur as A/λ is increased.

In contrast to the sawtooth FFS cases, the peak of the sinusoid is associated with a continuous vortex line. The maps of pressure coefficients in Figure 142 show that the topographic peak of the sinusoidal FFS is associated with a pressure peak. This is most clearly captured in the shallowest case (A/λ = 0.325), but is also present in the other three cases examined. The peak negative pressures at the topographic peaks are consistent with the convergence of the paint streaks onto the stable nodes, as observed in the flow visualisations.

The saddle points, located at the interface between the primary vortex structures and the secondary vortex structures, along the crest from the topographic peaks, correspond to local pressure maxima. They are local, insomuch as they are contained within the vortex structure; they are, however, at a lower pressure than the region outside of the vortex structure. These saddle points represent points where the pressure gradient is equal to zero. They are balance points where the suction generated at the topographic peak is balanced against the low pressure generated by the delta wing style vortex that gains vorticity and decreases in pressure as a function of downstream distance along the crest.

The development observed as a function of A/λ is a shifting of the stable node along the crest toward the trough point. In the shallower cases (lower values of A/λ), the stable node occurs farther upstream than in the steeper cases. This is consistent with the sawtooth FFS cases. The location of this stable node is alongside the peak negative pressure region and can be equated with where the delta wing style vortex separates from the crest.

In the A/λ = 0.325 case, shown in the top pane of Figure 142, the second pressure minima, which is associated with the positive node and the vortex separation from the crest, occurs farther upstream of the positive node than in the other A/λ cases. An adverse pressure gradient is observed through

the axis of the vortex. Given that a lower pressure minimum implies an increase in vorticity, the adverse pressure gradient indicates that vortex diffusion is occurring through the delta wing style vortex at a higher rate than vorticity is being generated from the flow separation over the sinusoidal crest.

In the subsequent cases, the pressure coefficient becomes more negative from the topographic peak through to the low pressure minimum near the trough. This low pressure region becomes more concentrated and closer in proximity to the trough point as A/λ is increased. The migration is consistent with the migration of the stable node towards the trough point that was identified by the surface shear stress visualisations. Again, the return to the conditions outside of the vortex structure occurs gradually along the trough line.

Finally, the distance between the pair of saddle nodes along the trough line consistently decreases with increased A/λ. As with the other saddle nodes that have been previously discussed, these saddle nodes represent a balance point. The saddle node on the trough point is the interface between the free-stream flow and the vortex structure. The saddle node farthest downstream represents the balance between the low pressure associated with the vortex separation from the crest and the free-stream flow.

7.2.3 Velocity Statistics
The A/λ = 0.325 case was examined by traversing through several planes above its surface with Cobra Probes, from which velocity statistics could be derived and static pressure could be measured. These results provide an insight into the three-dimensional structure of the flow topology and possible approaches to wind turbine micro-siting in these regions. The mean values for speed-up are presented in colour plots and contour plots in Figure 143. The turbulence intensity ratio is mapped in colour plots and contour plots in Figure 144. The static pressure is mapped in colour plots and contour plots in Figure 145.
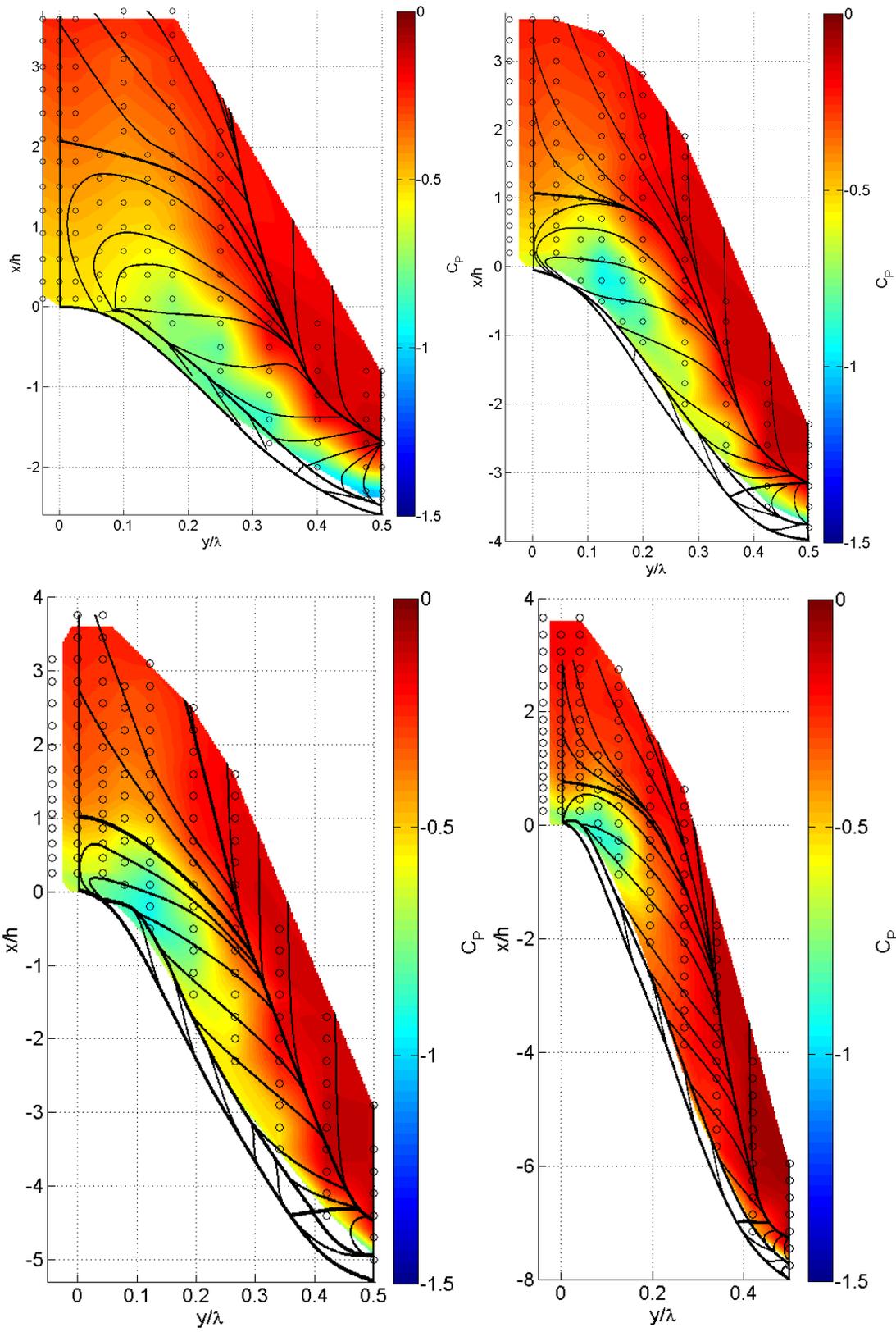
Figure 142: Surface pressure from the sinusoidal cases. *A/λ* = 0.325 (top left), 0.5 (top right), 0.65 (bottom left), 1 (bottom right).   Topology superimposed. Black markers represent pressure tap locations. Flow is from bottom of page to top.

The speed-up, observed in Figure 143, is increased above the surface of the sinusoidal protrusion. Greater than 10% increase in wind speed was measured through to $10h$ downstream of the trough point, however, strong wind speed reductions were also observed in the same plane. The speed-up regions were aligned with the peaks, while the speed deficit (speed-up less than unity) regions were aligned with the trough regions. Regions of speed deficit corresponded to increases in turbulence intensity. In Figure 144, where turbulence intensity ratio is presented, the maximum turbulence intensity ratio reaches 6 at $10h$ downstream of the trough, which, whilst extremely high, is less than that observed in the sawtooth cases.

The speed deficit and increase in turbulence intensity is entirely consistent with the persistence of the vortices generated along the crest of the FFS, separating near the trough, and persisting downstream into the far wake. As the vortices propagate downstream, they are observed to slowly diffuse. The static pressure, shown in Figure 145, is seen to return to the levels upstream of the step. However, the regions associated with speed deficit and elevated turbulence intensity ratio increase in area with distance downstream. At the location x/h = -1.3, the turbulence intensity ratio is increased in value up to a height of $0.5h$, which is more clearly illustrated in Figure 146. Above this height there is negligible difference in turbulence intensity. At x/h = 0, the height above which there is negligible difference in turbulence intensity is z/h = 1. By $10h$ downstream, the high turbulence intensity region extends beyond z/h = 2.5. Through a range of wind directions, Montlaur et al. (2012) showed that in the downstream region, the axes of the persistent vortices would realign themselves with the free-stream flow. The implication of such an alignment is that the vortices cannot be avoided through lateral adjustment to a wind turbine's location, as any change to the wind direction causes a corresponding lateral spread of the vortex structures. Thus, the siting of wind turbines becomes less optimal with increased distance from the crest of the FFS, as the regions of velocity deficit and increased turbulence intensity can be avoided neither by increasing the height above the ground of the rotor nor by careful consideration of the lateral placement along the cliff.

Development of pitch angle and veer angle are presented in Figure 147 and Figure 148 respectively at a height, z/h = 0.5. Four lateral positions are considered: y/λ = 0, 0.125, 0.175, and 0.25. By $2h$ downstream of the trough, the mean pitch and veer angles do not pose any problems for wind turbine siting. However, given the speed-up and turbulence intensity ratio statistics, the downstream region is of little value for the siting of wind turbines. At x/h = -1.3, where the speed-up and turbulence intensity ratios are more conducive to wind turbine siting, the pitch and yaw angles at y/λ = 0.25 are high. However, this location is directly above the crest, and not representative a realistic wind turbine location. The pitch angles return to their ±5° envelope by y/λ = 0.175. The veer angle affects a larger region of the flow, with the veer angle gradually decreasing from y/λ = 0.175 where it was above 10°, through to y/λ = 0.125 where the veer angle returned to below 5°. Thus, to avoid significant wind veer, wind turbines need to be sited in the central region of the protrusion between y/λ = ±0.125.

Similarly, lateral profiles of Reynolds Stress, R_{uw}, are presented in Figure 149. The heights of the lateral profiles correspond to the height where the largest magnitude Reynolds Stress occurs. The results are similar to the sawtooth case, whereby siting turbines above the height of these Reynolds Stress peaks is unlikely to be feasible for locations downstream of the trough. Above the unburst vortex, at x/h = -1.3, the turbulent fluctuations associated with the vortex structure are confined to below -0.5h, as can be seen in the vertical profiles presented in Figure 150.

This description of the speed-up and turbulence intensity development over the sinusoidal FFS is entirely consistent with what was observed in the sawtooth FFS cases. In the sawtooth FFS cases the regions of speed deficit and increased turbulence intensity were shown to be caused by vortex bursting, typically associated with delta wings. The consistency between the sawtooth FFS cases and the sinusoidal FFS cases imply that the speed deficit and increases in turbulence intensity are also attributable to the bursting of the delta wing style vortices.
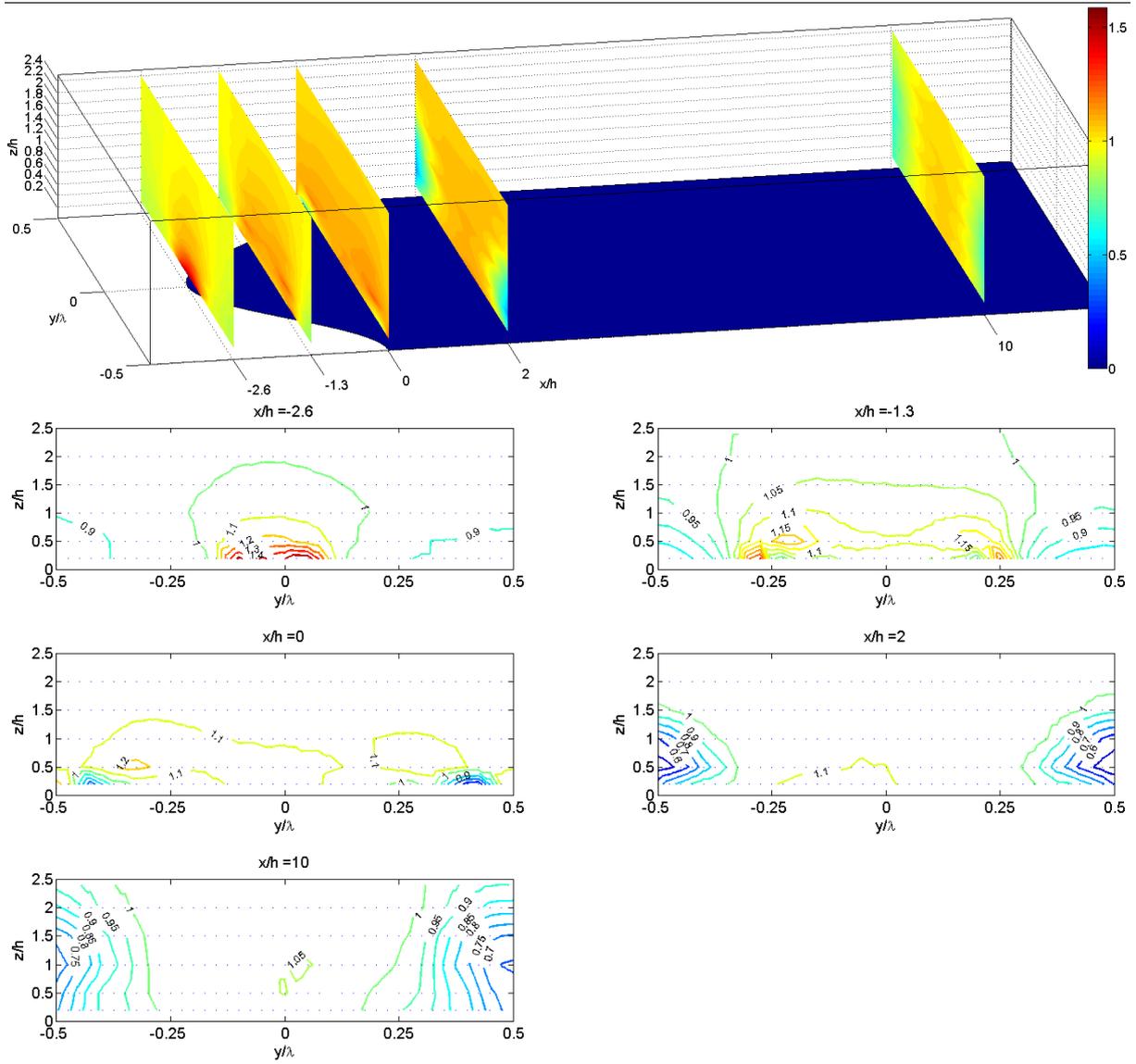
Figure 143: Speed-up colour plot (top) and contours (bottom) from Cobra Probe measurements over the _A/λ_ = 0.325 case. Blue dots represent measurement locations.
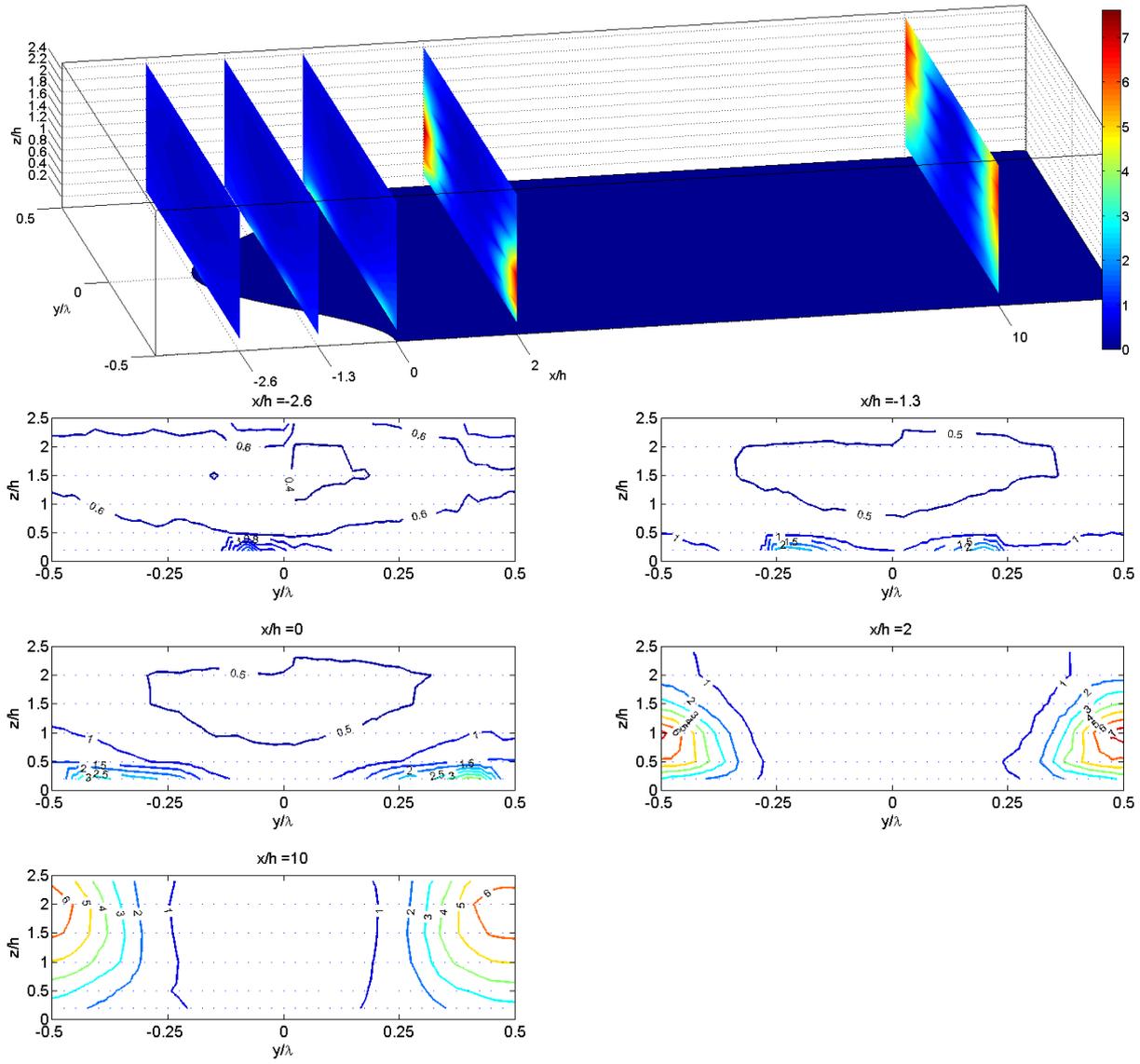
**Figure 144: Turbulence Intensity Ratio contours from Cobra Probe measurements over the *A/λ* = 0.325 case. Blue dots represent measurement locations.**
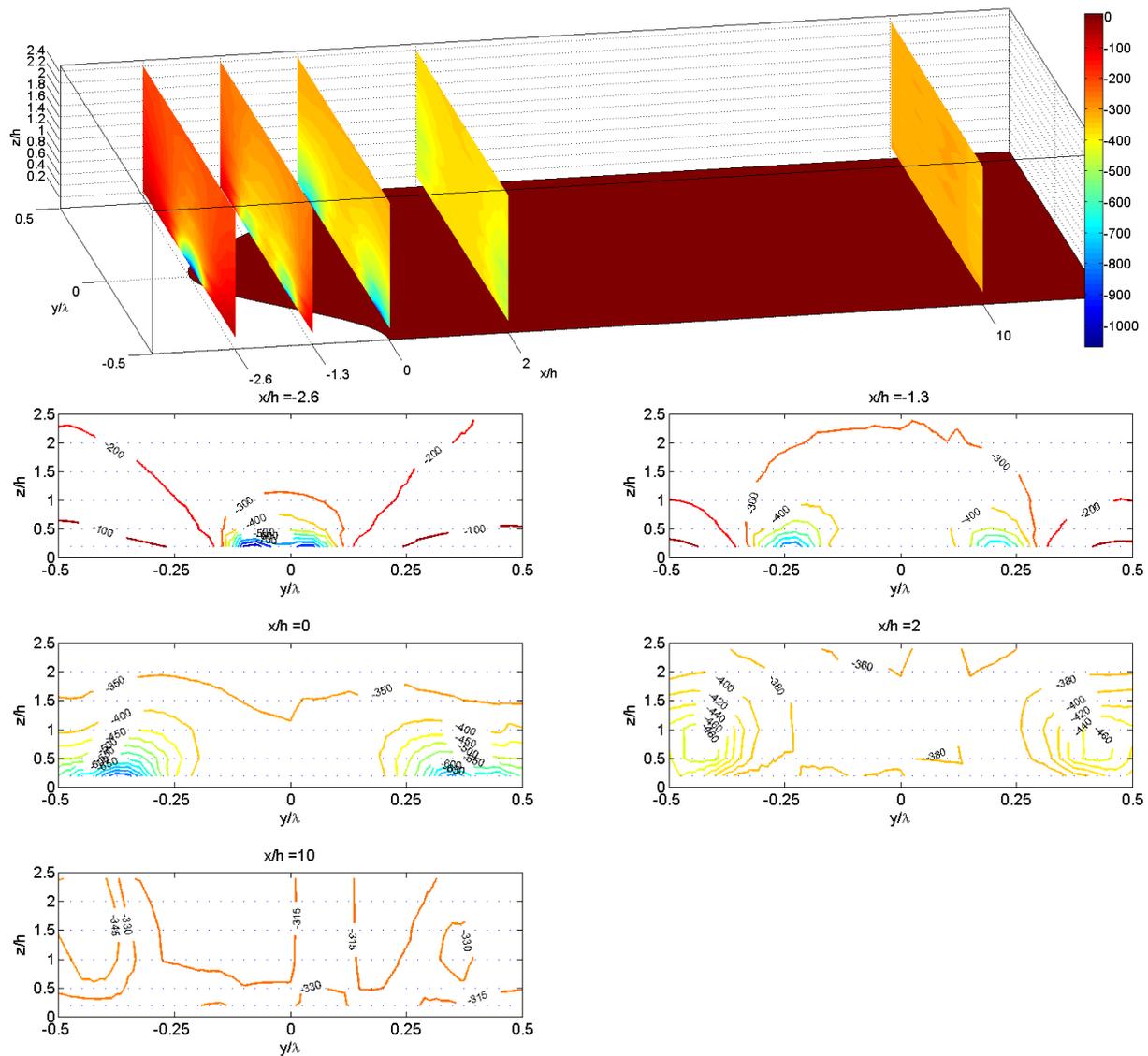
Figure 145: Static pressure contours measured in units of Pascals from Cobra Probe measurements over the *A/λ* = 0.325 case. Blue dots represent measurement locations.
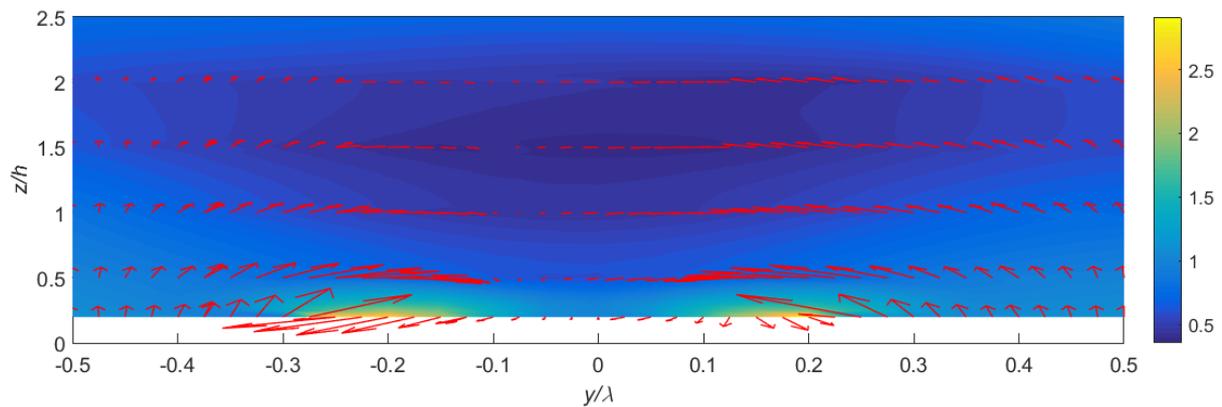

Figure 146: Turbulence Intensity Ratio superimposed with lateral and vertical velocity components at *x/h* = -1.3 in the *A/λ* = 0.325 case.

235
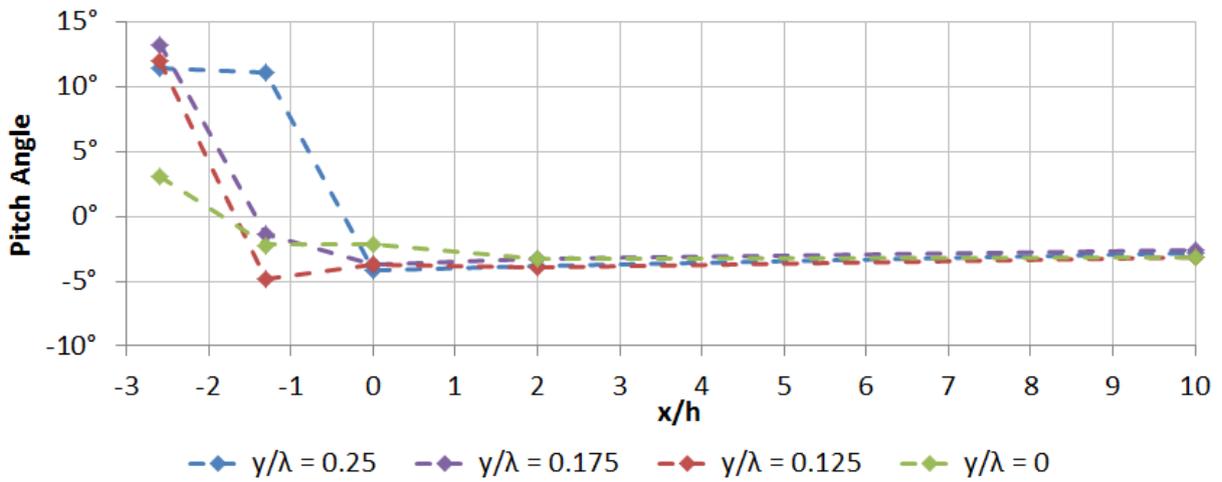
Figure 147: Development of pitch angle at height *z/h* = 0.5. The peak of the sinusoid corresponds to *y/λ* = 0.
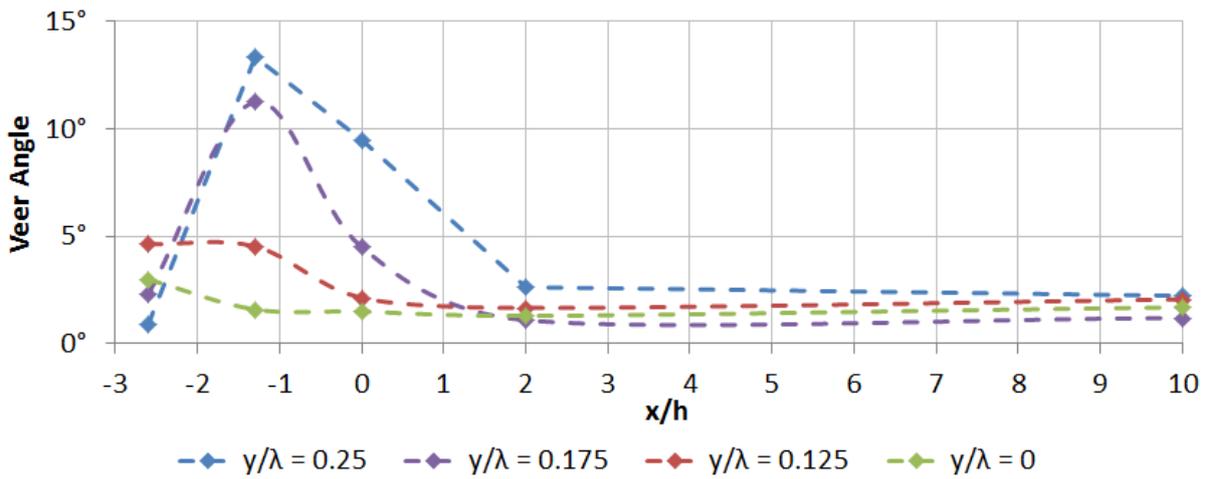
Figure 148: Development of veer angle at height *z/h* = 0.5. The peak of the sinusoid corresponds to *y/λ* = 0.
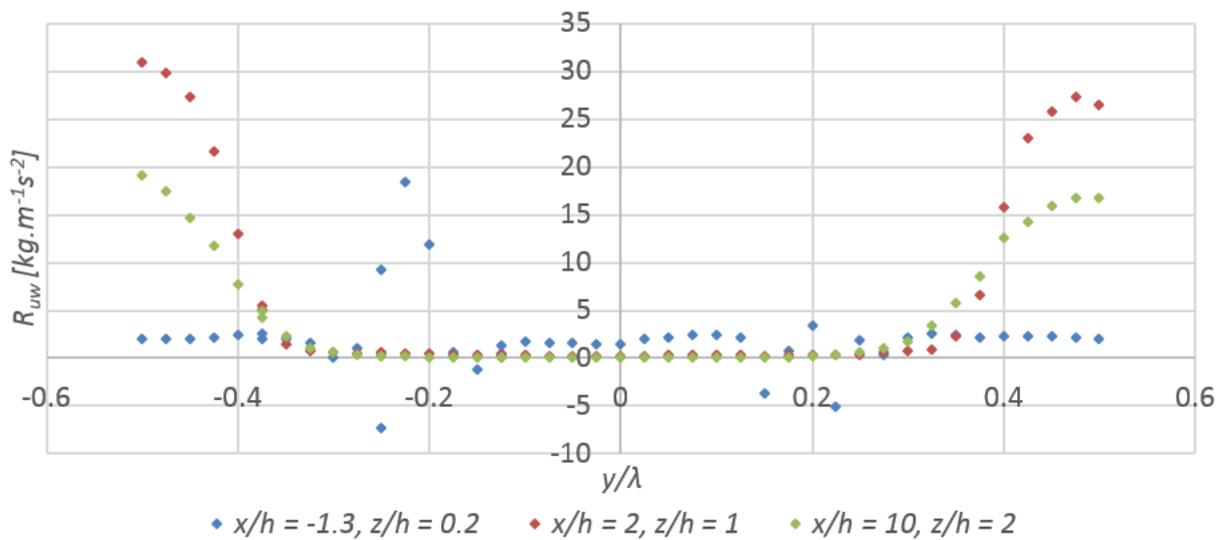

Figure 149: Lateral profiles of stream-wise-vertical Reynolds Stress, R_{uw} through the region of peak Reynolds Stress.
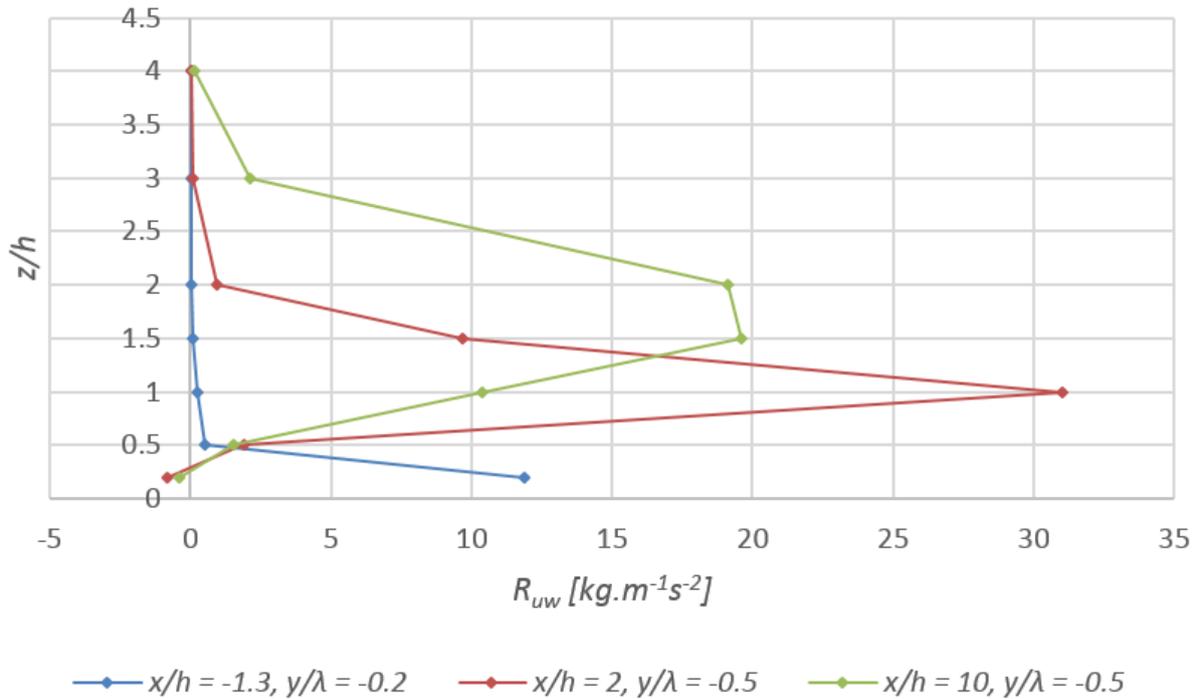
Figure 150: Development of stream-wise-vertical Reynolds Stress, R_{uw}.

## 7.2.4 Development of Strouhal Number

In the $A/\lambda = 0.325$ and the $A/\lambda = 0.5$ sawtooth cases, the step height-based Strouhal number was mapped, giving some indication of the dynamics associated, in particular, with the trough region. In those cases, broad spectral peaks were observed, and so the Strouhal number was binned in such a way as to show the development of relative energy content for a given Strouhal number as a function of spatial location over the model. The same approach is presented for the $A/\lambda = 0.325$ sinusoidal case from Figure 151 through to Figure 152. Values were averaged across the peak-line at $y/\lambda = 0$, which is a line of symmetry.

The results demonstrate that the flow is characterised by broad spectral peaks. In the upstream plane, $x/h = -2.6$, the flow is affected by the shallow peak of the sinusoid. The lowest Strouhal number bin, which contained the most energy in the undisturbed flow, seen at $y/\lambda = 0.5$, decreases in relative energy as y/λ decreases. An almost step change in energy content is seen between $y/\lambda = 0.35$ and $y/\lambda = 0.325$. The result is that the relative spectral energy in the central region is shifted to higher Strouhal numbers, between 0.06 and 0.4. There is no significant increase in relative spectral energy observed in the upstream region. A similar first phase of development was observed

237

in the sawtooth case, though in that case, the relative energy increases were confined closer to

y/λ = 0, due to the difference in geometry.

At x/h = -1.3, the energy peaks in the range 0.2 < St < 0.3 have established themselves over the top

of the model where the vortex structure is located. The measurements above the void created by

the trough (not above the elevated model surface) show little development from the upstream

plane. At the corresponding distance downstream in the sawtooth case, the spectrum was

dominated by shear layer vortices which caused high Strouhal numbers to dominate in the vortex

region.

By x/h = 0, the high frequency associated with the shear layer vortices become evident around the

trough region, otherwise, there is little change observed in the energy content. The turbulence

intensity results presented in Figure 144 also showed that increases in turbulence intensity had

virtually dissipated by a height z/h = 0.5 for measurements up to the trough point, that is x/h = 0.
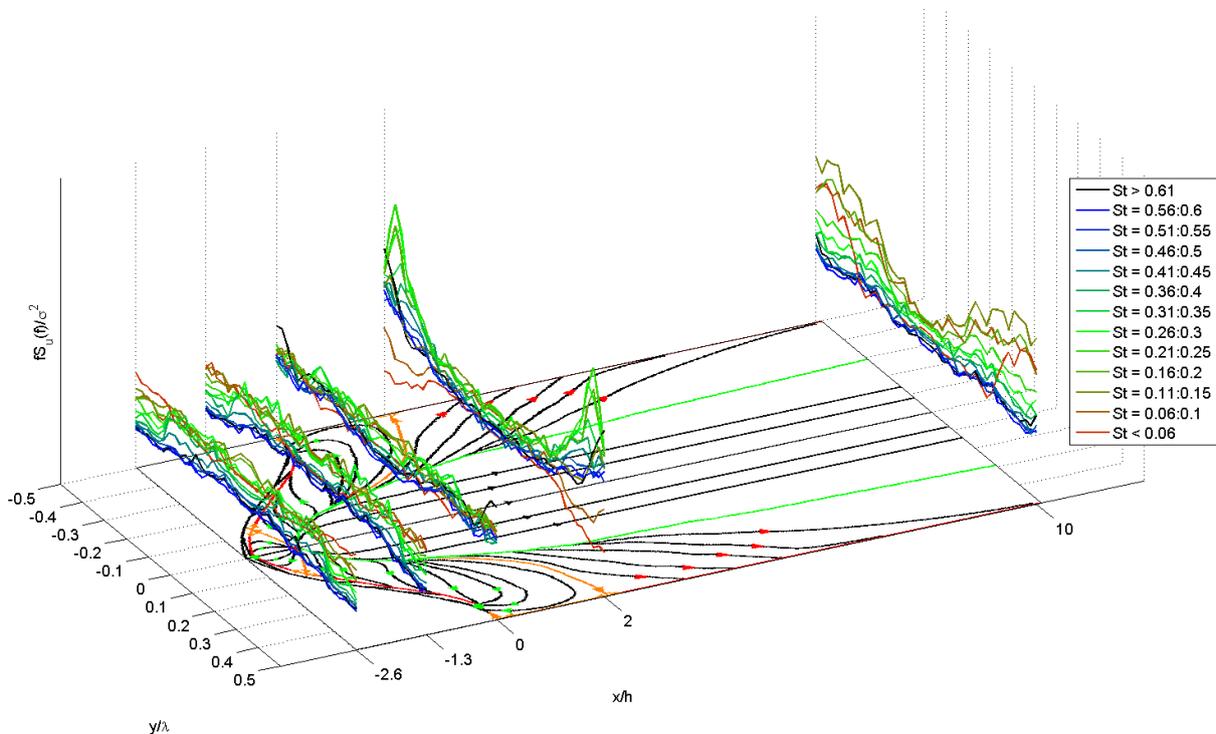
Figure 151: Power maxima from each Strouhal number bin, shown at spatial locations over the topological skeleton for a single height, z/h = 0.5. A/λ = 0.325.

Beyond the trough point the delta wing style vortices were observed to increase in diameter as they propagated downstream, consistent with Gursul's description of flow over delta wings (Gursul 1994). This rendered changes in turbulence intensity more obvious above z/h = 0.5. In the x/h = 2 plane, the relative energy content of the PSD was doubled in the region associated with the vortex growth. Two distinct vortex cores are evident, shedding in the range 0.21 < St < 0.25. Again, the high Strouhal number bin experiences an increase in relative spectral energy in the region aligned with the trough point, indicating that interaction between two vortices is occurring, generating a shear layer. At the corresponding location in the sawtooth case, the highest energy containing bin was 0.26 < St < 0.3, and contained approximately two-thirds of the relative energy content observed in the sinusoidal case examined here.
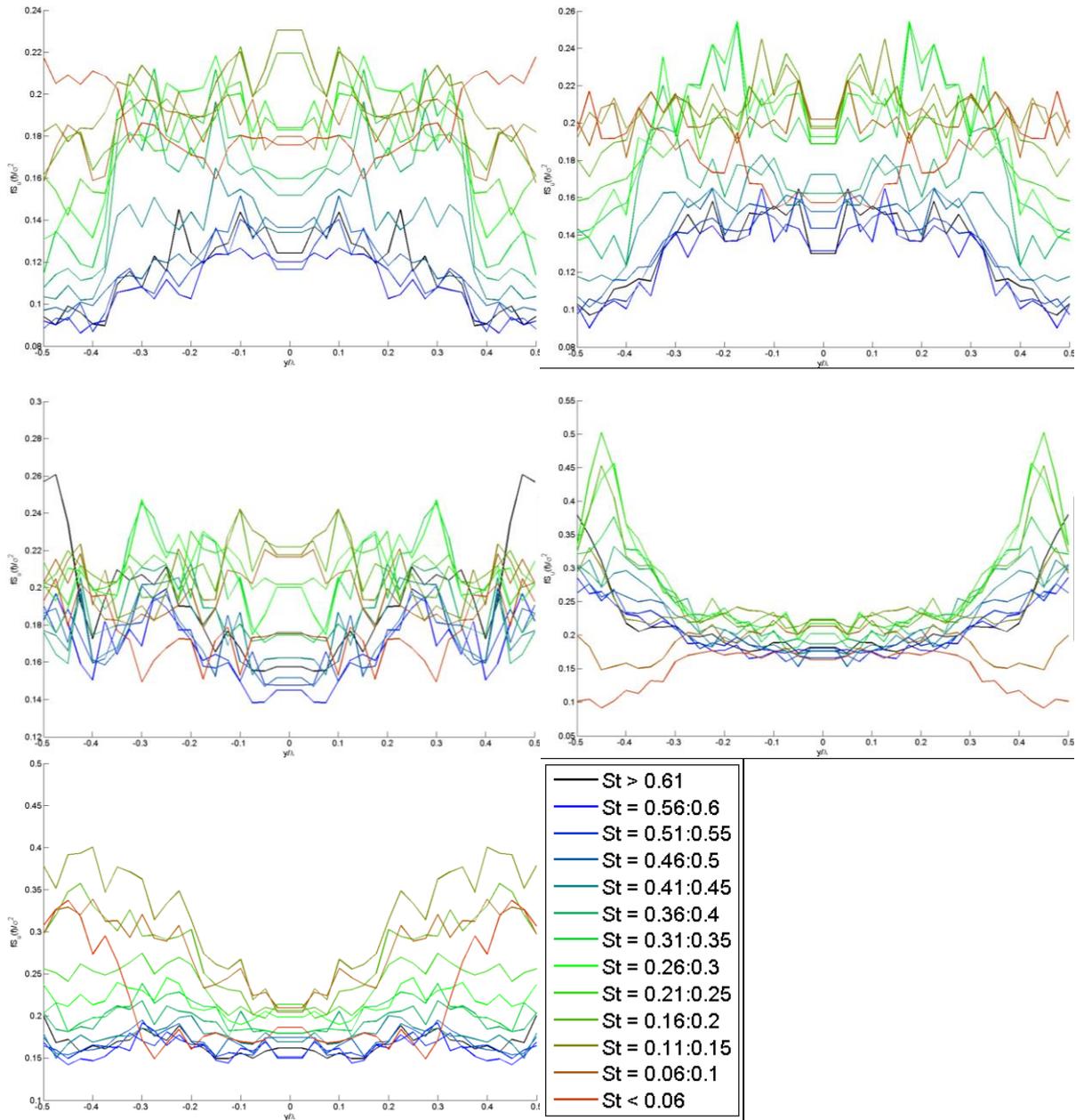
Figure 152: Power maxima from each Strouhal number bin, shown at lateral locations, centred on the peak of the sinusoid with *A/λ* = 0.325 and *z/h* = 0.5. Planes are *x/h* = -2.6 (top left), -1.3 (top right), 0 (middle left), 2 (middle right), 10 (bottom left).

In the farthest downstream plane at *x/h* = 10, shown in Figure 152, the energy content of the persistent vortices remained elevated. Lateral spread of the regions affected by the vortex structures was observed, consistent with a gradual diffusion of the vortex structures. The Strouhal number bin containing the peak relative energy also decreased; the 0.11 < St < 0.15 bin being the dominant bin, indicating a gradual reduction in the speed of the propagation of the vortices relative to the free-stream flow.

The energy content and Strouhal number was consistent with the equivalent measurements in the sawtooth case, as shown in the comparison presented in Figure 153. The comparison suggests that the sinusoidal case follows the Strouhal number development described by Gursul (1994) more closely than the sawtooth case.
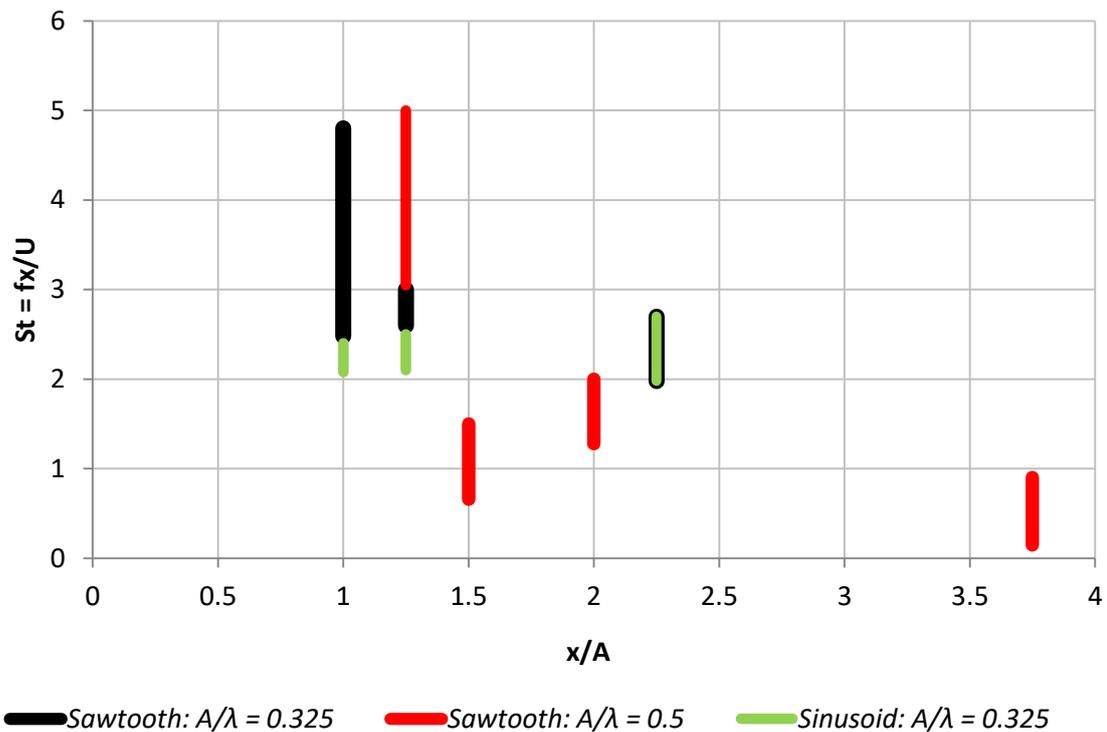

Figure 153: Ranges of dominant Strouhal numbers versus distance downstream of apex for the sawtooth *A/λ* = 0.325 case and the *A/λ* = 0.5 case, for comparison with the sinusoidal *A/λ* = 0.325 case. Note that the Strouhal number is calculated based on distance downstream of the peak or apex, as is the distance downstream, *x*. The distance downstream, *x*, is normalised by the amplitude, *A*.

7.3 Summary

This research has modelled flow over a FFS, using a sinusoidal lateral variation to model the natural ruggedness associated with cliffs. *A/λ* was varied, and the flow structure was derived through surface shear stress visualisations. The mean flow topology that was derived in each case was compared to surface pressure measurements where good agreement was observed.

The flow topology was shown to be invariant through the range of *A/λ* ratios investigated. The flow structure featured a recirculation region over the peak protrusion of the sinusoid which propagated downstream along the crest of the cliff, generating a delta wing style vortex structure. The dominant

vortex structure separated from the crest of the step and persisted downstream into the far wake. The separation point became closer to the trough point as A/λ increased.

Velocity measurements over the A/λ = 0.325 case revealed a speed-up over the protruding sinusoidal section, suggesting that there might be regions conducive to wind turbine siting associated with such geometries. Turbulence intensity, as well as pitch and yaw angles were measured. By siting wind turbines such that their rotors pass above half a cliff height at their lowest point, the potential to avoid extreme values of turbulence intensity, pitch angle, veer angle and Reynolds Stress was highlighted. Beyond the trough point, the flow structures experienced increases in height associated with the vortex interactions and the diffusion of the structures, making it difficult to site the turbines in such a way as to avoid the flow structures.

The dynamics of the flow were also investigated by mapping the development of the Strouhal number. This analysis was conducted at a height of $0.5h$. The analysis revealed that the relative spectral energy associated with the flow structure only became dominant beyond the trough region for heights above $0.5h$ above the surface of the model. In this downstream region, a large increase in relative spectral energy was observed in the regions associated with the delta wing style vortices that had persisted downstream as vortex pairs. Most of the energy was contained within the range $0.21 <$ St < 0.25. By $10h$ downstream the dominant Strouhal number had reduced to be within the range $0.11 <$ St < 0.15, indicating a gradual reduction in propagation speed of the vortices as they dissipated and as their vortex core increased in diameter, consistent with delta wing literature.

8. Conclusions

This research, in investigating flow over the FFS, has sought to tackle the problem from two perspectives. Being a project sponsored by the wind energy industry, with direct applicability to many Australian wind farms, it was necessary to take a wind engineering approach to the problem; that is, to consider specific wind farm topographies, and to strip back the complexity so as to draw conclusions that might be generally applied. The alternative perspective was that of the fluid dynamicist, whose approach is to take a simple geometry and to incrementally add complexity to it, focussing on the underlying mechanisms that give rise to the flow parameters, which are of concern to the wind engineer.

The simple geometry of the FFS has been considered in great detail in the literature; however there has been very little development beyond that base case. This investigation provided a validation of the methodology and equipment against the existing literature, before considering, first, the effect of wind direction, and secondly, the effect of ruggedness on the flow over the forward facing step. Approaches to wind turbine siting for both the straight-edged and rugged cases have also been recommended that provide an alternative to the recommendation of Cochard et al. (2012).

Wind tunnel experiments were used to investigate flow over various shaped cliffs. This began with validation studies, matching wind tunnel results against those found in the literature. Mean velocity and turbulence statistics matched well with the wind tunnel study of Bowen and Lindley (1977), with variation attributable to the different measurement techniques, the differences in boundary layer thickness and distribution, and Reynolds number. Reynolds stresses also compared well with those published by Ren and Wu (2011). Again, variations were attributable to the measurement techniques employed and the differences in the inflow conditions. The peak Strouhal number range of $0.15 - 0.25$ that was observed was in good agreement with the figure published by Camussi et al. (2008). The intermittent nature of the shedding meant that a broad frequency peak was measured, which is also consistent with the observations of Camussi et al. (2008). Finally, the mean reattachment lengths, measured using surface shear stress visualisations, compared well with the

results published in the literature. This consistent agreement with the published data provided confidence in the subsequent results. The limitations of the different measurement techniques in measuring recirculating flow is also an important part of understanding the comparison between the results presented here, and those published in the literature, and ultimately, the new results.

Having established that the base FFS case was consistent with the literature, original research was conducted on the effects of wind direction on the flow over the FFS. This element of the research revealed wind statistics that could be applied to wind turbine siting on cliffs, as well as providing insight into the underlying fluid mechanics.

The size of the recirculation bubble, measured through the proxy of mean reattachment length was the first element considered. The study concluded that a distinction could be made between low turbulence intensity cases and high turbulence intensity cases. In the low turbulence intensity cases, the mean reattachment length was already larger than each of the higher turbulence intensity cases. It was concluded that the turbulence intensity acts to break down the vortex structure. In the low turbulence intensity cases, when the wind direction was altered, the reattachment length increased until a yaw angle of 40° was reached, beyond which the reattachment length decreased. This increase in mean reattachment length was attributed to an increase in coherence induced by the flow being funnelled across the crest of the yawed step. Again, increases in turbulence intensity resulted in the breakdown of this coherence, and thus, no distinct relationship was observed between the yaw angle and the mean reattachment length in the high turbulence intensity cases. The surface shear stress visualisations also revealed a span-wise periodicity to the shedding from the recirculation region at the crest. This was observed only in the low turbulence intensity cases at high yaw angle, adding weight to the argument that the inflow turbulence intensity is a dominant parameter in the flow structure, affecting the breakdown of the vortex structures.

Yet, the direction of the streaks through the middle of the mean recirculation region, relative to the free-stream flow, while varying linearly with yaw angle, was consistent across the different inflow

conditions. This indicates that a consistent flow structure exists independently of turbulence intensity.

Velocity measurements were conducted for a single inflow condition for yaw angles of 0°, 20°, 30°, and 40°. The results were assessed in the context of wind turbine siting: balancing speed-up and the associated power increases with concerns for the fatigue loading and the potential for unbalanced loads across the wind turbine rotor. This was quantified by considering the following variables: speed-up, turbulence intensity ratio, pitch angle, wind veer, cross-covariance, and Strouhal number.

While observing conditions unsuitable for wind turbine siting within the recirculation region was unsurprising, observing the persistence of these conditions, in particular a three-fold increase in turbulence intensity and reduction in wind speed of the order of forty percent through to $10h$ downstream of the crest was of interest, relative to inflow conditions. The underlying mechanism was first described by Kiya and Sasaki (1983b) in terms of the flapping recirculation bubble that they observed experimentally.

While the increase in yaw angle ultimately resulted in conditions more quickly returning to the inflow conditions, the siting of wind turbines downstream of the mean recirculation bubble will subject them to lower wind speed and increased fatigue loading. A region half a step height downstream of the crest and above half a step height from the surface was associated with an increase in wind speed with a minimal increase in turbulence intensity, as can be seen in Figure 154. This aspect of the research begins to quantify the effects that the various flow structures observed would have on the inflow conditions. However, implementing such advice in wind farm design clearly needs to be done in conjunction with site-specific analysis. In many instances, solutions to the wind engineering problems may not be feasible due to geotechnical or planning issues.
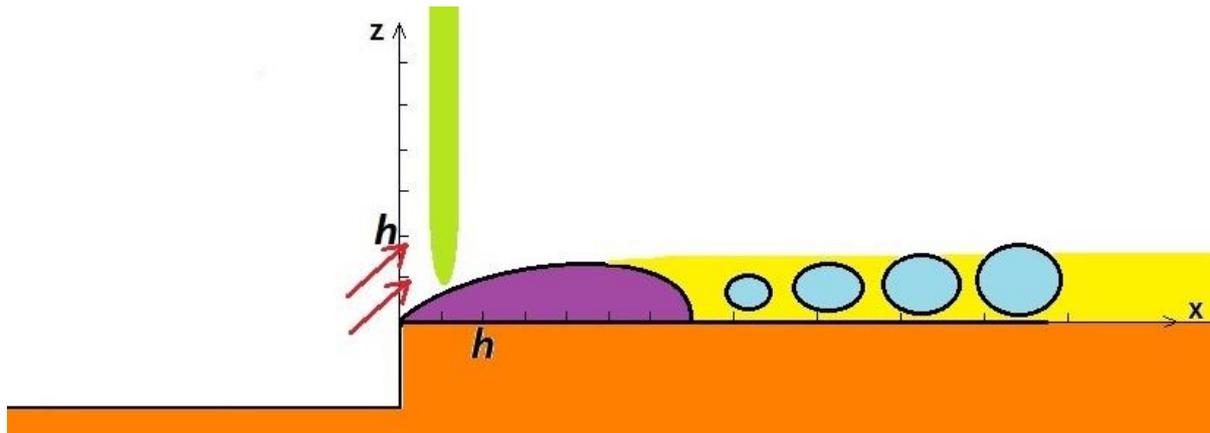
Figure 154: Illustration of siting approach, showing optimal siting location in green, recirculation region in purple, vortices shed from the recirculation region in blue, and the region of elevated turbulence intensity in yellow. The red arrows indicate regions of high inflow angle and wind veer (in non-zero yaw conditions).

The effect of ruggedness was also considered. Ruggedness was modelled first as a sawtooth lateral variation, and then as a sinusoidal variation. With each approach, the amplitude of the lateral variation was varied. While Cochard et al. (2012) and Montlaur et al. (2012) considered speed-up and turbulence statistics over a sawtooth case and made some general notes on the flow structure they did not consider the flow topology and its development in great detail, nor did they consider the sinusoidal case. This left considerable scope for the present investigation. Furthermore, analogies with flow over delta wings provided insight into the breakdown of the vortex structures. Both quantitative and qualitative comparisons with descriptions presented in the delta wing literature were made, and variations between the cases could be related back to the flow topology and, ultimately the topography. In particular, the identification of vortex bursting above and downstream of the sawtooth and sinusoidal topographic elements was consistent with the descriptions in the literature.

Considering a sawtooth lateral variation, with its sharp edges providing distinct locations for flow separation, it was expected that topological equivalence would be maintained between the four sawtooth FFS cases examined. In contrast, the sinusoidal cases were considered to be more complicated, due to the lack of distinct shedding points. The reverse was shown to be true. While

246

the sawtooth topology experienced significant development, the sinusoidal geometries were topologically self-consistent.

Two distinctions between the shapes were observed. First, the vortex structure was unbroken around the peak of the sinusoid, whereas the peak of the sawtooth provided a distinct starting point for the vortex line. Second, the number of secondary structures observed in the sawtooth cases increased as the amplitude to wavelength ratio was increased. This increase in the number of secondary structures resulted in an increase in the size of the region associated with the secondary vortices, that is, the bifurcation line (the delineation between the primary vortex structure and the secondary structures) was shifted farther from crest of the FFS. This induced rotation about stable nodes near the trough region. In contrast, the increase in A/λ had little impact on the secondary structures in the sinusoidal cases. The location of the bifurcation line between the primary vortex and the secondary structure relative to the crest of the FFS remained constant.

From these observations, it was concluded that the curvature associated with the sinusoidal cases had a stabilising effect on the flow topology by controlling the development of the secondary vortex structures.

The same approach to siting wind turbines near straight-edged cliffs needs to be taken when considering the siting of wind turbines in the vicinity of rugged cliffs. The three primary concerns are wind speed, fatigue loading, and the balance of aerodynamic loads across the rotor blades. As in the straight-edged cases, whether or not at zero yaw angle, the primary vortex regions will induce undesirable loads on the wind turbine rotors, and need to be avoided. In the cases where the flow topology is affected by ruggedness, such that vortices separate off the crest and persist downstream, as was observed in each of the cases where ruggedness was modelled in this research, the siting of wind turbines need to be managed such that contact with the resultant vortex structures, whether in their jet-like states or in their burst states, are avoided. Having burst, the vortices that persist downstream gradually diffuse, the result being that their effective diameter

increases, making them more difficult to avoid in downstream regions. The undesirable flow induced by these structures was shown to extend beyond ten step heights downstream of the trough point, in much the same way as the ejections from the recirculation bubbles along the straight-edged steps, except that the vortex axes were aligned with the free-stream flow when ruggedness was modelled.

Aligning wind turbines with the peaks of the ruggedness is an approach that would only prove beneficial if the wind direction was guaranteed to be unidirectional, perpendicular to the mean crest line. Montlaur et al. (2012) demonstrated that the axes of the persistent vortices would become aligned to the free-stream velocity, rendering such an approach impracticable for any real-world situation.

Siting wind turbines above the vortex structures is a possible approach to avoiding the vortex structures. But, as already discussed, the diffusion of the flow structures downstream makes this approach less viable. However, for a small cliff this approach may be feasible, though in the downstream regions, peak Reynolds Stresses (R_{uw}), associated with the largest loads on wind turbines, were observed at $2h$ above the surface.

The most promising approach based on this research is to site the wind turbines on the protrusions themselves, taking advantage of the graduated growth of the delta wing style vortices along the crest, as illustrated in Figure 155. While the sawtooth or sinusoidal protrusion is shown to be a region of vortex growth, induced by the flow-crest interaction, the vortices are contained to the vicinity of the crest. Cochard et al. (2012) observed that applying a yaw angle to a sawtooth FFS geometry had the potential to double the size of the region affected by the vortex, however, the vertical velocity profile was not considered. From the Cobra Probe measurements over the yawed FFS cases from Chapter 5, the vertical extent of the adverse wind conditions induced by the sawtooth ruggedness can be inferred. Even at non-zero yaw angles, they are confined to below $0.5h$ above the surface over the sawtooth protrusions, while regions where the speed-up is greater than

one extend vertically above the crest vortices. Thus the sketch provided in Figure 154 is still pertinent for the rugged FFS cases. The rugged FFS domain presented in Figure 155 does, however, confine the siting region to the topographic protrusion, and avoids the trough region.
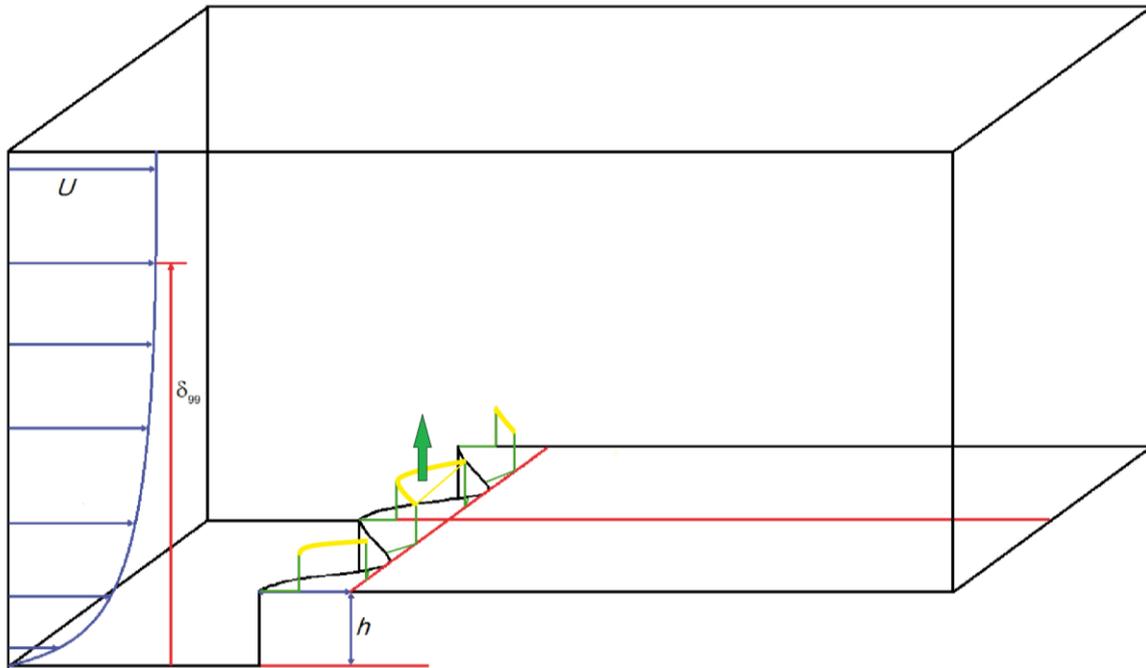
Figure 155: Siting approach over rugged cliffs. Green lines represent a distance of half a step height. The green arrow represents a possible turbine location.

There are, however, a range of caveats associated with this body of work. The most fundamental is that this work represents an approximation of real-world topography modelled at Reynolds numbers orders of magnitude below real world conditions. While the precise magnitudes of, for example, the size of the flow structures, the velocity profiles and turbulence intensity profiles vary, comparisons with field data demonstrate consistency in the flow structures that are observed.

Additional approximations and assumptions in this work include:

- Model geometries were highly idealised as sharp-edged crests, vertical cliffs, and a regular and symmetrical approximation of ruggedness.

- Surface roughness has not been considered.

- Atmospheric stability is assumed to be neutral.

- Inflow conditions do not match atmospheric conditions.

While these approximations and assumptions limit one's ability to apply the results directly to a given wind farm site, the flow structures identified provide a deeper understanding of the wind flow and how it is affected by different geometric features, enabling better informed analyses of an individual site's conditions. There is significant scope in future work to test these assumptions, with more detailed investigations into the effect of wind direction, and to consider a greater array of geometries and to explore the relationship between the cliff height and the parameters that describe the ruggedness. Further site measurements would also provide a valuable source of comparison.

9. List of Publications

Rowcroft, J. (2011). "Vertical wind shear profiles in downburst events and the insufficiency of wind turbine design codes." <u>13th International Conference for Wind Engineering</u>. Amsterdam.

Rowcroft, J., Sheridan, J., Blackburn, H.M., and Burton, D. (2013). "Surface flow visualisation over forward facing steps with varying yaw angle." <u>The Science of Making Torque from the Wind</u>. Oldenburg. Journal of Physics Conference Series **555**, 012086. DOI:10.1088/1742-6596/555/1/012086.

Rowcroft, J. Sheridan, J., Blackburn, H.M., and Burton, D. (2013). "Optimal Placement of Wind Turbines on Cliffs". <u>Australasian Wind Engineering Society Workshop</u>, Brisbane.

Rowcroft, J., Burton, D., Blackburn, H. M., and Sheridan, J. (2016) Siting wind turbines near cliffs—the effect of wind direction. <u>Wind Energy</u>, **19,** 1469–1484. DOI: 10.1002/we.1931.

Publications in preparation:

Rowcroft, J., Burton, D., Blackburn, H.M., and Sheridan, J. (2014). "Mean Topology Development on Forward Facing Steps with Sawtooth Lateral Variations".

Rowcroft, J., Burton, D., Blackburn, H.M., and Sheridan, J. (2014). "Mean Topology Development on Forward Facing Steps with Sinusoidal Lateral Variations for Wind Turbine Siting".

10. References

Cobra Probe. http://turbulentflow.com.au/Downloads/Flyer_CobraProbe.pdf. Victoria, Australia, Turbulent Flow Instrumentation Pty Ltd.

(2009). Renewable Energy (Electricity) Amendment Bill 2009. House of Representatives. **The Parliament of the Commonwealth of Australia**.

Abdalla, I. E., et al. (2009). "Computational analysis and flow structure of a transitional separated-reattached flow over a surface mounted obstacle and a forward facing step." International Journal of Computational Fluid Dynamics **23**(1): 25-57.

AS/NZS (2011). Structural design actions. Part 2: Wind actions. Sydney, Wellington, Standards Australia/Standards New Zealand. **AS/NZS 1170.2:2011:** 99.

Ayotte, K. W. (2008). "Computational modelling for wind energy assessment." Journal of Wind Engineering and Industrial Aerodynamics(96): 1571-1590.

Baker, C. J. (1985). "The determination of topographical exposure factors for railway embankments." Journal of Wind Engineering and Industrial Aerodynamics **21**: 89-99.

Bearman, P. W. and J. C. Owen (1998). "Reduction of bluff body drag and suppression of vortex shedding by the introduction of wavy separation lines." Journal of Fluids and Structures **12**: 123-130.

Bearman, P. W. and N. Tombazis (1993). "The Effects of Three-Dimensional Imposed Disturbances on Bluff Body Near Wake Flows." Journal of Wind Engineering and Industrial Aerodynamics **49**: 339-350.

Bendat, J. S. and A. G. Piersol (1993). Engineering Applications of Correlation and Spectral Analysis. Canada, John Wiley & Sons, Inc.

Bergh, H. and H. Tijdeman (1965). Theoretical and experimental results for the dynamic response of pressure measurement systems. Amsterdam, National Aero and Astronautical Research Institute.

Betz, A. (1919). Schraubenpropeller mit geringstem Energieverlust. Gottinger Nachrichten. Delft.

Bitsuamlak, G. T., et al. (2004). "Numerical Evaluation of Wind Flow over Complex Terrain: Review." Journal of Aerospace Engineering **17**(4): 135-145.

Bloor, S. (1964). "The transition to turbulence in the wake of a circular cylinder." Journal of Fluid Mechanics **19**: 290-304.

Bowen, A. J. (1979). SOME EFFECTS OF ESCARPMENTS ON THE ATMOSPHERIC BOUNDARY-LAYER. Mechanical Engineering. Christchurch, New Zealand, University of Canterbury. **Doctor of Philosophy:** 347.

Bowen, A. J. and D. Lindley (1977). "A wind tunnel investigation of the wind speed and turbulence characteristics close to the ground over various shaped escarpments." Boundary Layer Meterology **12**: 259-271.

Brun, C., et al. (2008). "Coherent Structures and their Frequency Signature in the Separated Shear Layer on the Sides of a Square Cylinder." Flow, Turbulence and Combustion **81**: 97-114.

Burton, T., et al. (2001). Wind Energy Handbook. Chichester, John Wiley & Sons.

Camussi, R., et al. (2008). "Statistical properties of wall pressure fluctuations over a forward facing step." Physics of Fluids **20**.

Carter, R. W. G. and C. D. Woodroffe, Eds. (1994). Coastal Evolution: Late Quaternary shoreline morphdynamics. A contribution to IGCP Project 274: Coastal Evolution in the Quaternary. Cambridge, United Kingdom, The Press Syndicate of the University of Cambridge.

Castro, I. P. and M. Dianat (1983). "Surface flow patterns on rectangular bodies in thick boundary layers." Journal of Wind Engineering and Industrial Aerodynamics(11): 107-119.

Chan, Y. X. (2012). Tube Response of Wind Tunnel Pressure Measurement Systems. Mechanical and Aerospace Engineering. Melbourne, Monash University. **Engineering**.

Chay, M. T., et al. (2006). "Numerical and analytical simulation of downburst wind loads." Engineering Structures **28**(2): 240-254.

Chen, J., et al. (2000). "Cobra probe measurements of mean velocities, Reynolds stresses and higher-order velocity correlations in pipe flow." Experimental Thermal and Fluid Science **21**: 206-217.

Chen, W. F. and E. M. Lui, Eds. (2005). Handbook of Structural Engineering, CRC Press.

Choi, E. (2004). "Field measurement and experimental study of wind speed profile during thunderstorms." Journal of Wind Engineering and Industrial Aerodynamics **92**: 275-290.

Cimbala, J. M., et al. (1988). "Large structure in the far wakes of two-dimensional bluff bodies." Journal of Fluid Mechanics **190**: 265 - 298.

Cochard, S., et al. (2011). PIV measurements of the velocity over triangular shaped cliffs. 13th International Conference for Wind Engineering. Amsterdam.

Cochard, S., et al. (2012). "Formation of tip-vortices on triangular prismatic-shaped cliffs Part 1: A wind tunnel study." Journal of Wind Engineering and Industrial Aerodynamics **109**: 9-20.

Cook, N. J. (1978). "Wind-tunnel simulation of the adiabatic atmospheric boundary layer by roughness, barrier and mixing-device methods." Journal of Industrial Aerodynamics **3**: 157-176.

Cook, N. J. (1997). "The Deaves and Harris ABL model applied to heterogeneous terrain." Journal of Wind Engineering and Industrial Aerodynamics **66**(3): 197-214.

Counihan, J. (1973). "Simulation of an Adiabatic Boundary Layer in a Wind Tunnel." Atmospheric Environment **7**: 673-689.

Counihan, J. (1975). "Adiabatic atmospheric boundary layers: A review and analysis of data from the period 1880-1972." Atmospheric Environment **9**: 871-905.

Cuevas-Cubria, C., et al. (2011). Energy in Australia 2011. Canberra, Commonwealth of Australia**: 93.

Darekar, R. M. and S. J. Sherwin (2001). "Flow past a square-section cylinder with a wavy stagnation face." Journal of Fluid Mechanics **426**: 263-295.

Davenport, A. G. (1960). "Rationale for determining design wind velocities." Proceedings of the American Society of Civil Engineers Journal of the Structural Division **86**(5): 39 - 68.

Davenport, A. G., et al. (1992). Wind Engineering Course Notes**: 806.

Deaves, D. M. and R. I. Harris (1978). A Mathematical Model of the Structure of Strong Winds, Construction Industry Research and Information Association.

Delnero, J. S., et al. (2005). "Experimental determination of the influence of turbulent scale on the lift and drag coefficients of low Reynolds number airfoils." Latin American Applied Research **35**(3): 183-188.

di Mare, L. and W. P. Jones (2003). "LES of turbulent flow past a swept fence." International Journal of Heat and Fluid Flow **24**(4).

Dropkin, A., et al. (2012). "Computation of Flowfield around an Airfoil with Leading-Edge Protruberances." Journal of Aircraft **49**(5): 1345-1355.

Eaddy, M. (2005). Lift Forces on Smooth and Rough Circular Cylinders in Low and High Turbulence Flows. Clayton, Monash University. **Doctoral thesis**.

Emeis, S., et al. (1995). "Modification of air flow over an escarpment - results from the Hjardemal experiment." Boundary-Layer Meteorology(74): 131-161.

ESAA (2012). Comparing Australian and International Electricity Prices, Energy Supply Association of Australia.

ESDU (1985). Characteristics of atmospheric turbulence near the ground Part II: single point data for strong winds (neutral atmosphere). London, IHS.

EUAA (2012). Electricity Prices in Australia: An International Comparison.

Farabee, T. M. and M. J. Casarella (1986). "Measurements of Fluctuating Wall Pressure for Separated/Reattached Boundary Layer Flows." Journal of Vibration, Acoustics, Stress, and Reliability in Design **108**: 301-307.

Farabee, T. M. and M. J. Casarella (1991). "Spectral features of wall pressure beneath turbulent boundary layers." Phys Fluids **3**: 2410-2420.

Faulstich, S., et al. (2010). "Wind turbine downtime and its importance for offshore deployment." Wind Energy.

Fritz, B. F. (2003). Measurement and Analysis of Atmospheric Stability in Two Texas Regions. 37th Annual National Agricultural Aviation Association Convention. Reno, Nevada, The Society for engineering in agricultural, food, and biological systems**:** 16.

Gad-el-Hak, M. and R. F. Blackwelder (1985). "The Discrete Vortices from a Delta Wing." AIAA Journal **23**(6): 961-962.

Ginger, J. D. and C. W. Letchford (1992). "Peak wind loads under delta wing vortices on canope roofs." Journal of Wind Engineering and Industrial Aerodynamics **41-44**: 1739-1750.

Gjerstad, J., et al. (1995). "An Analysis of Low-Frequency Maritime Atmospheric Turbulence." American Meteorological Society **52**(15): 2663-2669.

Gordnier, R. and M. R. Visbal (1994). "Unsteady Vortex Structure over a Delta Wing." Journal of Aircraft **31**(1): 243-248.

Gordnier, R. and M. R. Visbal (2003). Higher-order compact difference scheme applied to the simulation of a low sweep delta wing flow. 41st AIAA Aerospace Sciences Meeting and Exhibit. Reno, Nevada, AIAA. **2003-620:** 1-15.

Gsänger, S. (2013). The World Wind Energy Association Half Year Report 2013. Bonn, Germany, World Wind Energy Association.

Gursul, I. (1994). "Unsteady Flow Phenomena over Delta Wings at High Angle of Attack." AIAA Journal **32**(2): 225-231.

Gursul, I. (2005). "Review of Unsteady Vortex Flows over Slender Delta Wings." Journal of Aircraft **42**(2): 299-319.

Gursul, I., et al. (2005). "Unsteady aerodynamics of nonslender delta wings." Progress in Aerospace Sciences **41**(7): 515-557.

Gursul, I. and W. Xie (2000). "Origin of Vortex Wandering over Delta Wings." Journal of Aircraft **37**(2): 348-350.

Hall, M. G. (1972). "Vortex Breakdown." Annual Review of Fluid Mechanics **4**: 195-218.

Hand, M. M., et al. (2003). Identification of Wind Turbine Response to Turbulent Inflow Structures. 4th ASME/JSME Joint Fluids Engineering Conference. Honolulu, Hawaii.

Hansen, A. C. (1992). Yaw Dynamics of Horizontal Axis Wind Turbines. Salt Lake City, University of Utah.

Hansen, A. C. and C. P. Butterfield (1993). "Aerodynamics of horizontal-axis wind turbines." Annual Review of Fluid Mechanics **25**: 115-149.

Hansen, K. S., et al. (2012). "The impact of turbulence intensity and atmospheric stability on power deficits due to wind turbine wakes at Horns Rev wind farm." Wind Energy **15**(1): 183-196.

Harbig, R. (2013). RANS Modelling of Sawtooth Cliffs. J. Rowcroft. Melbourne.

Hattori, H. and Y. Nagano (2010). "Investigation of turbulent boundary layer over forward-facing step via direct numerical simulation." International Journal of Heat and Fluid Flow **31**(3): 284-294.

Heggem, T., et al. (1998). "Analysis of long time series of coastal wind." Journal of Atmospheric Sciences **55**(18): 2907-2917.

Hillier, R. and N. J. Cherry (1981). "The Effects of Stream Turbulence on Separation Bubbles." Journal of Wind Engineering and Industrial Aerodynamics **8**: 49-58.

Ho, C.-M. and L.-S. Huang (1982). "Subharmonics and vortex merging in mixing layers." Journal of Fluid Mechanics **119**: 443 - 473.

Ho, C.-M. and P. Huerre (1984). "Perturbed free shear layers." Annual Review of Fluid Mechanics **16**: 365-424.

Hoerner, S. F. and H. V. Borst (1985). Fluid-Dynamic Lift; Practical Information on Aerodynamic and Hydrodynamic Lift, Liselotte A. Hoerner.

Holmes, J. D. (2007). Wind Loading of Structures. London & New York, Taylor & Francis.

Holmes, J. D., et al. (1997). "Measurements of topographic multipliers and flow separation from a steep escaprment. Part I. Full scale measurements." Journal of Wind Engineering and Industrial Aerodynamics(69-71): 885-892.

Holmes, J. D. and S. E. Oliver (2000). "An empirical model of a downburst." Engineering Structures **22**: 1167-1172.

Hooper, J. D. and A. R. Musgrove (1991). Multi-hole Pressure Probes for the Determination of the Total Velocity Vector in Turbulent Single-Phase Flow. 4th International Symposium on Transport Phenomena in Heat and Mass Transfer. Sydney, NSW. **4:** 1364-1373.

Hooper, J. D. and A. R. Musgrove (1997). "Reynolds Stress, Mean Velocity, and Dynamic Static Pressure Measurement by a Four-Hole Pressure Probe." Experimental Thermal and Fluid Science **15**: 375-383.

Huang, R. F. and C. L. Lin (1995). "Vortex Shedding and Shear-Layer Instability of Wing at Low-Reynolds Numbers." AIAA Journal **33**(8): 1398-1403.

Hui, M. C. H., et al. (2009). "Wind turbulence characteristics study at the Stonecutters Bridge site: Part II: Wind power spectra, integral length scales and coherences." Journal of Wind Engineering and Industrial Aerodynamics **97**(1): 48-59.

Hunt, J. C. R., et al. (1978). "Kinematical studies of the flows around free or surface-mounted obstacles; applying topology to flow visualization." Journal of Fluid Mechanics **86**(1): 179-200.

IEC (2005). IEC 61400 Wind Turbines. Part 1: Design Requirements. Geneva, International Electrotechnical Commission.

Isyumov, N., Ed. (1999). Wind Tunnel Studies of Buildings and Structures. ASCE Manuals and Reports on Engineering Practice. Reston, American Society of Civil Engineers.

Jackson, D. W. T., et al. (2013). "Airflow reversal and alternating corkscrew vortices in foredune wake zones during perpendicular and oblique offshore winds." Geomorphology **187**: 86-93.

Jackson, P. S. and J. C. R. Hunt (1975). "Turbulent wind flow over a low hill." Quarterly Journal of the Royal Meteorological Society(101): 929-955.

Jacobson, M. Z. (2005). Fundamentals of Atmospheric Modelling. Cambridge, Cambridge University Press.

Johnston, J. P. (1970). "Measurements in a three-dimensional turbulent boundary layer induced by a swept, forward-facing step." Journal of Fluid Mechanics **42**(4): 823-844.

Kaimal, J. C., et al. (1972). "Spectral Characteristics of Surface Layer Turbulence." Q. J. R. Meteorol. Soc. **98**: 563-589.

Kaldellis, J. K. and D. Zafirakis (2011). "The wind energy (r)evolution: A short review of a long history." Renewable Energy **36**(7): 1887-1901.

Kalmikov, A., et al. (2011). Wind Power Fundamentals. Massachussetts, Massachussetts Institute of Technology.

Kaltenbach, H.-J. (2003). "The Effect of Sweep-Angle Variation on the Turbulence Structure in a Separated, Three-Dimensional Flow." Theoretical and Computational Fluid Dynamics **16**: 187-210.

Katz, J. (1999). "Wing/vortex interactions and wing rock." Progress in Aerospace Sciences **35**(7): 727-750.

Kim, J. and H. Hangan (2007). "Numerical simulations of impinging jets with application to downbursts." Journal of Wind Engineering and Industrial Aerodynamics **95**(4): 279-298.

Kiya, M. and K. Sasaki (1983a). "Free-Stream Turbulence Effects on a Separation Bubble." Journal of Wind Engineering and Industrial Aerodynamics **14**: 375-386.

Kiya, M. and K. Sasaki (1983b). "Structure of a turbulent separation bubble." Journal of Fluid Mechanics **137**: 83-113.

Kourta, A., et al. (1987). "Nonlinear interaction and the transition to turbulence in the wake of a circular cylinder." Journal of Fluid Mechanics **181**: 141-161.

Kragh, A. K. and M. H. Hansen (2014). "Load alleviation of wind turbines by yaw misalignment." Wind Energy **17**(7): 971-982.

Largeau, J. F. and V. Moriniere (2007). "Wall pressure fluctuations and topology in separated flows over a forward-facing step." Experiments in Fluids **42**(1): 21-40.

Larsen, G. C. (1998). Consequences of variations in spatial turbulence characteristics for fatigue life time of wind turbines. Investigation of Design Apsects & Design Options for Wind Turbines Operating in Complex Terrain Environments. S. M. Petersen and P. Vølund. Roskilde, Risø National Laboratory**:** 29.

Leclercq, D., et al. (2001). Forward-backward facing step pair: Aerodynamic flow, wall pressure and acoustic characterisation. 7th AIAA/CEAS Aeroacoustics Conference and Exhibit. Maastricht, The Netherlands, AIAA**:** 075113-075111 - 075113-075113.

Lenschow, D. H., et al. (1980). "Mean-Field and Second-Moment Budgets in a Baroclinic, Convective Boundary Layer." American Meteorological Society **37**(6): 1313-1326.

Letchford, C. W., et al. (2002). "Thunderstorms - their importance in wind engineering (a case for the next generation wind tunnel)." Journal of Wind Engineering and Industrial Aerodynamics **90**: 1415 - 1433.

Lippisch, A. (1981). The Delta Wing: History and Development, Iowa State University Press.

Lowson, M. V., et al. (1995). Flow Structures Over Delta Wings. 33rd Aerospace Sciences Meeting and Exhibit. Reno, NV, AIAA. **95-0586**.

Lubitz, W. D. and B. R. White (2007). "Wind-tunnel and field investigation of the effect of local wind direction on speed-up over hills." Journal of Wind Engineering and Industrial Aerodynamics **95**: 639-661.

Lynette, R. (1988). California wind farms operational data collection and analysis, Sol. Energy Res. Inst. Rep.

Mann, J., et al. (2012). Laser scanning of a recirculation zone on the Bolund escarpment. The Science of Making Torque from Wind. Oldenburg, IOP Publishing. **555**.

Manwell, J. F., et al. (2009). Wind Energy Explained: Theory, Design and Application. Chichester, John Wiley & Sons.

Mason, M. S., et al. (2009). "Numerical investigation of the influence of topography on simulated downburst wind fields." Journal of Wind Engineering and Industrial Aerodynamics **98**: 21-33.

Matsui, T. and M. Okude (1983). Formation of the Secondary Vortex Street in the Wake of a Circular Cylinder. Structure of Complex Turbulent Shear Flow: Symposium, Marseille, France August 31 –

September 3, 1982. R. Dumas and L. Fulachier. Berlin, Heidelberg, Springer Berlin Heidelberg**: 156-164.

McConville, A. C. (2009). "The physical simulation of thunderstorm downbursts using an impinging jet." <u>Wind and Structures</u> **12**(2): 133-149.

Merzkirch, W. (1974). <u>Flow Visualization</u>. New York, Academic Press, Inc.

Miskelly, A. (2011). "Wind Farm Performance." Retrieved 30 May 2011, 2011.

Mohsen, M. (1967). Experimental investigation of the wall pressure fluctuations in subsonic separated flows, Boeing.

Montlaur, A., et al. (2012). "Formation of tip-vortices on triangular prismatic-shaped cliffs. Part 2: A computational fluid dynamics study." <u>Journal of Wind Engineering and Industrial Aerodynamics</u> **109**: 21-30.

Moon, Y. J., et al. (2006). Numerical Investigation of the Aerodynamic Noise from a Forward-Facing Step. <u>ECCOMAS CFD 2006: European Conference on Computational Fluid Dynamics</u>. P. Wesseling, E. Oñate and J. Périaux. TU Delft, The Netherlands.

Mortensen, N. G., et al. (2009). Wind Atlas Analysis and Application Program: WAsP 10 Help Facility. Roskilde, Denmark, Risø National Laboratory for Sustainable Energy, Technical University of Denmark.

Moss, W. and S. Baker (1980). "Re-circulating flows associated with two-dimensional steps." <u>Aeronautical Quarterly</u> **31**(August): 151-172.

Mousley, P. (2011). <u>Getting Started: Series 100 Cobra Probe</u>. Victoria, Australia, Turbulent Flow Instrumentation.

Mouzakis, F., et al. (1998). "Fatigue loading parameter identification of a wind turbine operating in complex terrain." <u>Journal of Wind Engineering and Industrial Aerodynamics</u> **82**: 69-88.

Musgrove, A. R. and J. D. Hooper (1993). PRESSURE PROBE MEASUREMENT OF THE TURBULENT STRESS DISTRIBUTION IN A SWIRLING JET. <u>Third World Conference on Experimental Heat Transfer, Fluid Mechanics and Thermodynamics</u> M. D. Kelleher, R. K. Shah, K. R. Sreenivasan and Y. Joshi. Hawaii. **1:** 172-179.

Naughton, R. and P. Gervais (2002). "Aviation and Aeromodelling - Interdependent Evolution and Histories." <u>Flying Wings</u>. Retrieved 2 April 2014, 2014, from <u>http://www.ctie.monash.edu.au/hargrave/lippisch.html</u>.

Nieuwstadt (1984). "The Turbulent Structure of the Stable, Nocturnal Boundary Layer." American Meteorological Society: Journal of the Atmospheric Sciences **41**(14): 2202-2216.

Oke, T. R. (1978). Boundary Layer Climates, Methuen & Co. Ltd.

Oliver, S. E., et al. (2000). "A risk model for design of transmission line systems against thunderstorm downburst events." Engineering Structures **22**: 1173-1179.

Orfanidis, S. J. (2007). Optimum Signal Processing: An Introduction. New York, New Jersey, McGraw-Hill Publishing Company ECE Department Rutgers University.

Orłowski, B. (1973). "Polish Works and Serials in the History of Technology." Technology and Culture **14**(3): 461-473.

Peake, D. J., et al. (1972). "Three-Dimensional Flow Separation on Aircraft and Missiles." AIAA Journal **10**(5): 567-580.

Pearson, D. S., et al. (2013). "Turbulent separtion upstream of a forward-facing step." Journal of Fluid Mechanics **724**: 284-304.

Perry, A. E. and M. S. Chong (1987). "A description of eddying motions and flow patterns using critical-point concepts." Annual Review of Fluid Mechanics **19**: 125-155.

Perry, A. E. and M. S. Chong (1994). "Topology of Flow Patterns in Vortex Motions and Turbulence." Applied Scientific Research **53**: 357-374.

Petersen, E. L., et al. (1998). "Wind Power Meteorology. Part 1: Climate and Turbulence." Wind Energy **1**: 25-45.

Petrusma, M. S. and S. L. Gai (1994). "The effect of geometry on the base pressure recovery of segmented blunt trailing edges." The Aeronautical Journal **98**: 267-274.

Porté-Agel, F., et al. (2010). A large-eddy simulation framework for wind energy applications. The Fifth International Symposium on Computational Wind Engineering. Chapel Hill, North Carolina, USA**:** 21.

Porté-Agel, F., et al. (2014). Interactions between large wind farms and the atmospheric boundary layer. 23rd International Congress of Theoretical and Applied Mechanics. Montreal, Elsevier. **10:** 307-318.

Rediniotis, O. K., et al. (1989). "Vortex Shedding over Delta Wings." AIAA Journal **28**(5): 944-946.

Rediniotis, O. K., et al. (1993). "Periodic Vortex Shedding over Delta Wings." AIAA Journal **31**(9): 1555-1562.

Ren, H. and Y.-T. Wu (2011). "Turbulent boundary layers over smooth and rough forward-facing steps." Physics of Fluids **23**: 1-17.

Riley, A. J. and M. V. Lowson (1998). "Development of a three-dimensional free shear layer." Journal of Fluid Mechanics **369**: 49-89.

Rohatgi, J. and G. Barbezier (1999). "Wind turbulence and atmospheric stability - Their effect on wind turbine output." Renewable Energy **16**(1-4): 908-911.

Rohli, R. V. and A. J. Vega (2011). Climatology. Sudbury, Jones & Bartlett.

Roos, F. W. and J. T. Kegelman (1990). Recent explorations of leading edge vortex flowfields, NASA.

Rowcroft, J. (2011). Vertical wind shear profiles in downburst events and the insufficiency of wind turbine design codes. Proceedings of the 13th International Conference on Wind Engineering. . Amsterdam, The Netherlands.

Saathoff, P. J. and W. H. Melbourne (1996). "Effects of free-stream turbulence on surface pressure fluctuations in a separation bubble." Journal of Fluid Mechanics **337**: 1-24.

Sacré, C. (1973). Influence d'une Colline sur la Vitesse du Vent dans la Couche Limite de Surface. Nantes, Centre Scientifique et Technique du Bâtiment.

Sathe, A. and W. Bierbooms (2007). "Influence of different wind profiles due to varying atmospheric stability on the fatigue life of wind turbines." Journal of Physics: Conference Series **75**(1).

Sathe, A., et al. (2013). "Influence of atmospheric stability on wind turbine loads." Wind Energy **16**: 1013-1032.

Sengupta, A. and P. P. Sarkar (2008). "Experimental measurement and numerical simulation of an impinging jet with application to thunderstorm microburst winds." Journal of Wind Engineering and Industrial Aerodynamics **96**(3): 345-365.

Shepherd, I. C. (1981). "A Four Hole Pressure Probe for Fluid Flow Measurements in Three Dimensions." Journal of Fluid Engineering **103**(4): 590-594.

Sherry, M., et al. (2010). "An experimental investigation of the recirculation zone formed downstream of a forward facing step." Journal of Wind Engineering and Industrial Aerodynamics **98**(12): 888-894.

Shir, C. C. (1973). "A Preliminary Numerical Study of Atmospheric Turbulent Flows in the Idealized Planetary Boundary Layer." Journal of the Atmospheric Sciences **30**: 1327-1339.

Sigurdson, L. W. (1995). "The structure and control of a turbulent reattaching flow." Journal of Fluid Mechanics **298**: 139-165.

Simpson, R. L. (1989). "TURBULENT BOUNDARY-LAYER SEPARATION." Annual Review of Fluid Mechanics **21**: 205-234.

Snel, H. and J. G. Schepers (1991). Engineering models for dynamic inflow phenomena. European Wind Energy Conference. Amsterdam.

Sorensen, J. N. (1986). Three-level, viscous-inviscid interaction technique for the prediction of separated flow past rotating wings. Roskilde, Technical University of Denmark.

Steeneveld, G. J., et al. (2007). "Comments on deriving the equilibrium height of the stable boundary layer." Q. J. R. Meteorol. Soc. **133**: 261-264.

Stull, R. B. (1997). An introduction to boundary layer meteorology. Dordrecht, Kluwer Academic Publishers.

Sumner, J. and C. Masson (2006). "Influence of Atmospheric Stability on Wind Turbine Power Performance Curves." Journal of Solar Energy Engineering **128**(4): 531 - 538.

Sverdrup, H. U. (1934). "Momentum exchange and stability in the lowest air layers." Met. Z **53**: 10-15.

Swalwell, K. E. (2005). The Effect of Turbulence on Stall of Horizontal Axis Wind Turbines. Mechanical and Aerospace Engineering. Melbourne, Monash University. **PhD:** 315.

Swalwell, K. E., et al. (2001). The Effect of Turbulence Intensity on Stall of the NACA 0021 Aerofoil. 14th Australasian Fluid Mechanics Conference. Adelaide University, Adelaide, Australia**:** 941-944.

Taneda, S. (1959). "Downstream Development of the Wakes behind Cylinders." Journal of the Physical Society of Japan **14**(6): 843-848.

Tashie, M. F., et al. (2001). "Open channel boundary layer relaxation behind a forward facing step at low Reynolds numbers." Journal of Fluid Engineering **123**: 539-544.

Tobak, M. and D. J. Peake (1982). "TOPOLOGY OF THREE DIMENSIONAL SEPARATED FLOWS." Annual Review of Fluid Mechanics **14**: 61-85.

Travner, P. J., et al. (2006). "Reliability for wind turbines." Wind Energy **10**(1): 1-18.

Tropea, C., et al., Eds. (2007). Springer Handbook of Experimental Fluid Mechanics. Springer Handbooks. Berlin, Springer.

Türk, M. and S. Emeis (2010). "The dependence of offshore turbulence intensity on wind speed." Journal of Wind Engineering and Industrial Aerodynamics **98**: 466-471.

van den Berg, G. P. (2007). "Wind turbine power and sound in relation to atmospheric stability." Wind Energy **11**(2): 151-169.

Van der Hoven, I. (1957). "Power spectrum of horizontal wind speed in the frequency range from 0.0007 to 900 cycles per hour." J. Meteor. **14**: 160-164.

Verhaagen, N. G. and B. C. Van Bossuyt (2006). Flow on a 65-deg Blunt Apex. 24th Applied Aerodynamics Conference. San Francisco, California, AIAA.

Vincent, C. L., et al. (2010). "Wind fluctuations over the North Sea." International Journal of Climatology **31**(11): 1584-1595.

Vogelezang, D. H. P. and A. A. M. Holtslag (1996). "Evaluation and model impacts of alternative boundary layer height formulations." Boundary Layer Meterology **81**: 245-269.

von Kármán, T. (1948). "Progress in the Statistical Theory of Turbulence." Proceedings of the National Academy of Sciences of the United States of America **34**(11): 530-539.

Wei, T. and C. R. Smith (1986). "Secondary vortices in the wake of circular cylinders." Journal of Fluid Mechanics **169**: 513-533.

Welch, P. D. (1967). "The Use of Fast Fourier Transform for the Estimation of Power Spectra: A Method Based on Time Averaging Over Short, Modified Perodograms." IEEE Trans. Audio Electroacoustics **15**(2): 70-73.

Wentz, W. H. and D. L. Kohlman (1971). "Vortex breakdown on slender sharp-edged wings." Journal of Aircraft **8**(3): 156-161.

Werle, H. (1954). "Quelques Resultants Experimentaux sur les Ailes en Fleche, aux Faibles Vitesses, Obtenus en Tunnel Hydrodynamicque." La Recherche Aeronautique **41**.

Weyl, A. R. (1945). "Tailless Aircraft and Flying Wings: A Study of Their Evolution and Their Problems." Aircraft Engineering **17**(2): 41-46.

Winant, C. D. and F. K. Browand (1974). "Vortex Pairing: the mechanism of turbulent mixing-layer growth at moderate Reynolds number." Journal of Fluid Mechanics **63**(2): 237 - 255.

WindLabSystems (2012). Predicted wind speed at 80 metres above ground level, 1995-2005, Australia. Renewable Energy Resource Maps. Australia, Renewables SA.

Yahaya, S. and J. Frangi (2003). "Spectral response of cup anemometers."

Yaniktepe, B. and D. Rockwell (2004). "Flow Structure on a Delta Wing of Low Sweep Angle." AIAA Journal **42**(3): 513-523.

Zhang, C. (1994). "Numerical predictions of turbulent recirculating flows with a k-ε model." Journal of Wind Engineering and Industrial Aerodynamics **51**: 177-201.

Zou, L. and Y.-F. Lin (2009). "Force reduction of flow around a sinusoidal wavy cylinder." Journal of Hydrodynamics **21**(3): 308-315.

Appendix: Performance of Cobra Probes in Recirculating Flow

Cobra Probes are limited to only being able to capture velocity data while the flow is aligned within the 45° cone of acceptance (Hooper and Musgrove 1997). However, when the flow is outside of the cone of acceptance the Cobra Probes, ideally, would not record data. This is presented as the "Percent Good Data" parameter. This parameter divides the number of "good" points (points aligned within the cone of acceptance), by the total number of points in a sample.

There is potentially an issue when the alignment of the probe and the flow are not within the 45° cone of acceptance, and flow separation from the probe results in pressure being applied to the face of the probe that could be interpreted as flow from within the cone of acceptance.

To demonstrate this point, four Cobra Probes were placed on a rake, with spacing of 25 mm, 50 mm and 25 mm, corresponding to 9.6, 19.2, and 9.6 times the width of the head of the probes, respectively. Three of the four probes faced forward, into the flow, while one of the four probes was rotated 180°, so its head was shielded from the flow. Eight tests were performed: two tests each at speeds of 5 ms^{-1}, 10 ms^{-1}, 15 ms^{-1}, 20 ms^{-1}, and 25 ms^{-1}. The turbulence intensity was approximately 1.5%.

Sampling at 2000 Hz for 90 s in free stream flow, three probes should have recorded 100% good data (all data points from a direction within the cone of acceptance) and the fourth probe should have 0% good data (no data points from a direction within the cone of acceptance).

Figure 156, plotting the flow velocity and percentage good data for four probes sampling simultaneously shows that all but one of the probes (Probe 120), record 100% good data. Meanwhile Probe 120, which was rotated 180° to face away from the flow, records, on average, 47% good data. This result is in agreement with the hypothesis presented above.

Therefore, caution must be used when Cobra Probes are implemented in cases where the flow direction fluctuates outside of the cone of acceptance, as the probe cannot consistently distinguish that the flow direction is outside of its cone of acceptance.
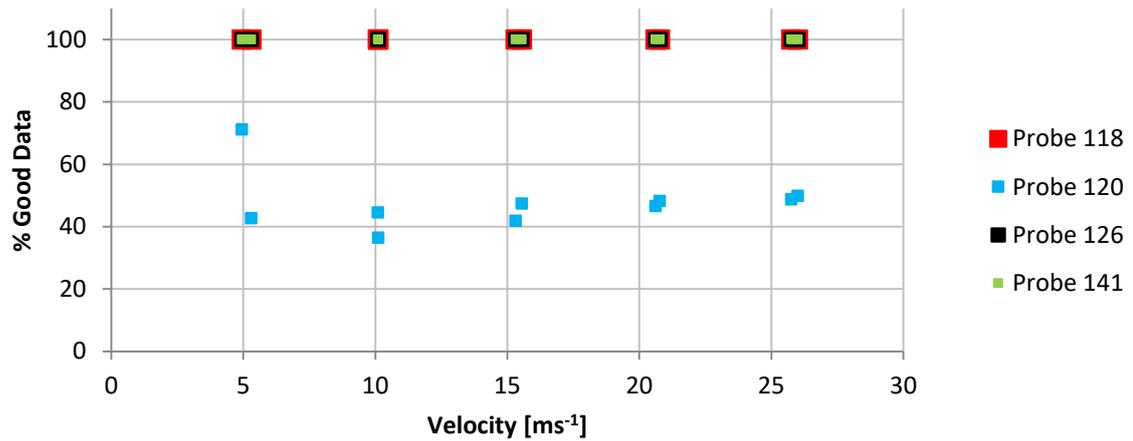
Figure 156: Plot of Percentage Good Data v Free-stream Velocity. Probes 118, 126 and 141 are correctly aligned into the flow. Probe 120 is aligned to capture reverse flow.

Appendix: Surface Shear Stress Visualisations – Forward Facing Step
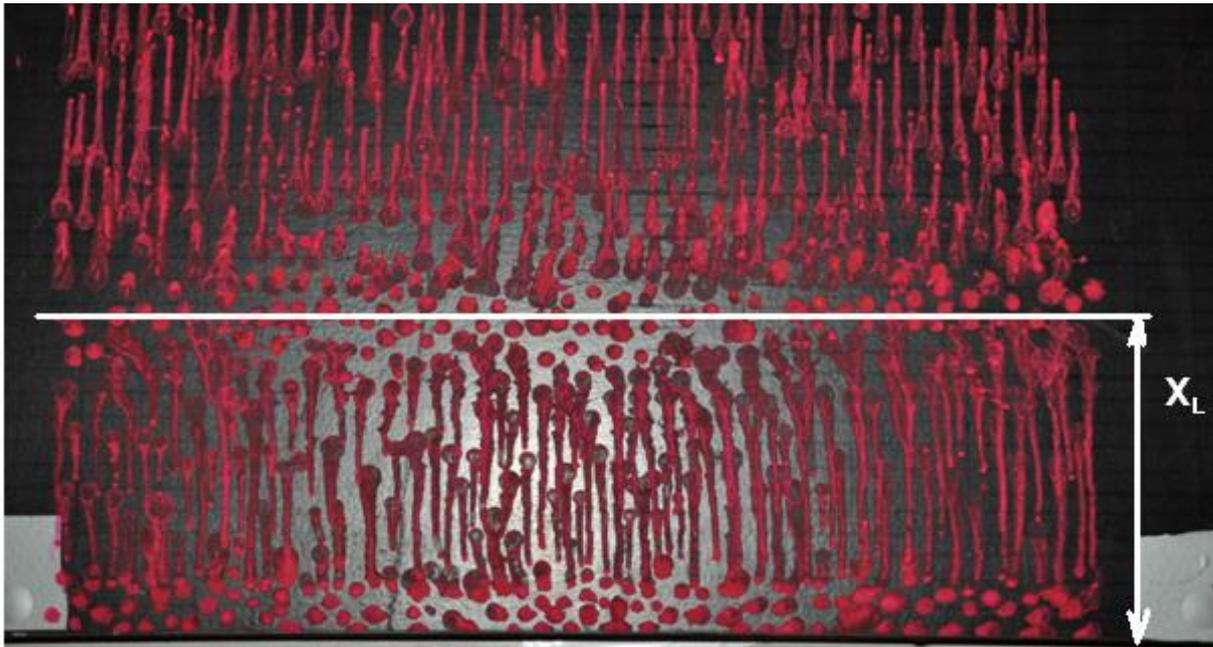
Figure 157: Boundary layer configuration 3, δ/h = 2, X_L/h = 2.8. Flow from bottom of photo to top.
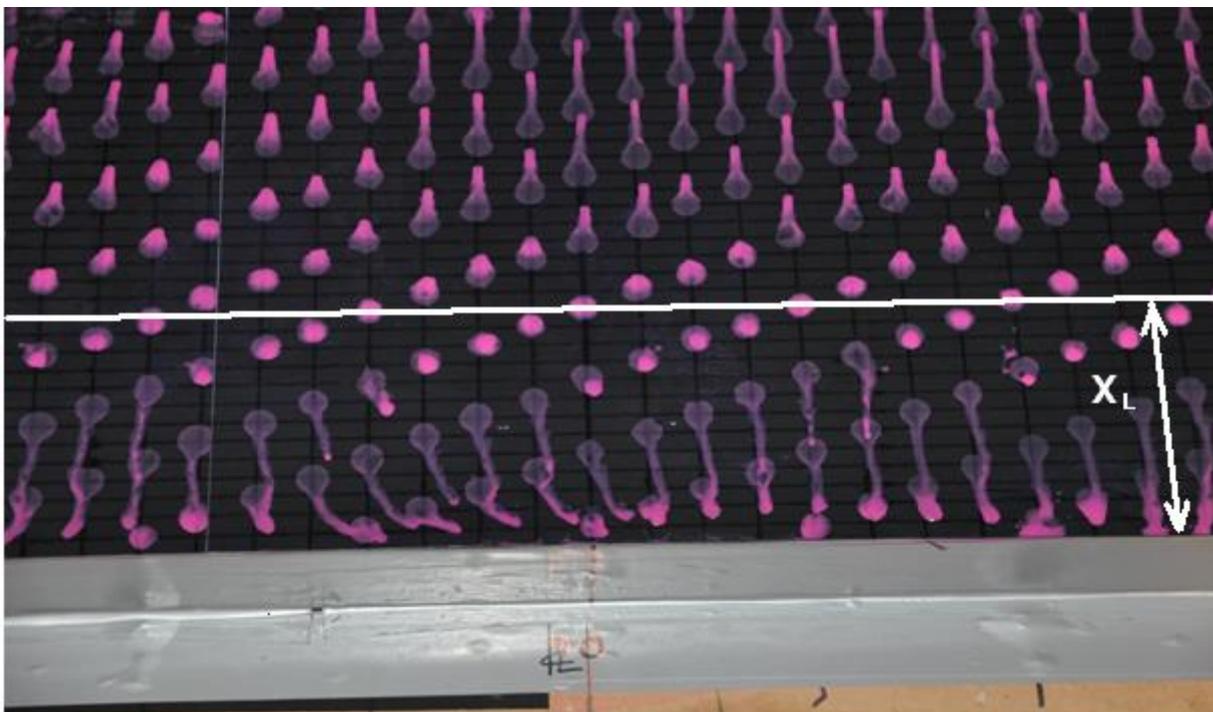
Figure 158: Boundary layer configuration 1, δ/h = 2.7, X_L/h = 2.6. Flow from bottom of photo to top.
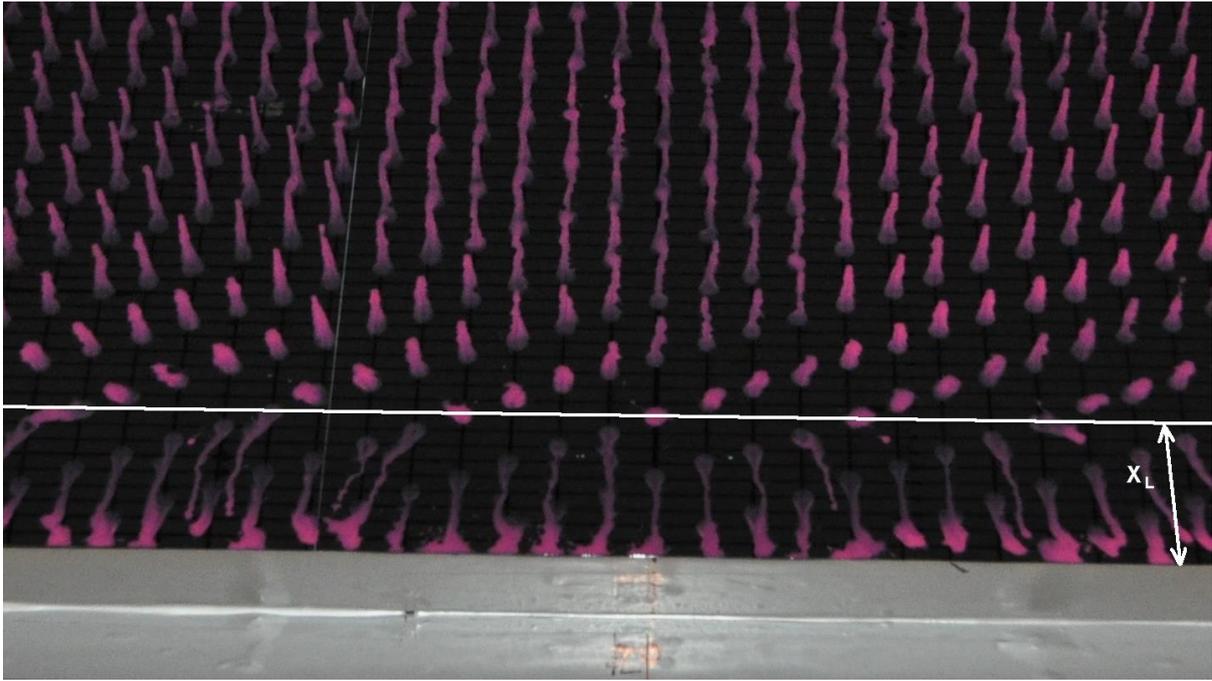
Figure 159: Boundary layer configuration 2, δ/h = 14.3, X_L/h = 1.8. Flow from bottom of photo to top.

Figure 160: Boundary layer configuration 1, δ/h = 1.35, X_L/h = 2.375. Flow from bottom of photo to top.

Figure 161: Boundary layer configuration 2, δ/h = 7.15, X_L/h = 1.9. Flow from bottom of photo to top.
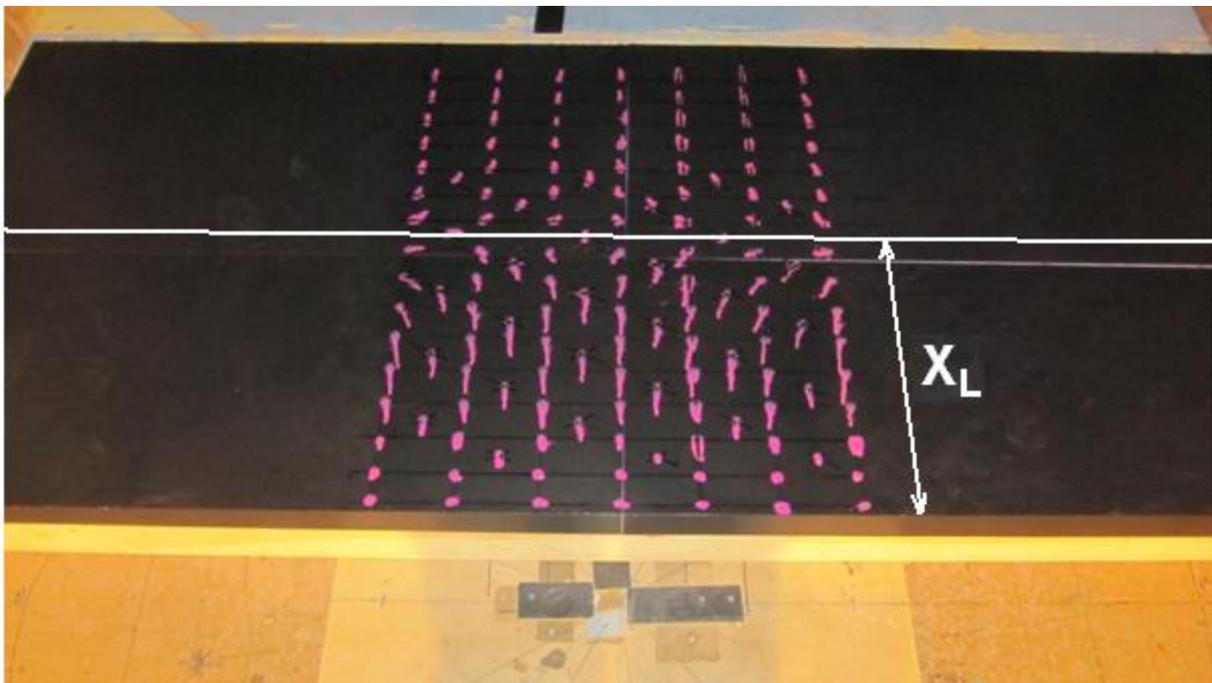
Figure 162: Boundary layer configuration 1, δ/h = 0.9, X_L/h = 2.835. Flow from bottom of photo to top.

270
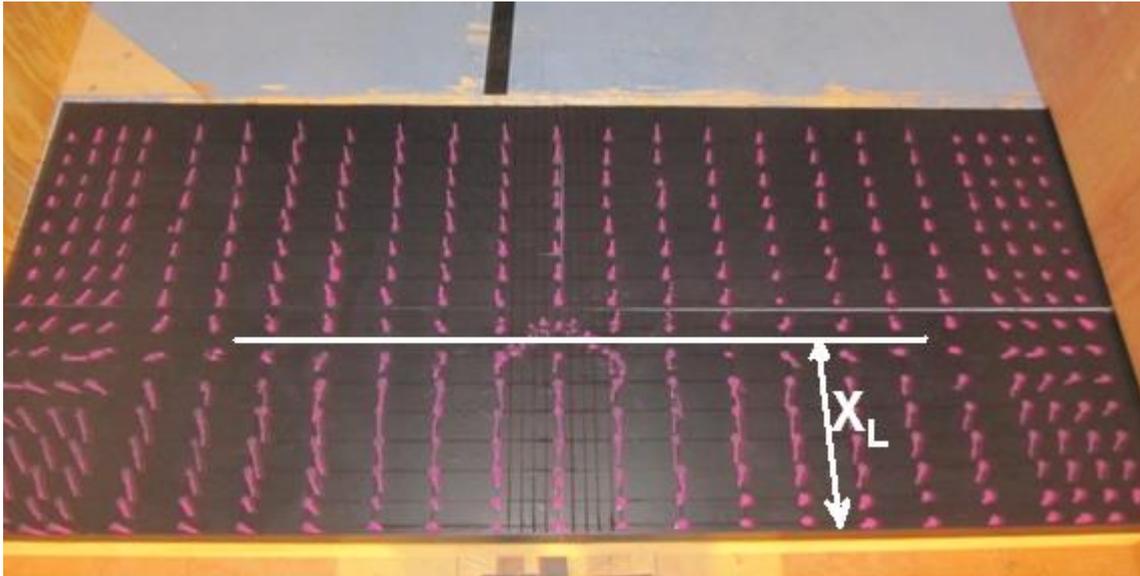
Figure 163: Boundary layer configuration 2, δ/h = 4.77, X_L/h = 2.165. Flow from bottom of photo to top.

Appendix: Surface Shear Stress Visualisations – Yaw
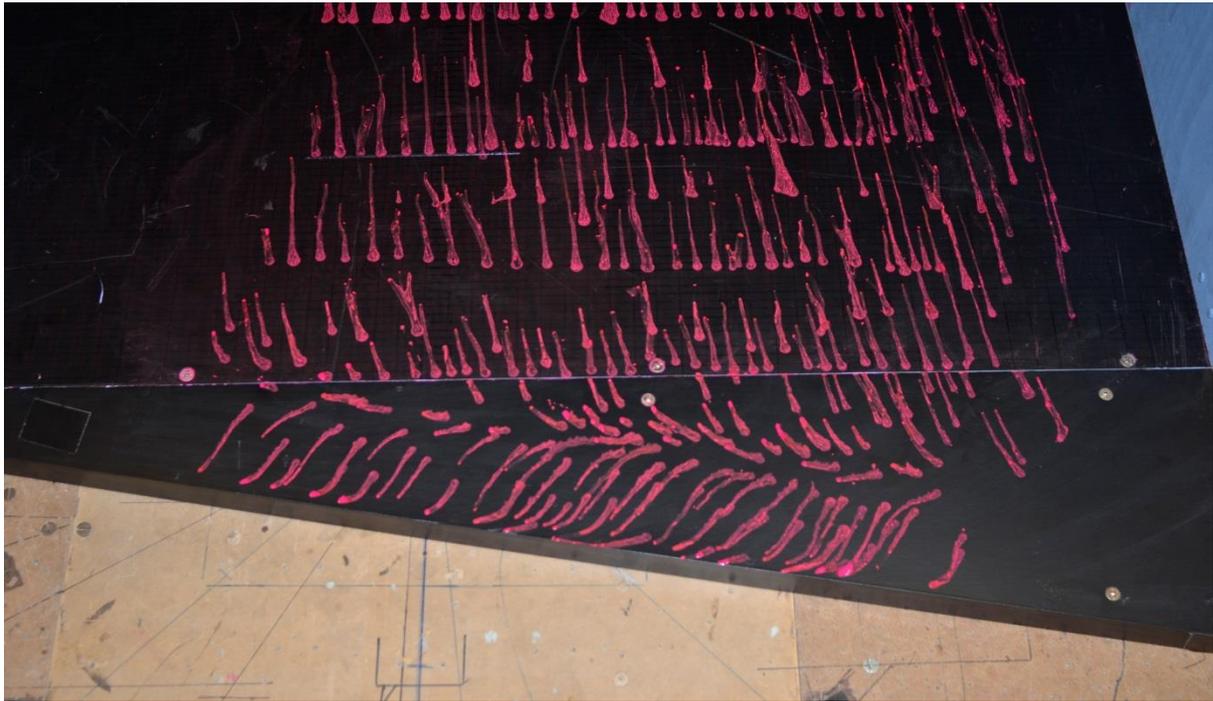
Figure 164: Paint droplet surface shear stress visualisation for _δ/h_ = 2.7. Yaw angle, θ = 10°. Inflow Configuration 1. Step height, _h_ = 50 mm. Flow direction from bottom of page to top.
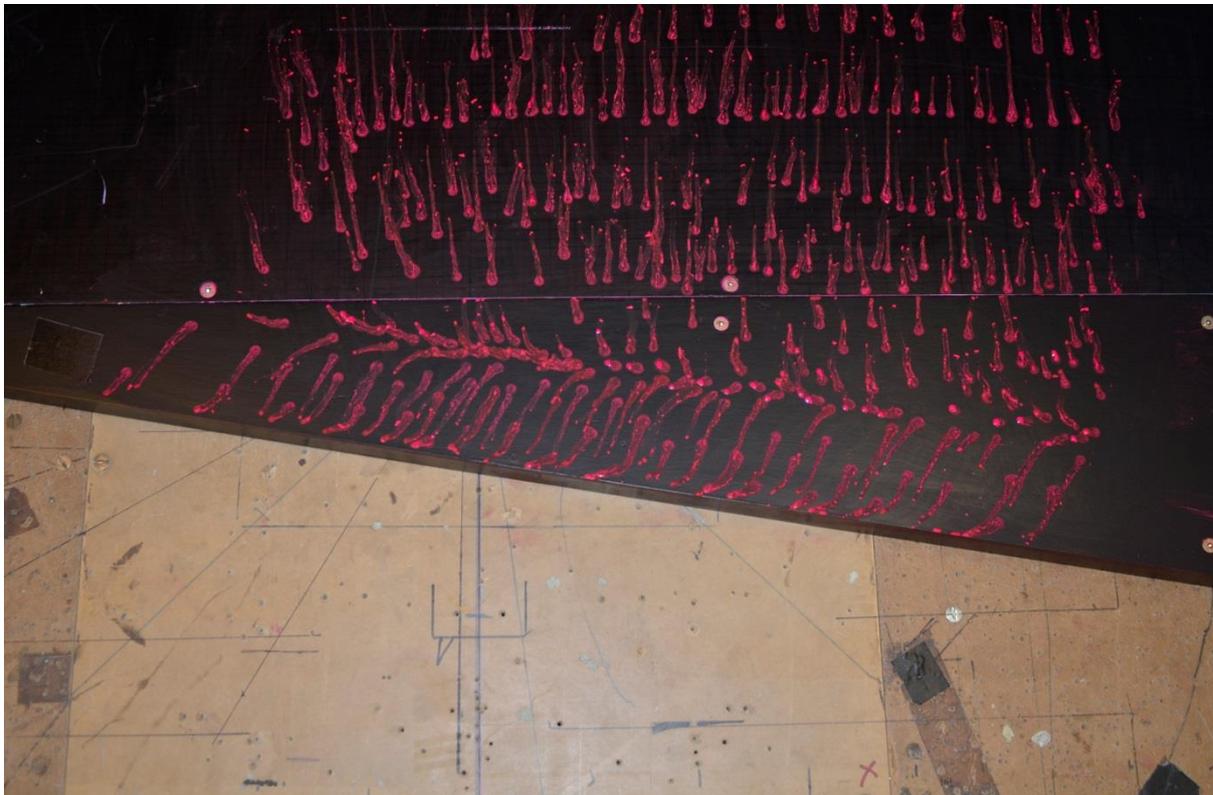
**Figure 165: Paint droplet surface shear stress visualisation for _δ/h_ = 14.3. Yaw angle, θ = 10°. Inflow Configuration 2. Step height, _h_ = 50 mm. Flow direction from bottom of page to top.**
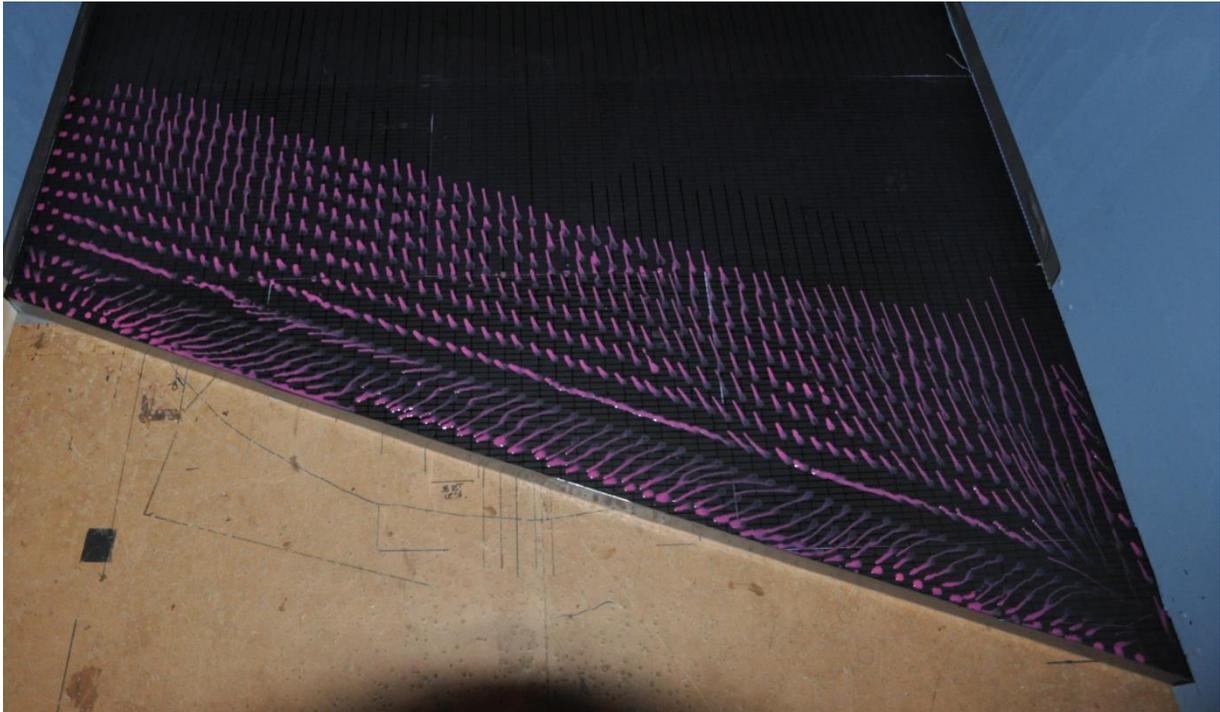
Figure 166: Paint droplet surface shear stress visualisation for δ/h = 2.7. Yaw angle, θ = 20°. Inflow Configuration 1. Step height, h = 50 mm. Flow direction from bottom of page to top.


**Figure 167: Paint droplet surface shear stress visualisation for δ/h = 14.3. Yaw angle, θ = 20°. Inflow Configuration 2. Step height, h = 50 mm. Flow direction from bottom of page to top.**
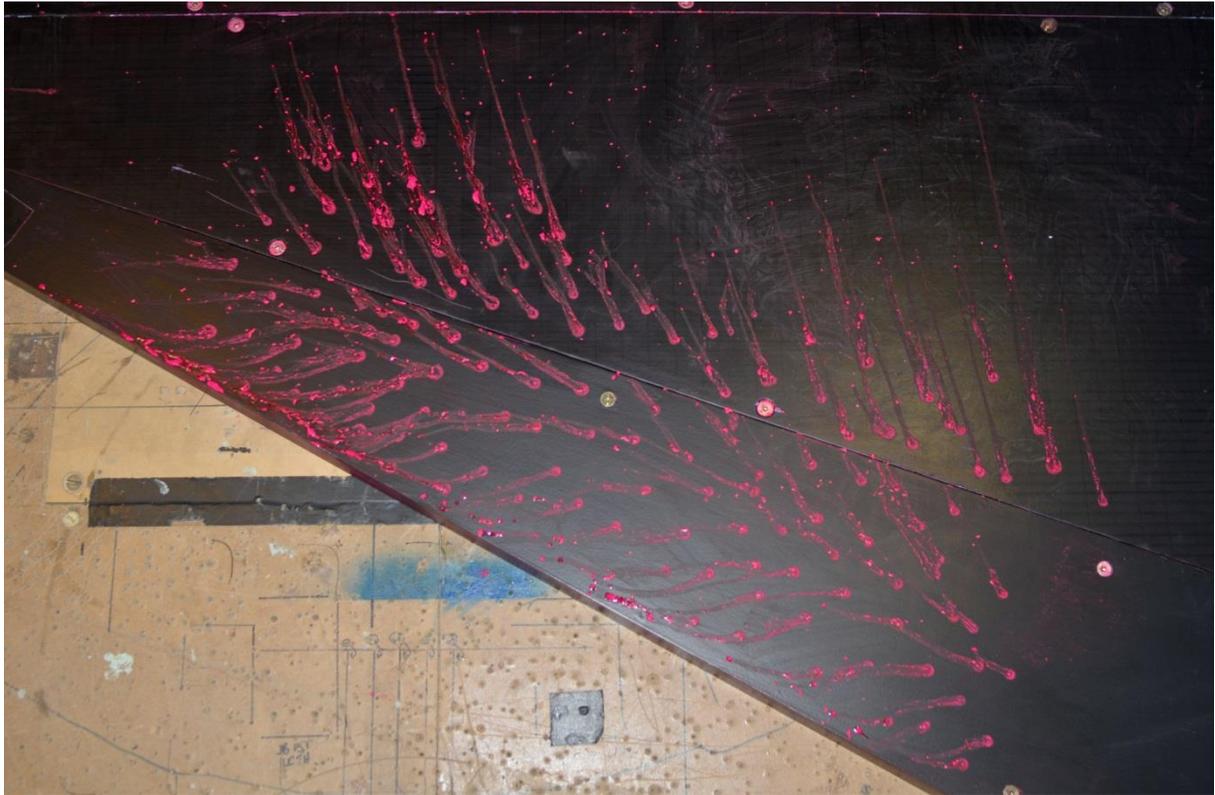
Figure 168: Paint droplet surface shear stress visualisation for δ/h = 2.7. Yaw angle, θ = 30°. Inflow Configuration 1. Step height, h = 50 mm. Flow direction from bottom of page to top.
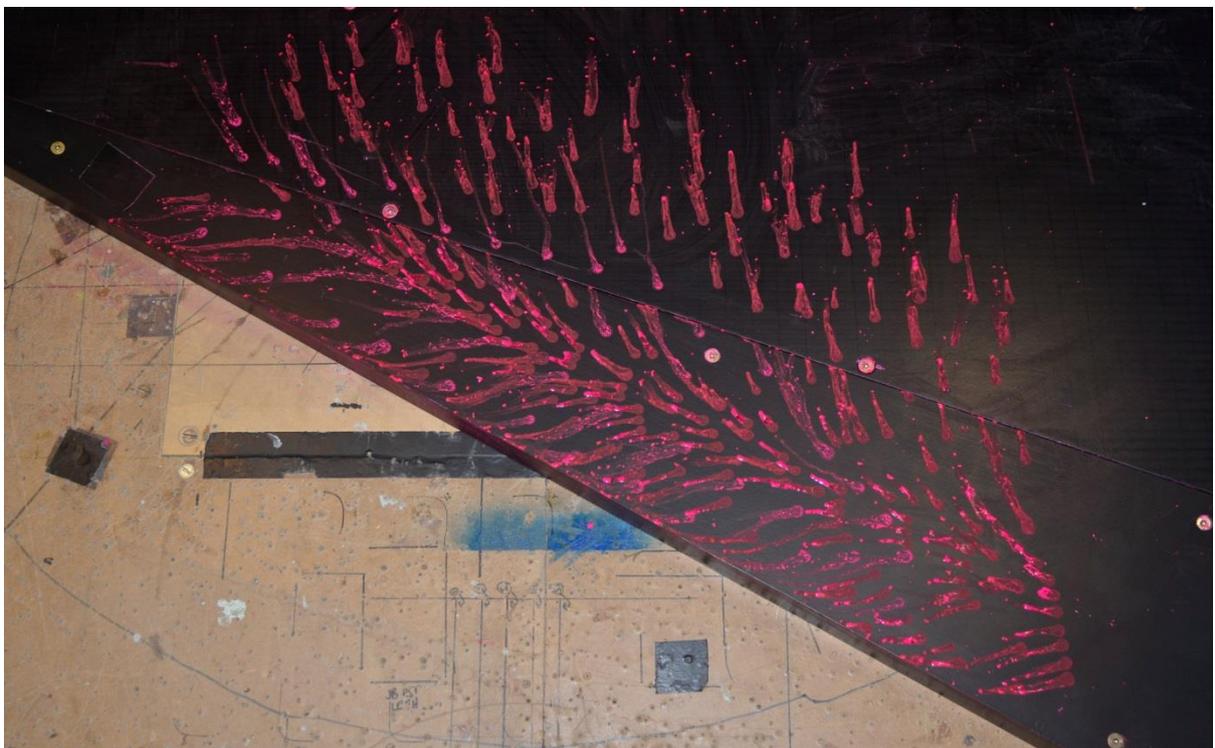
Figure 169: Paint droplet surface shear stress visualisation for δ/h = 14.3. Yaw angle, θ = 30°. Inflow Configuration 2. Step height, h = 50 mm. Flow direction from bottom of page to top.

Figure 170: Paint droplet surface shear stress visualisation for δ/h = 2.7. Yaw angle, θ = 40°. Inflow Configuration 1. Step height, h = 50 mm. Flow direction from bottom of page to top.
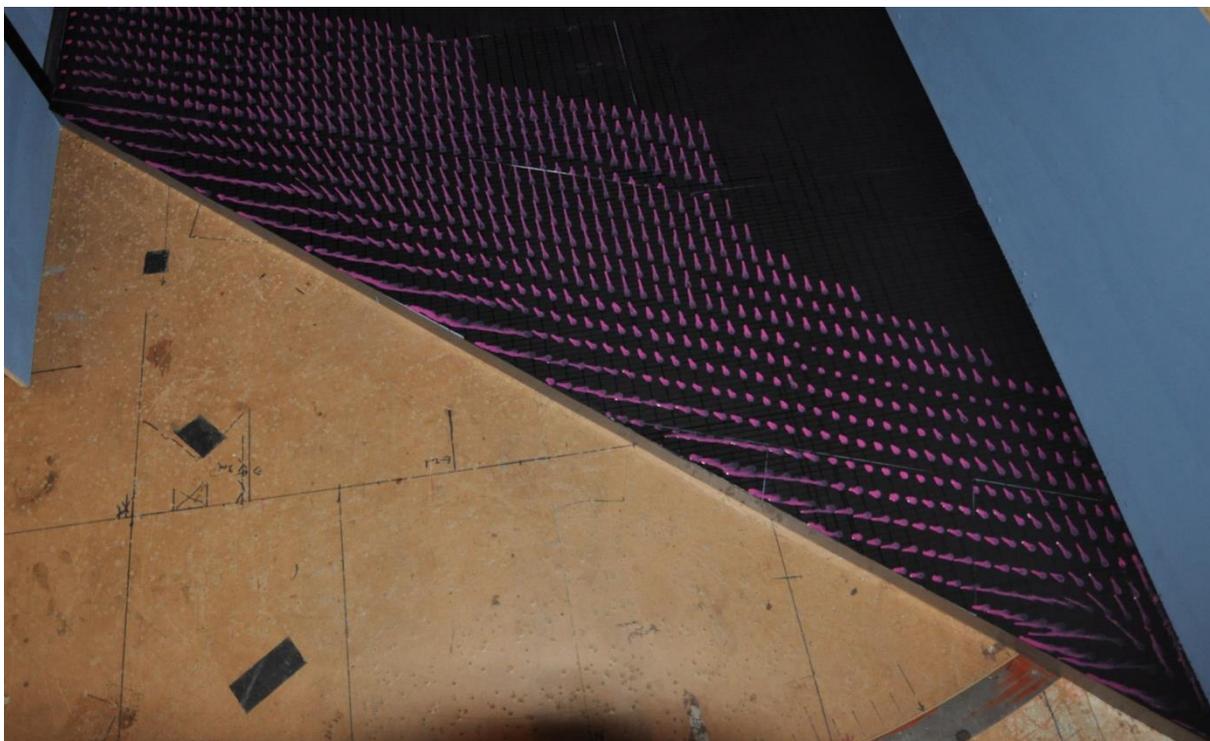
**Figure 171: Paint droplet surface shear stress visualisation for δ/h = 14.3. Yaw angle, θ = 40°. Inflow Configuration 2. Step height, h = 50 mm. Flow direction from bottom of page to top.**
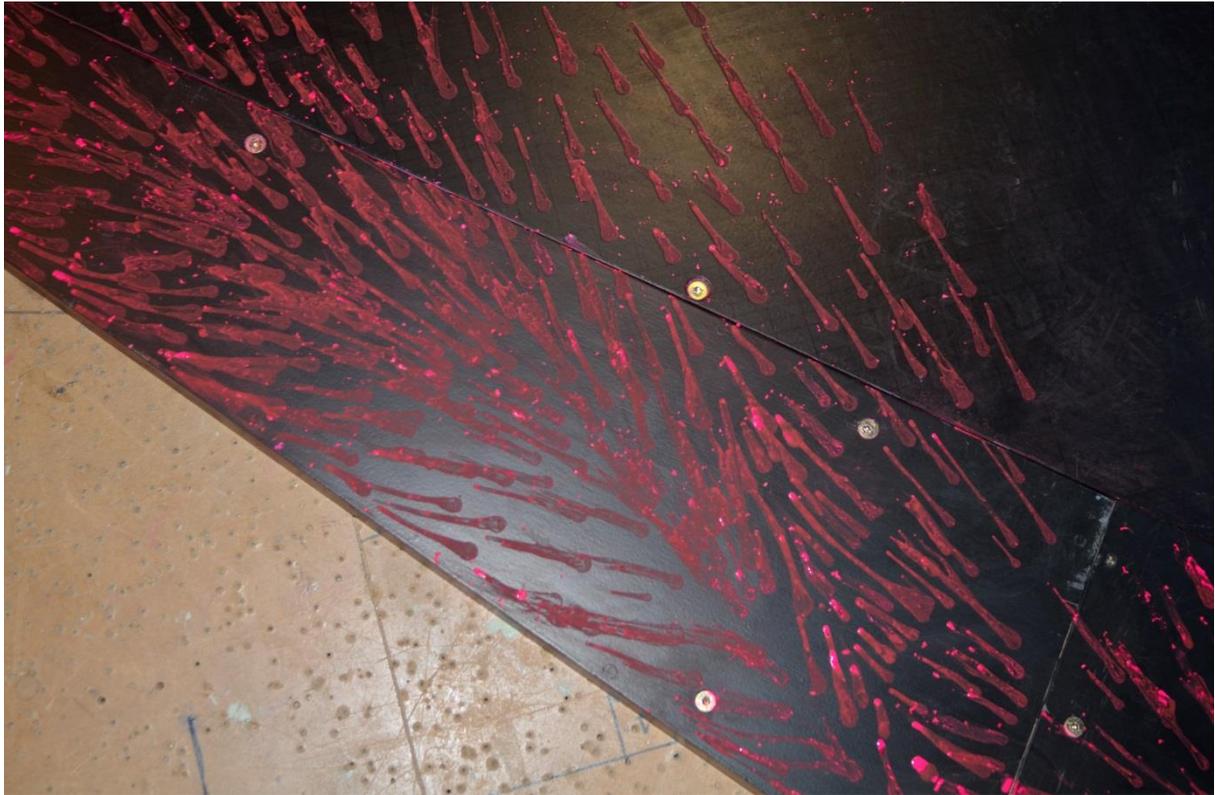
Figure 172: Paint droplet surface shear stress visualisation for δ/h = 2.7. Yaw angle, θ = 50°. Inflow Configuration 1. Step height, h = 50 mm. Flow direction from bottom of page to top.
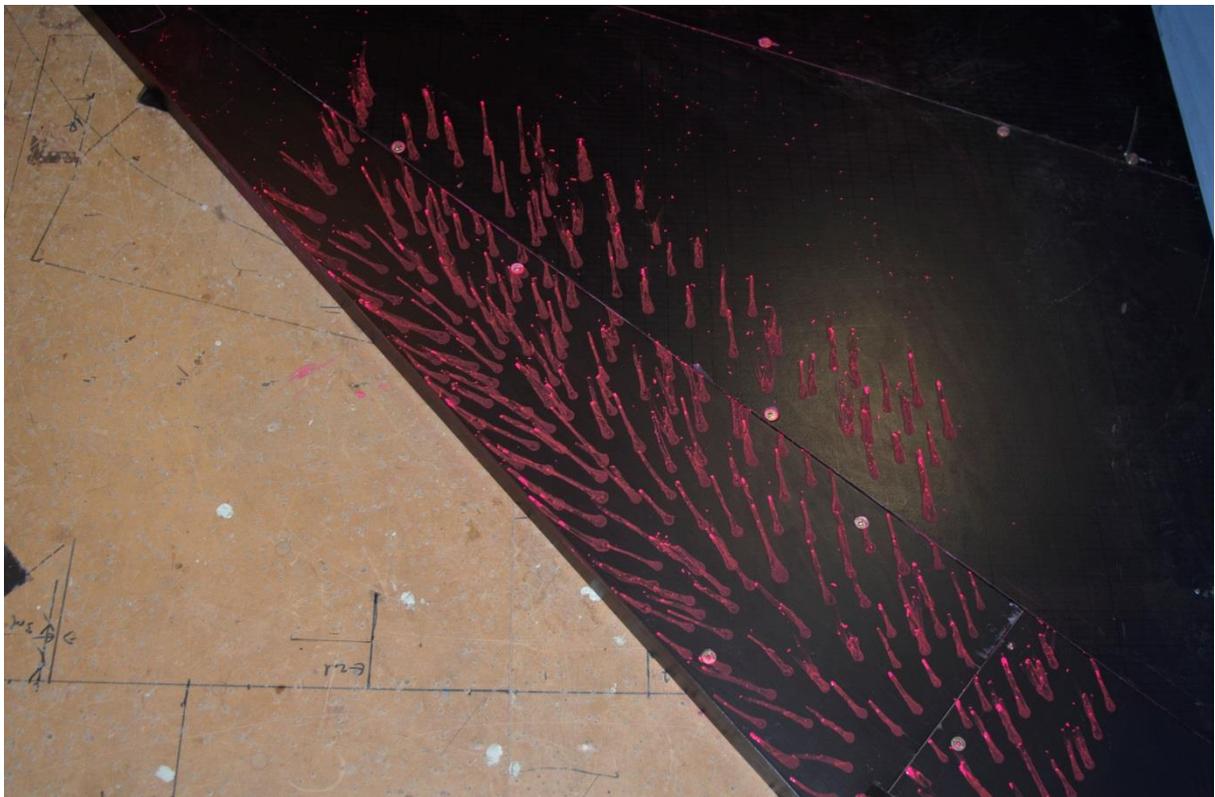
**Figure 173: Paint droplet surface shear stress visualisation for δ/h = 14.3. Yaw angle, θ = 50°. Inflow Configuration 2. Step height, h = 50 mm. Flow direction from bottom of page to top.**
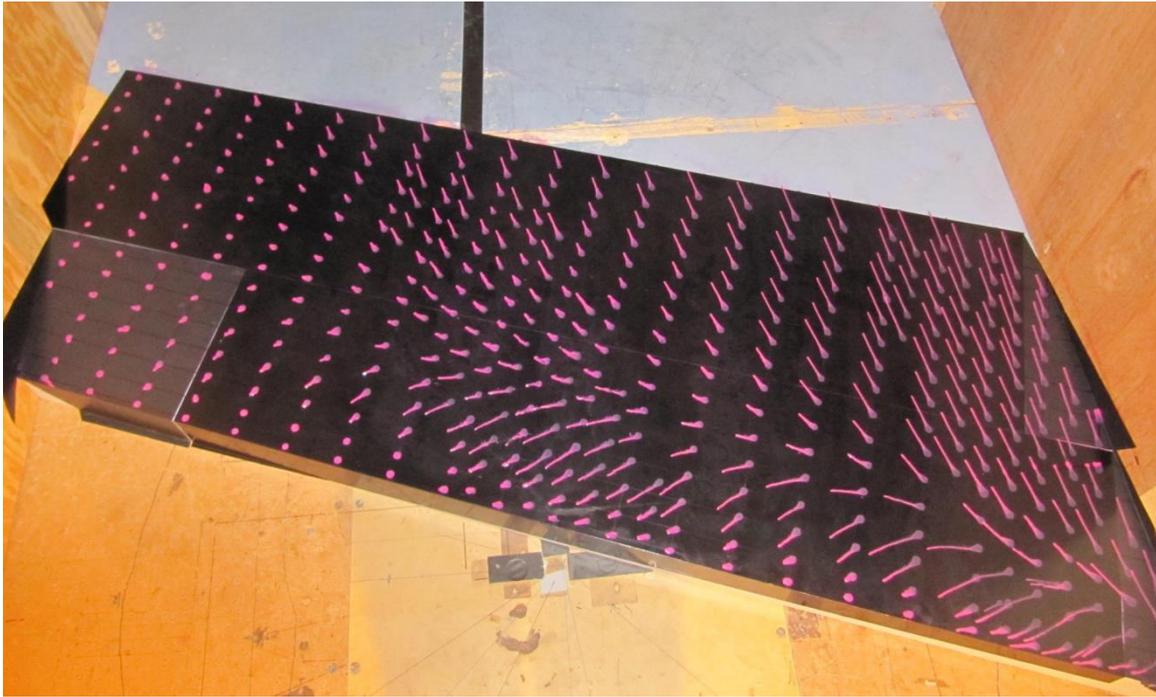
Figure 174: Paint droplet surface shear stress visualisation for δ/h = 1.35. Yaw angle, θ = 20°. Inflow Configuration 1. Step height, h = 100 mm. Flow direction from bottom of page to top.
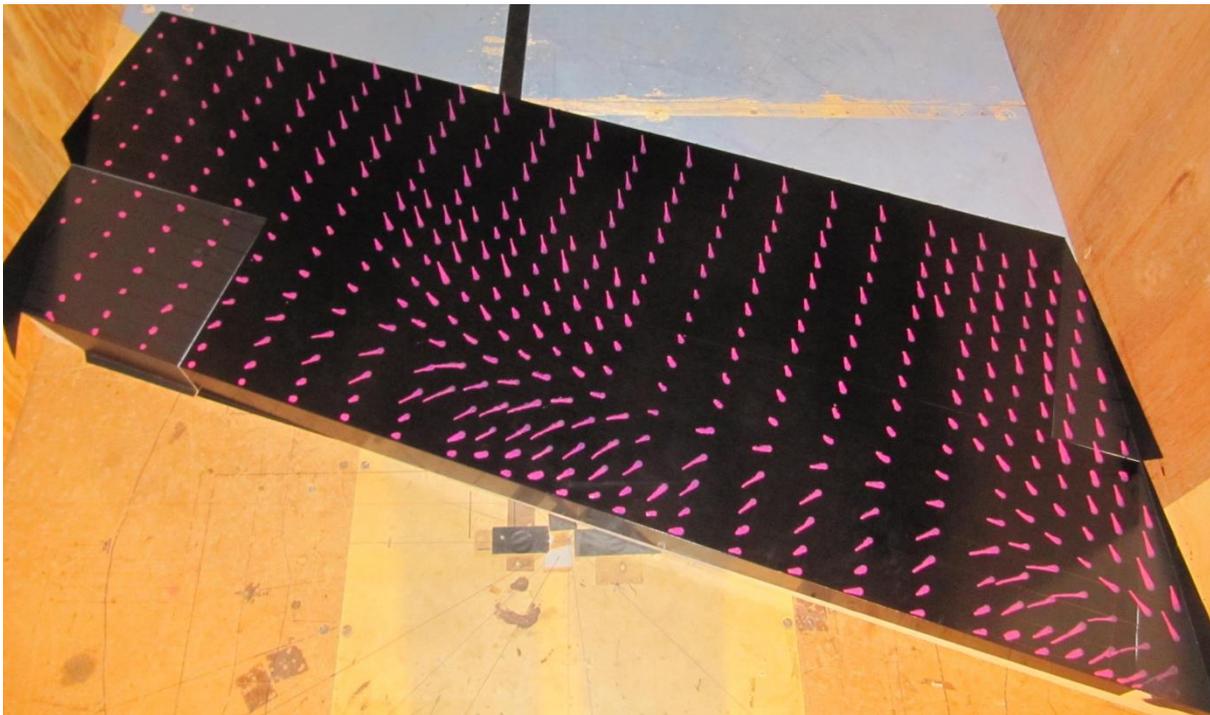
**Figure 175: Paint droplet surface shear stress visualisation for δ/h = 7.15. Yaw angle, θ = 20°. Inflow Configuration 2. Step height, h = 100 mm. Flow direction from bottom of page to top.**
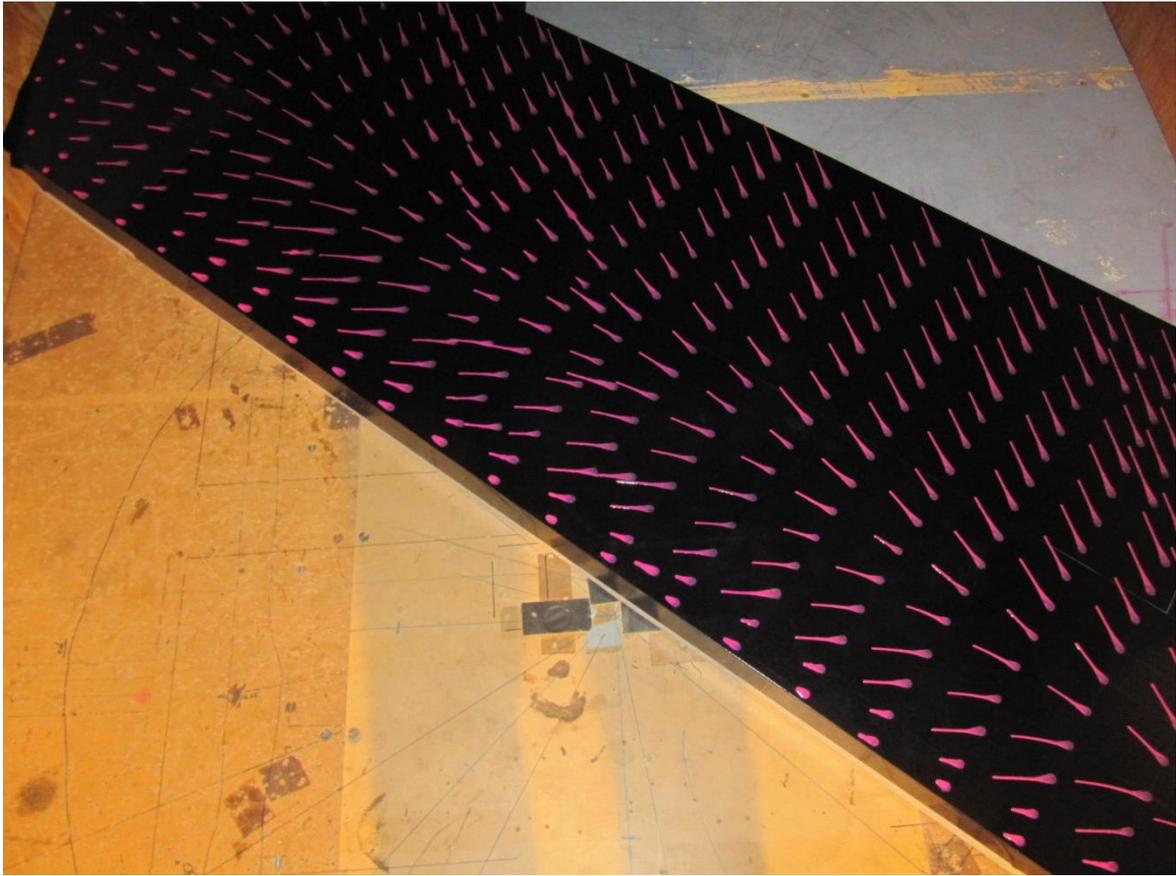
Figure 176: Paint droplet surface shear stress visualisation for δ/h = 1.35. Yaw angle, θ = 40°. Inflow Configuration 1. Step height, h = 100 mm. Flow direction from bottom of page to top.
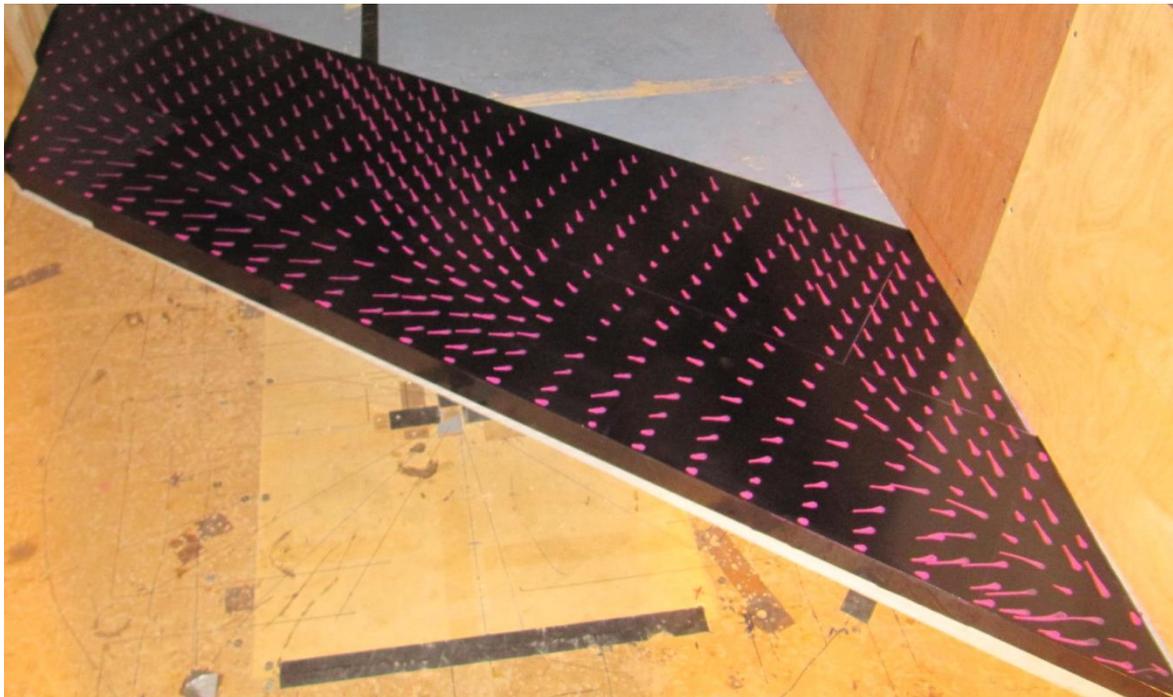
Figure 177: Paint droplet surface shear stress visualisation for δ/h = 7.15. Yaw angle, θ = 40°. Inflow Configuration 2. Step height, h = 100 mm. Flow direction from bottom of page to top.
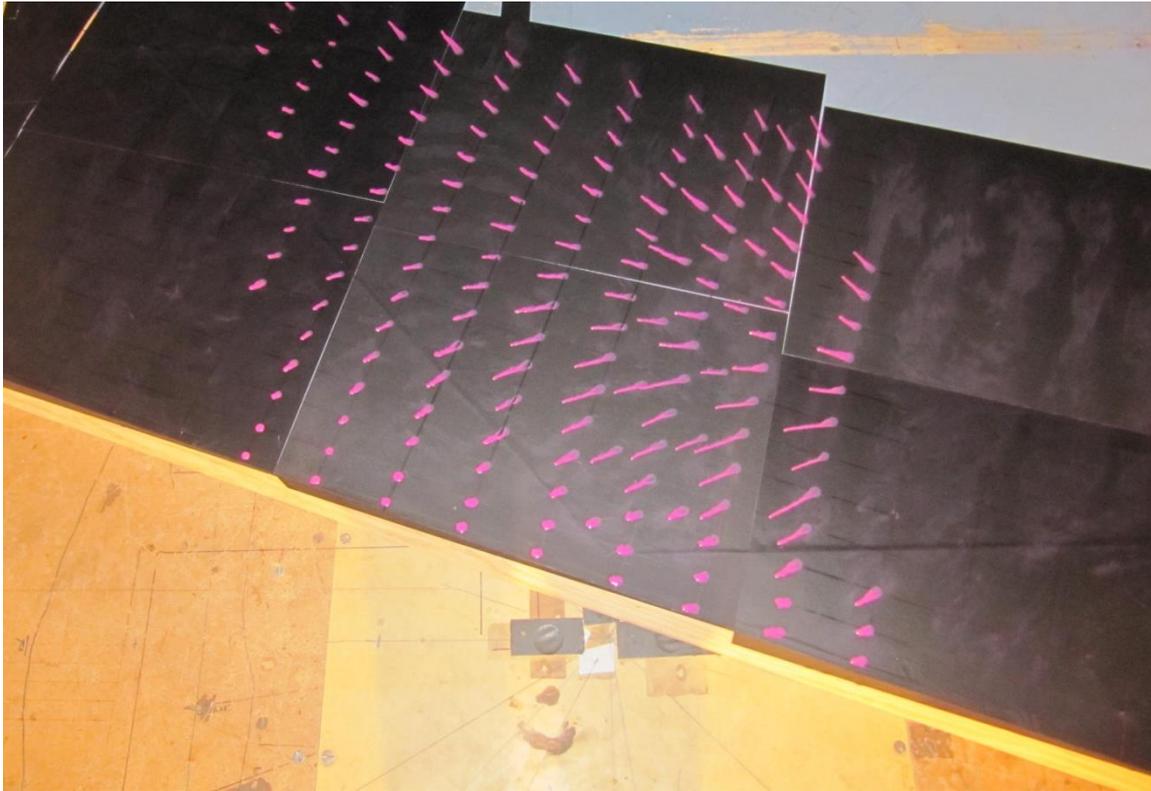
Figure 178: Paint droplet surface shear stress visualisation for δ/h = 0.9. Yaw angle, θ = 20°. Inflow Configuration 1. Step height, h = 150 mm. Flow direction from bottom of page to top.
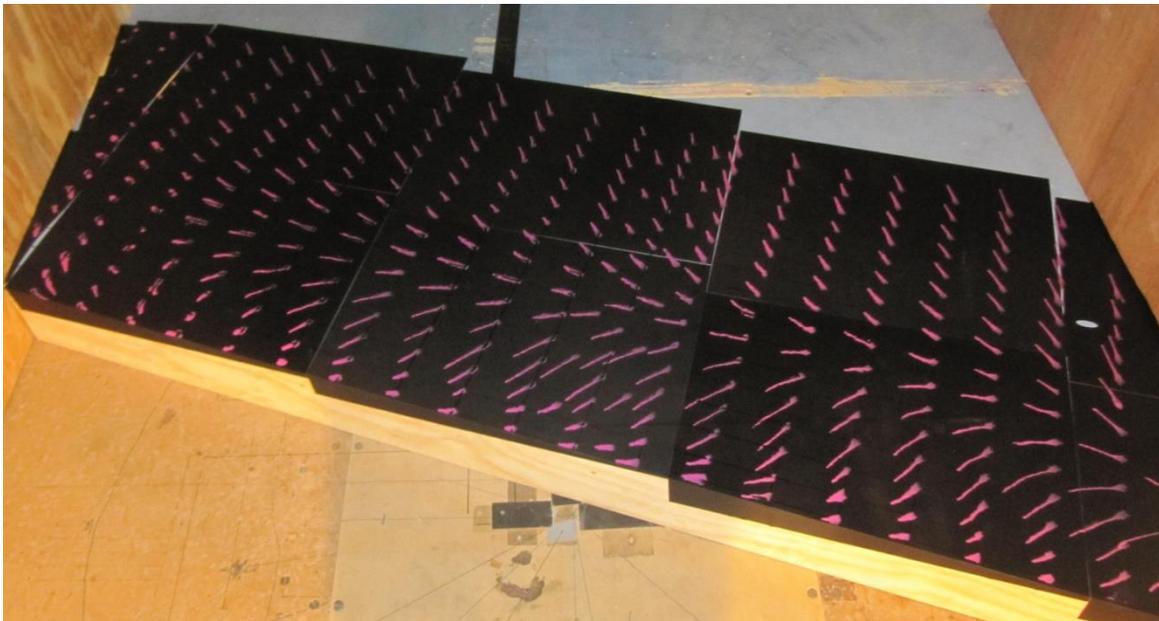
**Figure 179: Paint droplet surface shear stress visualisation for δ/h = 4.77. Yaw angle, θ = 20°. Inflow Configuration 2. Step height, h = 150 mm. Flow direction from bottom of page to top.**
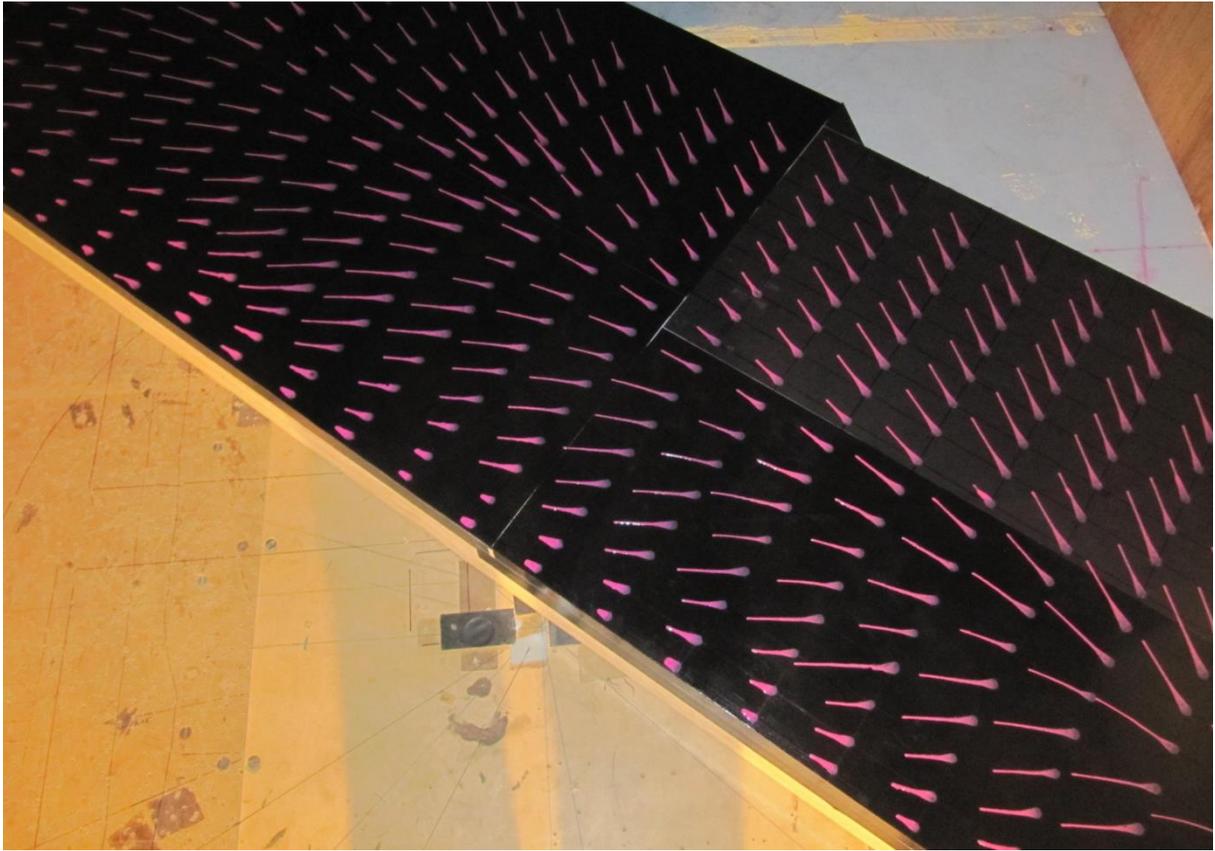
Figure 180: Paint droplet surface shear stress visualisation for δ/h = 0.9. Yaw angle, θ = 40°. Inflow Configuration 1. Step height, h = 150 mm. Flow direction from bottom of page to top.
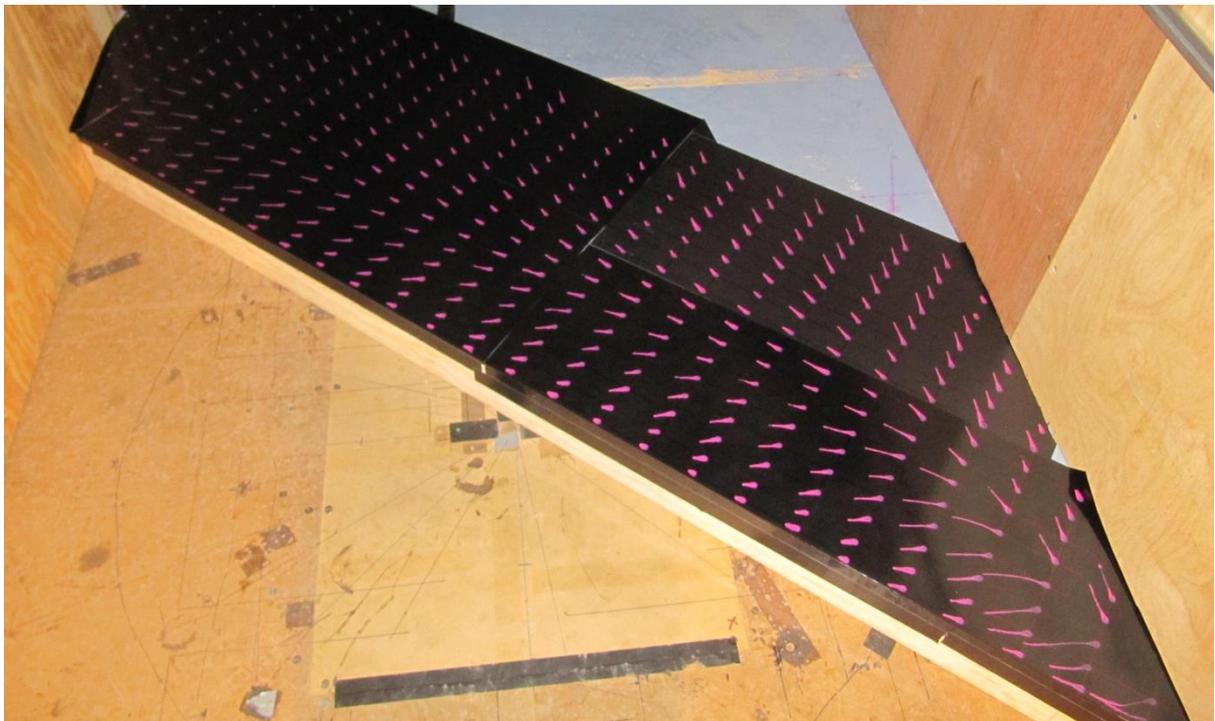
**Figure 181: Paint droplet surface shear stress visualisation for δ/h = 4.77. Yaw angle, θ = 40°. Inflow Configuration 2. Step height, h = 150 mm. Flow direction from bottom of page to top.**
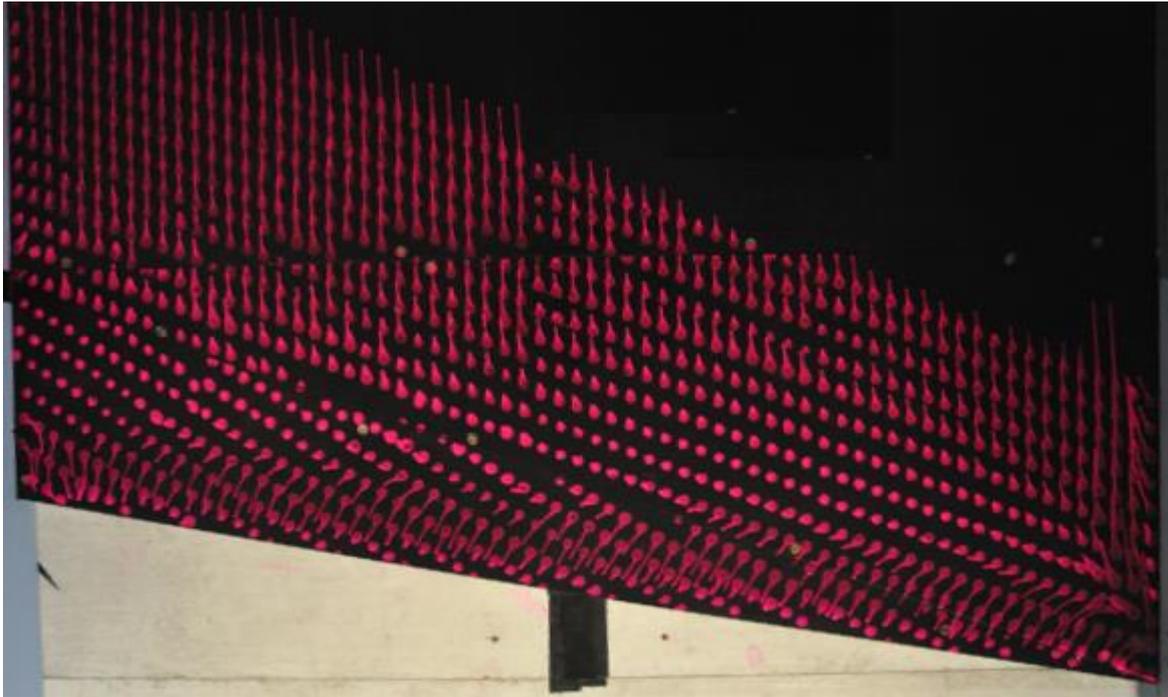
Figure 182: Paint droplet surface shear stress visualisation for *δ*/*h* = 2. Yaw angle, θ = 10°. Inflow Configuration 3. Step height, *h* = 50 mm. Flow direction from bottom of page to top.
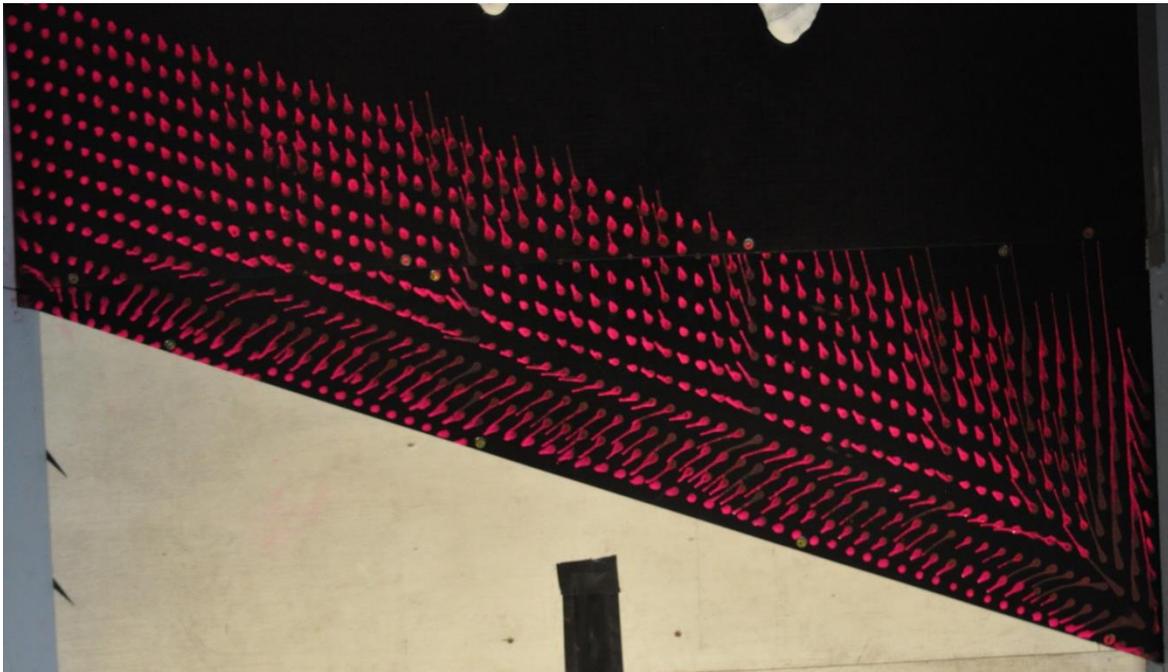
Figure 183: Paint droplet surface shear stress visualisation for *δ*/*h* = 2. Yaw angle, θ = 20°. Inflow Configuration 3. Step height, *h* = 50 mm. Flow direction from bottom of page to top.

Figure 184: Paint droplet surface shear stress visualisation for δ/h = 2. Yaw angle, θ = 30°. Inflow Configuration 3. Step height, h = 50 mm. Flow direction from bottom of page to top.
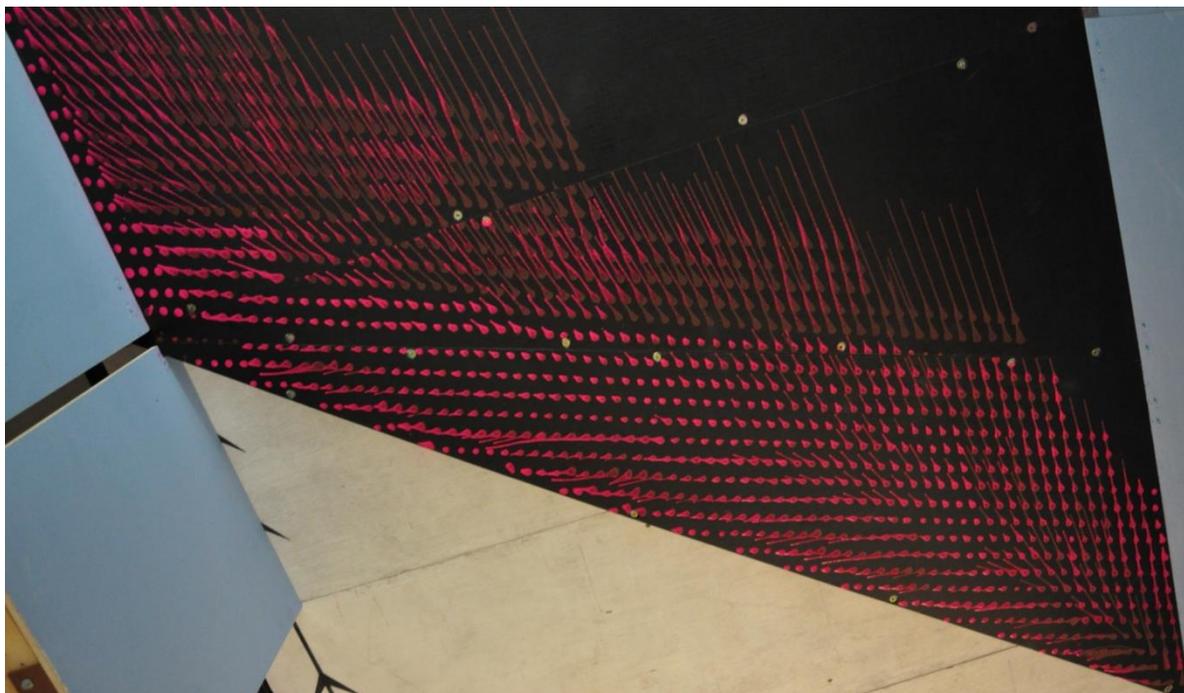
**Figure 185: Paint droplet surface shear stress visualisation for δ/h = 2. Yaw angle, θ = 40°. Inflow Configuration 3. Step height, h = 50 mm. Flow direction from bottom of page to top.**
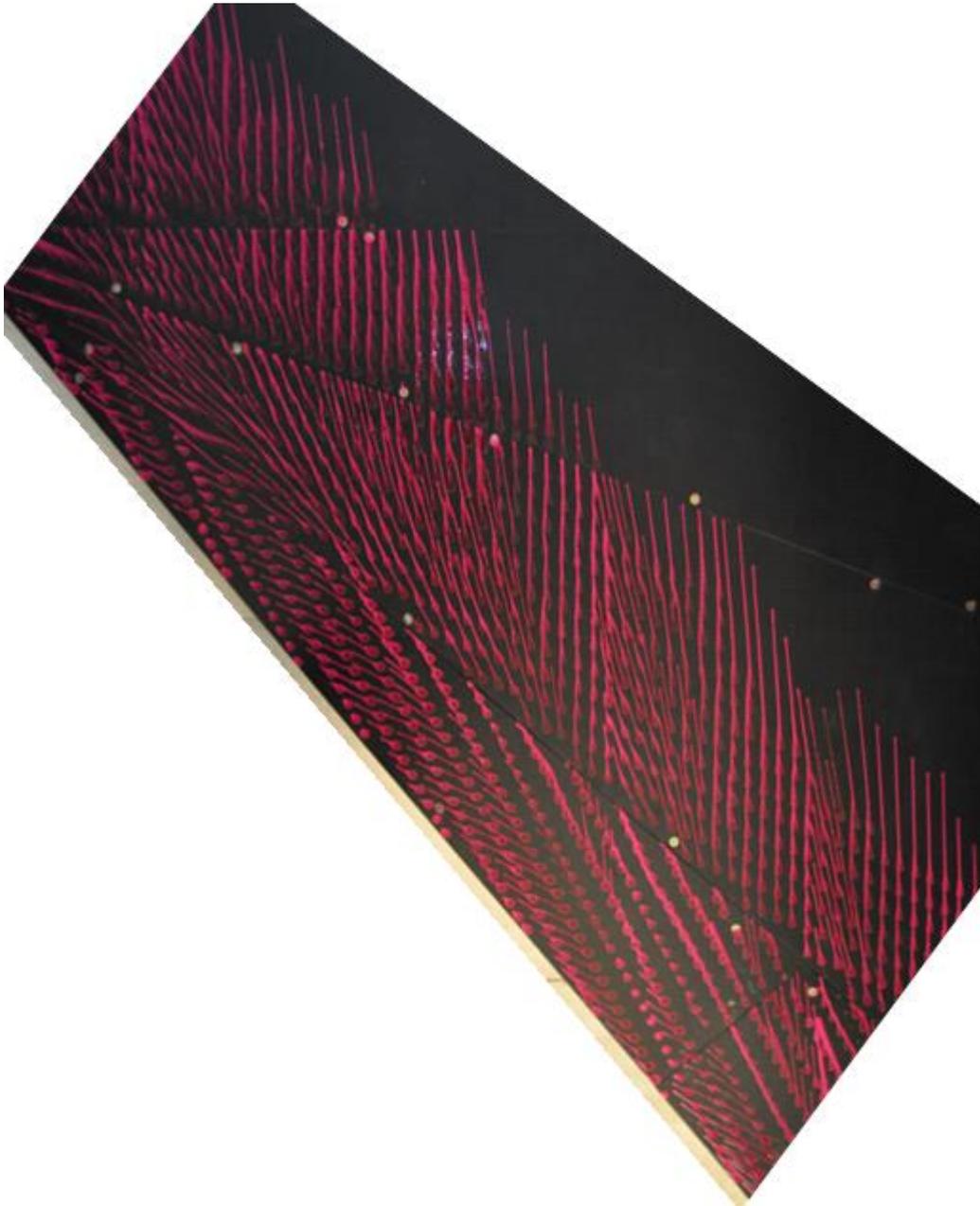
**Figure 186: Paint droplet surface shear stress visualisation for _δ/h_ = 2. Yaw angle, θ = 50°. Inflow Configuration 3. Step height, _h_ = 50 mm. Flow direction from bottom of page to top.**

Appendix: CFD Methodology

This methodology section was prepared with the assistance of Robert Harbig for the research paper:

Mean Topology Development on Forward Facing Steps with Sawtooth Lateral Variations (Rowcroft, et al., 2014).

Computational Fluid Dynamics (CFD) has been used to partner the experimental work, providing a useful comparison between Cobra Probe data, surface pressure tap data, and surface shear stress visualisation. Once a good match has been established between these experimental techniques, the CFD is useful for visualising flow structures. The four different sawtooth cases were modelled using *Ansys CFX*.

The inflow velocity to the CFD model was designed to match the wind tunnel boundary layer conditions, as seen in Figure 187. A log law profile was used, as described by the following equation:

$$U = \frac{U^*}{\kappa} \ln\left(\frac{z + z_0}{z_0}\right)$$

(A-1)

In this case, U is velocity; U^* is the friction velocity, which was set at 1.1459 ms^{-1}; κ is the von Kármán constant, which is 0.4; z is the height above the ground; and z_0 is the roughness length, set to 5.988×10^{-7} m. A simulation was run in which the cliff was removed to check the stream-wise development of the boundary layer profile. The average difference in the velocity profiles at the inlet and the cliff trough ($x = 0$) was found to be less than 2%. The inlet turbulence intensity was set to 5% and the eddy viscosity ratio was set to 10. This was done to allow for the decay of turbulence intensity upstream of the cliff and resulted in a free-stream turbulence intensity of approximately 1% at the cliff.
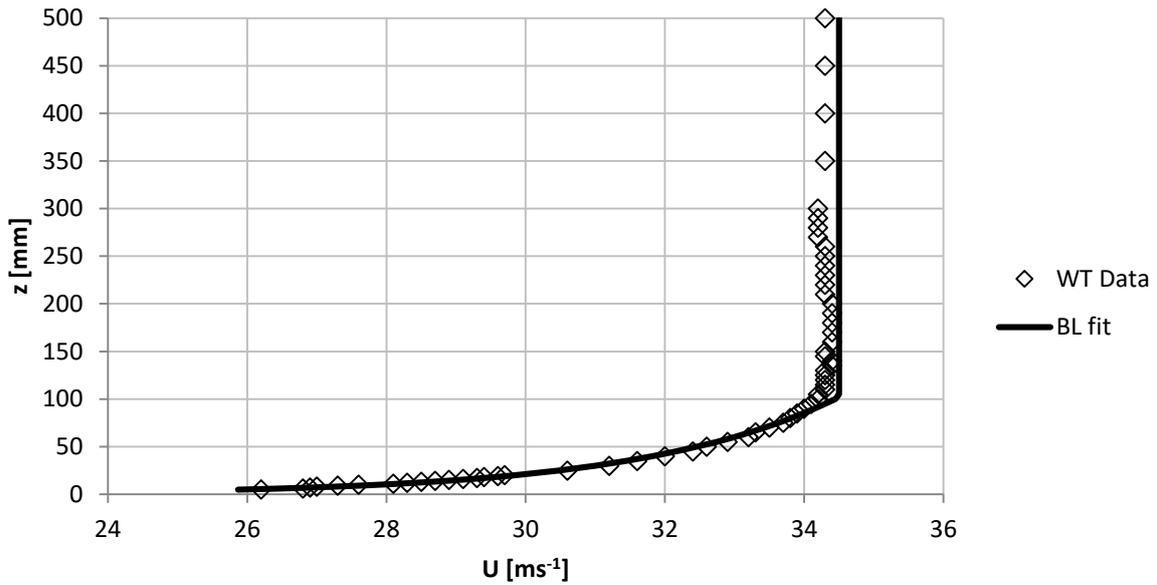
Figure 187: Comparison of wind tunnel boundary layer velocity profile with CFD inflow velocity profile.

The experimental domain extended 10*h* upstream and 20*h* downstream of the peak of the model.

The width of the model spanned one full period of the sawtooth, which was in each case 400 mm.

The intention was to match as closely as possible the conditions in the wind tunnel. The solid

surfaces were modelled with a no-slip smooth wall, while the roof of the domain was modelled with

a free-slip wall. The side walls were modelled with a periodic boundary condition, reflecting the lines

of symmetry to which they were aligned. A mean gauge pressure boundary condition of 0 Pa was set

across the outlet.

The domain in each case was meshed using an unstructured tetrahedral mesh with a region of

triangular prism elements near the floor in order to resolve the velocity gradients in this area. This

prism layer consisted of thirty layers with a first layer height of 0.01 mm and growth rate of 1.2. This

resulted in an average y^+ value of 0.95 on the cliff's surface. The size of the tetrahedral elements in

the rest of the domain was controlled using the regions shown in Figure 188. Mesh was

concentrated in the regions of interest, around the cliff and downstream of it. The mesh consisted of

over 18×10^6 elements, and over 5.5×10^6 nodes. Mesh details are presented in Figure 188.
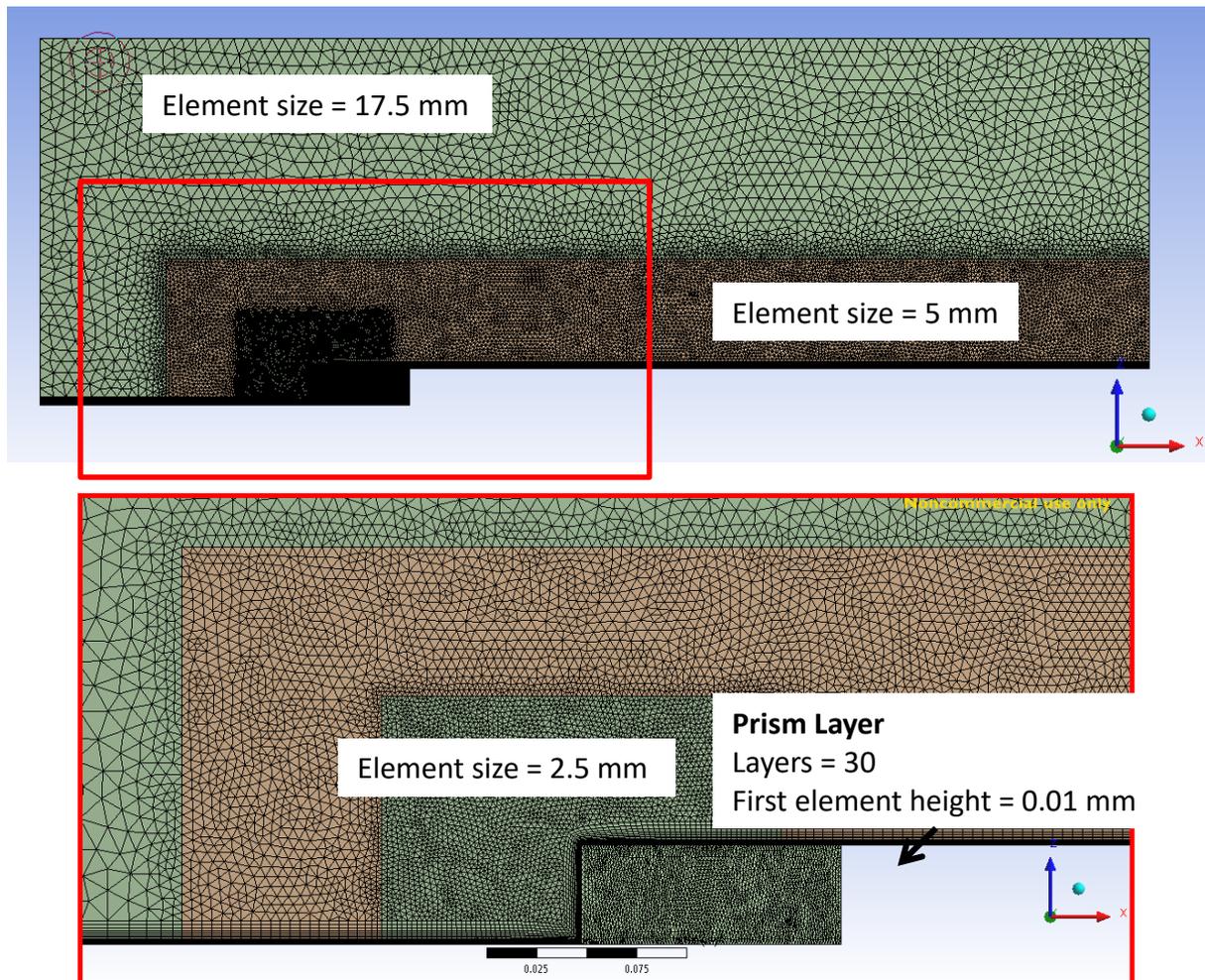
Figure 188: CFD meshing details.

A steady state RANS κ-ε model was used to solve the flow over each cliff. CFX's 'High Resolution' advection scheme was used for spatial discretisation and a first order upwind scheme was used for turbulence numerics. Each simulation was iterated until a residual target of 1×10^{-4} was met for pressure and momentum terms. The velocity at three points near the cliff's trough was monitored to ensure that the solution had settled down and reached a steady value. This was found for the A/λ = 0.325, 0.65 and 1 cases, however the velocity for the A/λ = 0.5 case was found to oscillate and the solution did not converge. Therefore, a transient RANS κ-ε model was used for this case, with a time-step size of 5×10^{-4} s. This resulted in improved convergence of the solution. The simulation was run for 1 s and the average flow field was calculated over this period to obtain an equivalent steady state solution.

Appendix: Static Calibration of Dynamic Pressure Measurement System Units

Two Turbulent Flow Instrumentation (TFI) Dynamic Pressure Measurement System (DPMS) modules are employed in the Monash University wind tunnel facilities. Regular validation of the accuracy of the modules is required.

In this test a known pressure is applied to the reference port of the modules and the resultant pressure in each of the channels is sampled. Error is reported as a percentage of full-scale range. Comparison can be made with the manufacturer's specifications, which are specified in Table 12.

Five different pressures were applied to the reference ports of the DPMS modules: -200 Pa, -50 Pa, 0 Pa, 50 Pa, and 200 Pa.

DPMS Specifications

Specifications are presented for the two DPMS modules in Table 12.

Table 12: DPMS Unit Specifications.

Unit	DPMS 1335	DPMS 1336
Full-Scale Range	±3000 Pa	±7000 Pa
Channels	2 x 32	2 x 32
Manufacturer's Full-Scale Accuracy	±0.1%	±0.1%
Manufacturer's Accuracy	±3 Pa	±7 Pa

Configuration

The DPMS modules output data to a TFI Data-acquisition Interface Unit (DIU), which feeds data to the controlling computer, where the data are logged. The logging process is controlled by the TFI Control Software.

DIU 5107 was used for this test.

Logging frequency was 1000 Hz, down-sampled to 500 Hz. The sample length was 16.384 s. This corresponds to 8192 samples. The output block size was 1024 samples.

The reference port of each module was connected to a first "T" section. The first "T" section was connected to a second "T" section. The second "T" section connected to a Betz manometer and a manual pressure pump.

The Betz manometer has a positive pressure input and a negative pressure input. To measure positive pressures, the second "T" section was connected to the positive pressure input. The negative pressure input was vented to atmosphere. To measure negative pressures, the second "T" section was connected to the negative pressure input. The positive pressure input was vented to atmosphere.

Each of the input channels of the DPMS modules was vented to still atmosphere.

Note that tubing lengths and diameters are not reported as the test is not concerned with the dynamic response of the system.

Experimental Procedure

The experimental system was allowed 45 minutes for the electronic components to warm up, before the measurements were conducted.

Temperature was logged with a thermocouple. Atmospheric pressure was measured at the start and end of testing with a *Tief Hoch* barometer.

The Betz manometer was levelled before use.

The conversion between pressure units of Pascals (units associated with the DPMS modules) and mmH2O (units associated with the Betz manometer) is based on the equation for hydrostatic pressure:

$$P = \rho g h \qquad\qquad\qquad\qquad \text{(A-2)}$$

P is the pressure, measured in Pascals; ρ is the fluid density, in this case, $H_2O_{(l)}$, assumed to be 997.6 kg.m^{-3} [6]; g is the gravitational acceleration, assumed to be 9.81 m.s^{-2}, h is the vertical displacement, measured in metres.

Thus, the applied pressures of 0 Pa, ±50 Pa, and ±200 Pa correspond to measurements on the Betz manometer of 0 mmH$_2$O, ±5.1 mmH$_2$O, and ±20.4 mmH$_2$O.

With the Betz manometer reading 0 mmH$_2$O and the apparatus in place, the DPMS modules were zeroed using the TFI Control Software.

Pressure was applied to the reference ports of the DPMS modules using the manual pressure pump. When the desired pressure was achieved, the pressure was logged for the sample time at the sample rates specified.

Through the logging process the Betz manometer readings were monitored visually and were constant within ±0.05 mmH$_2$O. The Betz manometer has increments of 0.1 mmH$_2$O.

The following pressures were applied and logged with the second "T" section connected to the negative pressure input of the Betz manometer: -50 Pa, -200 Pa, and 0 Pa.

The second "T" section was then removed from the negative pressure input and connected to the positive pressure input of the Betz manometer. The following pressures were then applied and logged: 50 Pa, 200 Pa, and 0 Pa.

Results

Mean pressures are presented as full-scale percentage errors in Figure 189 and Figure 190 and as absolute errors in Figure 191 and Figure 192. In Figure 191 and Figure 192 the vertical axes are

---

[6] Water density at 22.9°C, based on Table 6-6 *Standard Density of Water* in "Physical Constants of Organic Compounds", in CRC Handbook of Chemistry and Physics, Internet Version 2005, David R. Lide, ed., <http://www.hbcpnetbase.com>, CRC Press, Boca Raton, FL, 2005.

scaled to illustrate the range specified by the manufacturer. For DPMS 1335, the manufacturer specifies an accuracy of ±3 Pa. For DPMS 1336, the manufacturer specifies an accuracy of ±7 Pa.

Full-scale percentage error is calculated according to the following equation:

$$FS \ \% \ Error = \frac{P_{measured} - P_{applied}}{Full \ Scale \ Pressure \ Range} \tag{A-3}$$

Absolute error is calculated according to the following equation:

$$Absolute \ Error = \ P_{measured} - \ P_{applied} \tag{A-4}$$

Tests were conducted at an ambient temperature of 22.9°C.

The atmospheric pressure at the beginning of testing was measured at 757 mmHg.

The atmospheric pressure at the end of testing was measured at 757.5 mmHg.

Uncertainty associated with water density, based on atmospheric pressure and ambient temperature is considered negligible.

The uncertainty of the Betz manometer is taken as half the smallest measurement increment, which is h = 0.0001/2 m.

Thus, the uncertainty of the Betz manometer measurements in units of Pascals is:

$$Uncertainty \ in \ P_{applied} = \rho g h = 997.6 \times 9.81 \times 0.00005 = 0.489 \ Pa$$

The absolute error is of the same order of magnitude as the uncertainty in the applied pressure, as presented in Figure 191 and Figure 192.

Five channels appear to be outliers, yet of those five channels only two channels exceed the manufacturer's specifications.
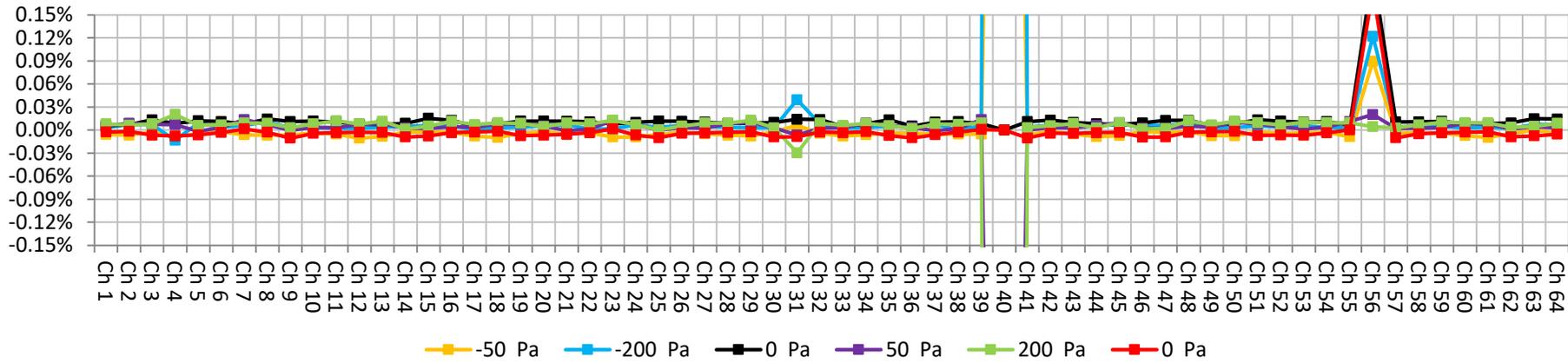
**Figure 189: Full-scale percentage error of DPMS Module 1335.**
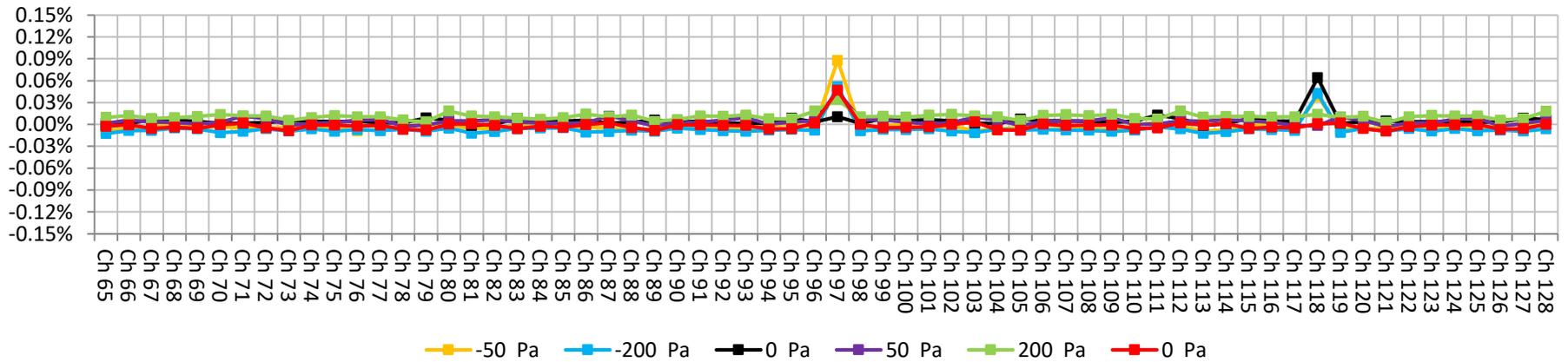
**Figure 190: Full-scale percentage error of DPMS Module 1336.**
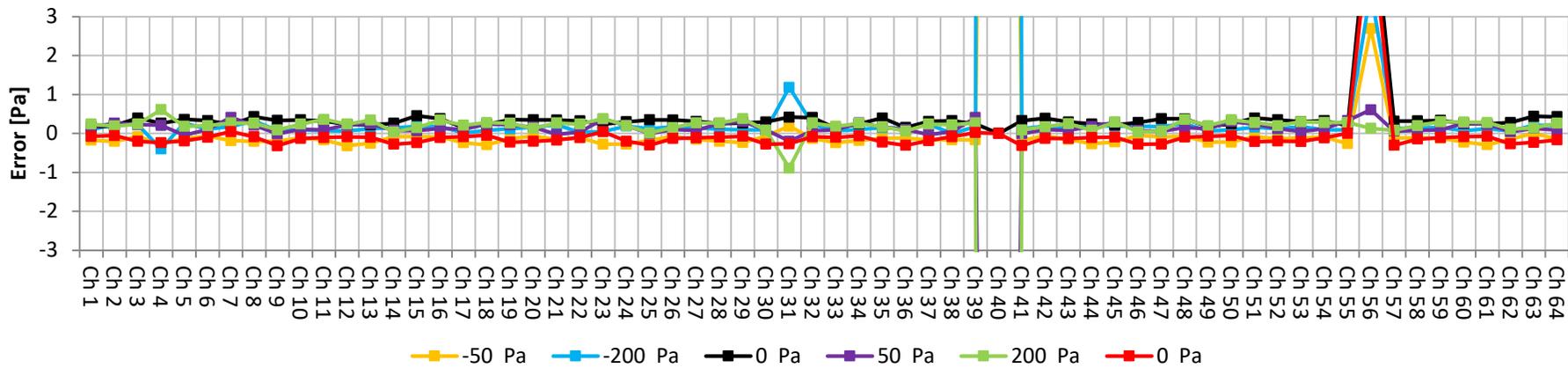
Figure 191: Absolute error of DPMS Module 1335. Note that vertical axis is scaled to illustrate manufacturer's specifications.
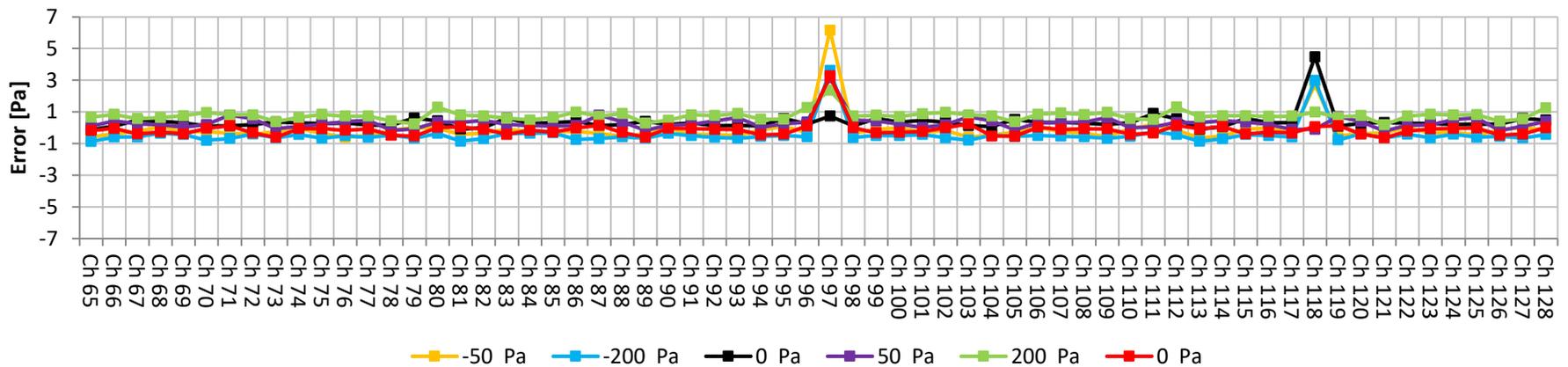

Figure 192: Absolute error of DPMS Module 1336. Note that vertical axis is scaled to illustrate manufacturer's specifications.

Conclusions

The following channels were identified as problematic:

- Channel 31 (DPMS 1335)

- Channel 40 (DPMS 1335)

- Channel 56 (DPMS 1335)

- Channel 97 (DPMS 1336)

- Channel 118 (DPMS 1336)

From the tests, the following conclusions can be drawn:

- Channel 31 (DPMS 1335) performed inconsistently. The ratio of absolute error of Channel 31 to mean error magnitude of unaffected channels from DPMS 1335 varied between 1.14 and 8.26. Maximum full-scale error was 0.0393%.

- Channel 40 (DPMS 1335) is a dead channel. This was known prior to testing.

- Channel 56 (DPMS 1335) performed inconsistently. Four of six measurements were outside of the manufacturer's specifications. Problems with this channel had been noted previously. Maximum full-scale error was 0.2072%.

- Channel 97 (DPMS 1336) performed inconsistently. The ratio of absolute error of Channel 31 to mean error magnitude of unaffected channels from DPMS 1336 varied between 2.46 and 21.9. Maximum full-scale error was 0.0880%.

- Channel 118 (DPMS 1336) performed inconsistently. The ratio of absolute error of Channel 31 to mean error magnitude of unaffected channels from DPMS 1336 varied between 0.251 and 15.1. Maximum full-scale error was 0.0640%.

Excluding the affected channels, the ratio of maximum absolute value of error for an unaffected channel from DPMS 1335 to mean error was 2.80. For DPMS 1336, the value was 3.02.

The mean full-scale error for DPMS 1335 was 0.0063%. The mean full-scale error for DPMS 1335 was 0.0057%.

Therefore, while Channel 31, Channel 97 and Channel 118 have not performed outside the manufacturer's specification, they are not performing at the same level of accuracy as the other channels, with variations in error of approximately one order of magnitude.

Excluding the identified channels, the maximum error magnitude measured was 0.021% of the full-scale range.

The mean error magnitude measured, excluding the identified channels, was 0.0063% for DPMS 1335 and 0.0057% for DPMS 1336, expressed as a percentage of the full-scale range.

Expressed in terms of absolute pressure, the mean error measured was 0.189±0.489 Pa for DPMS 1335, and 0.399±0.489 Pa for DPMS 1336.

Note that the uncertainty in each case is a constant value of 0.489 Pa or 0.0163% of full-scale range (DPMS 1335) or 0.00698% of full-scale range (DPMS 1336), based on half the smallest increment of the Betz manometer.

Appendix: Vertical wind shear profiles in downburst events and the insufficiency of wind turbine design codes

This paper represents a body of work that was commenced by the author whilst working for Hydro

Tasmania Consulting and was completed during the course of their PhD candidature. The paper

below was presented at the 13th International Conference for Wind Engineering, held in Amsterdam

from 10-15 July, 2011.

Vertical wind shear profiles in downburst events and the insufficiency of wind turbine design codes

Jerome Rowcroft [a]

[a]Department of Mechanical and Aerospace Engineering,
Monash University, Clayton, Victoria, 3800, Australia,
jerome.rowcroft@monash.edu

Introduction

The extreme wind speed model published in IEC61400-1 (2005) Wind Turbine – Part 1: Design Requirements has provision for predicting wind speeds based on an assumed shear exponent of 0.11, based on a power law vertical shear profile.

Based on data from sixteen Australasian wind monitoring sites, this model for shear in extreme wind speeds has been shown to be insufficient. The data collected raises serious doubts as to the appropriateness of fitting a power law profile in extreme wind events and that the shear profile is not sufficiently conservative. A large proportion of the extreme wind events captured appear to be downburst events. The data are likely to have been significantly impacted by topographic effects, however the extreme wind model (EWM) in IEC61400-1 (2005) makes no allowances for terrain complexity.

Wind monitoring was conducted at heights ranging from 10 m to 80 m above ground level (AGL). The monitoring was conducted for the purpose of wind farm development; therefore, the site details must remain anonymous.

The extreme wind model

Wind turbine generators are classified based on their ability to withstand extreme winds and turbulence. Extreme wind analysis is based on extreme-value statistical methods including the Gumbel analysis. Therefore long records, ideally 20 years, are required to give the analysis statistical veracity (Cook 1985; Gumbel 1958). Hub height long term records are not generally available; as a result, various techniques have been developed to work around this, including correlation with other wind speed data.

Extreme wind analysis thus often relies on below hub height measurements which are used to predict wind speeds at hub height. Prediction of wind speed from a lower height to a higher height is a common practice in wind analysis. This process often utilises a power law relationship of the following form:

$$V(z) = V_{hub}(z/z_{hub})^{\alpha} \qquad (1)$$

$V(z)$ is the wind speed at height z; V_{hub} is the velocity at hub height; z_{hub} is the hub height; α is a constant, representing the power law exponent, as defined in IEC61400-1 (2005) Wind Turbine – Part 1: Design Requirements.

This relationship is found to hold within acceptable tolerances where z is a minimum of three-quarters of z_{hub} in boundary layer winds (Gardener et al, 2009, p.39). The EWM in IEC61400-1 (2005) Wind Turbine – Part 1: Design Requirements consists of the power law relationship with a power law exponent α set at 0.11. The wind speeds in the context of the EWM are 3 s gust wind speeds.

One of the key parameters for selecting a wind turbine generator for a site is how its design class matches up with the extreme wind regime on-site. Classes of turbines, based on survival wind speeds are listed in Table 1. V_{ref} is the 10-minute averaged 50 year return period wind speed, while V_{e50} is the 3 s gust wind speed with 50 year return period.

Table 1: Wind Turbine Classes as specified by IEC61400-1 (2005) Wind Turbine – Part 1: Design Requirements

Wind Turbine Class	I	II	III
V_{ref} [m/s]	50	42.5	37.5
V_{e50} [m/s]	70	59.5	52.5

While wind turbine manufacturers and designers do not necessarily specifically design to this standard, their turbines are nonetheless accredited based on this standard, and matched to site wind conditions based on that accreditation.

Wind monitoring campaigns

The analysis is based on data that Hydro Tasmania Consulting (now Entura) have accumulated over a twenty year period. The bulk of the sixteen sites are based in south-eastern Australia, with one site in Western Australia and two sites in New Zealand. Seven of the sites are considered to be coastal sites. The remaining nine sites are considered to be inland sites, providing a good representation of coastal and inland sites.

Further sites across Australia, New Zealand, China, India and South Africa were examined, but no records of maximum gust wind speeds in excess of 40 m/s were identified, hence these sites were not included in the analysis.

The height of measurements is presented in Table 2. As can be seen, twelve of sixteen sites have instruments at 70 m and or 80 m. These sites were being investigated for utility scale wind energy generation. The hub heights of wind turbine generators intended for use at these sites are in the range of 30 m to 80 m, though typically closer to 80 m.

Time series for wind events with peak wind speeds greater than 40 m/s were extracted from the database. The length of each record was a minimum of 4 h, with 2 h of data recorded before the event and a further 2 h of data following the event.

Table 2: Site list, anemometry heights, locations and events greater than 40 m/s.

Site	10m	16.5m	20m	30m	45m	50m	70m	80m	Location	Events
1				X		X	X		Inland	1
2				X		X	X		Coastal	7
3	X			X		X			Coastal	4
4	X			X		X			Inland	3
5		X		X					Coastal	7
6				X		X	X		Coastal	8
7				X			X		Coastal	3
8				X		X	X	X	Inland	1
9				X		X	X	X	Inland	1
10				X		X		X	Inland	2
11				X		X		X	Inland	2
12				X		X		X	Inland	2
13				X		X		X	Coastal	2
14				X		X			Inland	1
15				X		X		X	Inland	4
16			X		X		X		Coastal	12

The anemometry at all but three of the sites was Vaisala cup anemometers (WAA151) and Vaisala vane (WAV151). The remaining sites used Risøe anemometers (P2546) and Vector wind vanes (W200P). These were all mounted on triangular lattice masts.

Thirteen of the sixteen arrangements do not conform to best practice installations based on IEC61400-12-1 Appendix G (2005) as the vanes and anemometers were mounted side by side and the boom arms were of rectangular cross-section rather than streamlined for minimal flow interference. The remaining three sites conform to current international best practice wind monitoring.

The monitoring conducted using the Vaisala instrumentation recorded 150 s means and 2 s gusts. The remaining sites recorded 600 s means and 3 s gusts.

Establishing the veracity of recorded wind events

Determining the veracity of the data is a significant task. Various attempts to determine the legitimacy of some of the events used in this analysis were performed by Hydro Tasmania and the results were inconclusive. Hydro Tasmania enlisted the services of Mason (2005, 2006) at the University of Sydney to investigate five events. The primary concern highlighted by Mason was the unusual profile of the data, with high shear between the top anemometer and the lower anemometers, with "normal" shear profiles recorded between lower anemometers. However, Mason highlighted the fact that while the wind speed data (maxima, mean, turbulence intensity) were all dependent on the "counts" variable (the number of turns of the anemometer axis in a given time period), the temperature data and the direction were all independently measured, and in all but one of the events investigated, there was a corresponding decrease in temperature, indicating an atmospheric event of some significance. Mason (2006) alluded to a similar event in New South Wales, Australia, which was also measured in a commercial context. As such the details of the event, its location and the associated wind monitoring apparatus are vague, to ensure anonymity. The unusual shear profile was attributed to a logging error due to the length of cabling. Similar aspersions have been cast on this data.

An example of a case that has been rejected due to internal inconsistency of the data is presented in Figure 1. This case is significant as there appears to be an extreme event occurring, evidenced by the sharp drop in temperature after 2:30:00, and the wind speeds recorded are high; however the gust speed recorded at various stages is lower than the mean, which is physically impossible. One possibility is that a logging problem has caused the temporal misalignment of the mean and gust values. The reason for this might be a physical event, such as a lightning strike, which has caused the instrument to become non-operational for a period of time. While the data presented in Figure 1 is obviously in error, it is difficult to ascertain whether the data without these obvious inconsistencies are valid.

Suggestions as to the cause of the unusual wind speed profiles include lightning strikes, and full-scale readings for a portion of the sample. In the case of the WAA151, the full-scale wind speed is 75 m/s. Thus, if the output is sampled at 4 Hz, and the averaging period is 2 s, then in the case where one period (0.25 s) spikes to full-scale, given a real average wind speed of 40 m/s would correspond to an increase in wind speed of 11 %. In some instances the high shear lasted for four 150 s periods. Other than the occurrence of an extreme weather event (wind and possibly lightning), there appears to be no other physical cause for the reading. The author would be interested in hearing of similar events and whether they have been attributed to data logging problems and on what grounds.

In each extreme wind case presented in this paper, the shear profile returns to an expected shape very soon after the extreme wind event. Furthermore, post-event wind tunnel calibrations were also performed for some of the anemometers involved and no fault could be found. Similarly, a group of temperature sensors were also recalibrated and were found to have been operating within their published uncertainty.
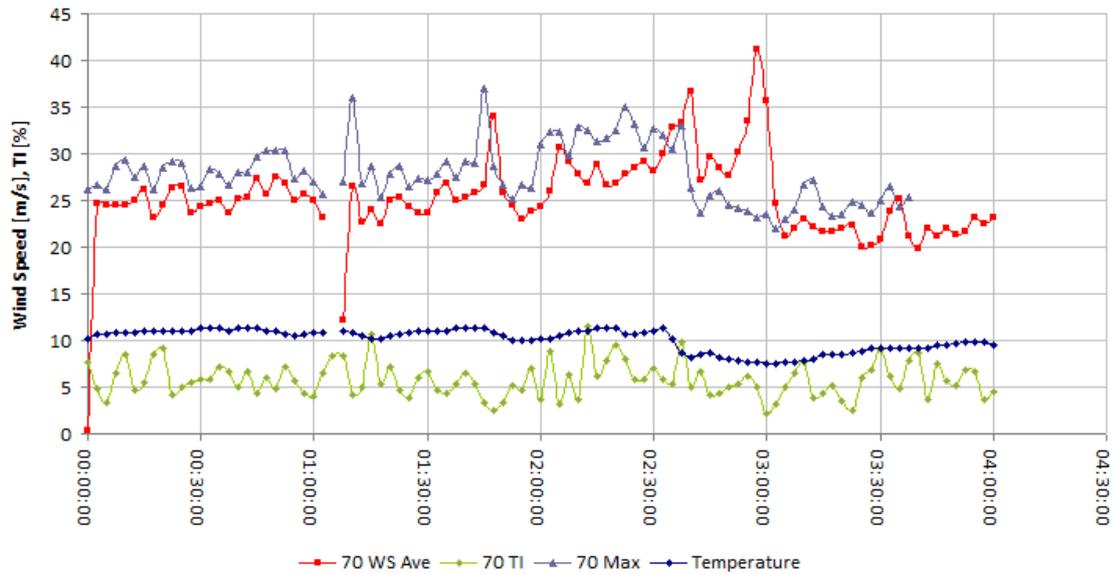
Figure 1. Data for excluded event at site 16. Includes mean speed, turbulence intensity, gust speed, temperature and direction. Temperature and wind speed records are calculated independently. This plot demonstrates internal inconsistencies in the data between the average and maxima measured at 70 m.

Characterising events as downbursts

Thunderstorm events are responsible for downburst events when warm moist air from the thunderstorm updraft can no longer be sustained (Letchford et al. 2002). The air cools and the density increases and cool air rushes downwards and spreads radially as it hits the ground. As such, downbursts are characterised by the following:

- Short lived event – lasting between 5 minutes and 30 minutes;
- Temperature drop – 1.5°C or more across the duration of the downburst;
- Increase in wind speed at more than one height;
- Wind speed differential greater than 10 m/s (Wilson et al. 1984).
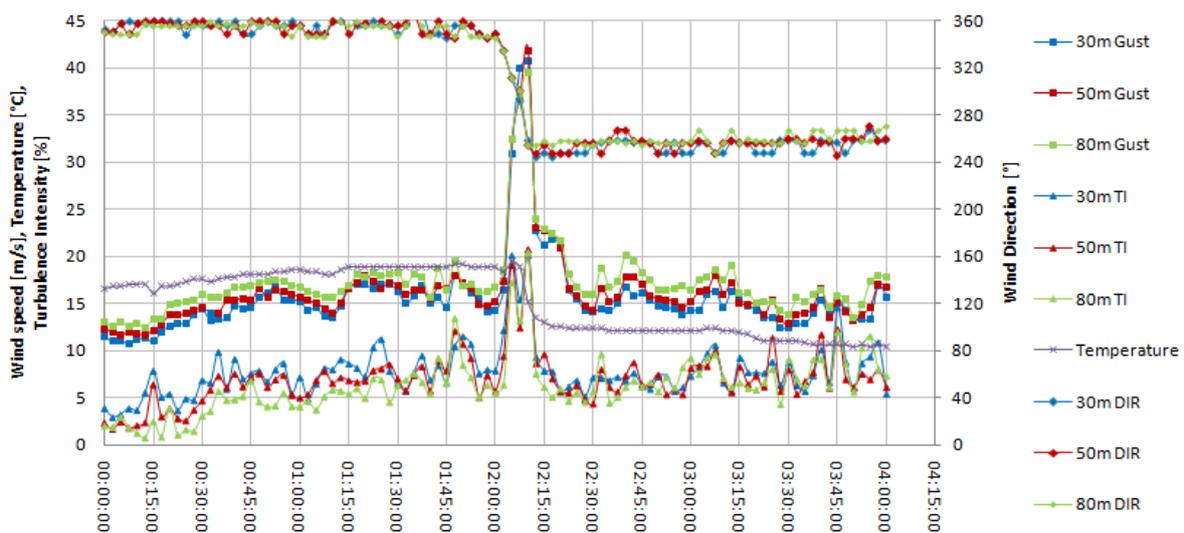
Figure 2. Data for textbook downburst event at site 15. Includes gust speed, turbulence intensity, temperature and direction. Note the large, short-lived spike in wind gusts at all levels, the dramatic change in wind direction and the sudden drop in temperature. The peak gust magnitudes occurs at 50 m, implying that the "nose" of the downburst is in that region.

299

Thunderstorm downbursts are also renowned for their distinctive vertical shear profiles with the maximum speeds, also known as the nose of the profile, typically between 50 m and 100 m AGL. Downbursts are sometimes, but not always associated with changes in wind direction.
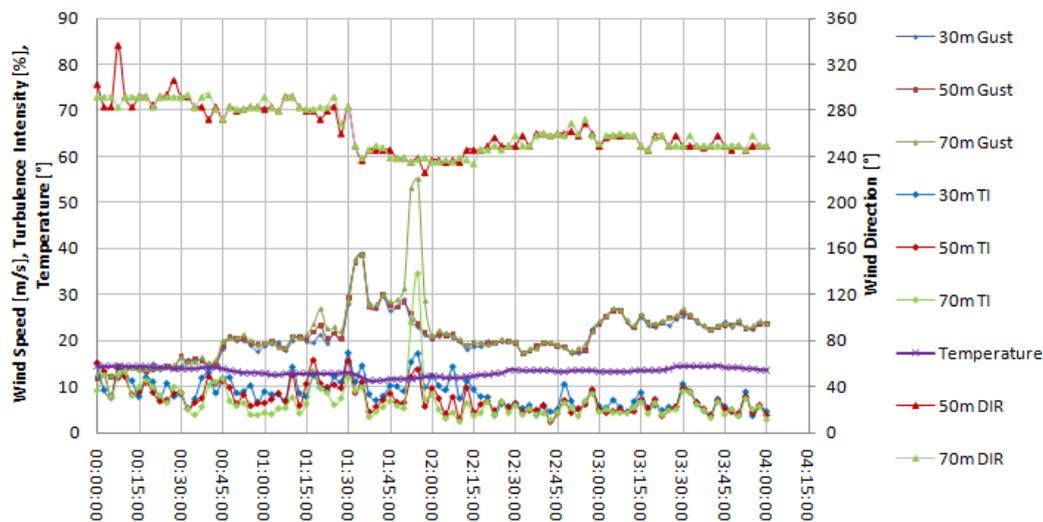

Figure 3. Data for wind event at site 2. Includes gust speed, turbulence intensity, temperature and direction. Note the initial event after 01:30:00 where the spike in wind speed occurs at all levels in association with the drop in temperature and change in wind direction. This is followed between 01:45:00 and 02:00:00 by the extreme wind event, with extreme shear. Note the increase in turbulence intensity at all levels as this occurs, matching the levels observed in the initial stages of the event.

Data series such as those found in Figures 1-4 have been examined according to these criteria and an assessment has been made as to whether a downburst event has occurred.

In the case of Figure 1, it is clear that the data is erroneous and the event was treated as such.

The case presented in Figure 2 appears to be a typical downburst profile, comparing favourably to previously published examples, with high wind speeds observed at all levels, for a short period of time, correlating with both a wind direction change and a significant temperature drop. The change of wind speed as a function of height above the ground is characterised by low shear that would not pose a problem when considered in terms of the EWM.

Figure 3 presents an event that is hypothesised to be a kind of downburst. The unusual aspect of the profile is a secondary peak gust seen directly in only the 70 m level that is much higher than any of the surrounding peaks, providing a shear profile that is in no way in accordance with the EWM. Interestingly, there is a rise in turbulence intensity in all levels at the same time as the large wind gust measured at 70 m. Additionally in Figure 3, there is evidence of a high shear wind gust occurring after 01:15:00, that, while not posing a large threat in terms of wind speed, can nonetheless be fitted with a power law shear exponent of magnitude 0.43, already four times what is prescribed in the EWM.

The event depicted in Figure 4 is one of the highest magnitude wind speed events in the dataset and has the potential to destroy a Class I wind turbine, according to the IEC classifications described in section 2. Again, the independently recorded temperature decreases over the period of the wind event. In keeping with the downburst characteristics, the event is also short-lived with a significant peak, as well as measuring peaks at other heights.

The concern is that the extreme wind events most commonly observed have more in common with the events depicted in Figures 3 and 4, than with the erroneous data or the "textbook" downbursts seen in Figures 1 and 2.
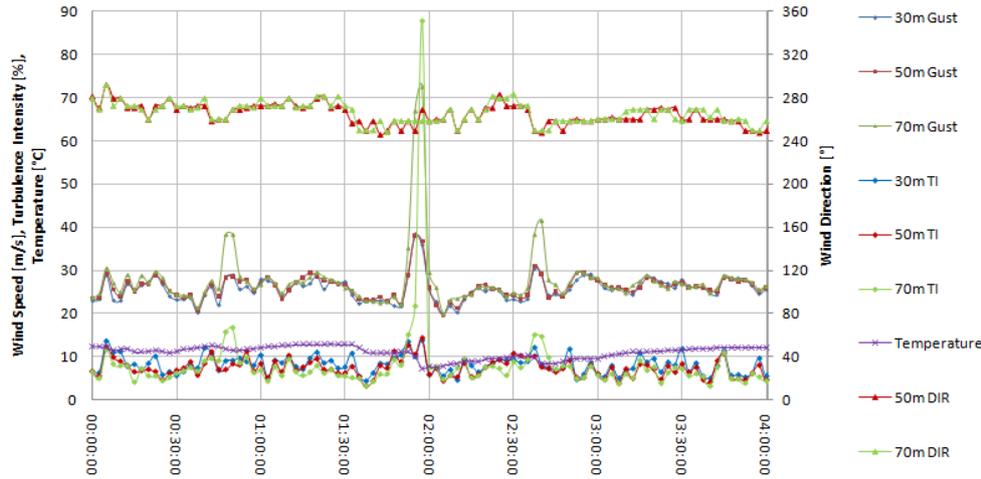
Figure 4. Data for wind event at site 2. Includes gust speed, turbulence intensity, temperature and direction. The shape of the peak in the 70 m wind gust curve is quite common in this dataset, though the magnitude of the peak is extreme.

Summary of profiles and Conclusions

Given the assertion that the wind events presented here are based on valid data, a significant number of extreme wind events can be attributed to downburst events, as seen in Table 3. With further independent verification, it can be confirmed that in southern Australia, downbursts are responsible for a large percentage of extreme wind events.

Table 3: Distribution of Downburst Events. Note that "Events" column includes all available records of data with wind gusts greater than 40 m/s. The column "Downburst Events" are filtered from erroneous data and are sorted according to the characteristics defined in section 5.

Site	Events	Downburst Events	Site	Events	Downburst Events
1	1	0	9	1	1
2	7	6	10	2	1
3	4	3	11	2	0
4	3	1	12	2	0
5	7	2	13	2	2
6	8	5	14	1	0
7	3	0	15	4	1
8	1	1	16	12	9
			TOTAL	60	32

This preliminary analysis of the frequency of extreme wind events, and subsequently the frequency of downbursts within that dataset, demonstrates that extreme wind models, in particularly that provided in IEC61400-1 (2005) Wind Turbine – Part 1: Design Requirements should account for such wind events. However, if the vertical wind shear profiles obtained are consistent with the EWM, there is no need for further refinement of the EWM.

Figure 5 and Figure 6 are plots of the natural logs of normalised wind speeds and heights from site 16. Figure 5 presents the 150 s mean profiles and Figure 6 presents the 2 s gust profiles. These results are typical of results from the other sites, in particular, the event measured at site 2, depicted in Figures 3 and 4. The other results have been omitted for clarity and brevity.

In a power law shear profile, including the profile from the aforementioned EWM, the points should be approximately linear with the gradient representing the power law exponent, α. The black line in each figure represents the EWM. Whilst data from only one site are shown in the figures, they still emphasise the insufficiency of the EWM, both in type (power law

profile) and in magnitude (exponent insufficiently conservative). The first point is clear from the fact that only events 2, 8 and 9 are remotely linear, and indeed, only Events 2 and 9 from data at site 16 fit with the prescribed shear exponent. Furthermore, Figure 6, representing 2 s wind gusts, demonstrates a far more significant divergence from the EWM than the 150 s mean profiles in Figure 5.
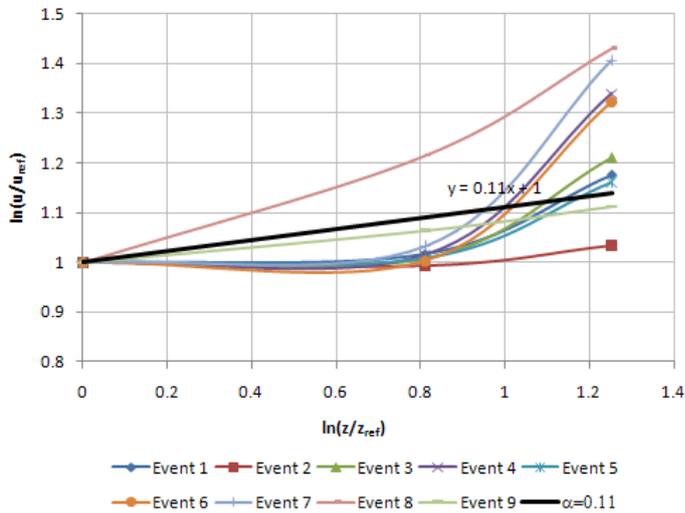

Figure 5. Natural logs of normalised 150 s mean wind speeds against natural logs of normalised heights for downburst events from site 16. (right)
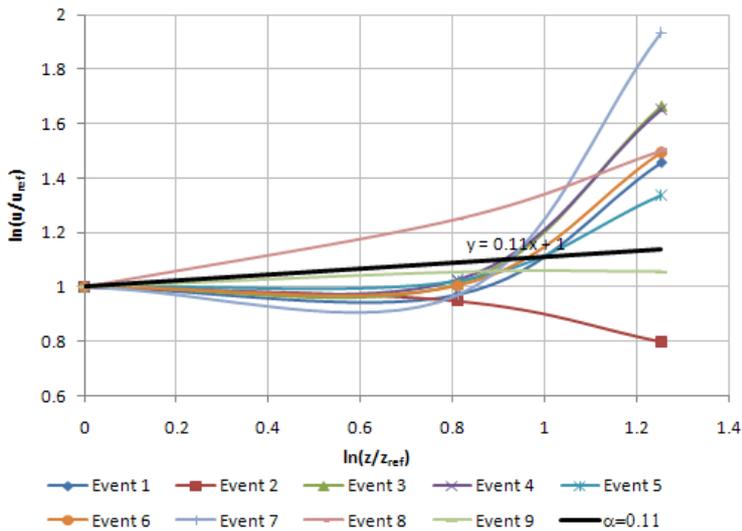

Figure 6. Natural logs of normalised 2 s gust wind speeds against natural logs of normalised height for downburst events from site 16.

Because long term site records are not typically available, it is common practice to obtain long term records from nearby weather stations. Weather stations usually have wind speed and direction data measured at 10 m AGL. A Gumbel analysis would be performed on the dataset to determine annual and 50-year return wind speeds. The results presented in this paper demonstrate that implementing the EWM to determine V_{e50} at hub height from measurements recorded at lower than hub height is ill-advised. The height at which the extrapolation is

performed is less of a concern than the inappropriateness of the curve, as the data obtained does not fit a standard atmospheric boundary layer profile.

The extreme wind speed data analysed here in no way validates the EWM presented in IEC61400-1 (2005).

The author acknowledges the difficulty in accepting all of the data as valid, as there appears to be a unique wind speed profile occurring in most of the events unreported in the current literature. However, given each of the wind monitoring campaigns referred to in this paper were conducted according to standard industry practice of the time, it would be unwise to disregard the data without sufficient grounds. Independent observations of similar profiles would add significant weight to the dataset.

Acknowledgements

References

IEC61400-1 (2005) Wind Turbine – Part 1: Design Requirements, 3rd Ed., International Electrotechnical Commission, Geneva.

Cook, N. J. (1985), The Designer's Guide to Wind Loading of Building Structures, Butterworths, London, Section 5.3.2 and Appendix C.

Gumbel, E. J. (1958), Statistics of Extremes, Columbia University Press, New York.

Gardner, P., A. Garrad, et al. (2009). Part 1: Technology. Wind Energy - The Facts. London, Earthscan, European Wind Energy Association: 29-152.

IEC61400-12-1 (2005), Power performance measurements of electricity producing wind turbines, 1st Ed., International Electrotechnical Commission, Geneva.

Mason, M., Wood, G. (2005). Report on extreme wind events recorded by Hydro Tasmania, Report S-1471.

Mason, M., Wood, G. (2006). Report S-1472.

Letchford, C.W.; Mans, C.; Chay, M.T. (2002). Thunderstorms – their importance in wind engineering (a case for the next generation wind tunnel), J. of Wind Eng. & Ind. Aero, 90, pp1415-1433.

Wilson, J. W., R. D. Roberts, et al. (1984). "Microburst wind structure and evaluation of Doppler radar for airport wind shear detection." Journal of Climate and Applied Meteorology 23: 898-915.